

THESIS FOR THE DEGREE OF DOCTOR OF PHILOSOPHY

Design and Optimization Considerations of  
Medium-Frequency Power Transformers in High-Power  
DC-DC Applications

MOHAMMADAMIN BAHMANI



Division of Electric Power Engineering  
Department of Energy and Environment  
Chalmers University of Technology  
Gothenburg, Sweden, 2016

**Design and Optimization Considerations of Medium-Frequency Power Transformers in High-Power DC-DC Applications**

MOHAMMADAMIN BAHMANI

ISBN 978-91-7597-344-9

©MOHAMMADAMIN BAHMANI, 2016.

Doktorsavhandlingar vid Chalmers tekniska högskola

Ny serie nr. 4025

ISSN 0346-718X

Division of Electric Power Engineering

Department of Energy and Environment

SE-412 96 Gothenburg

Sweden

Telephone +46 (0)31-772 1000

Printed by Chalmers Reproservice

Gothenburg, Sweden 2016

*To Aryan*



# Abstract

Recently, power electronic converters are considered as one of the enabling technologies that can address many technical challenges in future power grids from the generation phase to the transmission and consequently distribution at different voltage levels. In contrast to the medium-power converters (5 to 100 kW) which have been essentially investigated by the automotive and traction applications, megawatt and medium-voltage range isolated converters with a several kilohertz isolation stage, also called solid-state transformers (SST), are still in an expansive research phase.

Medium-frequency power transformers (MFPT) are considered as the key element of SSTs which can potentially replace the conventional low-frequency transformers. The main requirements of SSTs, i.e., high power density, lower specific losses, voltage adaptation and isolation requirements are to a great extent fulfilled through a careful design of MFPTs.

This work proposes a design and optimization methodology of an MFPT accounting for a tuned leakage inductance of the transformer, core and windings losses mitigation, thermal management by means of a thermally conductive polymeric material as well as high isolation requirements. To achieve this goal, several frequency-dependent expressions were proposed and developed in order to accurately characterize such a transformer. These expressions are derived analytically, as in frequency-dependent leakage inductance expression, or based on finite element method (FEM) simulations, as in the proposed expression for high-frequency winding loss calculation. Both derived expressions are experimentally validated and compared with the conventional methods utilizing detailed FEM simulations.

Utilizing the proposed design method, two down-scaled prototype transformers, 50 kW/5 kHz, have been designed, manufactured and measured. The nanocrystalline-based prototype reached an efficiency of 99.66%, whereas the ferrite-based transformer showed a measured efficiency of 99.58%, which are almost the same values as the theoretically predicted ones. Moreover, the targeted value of prototype's leakage inductances were achieved through the proposed design method and were validated by measurements.

Finally, using SiC MOSFETs and based on the contribution above, the efficiency and power density of a 1 / 30 kV, 10 MW turbine-based DC-DC converter with MFPT are quantified. It was found that, with respect to the isolation requirements,

there is a critical operating frequency above which the transformer does not benefit from further volume reduction, due to an increased frequency.

**Keywords**

Medium-Frequency Power Transformer, High-Power Isolated DC-DC Converter, Solid-State Transformers, Isolation Requirements, Leakage Inductance.

# Acknowledgment

This project has been funded by the Swedish Energy Agency. A great thank goes to them for the financial support.

I would like to express my sincere gratitude to my supervisor and examiner Prof. Torbjörn Thiringer who always finds time to support whenever needed, especially at the most desperate moments. His patience, guidance and emphasis on educating a researcher is very appreciated. Thank you! I would also like to thank my co-supervisor Dr. Tarik Abdulahovic for his friendship and contribution to the project.

Special thanks to Dr. Lars Kvarnsjö from VACUUMSCHMELZE for providing the nanocrystalline cores and useful discussions. Thanks to Assoc. Prof. Staffan Norrga from KTH for lending us the HF-ring transformer used for the laboratory setup.

My acknowledgments go to the members of the reference group Prof. Philip Kjaer, Dr. Anders Holm, Dr. Urban Axelsson, Dr. Aron Szucs, Dr. Thomas Jonsson, Dr. Frans Dijkhuizen and Dr. Luca Peretti. I would also like to thank Prof. Yuriy Serdyuk, Prof. Stanislaw Gubanski, Prof. Hector Zelaya, Prof. Hans Kristian Høidalen and Dr. Edris Agheb for their contribution at the early stage of the project.

Special thanks to all my Master and Bachelor thesis students, specially Majid Fazlali, Maziar Mobarrez, Hector Ortega Jimenez, Sadegh Moeinian, Junxing Huang and Mohammad Kharezy who helped me to improve my skills on several levels. Their contribution to the thesis is appreciated, in particular Mohammad. Kharezy who was involved in any detail of the prototype construction and measurements. For the latter, I would like to send a great thanks to ÅForsk, and SP, especially Johan Söderbom, who through financing and other efforts assisted in making this cooperation possible.

Many thanks to all my dear colleagues in the division of Electric Power Engineering for making such a great environment to work in, and to my roommates, Mattias and Mebtu, for being great friends. Special thanks to Robert Karlsson, Ali Rabiei and Carl Thiringer for the helps during the lab and to all the colleagues in the division of High Voltage Engineering for their patience during the noisiest part of the measurements, in particular at 2 kHz!

I would also like to thank my parents and my brother for all their help and sup-

port which I am forever grateful for. Last, but certainly not least, heartfelt thanks go to my wife, Aryan, for her love, encouragement and understanding. Without you this would have not been possible.

Amin Bahmani  
Göteborg, Sweden  
Feb, 2016



# List of Abbreviations

<b>1-D</b>	One Dimensional
<b>2-D</b>	Two Dimensional
<b>3-D</b>	Three Dimensional
<b>AC</b>	Alternating Current
<b>AUD</b>	Average Unsigned Deviation
<b>DAB</b>	Dual Active Bridge
<b>DC</b>	Direct Current
<b>DG</b>	Distributed Generation
<b>DUT</b>	Device Under Test
<b>FBC</b>	Full-Bridge Converter
<b>FEM</b>	Finite Element Method
<b>GSE</b>	Generalized Steinmetz Equation
<b>GTO</b>	Gate Turn-off Thyristor
<b>HF</b>	High Frequency
<b>HFPT</b>	High-Frequency Power Transformer
<b>HFT</b>	High-Frequency Transformer
<b>HV</b>	High Voltage
<b>IGBT</b>	Insulated-Gate Bipolar Transistor
<b>IGCT</b>	Integrated-Gate Commutated Thyristor

<b>IGSE</b>	Improved Generalized Steinmetz Equation
<b>ISOP</b>	Input Series Output Parallel
<b>LF</b>	Low Frequency
<b>LFT</b>	Low-Frequency Transformer
<b>LV</b>	Low Voltage
<b>M2DC</b>	Modular Multilevel DC Converter
<b>MF</b>	Medium Frequency
<b>MFPT</b>	Medium-Frequency Power Transformer
<b>MFT</b>	Medium-Frequency Transformer
<b>MOSFET</b>	Metal Oxide Field Effect Transistor
<b>MSE</b>	Modified Steinmetz Equation
<b>MV</b>	Medium Voltage
<b>OSE</b>	Original Steinmetz Equation
<b>PETT</b>	Power Electronic Traction Transformer
<b>PISO</b>	Parallel Input Series Output
<b>PMSG</b>	Permanent-Magnet Synchronous Generator
<b>PWM</b>	Pulse-Width Modulation
<b>RMS</b>	Root Mean Square
<b>SAB</b>	Single Active Bridge
<b>SiC</b>	Silicon Carbide
<b>SRC</b>	Series Resonant Converter
<b>SST</b>	Solid-State Transformer
<b>WCSE</b>	Waveform-Coefficient Steinmetz Equation
<b>ZCS</b>	Zero-Current Switching
<b>ZVS</b>	Zero-Voltage Switching

# Contents

<b>Abstract</b>	<b>v</b>
<b>Acknowledgment</b>	<b>vii</b>
<b>List of Abbreviations</b>	<b>ix</b>
<b>1 Introduction</b>	<b>1</b>
1.1 Background . . . . .	1
1.1.1 Semiconductor Switches . . . . .	3
1.1.2 HF/MF Power Transformers . . . . .	4
1.1.3 Purpose of the Thesis and Contributions . . . . .	5
1.2 Layout of Thesis . . . . .	7
1.3 List of Publications . . . . .	7
1.3.1 Journal Articles . . . . .	7
1.3.2 Conference Proceedings . . . . .	8
1.4 Potential Applications . . . . .	8
1.4.1 Collector Grid in All-DC Offshore Wind Farms . . . . .	8
1.4.2 Traction . . . . .	10
1.4.3 Flexible-HF Distribution Transformers / Solid-State Trans- formers (SSTs) Between MVAC and LVDC/AC for the Future Smart Grids . . . . .	11
1.4.3.1 MVAC/LVAC . . . . .	12
1.4.3.2 MVAC/LVDC . . . . .	13
<b>2 High-Frequency Winding Losses</b>	<b>15</b>
2.1 Introduction . . . . .	15
2.2 Validity Investigation . . . . .	16
2.2.1 Dowell's Expression for Foil Conductors . . . . .	16
2.2.2 Edge Effect Analysis . . . . .	24
2.2.3 Round Conductors . . . . .	25
2.3 Pseudo-Empirical Model Establishment . . . . .	30
2.3.1 Determinant Variable Definition . . . . .	32

2.3.2	Generic Parameters and the Domain of Validity . . . . .	34
2.3.3	Multi-Variable Regression Strategy . . . . .	35
2.3.3.1	Structure Selection . . . . .	35
2.3.3.2	Database Collection . . . . .	36
2.3.3.3	Primary Regression Process . . . . .	36
2.3.3.4	Secondary Regression Process (Model Extension) . . . . .	39
2.3.4	Accuracy Investigation for Round Conductors . . . . .	41
2.3.5	Accuracy Investigation for Interleaved Winding . . . . .	44
2.4	Experimental Validation . . . . .	46
2.5	Conclusions . . . . .	47
<b>3</b>	<b>Leakage Inductance</b> . . . . .	<b>51</b>
3.1	Introduction . . . . .	51
3.2	Expression Derivation . . . . .	55
3.3	Accuracy Investigation . . . . .	59
3.3.1	Comparison with Classical Expressions . . . . .	59
3.3.2	Comparison with Frequency Dependent Expressions . . . . .	62
3.4	Experimental Validation . . . . .	65
3.5	Conclusions . . . . .	66
<b>4</b>	<b>Magnetic Core</b> . . . . .	<b>67</b>
4.1	Introduction . . . . .	67
4.2	Magnetic Material Selection . . . . .	68
4.3	Core Loss Calculation Methods . . . . .	70
4.3.1	Loss Separation Methods . . . . .	70
4.3.1.1	Eddy Current Losses . . . . .	71
4.3.1.2	Hysteresis Losses . . . . .	71
4.3.1.3	Excess Losses or Anomalous . . . . .	72
4.3.1.4	Total Core Losses . . . . .	72
4.3.2	Time Domain Model . . . . .	73
4.3.3	Empirical Methods . . . . .	75
4.3.3.1	OSE . . . . .	75
4.3.3.2	MSE . . . . .	76
4.3.3.3	GSE . . . . .	76
4.3.3.4	IGSE . . . . .	77
4.3.3.5	WCSE . . . . .	77
4.4	Modified Empirical Expressions for Non-Sinusoidal Waveforms . . . . .	78
4.4.0.6	Modified MSE . . . . .	79
4.4.0.7	Modified IGSE . . . . .	79
4.4.0.8	Modified WCSE . . . . .	79
4.4.1	Validity Investigation for Different Duty Cycles, $D$ . . . . .	80
4.4.2	Validity Investigation for Different Rise Times, $R$ . . . . .	81

4.5	Conclusions . . . . .	83
<b>5</b>	<b>Design Methodology with Prototypes</b>	<b>85</b>
5.1	Introduction . . . . .	85
5.2	DC-DC Converter Topology . . . . .	86
5.3	Optimization Procedure . . . . .	87
5.3.1	System Requirements and Considerations . . . . .	88
5.3.2	Fixed Parameters . . . . .	88
5.3.2.1	Magnetic Core Material . . . . .	88
5.3.2.2	Windings . . . . .	91
5.3.2.3	Insulation Material and Distances . . . . .	93
5.3.3	Free Parameters . . . . .	93
5.3.4	Geometry Determination with Rectangular Litz Conductors . . . . .	95
5.3.4.1	Isolation Distance, $d_{iso}$ . . . . .	97
5.3.5	Losses Calculations . . . . .	98
5.3.5.1	Core Losses . . . . .	98
5.3.5.2	Windings Losses . . . . .	99
5.3.5.3	Dielectric Losses . . . . .	100
5.3.6	Thermal Analysis . . . . .	100
5.3.6.1	Isotherm Surface Model . . . . .	101
5.3.6.2	Thermal Network Model . . . . .	103
5.4	Down-Scaled Prototype Design and Optimization . . . . .	111
5.4.1	Design and Optimization Results . . . . .	112
5.4.2	Built Prototypes . . . . .	114
5.5	Experimental Verification . . . . .	117
5.5.1	Core Losses Verification . . . . .	118
5.5.1.1	Cut-Core Effects . . . . .	120
5.5.2	Winding Losses Verification . . . . .	121
5.5.3	Leakage Inductance Verification . . . . .	122
5.6	Conclusions . . . . .	123
<b>6</b>	<b>High-Power Isolated DC-DC Converter in All-DC Offshore Wind Farms</b>	<b>125</b>
6.1	Introduction . . . . .	126
6.2	Design and Optimization Approach . . . . .	128
6.2.1	System Specifications . . . . .	128
6.2.2	Converter Topology . . . . .	128
6.2.2.1	DAB Operation . . . . .	130
6.2.3	Semiconductor losses . . . . .	134
6.3	Optimized Medium-Frequency Power Transformer . . . . .	135
6.3.1	Transformer Topology . . . . .	136
6.3.2	Transformer Design . . . . .	136

---

6.3.3	Geometry Construction with Foil Conductors . . . . .	137
6.3.3.1	Isolation Distance . . . . .	139
6.3.3.2	Core Losses . . . . .	141
6.3.3.3	Conductor Losses . . . . .	141
6.3.3.4	Dielectric Losses . . . . .	142
6.3.3.5	Thermal Management . . . . .	143
6.3.4	Transformer Optimization Approach . . . . .	143
6.3.5	Optimization Results . . . . .	146
6.4	Losses Breakdown . . . . .	147
6.5	Optimum Frequency . . . . .	148
6.6	Conclusion . . . . .	150
<b>7</b>	<b>Conclusions and Future Work</b>	<b>153</b>
7.1	Conclusions . . . . .	153
7.2	Future Work . . . . .	154
	<b>Bibliography</b>	<b>155</b>

# Chapter 1

## Introduction

### 1.1 Background

Moving towards higher power densities in power conversion units is an activity that has been receiving wide attention over the past decade, particularly in highly restricted applications such as remotely located offshore wind farms and traction [1,2]. Increasing the operational frequency is the most common solution to achieve higher power densities, since the weight and volume of the magnetic part, perhaps the bulkiest element in power electronic converters, are then decreased. This solution is well established in low-power high frequency applications, while in the recent decade, the possibility of utilizing high frequency at higher power and voltage levels has generated wide interest as well [3,4]. However, taking high power, high voltage and high frequency effects into account, there are several challenges to be addressed since the technology in this field is not mature enough yet.

Recently, power electronic converters are considered as one of the enabling technologies that can address many technical challenges in future power grids from the generation phase to the transmission and consequently distribution at different voltage levels [5,6]. In contrast to the medium power converters (5 to 100 kW) which have been essentially investigated by the automotive and traction applications, megawatt and medium voltage range isolated converters with a several kilohertz isolation stage are still in an expansive research phase [7].

Under the scope of grid applications, one of the most cited terminologies for these kinds of high-power converters is called solid-state transformer (SST) which is in fact AC-AC or DC-DC high power converters whereby the voltage adaptation and high-frequency isolation, to reduce the weight and volume, are achieved [8,9]. An example of such a conversion unit is illustrated in Fig. 1.1 which is a three-stage SST. Additionally, these SSTs provide new functionalities and advantages for the grid and conversion system which were not possible with conventional passive AC transformers. One of the main new functionalities, among others, is the higher flex-

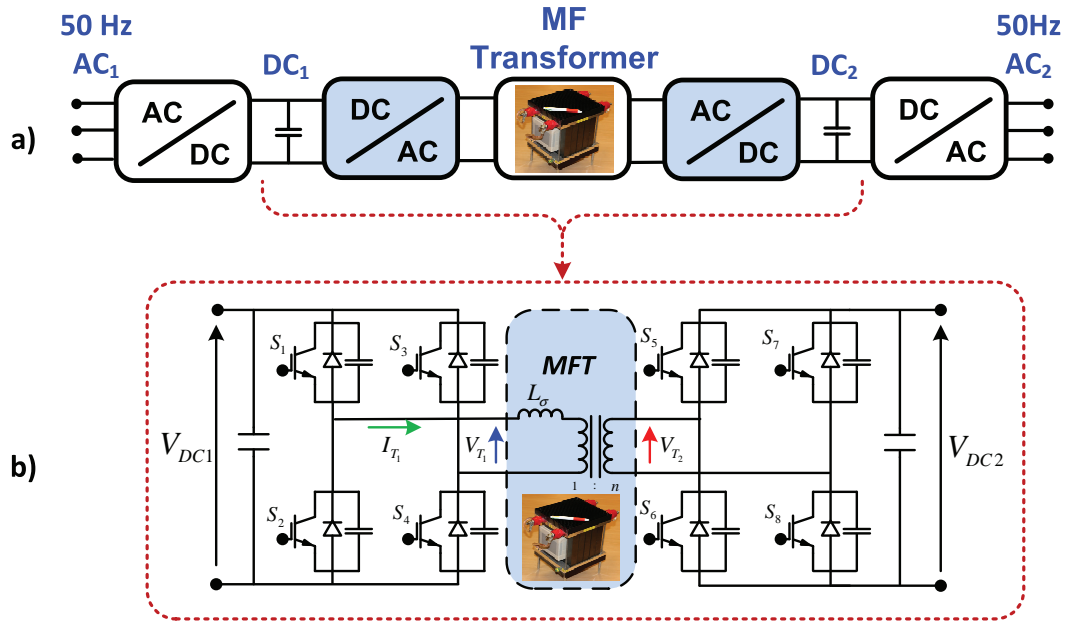


Figure 1.1: (a) A three-stage AC-AC solid-state transformer. (b) The high-power isolated DC-DC stage with medium-frequency transformer

ibilities, disturbance isolation and the control of the power flow since voltage and current regulation is possible using power semiconductors. Moreover, the availability of the LV DC bus enables easier integration of energy storages and distributed generations (DGs) as well as DC micro-grids. Additionally, the availability of the MV DC bus gives the possibility of a likely future DC-grid expansion in which high-power isolated DC-DC converters play the equivalent role of the existing electromagnetic transformers in AC grids with the aforementioned additional functionalities [10].

The specific design requirements and implementation of SSTs directly depends on the application in which it will be used. Although, it can be stated that general design requirements of SSTs to be used in likely future generation, transmission and distribution systems, are

- High efficiency.
- High power density.
- Handling high voltage and high frequency.
- Modularity as a measure to handle the high power (MW) and to achieve a robust system.
- High isolation requirements of the transformers.



- Power flow control.
- Availability of DC buses throughout the multi-stage conversion in the power flow direction.

Despite that the general structure of SSTs do not seem to largely differ from other power electronic converters, there are several main challenges for the design and implementation of the concept. These challenges essentially originate from the basic requirements of SSTs, i.e., simultaneous fulfillment of high power, high voltage and high frequency requirements.

These requirements are in particular challenging when it is imposed on the high-power isolated DC-DC stage, which provides the voltage conversion and high-frequency galvanic isolation, and is the main contributor to achieve the high efficiency and high-power density [10,11]. In principle, the challenges within the isolated DC-DC stage can be divided into two main categories, i.e., semiconductor switches and the HF/MF power transformers. The latter is the main scope of this thesis.

### 1.1.1 Semiconductor Switches

Taking the MW, kV and kHz ranges of the considered SSTs into account, the current semiconductor technologies, e.g., IGBTs, IGCTs and emitter turn-off thyristors should undertake a revolutionary phase to be able to cope with these high voltage and current stresses as a single device. This seems to be very unlikely in the early future. Under this scope, one of the key concerns is the rating of the power devices [12].

One possible solution is to consider the newly developed wide-bandgap materials, i.e., silicon carbide (SiC) material which has a potential to be the basis for the next generation of ultra HV devices. Many investigations have recently turned to the characterization of these devices [13, 14], in particular the 10 kV/10 A SiC MOSFETs and the 15 kV/20 A SiC IGBTs are extensively investigated in [15]. The overall investigation indicates that, in future high-power electronics, SiC MOSFETs and IGBTs will be natural choices at voltage levels below 20 kV, whereas for higher voltage levels SiC GTOs or thyristors are likely to be used.

Although the voltage and current rating of the SiC devices are likely to improve in the early future, as for example the recent fabrication of the 15 kV/10 A SiC MOSFETs by Cree Inc [16], they are still far from commercial availability and have long paths ahead to be competitive with their silicon counterpart, therefore, they should only be seen as one of the possible future solutions.

Series connection of LV devices, Fig. 1.2(a), might be another solution to achieve higher blocking voltages, however, voltage balancing during the dynamic transient is a challenge dictating lower switching frequencies [15]. Extra snubber circuits are also necessary in this solution.

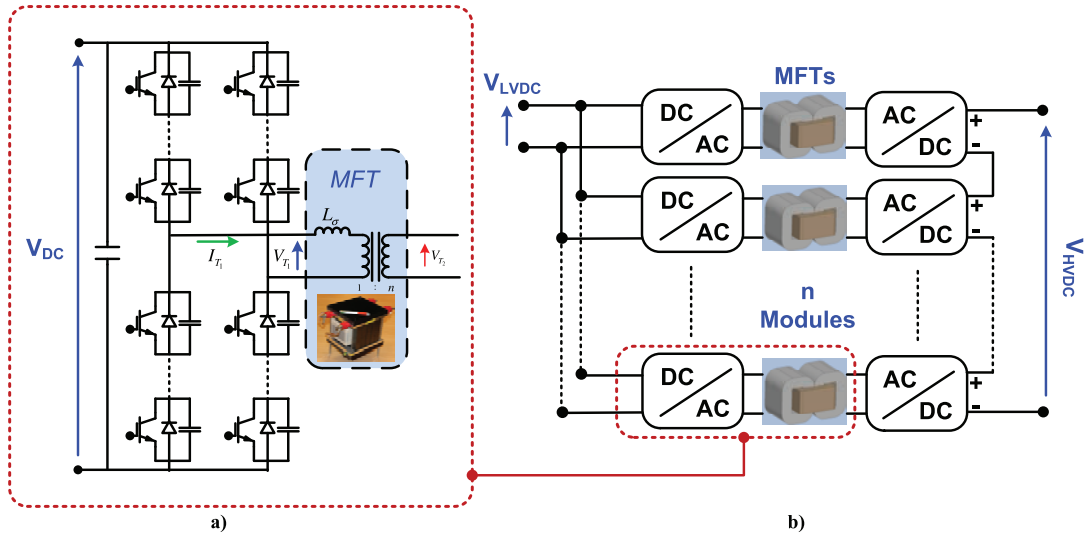


Figure 1.2: (a) Modularity from device-level (b) modularity from converter level as series/parallel connections of building blocks.

Apart from the modularity in device level (series connection of LV devices), modularization at converter level in the voltage direction is another voltage scalability factor, Fig. 1.2(b). This can be achieved by making series or parallel connection of converter modules as building blocks in MV or LV DC links or even on the AC side of the SST when a multi-stage conversion system is considered. Each power cell in this topology requires an MFT which should handle the entire voltage of the MV DC link.

### 1.1.2 HF/MF Power Transformers

Medium-frequency power transformers are the key elements of SSTs which can potentially replace the conventional LF transformers. The main requirements of SSTs, i.e., high power density, lower specific losses, voltage adaptation and isolation requirements are entirely or to a great extent fulfilled through a careful design of medium-frequency power transformers.

However, taking high power, high voltage and high frequency effects into account, there are several challenges to be addressed. These challenges are basically related to the extra losses as a result of eddy current in the magnetic core, excess losses in the windings due to enhanced skin and proximity effects [17] and parasitic elements, i.e., leakage inductance and winding capacitances, causing excess switching losses in the power semiconductors, which are usually the dominant power losses at higher frequencies [18]. These extra losses together with the reduced size of the transformer lead to higher loss densities requiring a proper thermal management scheme in order to dissipate these power losses from a smaller component. This would be even more

challenging when, unlike for a line-frequency power transformers, an oil cooled design is not a preference and the transformer needs to fulfill MV isolation requirements.

Most of the classical attempts for high frequency transformer design were focused on a parameter called area product whereby the power handling capability of the core is determined [19, 20]. However, it remains unclear whether this parameter is valid for high power high frequency applications or not. Petkov in [21] presented a more detailed design and optimization procedure of high power high frequency transformers. Some years later, Hurley [22] reported a similar approach accounting for non-sinusoidal excitations. However, the effect of parasitics are essentially neglected in both approaches. In [23], design considerations of a 3 MW, 500 Hz transformer were presented and it was shown that the designed transformer can be more than three times lighter than the equivalent 50 Hz one. In [24], two 400 kVA transformers based on silicon steel and nanocrystalline material for railway traction applications operating at 1 and 5 kHz, respectively, were designed. A systematic analysis, design and prototyping of two 166 kW/ 20 kHz solid-state transformers was presented in [25, 26]. Utilizing round-litz conductors and water-cooled aluminum plates, one of the medium-frequency transformers achieved the high power density of 32.7 kW/liter, however, this was at the expense of considerable extra losses, nearly 50% of the copper losses, due to the use of aluminum plates.

Despite the achievements in the aforementioned works, the design and optimization of MF transformers should be further investigated to ensure efficient and compact design. This can be realized by incorporating special thermal management schemes, new generation of magnetic materials, a careful selection of conductor type and winding strategy, better insulation mediums, among other determinant design factors. Moreover, although considerable research has been devoted to high frequency transformer design, rather less attention has been paid to the validity of the conventional theoretical and empirical methods to evaluate the power losses and parasitics. Considering the above mentioned facts, it is important to investigate the validity of conventional methods and to modify and improve their accuracy in some cases. This is particularly of importance at high power and high-frequency applications in which the design is pushed to its limits and the component enhanced loss density makes it necessary for researchers and designers to more accurately evaluate these losses in order to properly implement a thermal management scheme.

### 1.1.3 Purpose of the Thesis and Contributions

The main objective of the work reported in this thesis is to propose a design and optimization methodology of an MFPT accounting for a tuned leakage inductance of the transformer, core and windings losses mitigation, thermal management by means of a thermally conductive polymeric material as well as high isolation requirements, particularly in remote DC-offshore application, where a converter module should

withstand the entire MVDC or HVDC-link voltage. To the best of the author's knowledge, the main contributions of the thesis are:

- Proposing a design and optimization methodology of an MFPT based on the modified and developed theoretical expressions in this work. Unlike conventional power electronic transformer designs, the leakage inductance is considered as one of the design inputs in the same manner as power ratings or voltage levels. In addition, applicability of the square-type litz conductors and nanocrystalline magnetic materials are different design aspects addressed in the proposed approach.
- Based on the contribution above, the efficiency and power density of a 1/30 kV, 10 MW turbine-based DC-DC converter with MFPT are quantified. It was found that, with respect to the isolation requirements, there is a critical operating frequency above which the transformer does not benefit from further volume reduction, due to an increased frequency.
- Validating the proposed design and optimization approach by applying it on two down-scaled 50 kW, 1 / 3 kV, 5 kHz prototype transformers. The optimized designs have then been carefully manufactured and successfully measured, fulfilling the efficiency, power density and leakage inductance requirements that the prototypes were designed for.
- Proposing a pseudo-empirical expression to accurately calculate the AC resistance factor of foil and round type conductors in switch-mode magnetics without the need to use finite element simulations for each design variant. This expression can be used for both foil and round conductors in a wide range of frequencies and for the windings consisting of any number of layers with free number of turns per layer. The validity and usage of the expression is experimentally validated. Moreover, a validity investigation performed on the conventional models comprising of theoretical investigations, simulations and measurements.
- Proposing an analytical expression to accurately calculate the value of leakage inductance particularly when the transformer operates at high frequencies. The expression takes into account the effects of high frequency fields inside the conductors as well as the geometrical parameters of the transformer windings. This expression is also validated using FEM simulations as well as measurements.

## 1.2 Layout of Thesis

The thesis structure is arranged in the way that the chapters correspond to different work efforts, topic-wise, rather than being arranged as full thesis covering chapters as theory, case-set-up, simulations, measurement and analysis.

## 1.3 List of Publications

### 1.3.1 Journal Articles

- [I] Bahmani, M.A.; Thiringer, T., “Accurate Evaluation of Leakage Inductance in High-Frequency Transformers Using an Improved Frequency-Dependent Expression,” *IEEE Transactions on Power Electronics*, vol.30, no.10, pp.5738-5745, Oct. 2015.
- [II] Bahmani, M.A.; Thiringer, T.; Ortega, H., “An Accurate Pseudoempirical Model of Winding Loss Calculation in HF Foil and Round Conductors in Switchmode Magnetics,” *IEEE Transactions on Power Electronics*, vol.29, no.8, pp.4231-4246, Aug. 2014.
- [III] M. A. Bahmani, E. Agheb, T. Thiringer, H. K. Hoildalen and Y. Serdyuk, “Core loss behavior in high frequency high power transformers: Effect of core topology,” *AIP Journal of Renewable and Sustainable Energy*, , vol. 4, no. 3, p. 033112, 2012.
- [IV] E. Agheb, M. A. Bahmani, H. K. Hoildalen and T. Thiringer, “Core loss behavior in high frequency high power transformers: Arbitrary excitation,” *AIP Journal of Renewable and Sustainable Energy*, , vol. 4, no. 3, p. 033113, 2012.
- [V] Bahmani, M.A.; Thiringer, T.; Rabiei, A.; Abdulahovic, T., “Comparative Study of a Multi-MW High Power Density DC Transformer with an Optimized High Frequency Magnetics in All-DC Offshore Wind Farm” To Appear in *IEEE Transactions on Power Delivery*, 2016.
- [VI] Bahmani, M.A.; Thiringer, T.; Kharezy, M., “Design Methodology and Optimization of a Medium Frequency Transformer for High Power DC-DC Applications” *IEEE Transactions on Industry Applications*, under second review.
- [VII] Bahmani, M.A.; Thiringer, T.; Kharezy, M., “Design, Optimization and Experimental Verification of Medium-Frequency High-Power Transformer Using Rectangular Litz Conductors,” submitted to *IEEE Transactions on Power Electronics*.

### 1.3.2 Conference Proceedings

- [I] 1. Bahmani, M.A.; Thiringer, T.; Kharezy, M., “Optimization and Experimental Validation of a Medium-Frequency High Power Transformer in Solid-State Transformer Applications,” Accepted in *Applied Power Electronics Conference and Exposition (APEC), 2016 IEEE 10th International Conference on*, March 2016.
- [II] Bahmani, M.A.; Thiringer, T.; Kharezy, M., “Design methodology and optimization of a medium frequency transformer for high power DC-DC applications,” in *Applied Power Electronics Conference and Exposition (APEC), 2015 IEEE*, pp.2532-2539, March 2015.
- [III] Bahmani, M.A.; Thiringer, T., “An Accurate Frequency-Dependent Analytical Expression for Leakage Inductance Calculation in High Frequency Transformers,” *PCIM South America 2014*, p. 275-282, Oct 2014.
- [IV] Bahmani, M.A.; Thiringer, T., “A high accuracy regressive-derived winding loss calculation model for high frequency applications,” *Power Electronics and Drive Systems (PEDS), 2013 IEEE 10th International Conference on*, pp.358,363, 22-25 April 2013.
- [V] M. Mobarrez, M. Fazlali, M. A. Bahmani, T. Thiringer, “Performance and loss evaluation of a hard and soft switched 2.4 MW, 4 kV to 6 kV isolated DC-DC converter for wind energy applications,” *IECON 2012 - 38th Annual Conference on IEEE Industrial Electronics Society*, pp.5086,5091, 25-28 Oct. 2012.
- [VI] M. A. Bahmani, E. Agheb, Y. Serdyuk and H. K. Hoildalen, “Comparison of core loss behaviour in high frequency high power transformers with different core topologies,” *20th International Conference on Soft Magnetic Materials (SMM)*, p. 69, Sep. 2011.

## 1.4 Potential Applications

### 1.4.1 Collector Grid in All-DC Offshore Wind Farms

The power rating of future offshore wind farms is expected to reach a multi GW range which might require new installation of offshore wind parks far from the coast. These distances are today reaching such lengths that high voltage DC (HVDC) transmissions are becoming common to be used due to the AC cable transmission length limitations [27]. However, for these first cases with HVDC transmissions, the collection radials are still in AC causing higher power losses, particularly where

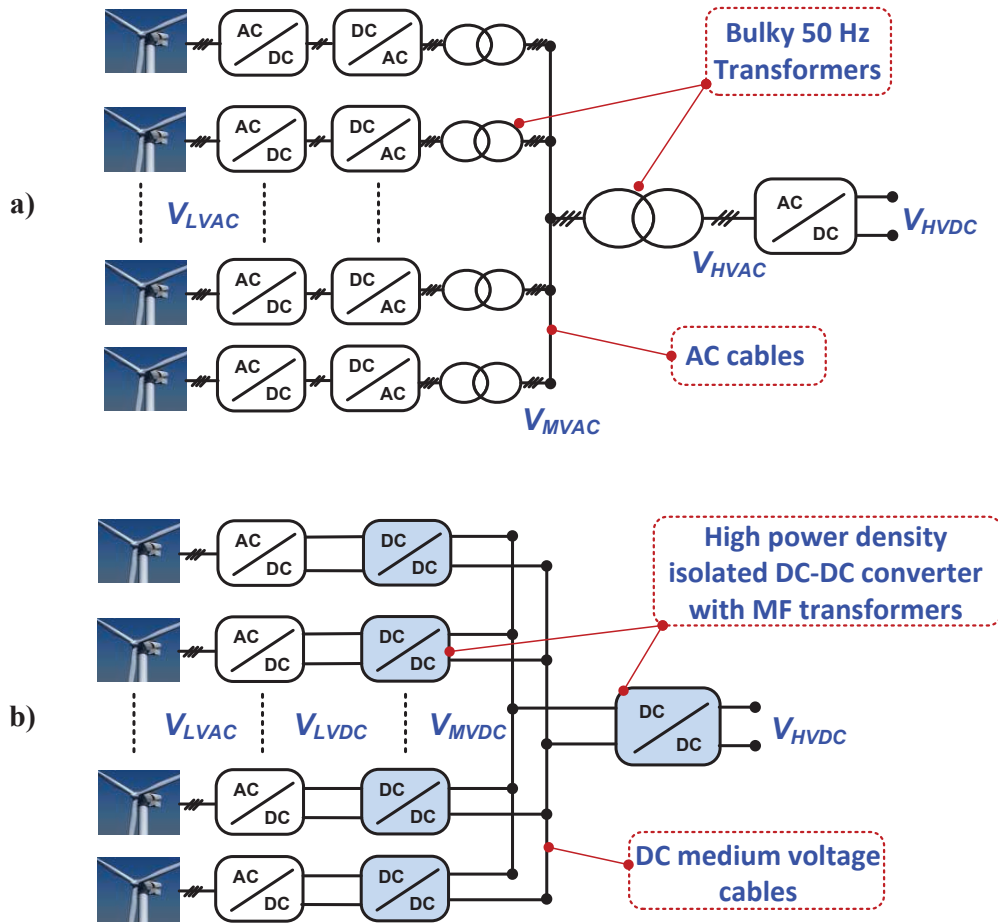


Figure 1.3: (a) Existing VSC-HVDC with AC collection grid (b) Future all-DC collection grid.

the distance between the HVDC platform and turbines are likely to be increased. Accordingly, a qualified guess is that in the future, DC could be used here as well [28–30].

This, among other factors, leads to an increasing attention towards all-DC offshore wind parks in which both the collection grid and transmission stage are DC based. Such a wind park topology, as shown in Fig. 1.3 (b), is based on high power isolated DC-DC converters, often referred to as the solid-state transformer [12] or even the DC transformer [6]. Utilizing high frequency, the weight and volume of the high frequency transformer within such a converter becomes substantially smaller, which is a key advantage in any weight and volume restricted application, and definitely in an offshore application in which the wind turbine construction and installation cost will be reduced by utilizing the lower weight and volume of the high

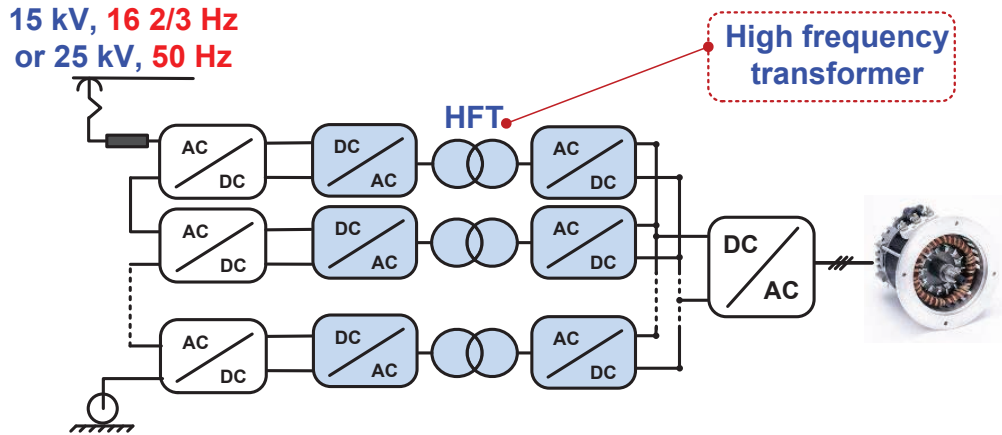


Figure 1.4: Traction application with MF/HF transformers.

frequency transformer. Apart from the voltage adaptation, this transformer should account for the relatively high isolation level dictated by the wind-park voltage levels.

In order to obtain another voltage scalability factor for the high voltage DC voltage and more importantly, because of the power rating limitations of modern semiconductor devices, a modular concept enabling parallel connection on the input low voltage side and series connection on the high voltage side (PISO) as shown in Fig. 1.2 (b), will most likely be considered [31]. The benefit of using this concept is investigated in a recent contribution by Engel [32] in which the modular multilevel dc converter (M2DC) is compared with the modular concepts based on dual active bridge converters as the building blocks. There, it was shown that the M2DC is not suitable for high voltage ratios in HVDC and MVDC grids, mainly because of the circulating current and consequently lower efficiency compared to the modular DAB based converter. Moreover, M2DC converter requires a substantially higher number of semiconductors which are highly cost contributive elements in the total cost of the converter. It is worth to point out that the high frequency transformer of each single module must withstand the total voltage over the output series connected modules, MVDC voltage.

## 1.4.2 Traction

The possibility of using high frequency transformers in traction application has been extensively studied in recent years [7]. The design of a 350 kW/8 kHz transformer, as an alternative for the bulky 16.7 Hz transformer, is presented in [33], reporting a substantial weight and volume reduction on board railway vehicles. A 1.2 MW power electronic traction transformer (PETT) prototype comprising of 9 modules with ISOP modularization and oil based MFTs at 1.8 kHz was successfully demonstrated



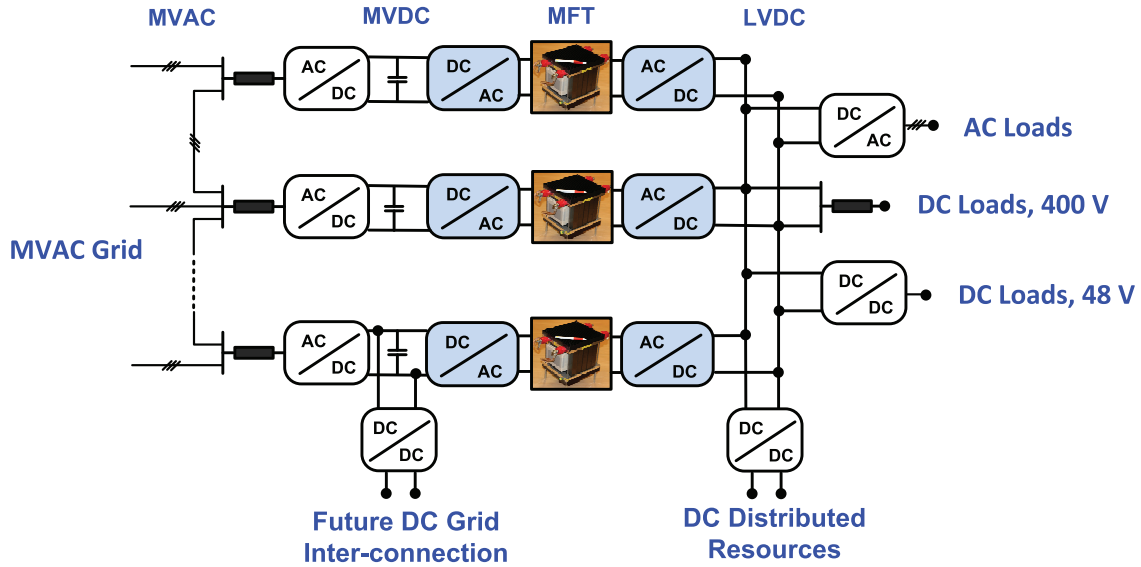


Figure 1.5: Future SST based conversion units between MVAC-LVDC/AC .

on the field [34]. All of these studies have primarily tended to focus on the benefit of utilizing higher frequencies, rather than on the design methodology and optimization of such a transformer.

### 1.4.3 Flexible-HF Distribution Transformers / Solid-State Transformers (SSTs) Between MVAC and LVDC/AC for the Future Smart Grids

The development of wide-bandgap power semiconductors and new magnetic materials, has led to the hope that the integration of HF distribution transformers or SSTs within the AC grids might be a more flexible and efficient solution for the future power system architecture which is in line with the concept of smart grid implementation. This integration gives many advantages, e.g, higher flexibility, smaller components, harmonic filtering and easy integration of energy storages and DGs by the availability of the LVDC bus. Additionally, the multi-stage conversion and the availability of the MVDC bus gives a possibility of future DC grid extension, possibly with different voltage levels, in which the solid state transformer is the equivalent of the existing conventional transformers in the AC grid.

Fig. 1.5 illustrates an exemplary configuration of such a system, in which the solid state transformer operating at medium frequency directly connects the MVAC grid to the LVDC network, hence, the size and volume is reduced and the additional functionalities listed above are completely or to a great extent achieved by replacing the LF transformers by SSTs.

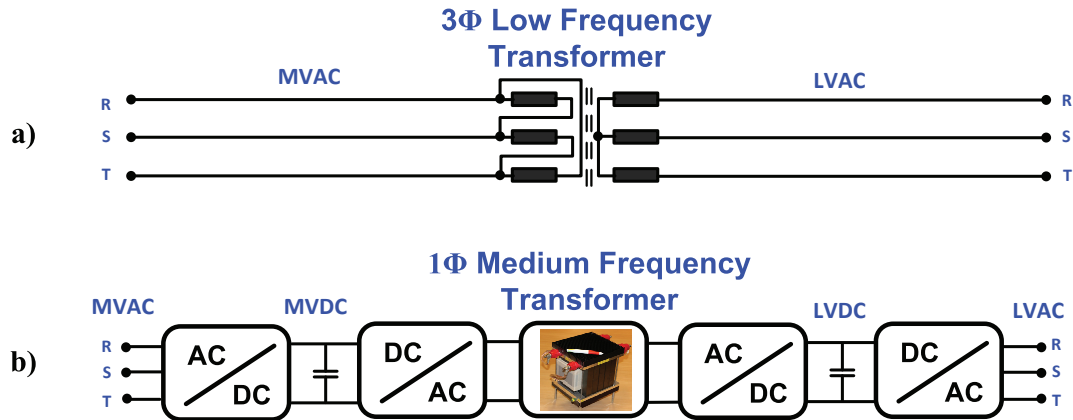


Figure 1.6: MVAC-LVAC conversion unit using (a) conventional AC electromagnetic transformers (b) SST based conversion system.

#### 1.4.3.1 MVAC/LVAC

With more than a century of experience in transformer design, since the first power transformer designed and built by ABB [35], LF transformers are the obvious solution for voltage adaption within AC grids all around the world. Despite the fact that the current LF transformers are among the most efficient electrical components ever designed, distribution transformers are estimated to be in charge of the nearly 2% of the total power losses in current electricity grids, i.e., almost one-third of the total losses in the transmission and distribution grid [36].

The efficiency requirements for conventional dry-type three phase distribution transformers varies from 97%, in a 15 KVA transformer, and goes up to nearly 99%, in a 1.5 MVA transformer, depending on the power and voltage levels [37]. The standard efficiency is even higher in case of single-phase transformers in which the standard efficiency starts from 97.7% up to about 99% in a 333 KVA distribution transformer [37]. Comparing merely about the AC conversion units, i.e., the LF transformer with its SST counterpart, the increase of unique functionalities in SSTs as stated earlier is at the expense of new conversion stages, shown in Fig. 1.6(b), resulting in more expected power losses and possibly lower efficiencies.

Therefore, the expected lower efficiency of SSTs compared to LF distribution transformers, together with the fact that lower weight and volume in land grid application is not as critical as in offshore wind farms or in traction, the replacement of LFTs by SSTs in the AC grid, and merely for AC conversion units, seems to some extent unlikely in a foreseeable future. In contrast, the situation can be different when considering low voltage DC grids as the targeted application as explained in the next part (MVAC/LVDC).

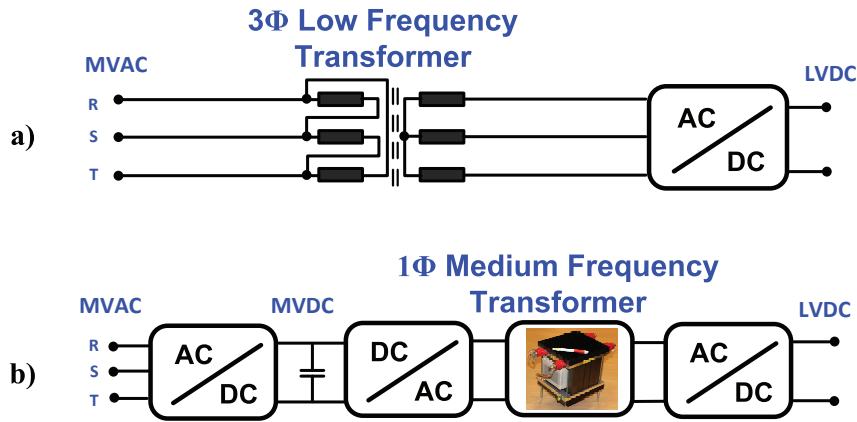


Figure 1.7: MVAC-LVDC conversion unit using (a) conventional AC electromagnetic transformers and three phase rectifier (b) SST based conversion system.

#### 1.4.3.2 MVAC/LVDC

The SST based structure for connecting the MVAC, e.g. 10 kV, to LVDC, e.g. 400 V, seems to be an interesting solution which not only brings the typical advantages of the SSTs, e.g. higher flexibility, smaller components, disturbance isolation and easy integration of energy storages and DGs by the availability of a LVDC bus, but could also potentially improve the efficiency of the total conversion system from MVAC to LVDC. Fig. 1.7(a) shows the conventional solutions in which the 10 kV medium-voltage is stepped down to 400 V AC by the bulky 50 Hz three phase transformer and then three phase PWM rectifiers feed the common 400 V DC bus. Whereas, in SST based solutions, as shown in Fig. 1.7(b), the MVAC grid is directly connected to the LVDC grid by a two-stage SST conversion unit. This consists of a rectifier stage with the corresponding DC-link, as well as the high power density DC-DC stage with a medium frequency isolation enabling lower foot-print. The 400 DC voltage can directly supply the big DC loads such as ever growing data centers.

The proposed SST based MVAC/LVDC conversion unit that is shown in Fig. 1.7(b) can be implemented in a fully modular manner, as proposed in Fig. 1.8, consisting of phase modularity, modularity in power direction with DC inter-link as well as the modularity in voltage direction, because of the limitations of the current semiconductor technology discussed previously in this chapter. Additionally, this full modularity provides the possibility of independent design and optimization of one single module as a building block for the whole structure.

Focusing on the energy losses in Fig. 1.8(a), according to [37] the typical efficiency of a state of the art dry-type three phase LF transformer in the power range of 1 MVA is about 99%. Apart from the transformer, the typical efficiency of an IGBT based three phase PWM rectifier/inverter is around 98% which gives the total efficiency

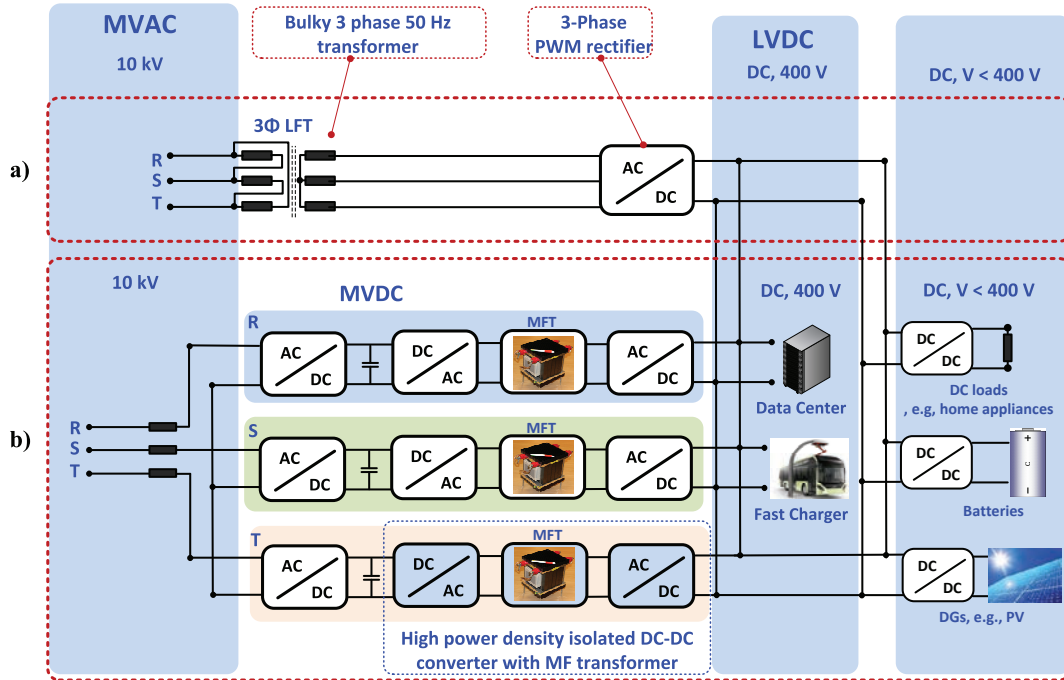


Figure 1.8: conventional MVAC-LVDC system (b) modular structure for an SST based MVAC/LVDC conversion system.

of about 97% in case of a conventional MVAC/LVDC conversion system. These relatively high power losses, about 3%, envision a better possibility for SSTs to demonstrate a higher efficiency than the LF solutions counterpart. As an indication for such a possibility, by utilizing the SiC based MOSFETs and the optimized MF transformer design proposed in this thesis, an efficiency of 98.5% for a MW range SST is achievable at around 5 kHz where the passive part is also considerably smaller.

Therefore, the solution presented in Fig. 1.8(b), which incorporates a fully modular rectification and DC-DC converter stages, represents an attractive solution which can potentially improve the energy efficiency in MVAC/LVDC conversion units. Apart from the energy efficiency, all the additional functionalities which are expected from SST based solutions, previously mentioned, are achieved in this structure. Moreover, utilizing the MF conversion stage, the power density of the proposed solution is considerably higher than of the one with the conventional transformer.

# Chapter 2

## High-Frequency Winding Losses

This chapter is based on the following articles:

- [I] Bahmani, M.A.; Thiringer, T.; Ortega, H., “An Accurate Pseudoempirical Model of Winding Loss Calculation in HF Foil and Round Conductors in Switchmode Magnetics,” *IEEE Transactions on Power Electronics*, vol.29, no.8, pp.4231-4246, Aug. 2014.
- [II] Bahmani, M.A.; Thiringer, T., “A high accuracy regressive-derived winding loss calculation model for high frequency applications,” *Power Electronics and Drive Systems (PEDS), 2013 IEEE 10th International Conference on*, pp.358,363, 22-25 April 2013.

### 2.1 Introduction

Bennet and Larson [38] were the first ones who solved and formulated the multilayer winding loss based on simplified 1-D Maxwell equations, however, the most popular analytical formula, widely used by designers to evaluate winding loss in transformers, has been derived by Dowell [39]. The physical validity of the original Dowell’s equation has been questioned in several publications [40, 41] in which the main assumption by Dowell regarding the interlayered parallel magnetic field has been shown to be violated [42]. Utilizing 2-D finite element method, these works mostly focused on to improve Dowell’s formula accuracy by defining new correction factors which present better understanding of the high frequency conductor losses [43, 44]. Although 2-D finite element method takes the 2-D nature of the magnetic field between winding layers and core into account, it requires a time consuming process to create a model and solve it for only one specific magnetic device, i.e., a transformer, inductor, and so on and on the other hand, the formulas derived by this method are usually limited to some part of the possible winding configurations [45].

Most of the classical attempts for winding loss calculation were focused on foil type conductors, widely used in high power magnetic components due to their relatively larger copper cross-section needed for keeping the maximum current density within an acceptable range [19]; however, by defining some forming and porosity factors, they have been applied on solid round wires as well [46, 47]. Apart from those Dowell base expressions, Ferreira [48] proposed a formula derived from the exact solution of the magnetic field in the vicinity of a solid round conductor, However, Sullivan [49] described a relatively high inaccuracy for Ferreira's method and Dimitrakakis [45] examined its deviation from FEM simulation. Moreover, several publications proposed different approaches resulting in an optimum diameter for which the skin and proximity effect are minimized [50, 51].

The main aim of this chapter is to propose a pseudo-empirical formula to precisely calculate the AC resistance factor of the foil and round type conductors in switchmode magnetics without the need to use finite element simulations. In order to obtain such a formula, an intensive 2-D FEM simulation set to cover a wide range of possible winding configurations has been performed and the obtained AC resistance factor summarized in a multi-variate Pseudo-empirical expression. Unlike previous attempts which either covered parts of the possible winding configurations or defining correction factors for previously available well-known analytical expressions [52], this formula can be used for both foil and round conductors in a wide range of frequencies and for the windings consisting of any number of layers with free number of turns per layer.

The first part of this chapter, provides an overview of the previous well-known analytical methods for calculation of AC resistance factor in foil and round conductors. Furthermore, a quantitative comparison between those models and FEM simulations has been performed in order to specify the magnitude of deviation and gives a clear picture of the validity range of each method. The next part, thoroughly explains the methodology used to derive the final Pseudo-empirical formula and provides a full range comparison between Dowell's expression and the new pseudo-empirical in terms of accuracy and domain of validity. At the end, the experimental results are presented. Several transformers with different winding configurations have been built to verify the accuracy of the new method over the domain of validity.

## 2.2 Validity Investigation

### 2.2.1 Dowell's Expression for Foil Conductors

The influence of skin and proximity effects on transformer AC resistance has been studied for many years, based on the expression proposed by Dowell [39]. This model was initially derived from solving the Maxwell equations under certain circumstances, shown in Fig. 2.1(a), resulting in one dimensional diffusion equation.

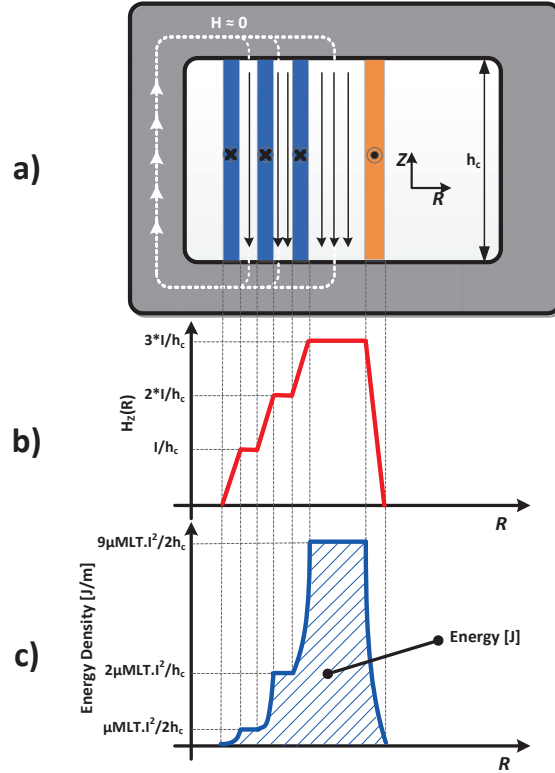


Figure 2.1: (a) Cross-sectional view of the winding configurations according to Dowell's assumptions. (b) Magnetic field distribution. (c) Energy distribution.

As can be seen in Fig. 2.1(a), the main assumptions in Dowell's expression is that each winding portion consisting of several layers of foil conductors occupies the whole core window height. The permeability of the magnetic core is assumed to be infinity, therefore the magnetic field intensity within the core is negligible while it is closing its path along the foil conductors and intra-layer spaces inside the core window. As a result, the magnetic field vectors has only  $Z$  components and vary only in  $R$  direction, therefore, the diffusion equation can be written as a second order differential equation

$$\frac{\partial^2 H_z(R)}{\partial R^2} = j\omega\sigma\mu H_z(R) \quad (2.1)$$

where  $\sigma$  and  $\mu$  are the conductivity and permeability of the foil conductors respectively.

Fig. 2.1(b) shows the distribution of the magnetic field inside the core window when the frequency is low enough to homogeneously distribute the current inside the foils. As can be seen in Fig. 2.1(b), the magnetic field is zero outside the

windings area and it is at its maximum in the area between the two windings; This condition has been applied to (2.1) as boundary conditions to obtain the magnetic field distribution inside the conductors, however, in Fig. 2.1(b), the frequency is assumed low enough to have a homogenous distribution of current inside the foils. In the same fashion, the magnetic energy stored in the leakage inductance of the transformer has been shown in Fig. 2.1(c).

Given the magnetic field distribution achieved from (2.1), Dowell calculated the current distribution and its associated power loss resulting in an easy to use formula which gives the AC resistance factor of the transformer windings as

$$RF = \frac{R_{AC}}{R_{DC}} = M(\Delta) + \frac{m^2 - 1}{3} D(\Delta) \quad (2.2)$$

where the terms  $M$ ,  $D$  and  $\Delta$  are defined as

$$\begin{aligned} M(\Delta) &= \Delta \frac{\sinh 2\Delta + \sin 2\Delta}{\cosh 2\Delta - \cos 2\Delta} \\ &= \Delta \frac{e^{2\Delta} - e^{-2\Delta} + 2\sin 2\Delta}{e^{2\Delta} + e^{-2\Delta} - 2\cos 2\Delta} \end{aligned} \quad (2.3)$$

$$\begin{aligned} D(\Delta) &= 2\Delta \frac{\sinh \Delta - \sin \Delta}{\cosh \Delta + \cos \Delta} \\ &= 2\Delta \frac{e^{\Delta} - e^{-\Delta} - 2\sin \Delta}{e^{\Delta} + e^{-\Delta} + 2\cos \Delta} \end{aligned} \quad (2.4)$$

$$\Delta = \frac{d}{\delta} \quad (2.5)$$

where  $m$  is the number of layers for each winding portion,  $\Delta$  is the penetration ratio which is the ratio between the foil thickness,  $d$ , and the skin depth,  $\delta$  at any particular frequency.

The initial assumption of Dowell's expression regarding the height of the copper foil is not applicable in many practical cases where the height of the foil can not be the same as window height, e.g., tight rectangular conductors, short foils and so on. In order to take these cases into account, Dowell introduced the porosity factor,  $\eta$ , which is the ratio of the window height occupied by the foil conductors to the total window height [39].

One of the purposes of this chapter is to investigate the validity range of the well-known classical models. Although experimental measurements is the most accurate way to check the validity of the theoretical models, FEM simulations are the most popular way to do this investigation since it provides the possibility of sweeping different parameters in the model. All of the FEM simulations in this chapter are performed using the commercial electromagnetic software, Ansys Maxwell [53],



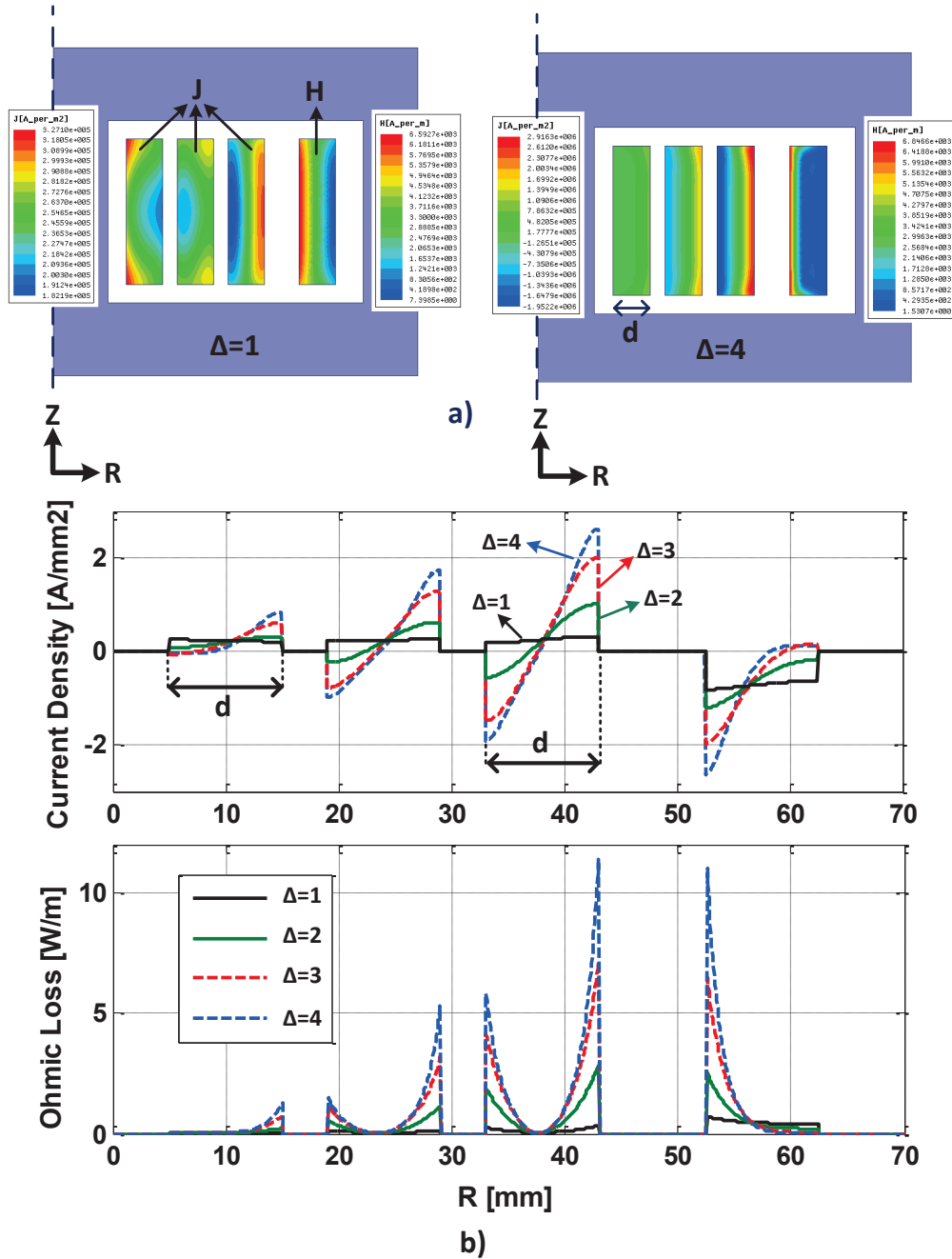


Figure 2.2: (a) Sample 2D axisymmetric FEM simulation at two different  $\Delta$ . (b) Normalised current density and ohmic loss at core window space.

in which both the skin and proximity effect are taken into account, however the precision of the computation is dependent on the mesh quality. For this reason, firstly, at least six layers of mesh are applied within the first skin depth from the sides of all the conductors in the simulation's geometry and secondly, the mesh structure of each geometry structure is refined in several stages until the simulation error reduces to less than 0.5%. As a result, each simulation creates a substantial number of mesh elements resulting in a longer computational time [54], whereby, using three dimensional geometries requiring much more mesh elements seems to be inefficient, making iterative simulations unfeasible [55]. Consequently, all the simulations in this chapter have been performed under 2D symmetry pattern around Z axis where the windings should be wound around the middle limb of the transformer in order to retain the symmetrical shape of the magnetic field. Nevertheless, the real geometry of most of the transformers, except for the pot core transformer, consist of the winding portions that are not covered by the core, e.g., E core, C core and so on, whereas in 2D axisymmetric simulations windings are thoroughly surrounded by the core. For this reason, the ohmic loss of several transformers were compared in both 2D axisymmetric and 3D simulations with an extremely fine mesh, in order to have a comparable mesh densities between 2D and 3D, which showed a negligible difference between 2D and 3D simulations in terms of the magnetic field distribution and resulting ohmic losses. The worst case studied was for a very low value of  $\eta$ , 0.2, on which the 3D simulation showed 6% less ohmic loss than the one in the 2D case which is still an acceptable error justifying the use of 2D simulations over the time consuming 3D one.

Fig. 2.2(a) shows a sample 2D axisymmetric FEM simulations of the transformer windings at different values of  $\Delta$  illustrating the computed current density distribution and magnetic field intensity in the primary and secondary windings respectively. The dimensions of the geometry were kept constant and different values of  $\Delta$  were achieved by applying the frequencies corresponding to those values. In other words, the analysis is based on a dimensionless parameter,  $\Delta$ , taking into account the effects of both frequency and geometrical dimensions. The normalised current density and ohmic loss distribution on inter-layer space, obtained from the same FEM simulation at four different values of  $\Delta$ , are shown in Fig. 2.2(b) top and bottom respectively.

As can be seen in Fig. 2.2(b), the current density increases by adding the number of layers, resulting in higher ohmic losses on the third layer of the primary windings than the ohmic losses in the first and second layer, due to this fact that in contrast to the first layer, which does not suffer from the magnetic field on its left hand side, the second layer and more significantly the third layer suffer from the presence of the magnetic field on their left hand side, causing an induced negative current on the left hand side of the conductor. Hence, the ohmic loss on the second and third layer are close to five and thirteen times, respectively, higher than the ohmic loss in the first layer of the primary windings. Moreover, the penetration ratio,  $\Delta$ , is another

major determinant of ohmic loss pattern which significantly changes the distribution of current within a conductor. As illustrated in Fig. 2.2(b), the AC resistance of the windings rapidly increases by increasing the penetration ratio, i.e, by either increasing the frequency or increasing the foil thickness, leading to significantly higher ohmic losses. Despite the major redistribution of the current due to the skin and proximity effects, one can notice that the net value of the current in each layer is constant. For instance, as can be seen in Fig. 2.2(b), although the positive current significantly increases by increasing  $\Delta$ , there is an opposite negative current on the other side of the conductor which balances the net current in each layer.

In order to determine the limitations and validity range of Dowell expression used in many magnetic design approaches, the result of a series of numerical tests, examining the effect of variation in different geometrical aspects on AC resistance factor at different frequencies, are compared with the AC resistance factor obtained from Dowell's equations. The dimensions of these numerical tests were kept constant and higher  $\Delta$  achieved by increasing the frequency for each  $\eta$  and each number of layer. Fig. 2.3 shows that the Dowell's resistance factor deviation from FEM resistance factor, calculated as (2.6), versus  $\eta$  for 4 different number of layers up to 4 layers and 5 different penetration ratios up to 5.  $RF_{Dowell}$  can be calculated by (2.2), however in order to obtain  $RF_{FEM}$ , first, the value of ohmic loss  $P_\omega$  over the winding area should be extracted from the solved simulation and then, by knowing the value of current through the conductors, AC resistance can be calculated for the frequencies and geometries of interest. The porosity factor varies from 0.3 to 1, although it should be noted that porosity factors of less than 0.4 is very implausible in practice and including such low values is only for the sake of comparison.

$$RF_{Error} [\%] = 100 \times \frac{RF_{Dowell} - RF_{FEM}}{RF_{FEM}} \quad (2.6)$$

Some remarks can be highlighted in Fig. 2.3. First, it is worth mentioning that the variation in penetration ratio,  $\Delta$ , substantially affect the Dowell's expression accuracy. As shown in Fig. 2.3 the accuracy of Dowell's expression reduces by increasing  $\Delta$ , for any number of layer,  $m$ , and porosity factor,  $\eta$ , resulting in an unreliable transformer design aiming to work at higher  $\Delta$ . The second parameter which adversely affect Dowell's expression accuracy is the porosity factor. As illustrated in Fig. 2.3, for any  $m$  and  $\Delta$ , for a higher porosity factor ( $\eta \geq 0.8$ ) the accuracy of Dowell's expression is within  $\pm 15\%$  which is a relatively acceptable deviation for an analytical tool. However, the equation does not retain its precision for lower values of  $\eta$  in which its accuracy is within  $\pm 60\%$ . This high deviation becomes more problematic when it is negative since it corresponds to the cases where Dowell's expression underestimates the ohmic loss or AC resistance factor. Moreover, this deviation becomes more prominent by increasing the number of winding layers as proximity effect becoming more influential on the current distribution inside the conductors.

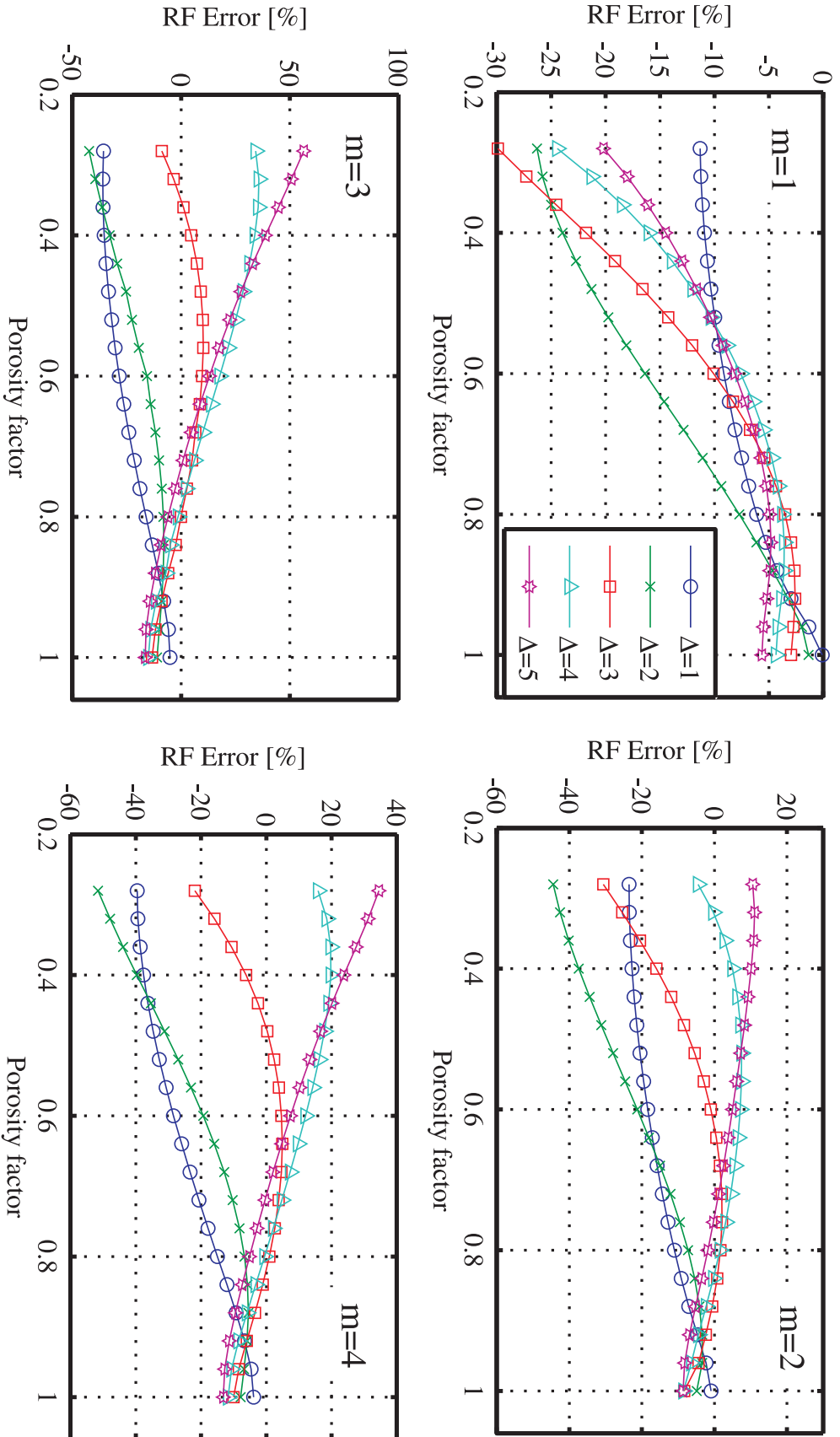


Figure 2.3: Dowell's Foil Resistance factor deviation from FEM resistance factor versus  $\eta$  at 5 different values of  $\Delta$  and 4 different number of winding layer,  $m$ .

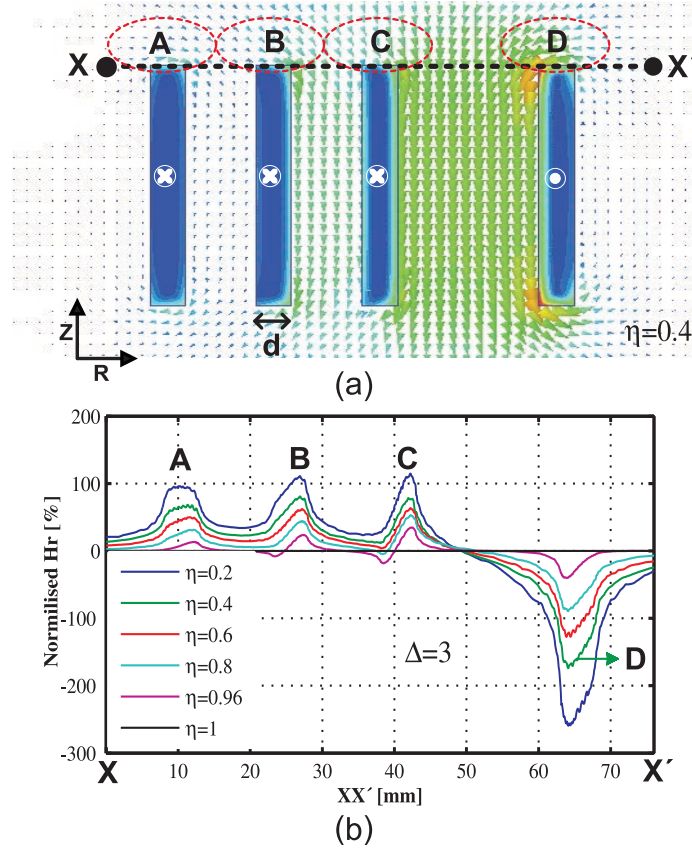


Figure 2.4: (a) 2D simulation of edge effect on magnetic field at  $\eta = 0.4$ . (b) Normalised radial magnetic field intensity on  $XX'$  at 6 different values of  $\eta$ .

This inaccuracy could stem from the rigorous assumptions Dowell made to simplify the derivation process. The major simplification which could contribute to the noted deviation is that the foil windings are assumed to occupy the total height of the transformer window, resulting in the presence of only Z component of magnetic field within and between foil layers. However, this assumption is usually being violated in many practical designs due to the safety requirements [56], causing the presence of the second component of magnetic field. Therefore, the 2D magnetic field intensifies by decreasing the length of the foil conductors (decreasing  $\eta$ ), causing inaccuracy in Dowell's expression. Consequently, one can say that the 1D approach is generally applicable among designers as long as the foil conductors covers the majority of the transformers window height [57, 58].

## 2.2.2 Edge Effect Analysis

The aim of this section is to quantitatively investigate the cause of inaccuracy in the analytical expressions, i.e. Dowell, Ferreira and other analytical expressions derived based on simplifying initial assumptions. In order to perform edge effect analysis, the magnetic field distribution inside a transformer window, comprising of three layers of foil conductors as primary and one layer of foil as secondary, has been studied. Fig. 2.4(a) shows the magnetic field distribution inside a transformer window consisting of foil conductors with  $\eta = 0.4$  and  $\Delta = 3$ . As can be seen at areas shown by the red ellipse, the magnetic field vectors are not only in Z direction but also their R component is considerable particularly at the end windings between the primary and secondary windings at which the magnetic field intensity is significant [59].

In order to more quantitatively examine the influence of winding height on the formation of the second component of the magnetic field, 6 simulations performed on the geometry shown in Fig. 2.4(a) with different conductor heights corresponding to the porosity factors of 0.2 to 1. Frequency and foil thickness are fixed to accomplish  $\Delta = 3$ . The magnetic fields in radial direction are then extracted on an imaginary line,  $XX'$ , connecting the edge of the inner primary foil to the edge of the secondary foil conductors for different values of  $\eta$ . Moreover, these values are normalised to the maximum magnetic field between the primary and secondary windings,  $\max(H_Z)$ , when the foil conductors occupy the whole window height at which the magnetic field exists only in Z direction.

The phenomenon, edge effect, is clearly demonstrated in Fig. 2.4(b) where the ratio of radial magnetic field intensity to the maximum value of magnetic field in Z direction on  $XX'$  is illustrated in percentage for 6 different values of  $\eta$ . The result reveals that the magnetic field distribution inside the transformer window is highly two dimensional at sides of the conductors highlighted in Fig. 2.4(a) and (b). Moreover, by reducing the height of the foil conductors, edge effects considerably increase, e.g. the normalized radial magnetic field at region D is -250%, -170% and -80% for the porosity factors of 0.2, 0.4 and 0.8, respectively whereas as shown in Fig. 2.4(b), the contribution of radial magnetic field at  $\eta = 1$  is almost 0% which agrees with Dowell's initial assumption.

Comparing the results shown in Fig. 2.3 and Fig. 2.4(b), one can conclude that Dowell's general overestimation is associated with percentage of the second component of the magnetic field [60]. It is now more clear to justify the inaccurate results obtained by Dowell's equation when a transformer window is not fully occupied by the conductors. It should be noted that although in some cases, e.g.  $\eta \approx 0.2$ , the radial magnetic field intensity could be as high as 250% of its orthogonal component, the total deviation of 1D models from FEM is not more than 70% as previously shown in Fig. 2.3. This is because those highly two-dimensional magnetic field are limited to the specific areas inside the transformer window whereas the magnetic

field direction is mostly in Z direction at other regions. It is worthwhile mentioning that edge effect does not always result in extra losses, but also could reduce the total losses in the windings. This attribute is demonstrated in Fig. 2.3 where at high values of  $\Delta$  (4 and 5) and  $m > 1$ , the total copper losses seem to be improved by intensifying edge effect. However, it should be expressed that, specifying the condition in which edge effect improves the winding losses, is strongly dependent on the geometrical characteristics of the transformer making the conclusion more complex [45].

### 2.2.3 Round Conductors

Solid round conductors, magnet wires, are widely used in transformers, motors and other magnetic components since they are commercially available in a wide range of diameters with a relatively low price [51, 61]. Also, round wires require less practical efforts to be tightly wound around a core [19, 62]. In this part, two of the most commonly used analytical expression, among others, for calculating AC resistance factor in round wires, Dowell and Ferreira, are introduced. The accuracy of these methods are then examined by setting a large number of FEM simulations covering a wide range of parameter variations in order to determine their domain of validity.

Dowell [39] proposed a special factor in order to evaluate the AC resistance factor with a similar approach as in the foil analysis. In this method, the round wire cross section is related to the equivalent rectangular solid wire with the same cross sectional area and by taking the distance between wires into account, it relates every layer of round wire to its equivalent foil conductors. Therefore, the main structure of (2.2) is proposed to be viable for round wires by replacing  $\Delta$  as

$$\Delta' = \frac{d_r}{2\delta} \sqrt{\pi \cdot \eta} \quad (2.7)$$

where  $d_r$  is the diameter of the solid round wire and  $\eta$  is the degree of fulfillment of window height as described in the foil section.

In addition, Ferreira [47] proposed another closed form formula derived based on the exact solutions of the magnetic field inside and outside a single solid round wire by considering the orthogonality between skin and proximity effects [48]. As Dowell's approach, Ferreira took into account the multilayered arrangement of round wires in order to calculate the AC resistance factors for each winding portion, however, Ferreira's original method is generally referred to as inaccurate since it did not account for the porosity factor [45]. Therefore, Bartoli [63] modified Ferreira's formula by defining porosity factors similar to the one in Dowell's expression, although this method is still referred to as Ferreira's expression given as

$$RF = \frac{\Delta}{2\sqrt{2}} \left( M_1(\Delta) - 2\pi\eta^2 \left( \frac{4(m^2 - 1)}{3} + 1 \right) M_2(\Delta) \right) \quad (2.8)$$

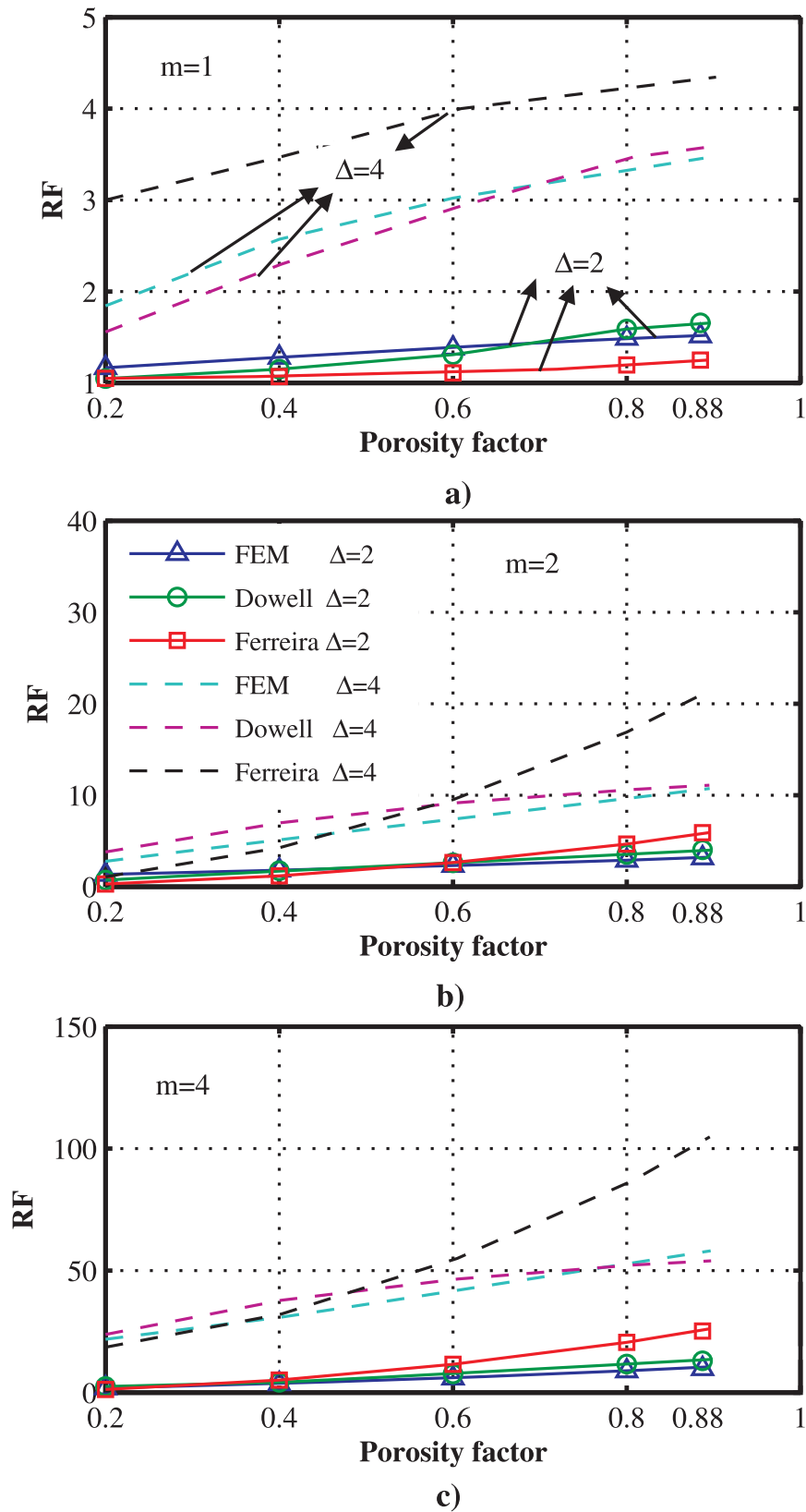


Figure 2.5: Comparison between resistance factors obtained from analytical models, Dowell and Ferreira, relative to the FEM results performed at different values of  $\eta$ ,  $\Delta$  and  $m$ .



$$\Delta = \frac{d_r}{\delta} \quad (2.9)$$

where  $m$  is the number of layers,  $\eta$  accounts for the percentage of copper covering the transformer window height and  $d_r$  is the diameter of the solid round wire.  $\Delta$ ,  $M_1(\Delta)$  and  $M_2(\Delta)$  are defined as

$$M_1(\Delta) = \frac{ber(\frac{\Delta}{\sqrt{2}})bei'(\frac{\Delta}{\sqrt{2}}) - bei(\frac{\Delta}{\sqrt{2}})ber'(\frac{\Delta}{\sqrt{2}})}{(ber'(\frac{\Delta}{\sqrt{2}}))^2 + (bei'(\frac{\Delta}{\sqrt{2}}))^2} \quad (2.10)$$

$$M_2(\Delta) = \frac{ber_2(\frac{\Delta}{\sqrt{2}})ber'(\frac{\Delta}{\sqrt{2}}) + bei_2(\frac{\Delta}{\sqrt{2}})bei'(\frac{\Delta}{\sqrt{2}})}{(ber(\frac{\Delta}{\sqrt{2}}))^2 + (bei(\frac{\Delta}{\sqrt{2}}))^2} \quad (2.11)$$

The functions  $ber$  and  $bei$ , Kelvin functions, are the real and imaginary parts of Bessel functions of the first kind, respectively.

In order to analyze the accuracy of the aforementioned methods, a set of parametric FEM simulations covering a wide range of parameter variations, i.e.  $0.2 \leq \eta \leq 0.88$ ,  $1 \leq m \leq 4$  and two values  $\Delta$ , have been performed. The results were then compared with the resistance factors obtained from Dowell and Ferreira's expression and illustrated in Fig. 2.5.

As can be seen in Fig. 2.5, Ferreira's formula generally shows a high inaccuracy for almost the whole range of investigation. For instance, at  $m = 4$ ,  $\eta = 0.8$  and  $\Delta = 4$ , Ferreira estimates the resistance factor as high as 80 whereas FEM analysis shows about 50 which is a significant overestimation resulting in unrealistic and costly magnetic design. This inaccuracy could stem from the rigorous assumption Ferreira made regarding the orthogonality between skin and proximity effect which is not a valid assumption when a solid round wire, conducting high frequency currents, is surrounded by a large number of other conductors with a complex arrangement. This attribute can be seen in Fig. 2.5(b) and (c) where Ferreira's resistance factor becomes closer to the FEM result by decreasing  $\eta$ . In other words, by having a sparser winding arrangement, the behaviour of the magnetic field inside the conductors becomes closer to the initial assumption resulting in a relatively more orthogonal skin and proximity magnetic field [45].

Unlike Ferreira's model, Dowell shows an acceptable accuracy particularly at  $\Delta = 2$  which is cited to be the optimum penetration ratio for a solid round conductors [50]. However, as shown in Fig. 2.5, at lower values of  $\eta$ , Dowell's expression loses its validity because of the edge effect forming 2D magnetic field inside transformer window. On the other hand, for  $\eta \geq 0.6$  Dowell's expression leads to deviations of always less than 20%, nevertheless at lower  $\Delta$ , around 2, this deviation improves up to approximately 10% which is substantially more accurate than Ferreira's method.

It is worthwhile mentioning that besides violating the initial assumptions, the aforementioned theoretical methods do not account for all the geometrical aspects

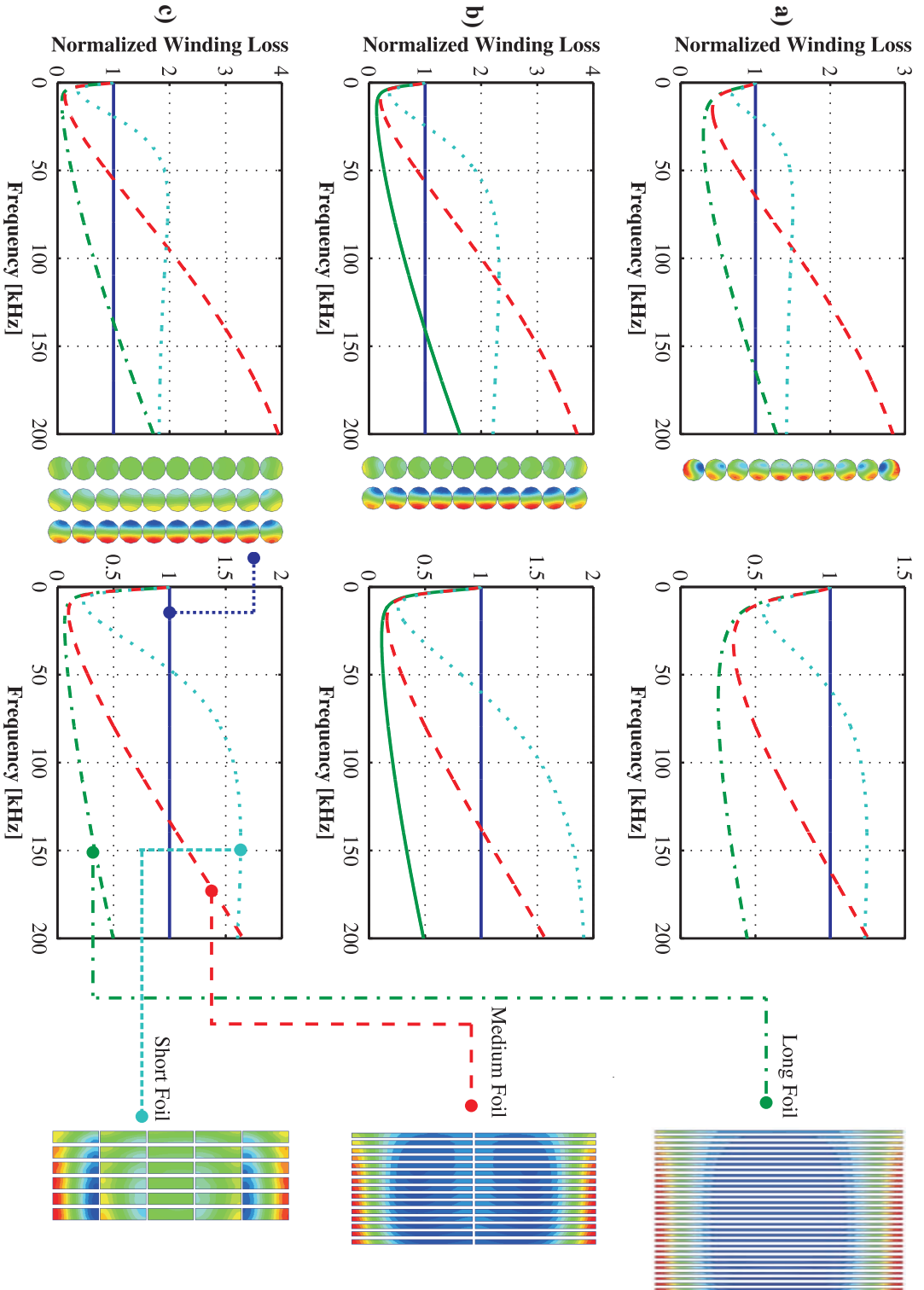


Figure 2.6: AC winding loss comparison between the round conductors and the corresponding foil conductor with different arrangements and the same current density (a-left)  $m = 1, \eta = 1$ . (a-right)  $m = 1, \eta = 0.7$ . (b-left)  $m = 2, \eta = 1$ . (b-right)  $m = 2, \eta = 0.7$ . (c-left)  $m = 3, \eta = 1$ . (c-right)  $m = 3, \eta = 0.7$ .

of a real winding arrangement such as inter-layered distances, vertical and horizontal clearing distances of the winding portion to the core, causing relatively high inaccuracy at high frequency applications. These are the reasons why researchers and designers have been seeking for alternatives methods. One of the essentially reliable methods is performing FEM simulation for every case study instead of using theoretical models, resulting in a time consuming optimization process in which thousands of scenarios may be needed to be examined. Consequently, several investigations have been performed [41, 52, 64] in order to develop the well-known closed form expression by introducing several correction factors obtained from numerous finite element simulations. However, their applicability is usually limited since the conditions in which the FEM analysis carried out is not sufficiently general, e.g. considering only single layer configuration or neglecting the determinant parameters on winding loss. Under this scope, a pseudo-empirical formula, accounting for the influence of all the determinant geometrical aspects on the magnetic field, with adequate degree of freedom, has been proposed and validated in this chapter. Integrating the accuracy of FEM simulations with an easy to use pseudo-empirical formula accounting for almost all practical winding arrangements, this method covers the area in which previous closed form analytical models, either the classical models or the FEM based modified models, substantially deviates from the actual conductor losses.

As mentioned before, round conductors are widely used in switch-mode magnetics due to the availability of different types as well as ease of use while foil conductors require more practical efforts to be wound around a core particularly when a complex winding strategy needs to be implemented. However more investigations are needed to determine the suitability of one conductor type in different application. For instance, having a higher winding filling factor is one of the important design requirements in high power density applications where the weight and volume of the magnetic components should be decreased and on the other hand different losses need to be reduced.

Fig. 2.6 presents a FEM-based comparison of the obtained AC winding losses between the round and foil conductors in different steps and on the basis of the same current density inside round and its respective foil conductors. The overall results indicate that there is always a crossover frequency where the AC winding losses of the foil conductors exceeds the AC winding losses of its corresponding round conductors with the same current density and porosity factor. For instance, Fig. 2.6(c)(right) illustrates the winding loss of a winding portion comprising of three layers of round wires, 10 turns in each layer, and the porosity factor of 0.7 (solid blue line). The dash lines represent value of the AC winding losses of the long foil with the highest number of layers, 30, the medium foils with 15 layers, 2 turns each, and the short foils with 6 layers, 5 turns each, respectively normalized by the AC winding losses of the respective 3 layers of round wire (shown in the right side of

the Fig. 2.6). The current density in all of the configurations is constant and set to  $2.5 A/mm^2$  and the porosity factor is 0.7. It can clearly be seen that until a certain frequency the AC winding loss of the foil conductor is less than the one for the corresponding round conductors. This crossover frequency increases by having the longer foils which obviously have thinner thicknesses compared to the shorter foils. This attribute, along with the higher filling factor of the foil conductors, makes this kind of conductor an interesting option for high power density applications. However, one should consider that having the highest number of layers and the thinnest foils could not always be a realistic solution since this structure would suffer from the high value of the winding capacitance particularly at high voltage applications. Therefore, there is always a compromise between the number of layers, size of the transformer and the maximum allowed winding loss with respect to the transformer application. The discussed crossover frequency is shifted towards lower frequency at higher values of the porosity factor, therefore there is still a frequency range where foil conductor has preference over its corresponding round conductors. This attribute can be seen in Fig. 2.6(c)(left) which is similar to the right one but with the porosity factor of 1. Similar results are obtained for 2 and 1 layer of round conductors as illustrated in Fig. 2.6(a) and (b).

Being limited to just one type of conductor, foil or round, one can say, if possible, by decreasing the number of layers and increasing the transformer window height, the AC resistance factor and accordingly the AC winding loss reduces because of the less compact winding arrangement reducing the proximity effect. This is what already observed during the validity investigations of the well-known analytical models. However, due to mechanical and practical issues this option is usually limited.

## 2.3 Pseudo-Empirical Model Establishment

The main purpose of this section is to propose an easy-to-use closed form formula to accurately calculate the AC resistance factor at given geometrical dimensions as well as at different frequencies. The proposed strategy to obtain such a pseudo-empirical expression is illustrated in Fig. 2.7, summarized as follows.

- [I] The determinant geometrical parameters required to form a unique transformer window is introduced and their influence on winding loss is investigated.
- [II] The effective geometrical variables are then merged to form a set of generic dimensionless variables.
- [III] A proper range of variation, forming most of the feasible transformer window configuration, is defined for each generic parameters to be used as the input

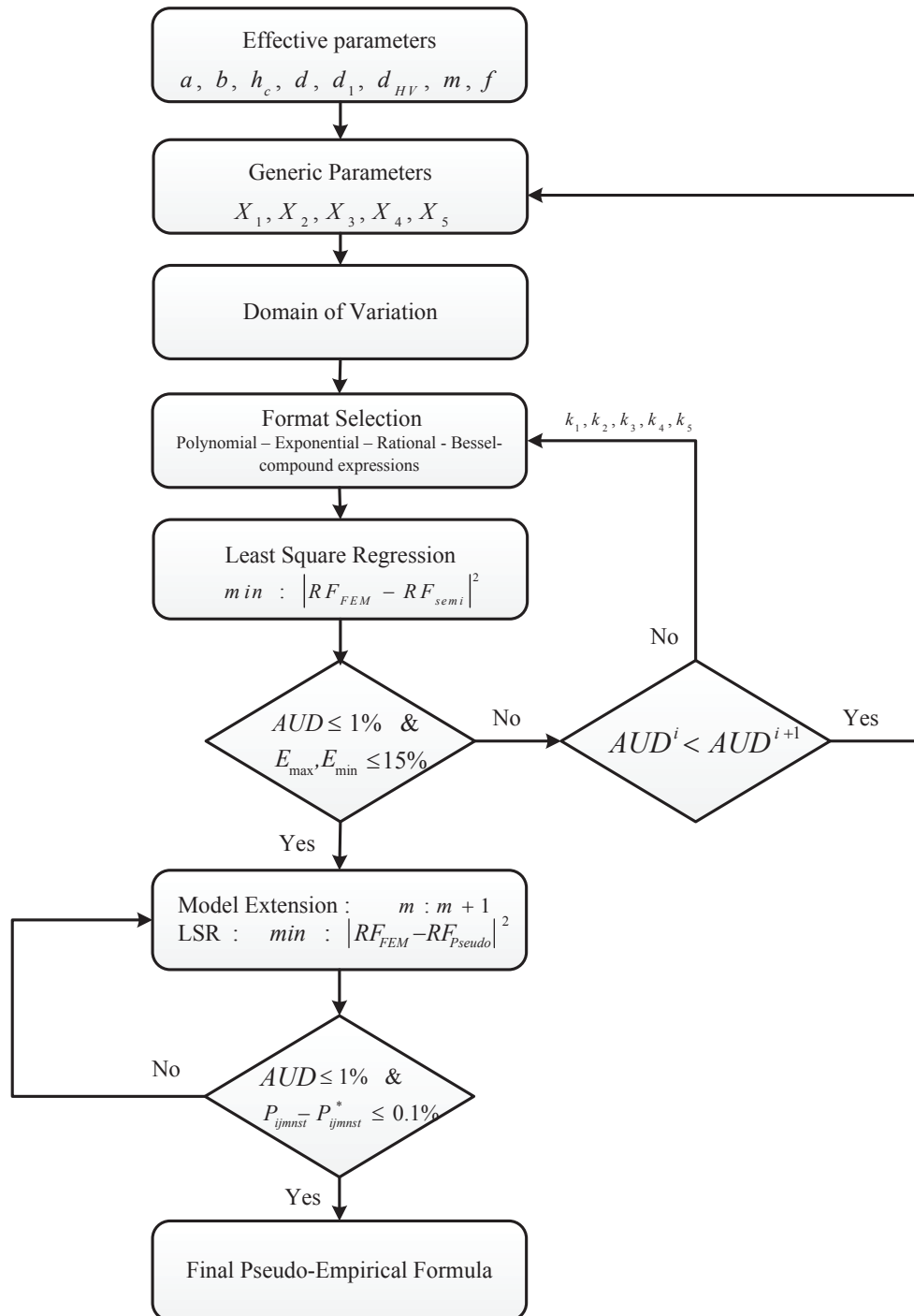


Figure 2.7: Approach to establish the pseudo-empirical model.

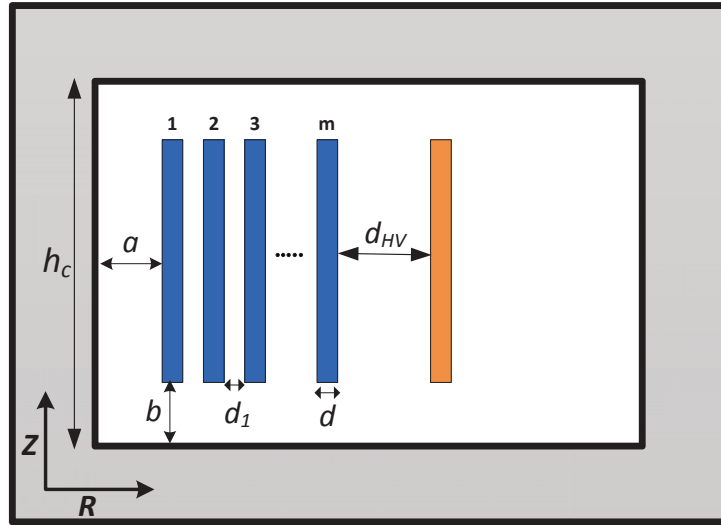


Figure 2.8: Definition of the variables.

variables for FEM simulations.

- [IV] After extracting the matrices of AC resistance factors, corresponding to the generic variables, from the numerous FEM simulations, a mathematical regression is performed in order to determine the coefficients needed to fit the prospective formats of the final expression with respect to the desired precision.
- [V] Once the selected structure of the expression fulfilled all the requirements, a new regression process triggers by expanding the variation range of one of the generic parameters in order to reinforce the validity of the final expression.

Each step is now described in detail.

### 2.3.1 Determinant Variable Definition

The first step to obtain such a formula is to determine all the parameters, either geometrical or electrical, which can influence the magnetic field distribution and accordingly the AC resistance factor. In addition, the sensitivity of the resistance factor to those parameters is examined in order to decrease the number of influencing factors since the complexity of the regression process and the number of the coefficients for the final formula substantially depends on the number of the input parameters.

In this part, different geometrical and electrical variables affecting the resistance factor are examined in order to take the most influencing ones in to account. Fig. 2.8

Table 2.1: Sensitivity analysis of the geometrical parameters.

$m$	$\frac{\partial RF}{\partial a}$	$\frac{\partial RF}{\partial b}$	$\frac{\partial RF}{\partial d_1}$	$\frac{\partial RF}{\partial d_{HV}}$	$\frac{\partial RF}{\partial d}$
1	-0.00012	-0.00145	-	0.000011	0.542
2	-0.001	-0.0179	0.0081	-0.000025	2.097
3	-0.0025	-0.0512	0.0337	-0.000025	4.911
4	-0.0071	-0.1021	0.0723	-0.000025	8.861

shows the schematic of a transformer window comprising of a magnetic core with a relatively high permeability of 20000 and the copper foil winding. This high value of the permeability belongs to the extremely low core-loss magnetic materials called nano-crystalline, however other magnetic materials does not have such high values. Hence, prior to deriving the Pseudo-Empirical model, it is necessary to monitor the effect of different values of the relative permeability on the AC resistance factor. For this purpose the powder core magnetic materials which usually has the lowest relative permeability of around 60 is simulated. It was seen that the obtained value of the AC resistance factor is only 0.3% less than the one with the permeability of 20000. This is because of the fact that the main reason of considering high permeability in winding loss study is to make sure that the magnetic field intensity inside the magnetic core is close to zero. This can be fulfilled even with the magnetic cores with low permeabilities of around 60 to 100.

The whole geometry can be uniquely described by 7 parameters defined in Fig. 2.8, in which  $h_c$  is the window height,  $m$  is the number of foil layers in primary side,  $d$  is the foil thickness,  $d_1$  is the insulation thickness between the primary foils,  $d_{HV}$  is the clearance between the primary and secondary windings,  $a$  and  $b$  are the horizontal and vertical creepage distance respectively.

In order to determine how these parameters affect the AC resistance factor, a sensitivity analysis has been carried out by sweeping the geometrical variables using FEM simulations. The studied parameter is assigned 20 different values while other parameters are kept constant. Afterwards, the average value of the partial derivative of the AC resistance factor with respect to the varying parameter has been explored to determine the most and the least sensitive parameters on the AC resistance factor.

Table. 2.1 shows the average value of  $\frac{\partial RF}{\partial x}$  over the range of variation of the variable  $x$  at 4 different number of turns of primary windings where  $x$  can be replaced by each of the geometrical parameters defined in Fig. 2.8. As can be seen in Table. 2.1, the foil thickness is the most effective variable on  $RF$ , whereby the AC resistance factor substantially increases by increasing foil thickness, e.g. for  $m = 3$  at  $2 \text{ kHz}$ , the incremental rate of  $RF$  for a 1 millimeter increase in  $d$  is 4.911. On the other hand, the distance between the primary and secondary windings,  $d_{HV}$ , shows to

Table 2.2: Generic parameters with corresponding range of variation.

	Definition	Min	Step size	Max	Number of steps
$X_1$ :	$\frac{d}{\delta}$	0.5	0.5	6	12
$X_2$ :	$\frac{h_c-2b}{hc}$	0.2	0.2	1	5
$X_3$ :	$\frac{a}{hc}$	0.02	0.04	0.18	5
$X_4$ :	$m$	1	1	9	9
$X_5$ :	$\frac{d_1}{hc}$	0.01	0.01	0.05	5

have the least influence ( at least 2 order of magnitudes ) on the resistance factor of the primary windings portion, causing it to be excluded from the pseudo-empirical derivation process, thus avoiding the number of required FEM simulations to be multiplied in the next section. It should be mentioned that all the FEM simulations in this part, have been performed at 2  $kHz$  and  $h_c = 100$  mm, therefore the values presented in Table 2.1 can change at other frequencies and window heights, however, this will not alter the effectiveness sequence of the studied parameters.

### 2.3.2 Generic Parameters and the Domain of Validity

After determining the influencing variables, in order to have a generalized model, it is necessary to compound the selected variables to create dimensionless variables like the penetration ratio variable introduced by Dowell [39] as the ratio between the thickness of the conductor to its skin depth at each particular frequency. A proper range of variation is then defined for each of the selected variables, resulting in thousands of 2-D finite element simulations which covers a wide range of transformers in terms of its dimensions, operating point and application.

The number of layers,  $m$ , is dimensionless by itself, hence it needs no modification to be one of the generic parameters. The frequency of the applied current is another non-geometrical variable, affecting the winding loss, which is classically addressed by its corresponding skin depth [39]. In this fashion, the skin depth (frequency), together with the foil thickness, can form the second dimensionless variable to be used later in the regression process. Similarly, the other geometrical variables,  $d_1$ ,  $a$  and  $b$ , are normalised to the window height,  $h_c$ , resulting in total 5 distinct generic parameters. The definition of the generic variables,  $X_1$  to  $X_5$  and the corresponding range of variations are given in Table. 2.2.

As shown in Table. 2.2, the parameter  $X_1$  is assigned to sweep from 0.5 to 6 ( 12 values ) which is achieved by altering the foil thickness while the frequency and consequently the skin depth,  $\delta$  is fixed. Likewise,  $X_2$ ,  $X_3$  and  $X_5$  obtained 5 different values by varying  $b$ ,  $a$  and  $d_1$ , respectively, in which the transformer window



height,  $h_c$  was assumed to be fixed. Covering these range of variations requires 1500 distinct 2-D FEM simulations for each number of turns at the primary side, resulting in 12300 FEM simulations in total, since the number of layers at the primary side,  $m$ , increased up to 9 layers. However, the first 5 layers is considered for the primary regression process (6300 simulations), and another 4 layers gradually supplied to the derivation process at the secondary regression process (model extension), resulting in an extra 6000 simulations.

Not being limited to a specific dimension of a transformer or certain range of frequency is the most important advantage of introducing the generic parameters. Besides, the assigned range of variation for each parameter, covers not only most of the available transformer window arrangements used in different practical applications [19, 62], but also extreme conditions such as  $X_1 \geq 3$  or  $X_2 \leq 0.5$  which are basically more than sufficient.

### 2.3.3 Multi-Variable Regression Strategy

The proposed primary regression process comprises four steps as follows.

#### 2.3.3.1 Structure Selection

The most important step is to identify the main format of the formula since the nature of the resistance factor is strongly nonlinear and unpredictable, particularly when the edge effect is taken into account, for this reason, it is hardly possible to propose one specific format for the final expression. For these reasons, four different structures have been considered as the candidate formats as follows.

- Polynomial structure comprising five independent variable with degree of 2 to maximum 6 as

$$\sum_{i=0}^5 \sum_{j \geq i}^5 \sum_{m \geq j}^5 \sum_{n \geq m}^5 \sum_{s \geq n}^5 \sum_{t \geq s}^5 P_{ijmst} X_i X_j X_m X_n X_s X_t \quad (2.12)$$

However, the structure shown in (2.12) is for the maximum degree of 6, the parameter  $1 \leq k_1 \leq 6$ , specifying the maximum degree of the polynomial expression, will later be used in the primary regression process to achieve the least regression error without unnecessary increasing the number of the coefficients.

- Exponential structure comprising  $(X_1 \cdot X_2)$  as exponent and the second order polynomial with maximum degree of 6 for the coefficients as

$$\sum_{m=1}^{k_2} \sum_{i=0}^5 \sum_{j \geq i}^5 P_{ijm} X_i X_j e^{-(X_1 X_2)^m} \quad (2.13)$$

where the free variable  $k_2$  is the maximum degree of the exponent while the maximum degree of the coefficient is 2.

- Bessel expression consisting of  $(X_1 X_2)$  arguments and polynomial coefficients as

$$\sum_{m=1}^{k_3} \sum_{n=1}^{k_4} \sum_{i=0}^5 \sum_{j \geq i}^5 P_{ijmn} X_i X_j [J_1((X_1 X_2)^m) + J_2((X_1 X_2)^n)] \quad (2.14)$$

where  $J_1$  and  $J_2$  are the first and second order of the Bessel function of the first kind, respectively. Also  $k_3$  and  $k_4$  are the maximum degree of the bessel's arguments varying at the primary regression process to fulfill the accuracy requirements.

- Rational terms which was not initially considered in our regression process, however a limited format of rational terms as (2.15) was finally utilised to adjust the accuracy of the pseudo-empirical expression.

$$\sum_{i=1}^{k_5} P_i \frac{X_4^2}{(X_1 X_2)^i} \quad (2.15)$$

where  $k_5$  is the maximum allowed degree of the denominator's exponent.

It should be noted that the variables  $k_1$  to  $k_5$  will later be used in the regression strategy section to tune the final pseudo-empirical expression with respect to the precision requirements and  $X_0$  is assumed to be 0 in all of the structure candidates.

### 2.3.3.2 Database Collection

Determining five independent generic parameters shown in Table. 2.2, one can depict 6300 distinct winding arrangement of the geometry shown in Fig. 2.8 for  $1 \leq X_4 \leq 5$  required for the primary regression process. The AC resistance factor of the primary windings,  $RF$ , have then been extracted by performing 6300 2D FEM simulations, resulting in a huge database comprising of 6300 elements, each consisting of 5 independent inputs,  $X_1$  to  $X_5$ , and the corresponding  $RF$  as the output. It should be noted that the core is considered to be with no air gap and with a very high permeability, around 20000.

### 2.3.3.3 Primary Regression Process

After obtaining the resistance factors, corresponding to each set of generic variables, from the FEM simulations, the aforementioned alternatives structures need to be

Table 2.3: AUD, maximum overestimation and underestimation.

	Polynomial	Bessel	Compound	Separated Comp
<i>AUD</i> :	2.89%	73.24%	0.65%	0.51%
<i>MaxOver</i> :	25%	353%	16.8%	9.06%
<i>MaxUnder</i> :	-29%	-214.3%	-20.6%	-6.15%

fitted in the database of 6300 resistance factors to get the final expression as a function of  $X_1$  to  $X_5$ . The least square regression is selected as the regression method, applied on different structures while the free parameters  $k_1$  to  $k_5$  takes different values to fulfill the precision requirements. The approach, whereby the free parameters can be determined are explained in several steps as follows.

First, the regression accuracy requirements should be defined. As can be seen in Fig. 2.7, the average unsigned deviation (AUD) of the calculated  $RF$  from the simulated one is defined to be less than 1 %. This criteria is considered as the main precision indicator of the pseudo-empirical formula, however to prevent extreme sectional error, it is necessary to restrict the maximum allowed deviation of simulated points, hence, maximum 15 % deviation is defined as the second regression criteria applied on all studied arrangements of the generic variables.

Defining the regression accuracy criteria, the least square regression has been exclusively applied on each structure when  $k_1$  to  $k_5$  varied from 1 to 6. It was found that none of the aforementioned structures can meet the regression requirements even with the maximum defined  $k$ . For instance, for the polynomial structure given in (2.12) at the maximum allowed degree ( $k_1 = 6$ ), AUD was 2.89 % and the maximum underestimation and overestimation were -29% and 25%, respectively, which exceed the regression criteria, nevertheless it showed the highest accuracy among the studied structures. On the other hand, the Bessel structure seems to be the worst proposed structure, between the studied ones, showing the highest AUD, maximum underestimation and overestimation of 73.24%, -214.3% and %353, respectively, hence it is excluded from further regression process comprising combined structures.

Since each of the proposed structures has failed to fulfill the regression requirements, a compound format comprising two or three of the mentioned structures is taken into account with the priority for the polynomial structure which demonstrated the highest accuracy among others. It should be noted that the generic variable  $X_5$  which indicates the normalized value of the insulation distance between the primary foils is assumed to be 0 for  $X_4 = 1$  where there is only one layer of conductors. Considering the compound structure, the accuracy of the pseudo-empirical expression significantly improved. For example, by compounding all the structure, polynomial, exponential and rational, with the highest allowed degree of

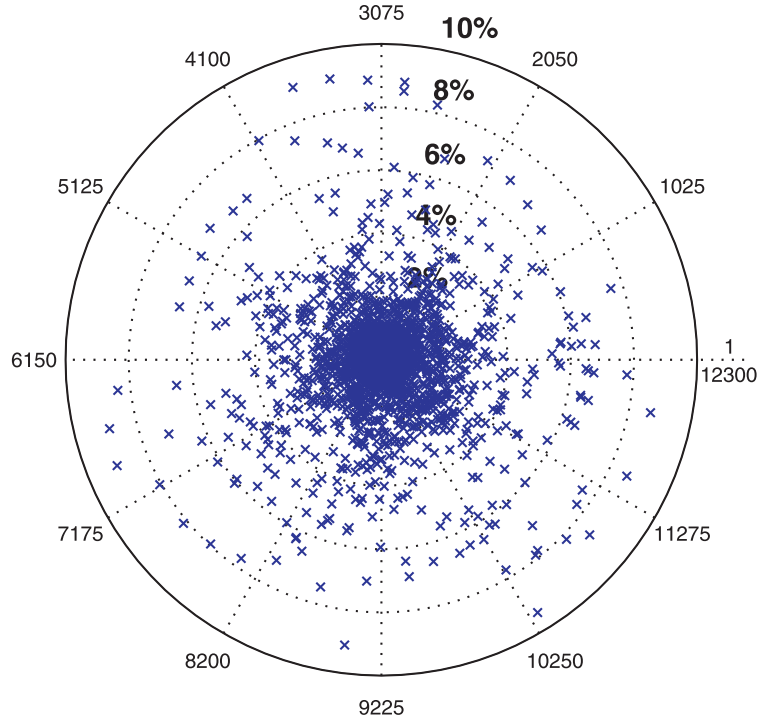


Figure 2.9: Accuracy overview of the pseudo-empirical expression.

coefficients and exponents ( $k_1, k_2, k_5 = 6$ ), AUD dropped to 0.65% which is far below the defined criteria, however the maximum overestimation and underestimations were 16.8% and -20.6% which are slightly higher than the defined requirements. It was noticed that most of the extreme deviations belongs to the set of data in which  $X_4 = 1$ , therefore, it is decided to separately derive an expression for the case in which  $X_4 = 1$ , and to form a conditional pseudo-empirical expression. Accordingly the final pseudo-empirical expression for the multi-layer windings ( $X_4 > 1$ ) is

$$\begin{aligned}
 RF &= f(X_1, X_2, X_3, X_4, X_5) \\
 &= \sum_{i=0}^5 \sum_{j \geq i}^5 \sum_{m \geq j}^5 \sum_{n \geq m}^5 \sum_{s \geq n}^5 \sum_{t \geq s}^5 P_{ijmnst} X_i X_j X_m X_n X_s X_t \\
 &+ \sum_{m=1}^3 \sum_{i=0}^5 \sum_{j \geq i}^5 P_{ijm} X_i X_j e^{-(X_1 X_2)^m} + \sum_{i=1}^5 P_i \frac{X_4^2}{(X_1 X_2)^i}
 \end{aligned} \tag{2.16}$$

whereas for the single-layer configuration ( $X_4 = 1$ ), the AC resistance factor can be calculated from

$$\begin{aligned} RF &= f(X_1, X_2, X_3, X_4) \\ &= \sum_{i=0}^3 \sum_{j \geq i}^3 \sum_{m \geq j}^3 \sum_{n \geq m}^3 \sum_{s \geq n}^3 P_{ijmns} X_i X_j X_m X_n X_s \end{aligned} \quad (2.17)$$

where the AC resistance factors defined as a polynomial with the maximum degree of 5 for winding portions comprising only one layer of conductors; and a combination of polynomial, exponential and rational structures with  $k_1 = 6$ ,  $k_2 = 3$  and  $k_5 = 5$ , respectively, were derived for winding portions consisting of more than one layer. As a result, not only the maximum deviations dropped to -6.15% and 9.06% for underestimation and overestimation, respectively, but also AUD slightly improved (0.51%) which are far below the regression requirements.

### 2.3.3.4 Secondary Regression Process (Model Extension)

In this section the secondary regression has been performed on (6.53) in order to investigate the validity of the expression for winding portions consisting of higher number of layers. Therefore, as shown in Fig. 2.7, the accuracy of the proposed structure has been examined in a closed loop when the number of layers,  $X_4$  is increasing until the obtained expression fulfills the new criteria. These criteria were defined as

$$\frac{\sum_{i=1}^{300+1500(X_4^{max}-1)} (RF_{Pseudo}^i - RF_{FEM}^i)}{300 + 1500(X_4^{max} - 1)} \times 100 \leq 1\% \quad (2.18)$$

$$\frac{|P_{ijmnst}^* - P_{ijmnst}|}{P_{ijmnst}} \times 100 \leq 0.1\% \quad (2.19)$$

where (2.18) is the definition of AUD,  $RF_{Pseudo}^i$  is the resistance factor calculated by (6.53). The second criterion, shown in (2.19), is a rigorous demand of having changes of below 0.1% for any coefficients in (6.53) compared to the corresponding coefficient obtained from the previous regression with lower number of layers. This approach resulted in adding the number of layers in four steps up to  $X_4 = 9$ , requiring another 6000 FEM simulations to be solved. On the basis of these strict criteria, resulting in slight changes in the coefficients ( $P_{ijmnst}$ ), it can be deduced that within the validity domain demonstrated in Table. 2.2, the pseudo-empirical formula derived in (6.53) is generally valid for any number of layers with a negligible impact on its accuracy.

Fig. 2.9 illustrates an overview of the residual deviation of the resistance factors, calculated by (6.53), compared to the corresponding resistance factors obtained from the FEM analysis as

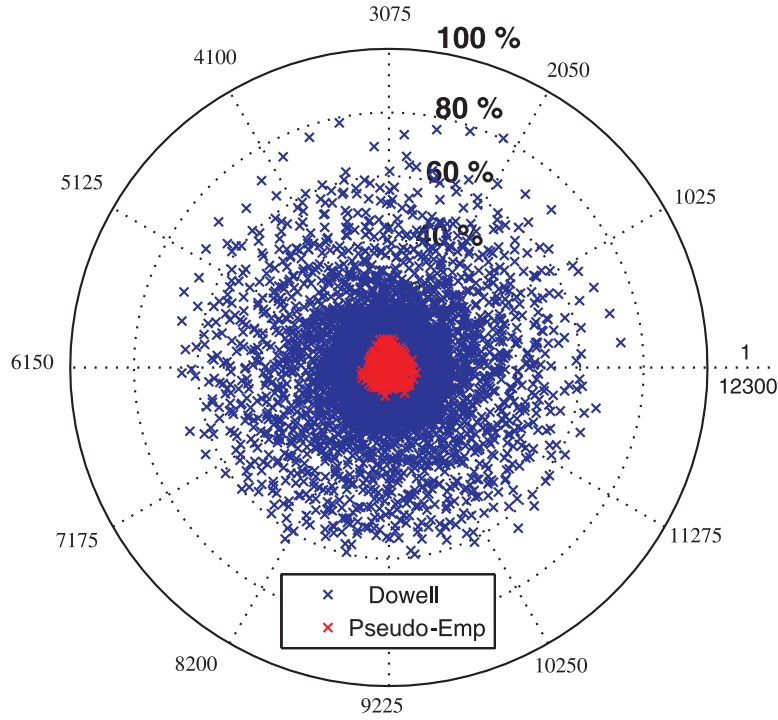


Figure 2.10: A comparative accuracy overview between the pseudo-empirical (red) and Dowell's (blue) model.

$$UD^i\% = \frac{RF_{Pseudo}^i - RF_{FEM}^i}{RF_{FEM}^i} \times 100 \quad (2.20)$$

In(2.20),  $UD^i$  accounts for the percentage of the unsigned difference between the resistance factors obtained from (6.53) and the corresponding RF extracted from FEM simulations for the  $i$  th case-study where  $i$ , shown on the circumference of Fig. 2.9, varies between 1 to 12300. Hence, each blue cross located in Fig. 2.9 represents a distinct winding transformer arrangement examined in the regression process, whereby, the further each point is located from the center, the higher deviation from FEM result it suffers. The accuracy overview shown in Fig. 2.9 indicates that more than approximately 99% of the studied cases are located within the area in where  $UD$  is less than 1%.

Fig. 2.10 illustrates a comparative overview between Dowell (blue) and the pseudo-empirical formula's (red) accuracy in the whole range of validity determined in Table. 2.2 ( each points corresponds to one unique simulation). The overall results indicate a substantial improvement of the pseudo-empirical model over Dowell's model, for example in some cases Dowell underestimate the RF up to 80% whereas

the maximum deviation of pseudo-empirical's expression is only 9.06% for the extreme cases. The AUD as the most informative comparison indicator between two expression, demonstrates the value of 0.51% for pseudo-empirical whereas the AUD of Dowell's expression shows a fairly high value of 24.31% over the studied points. In addition, Dowell's extreme deviation is in the range of 80% causing a substantially unreliable magnetic design. This attribute can clearly be seen in Fig. 2.10 while the pseudo-empirical expression's extreme deviations (red crosses) are confined within 9%. Apart from the extreme cases (low values of  $X_2$ , high values of  $X_1$  and so on) in which the pseudo-empirical formula deviation is fairly negligible compared to Dowell's expression. In normal cases where Dowell is commonly considered accurate, the pseudo empirical formula shows even more accurate results than what Dowell does. To be more specific, the pseudo-empirical  $UD$  is generally less than 0.2% for the normal cases while  $UD$  of up to 10% is normally considered accurate for Dowell's expression.

Fig. 2.11 demonstrates a more specific presentation of the resistance factors obtained from (6.53), (2.2) and the FEM simulation in order to examine the applicability of each method. The AC resistance factors have been calculated versus the generic parameter,  $X_2$ , at four different combinations of  $X_2$  and  $X_4$  as shown in Fig. 2.11. The dimensions of the investigated transformers is significantly larger than the dimensions of the 12300 transformers used in the regression process in order to examine the validity of the initial claim regarding the generality of the pseudo-empirical expression based on the dimensionless generic parameters. As clearly can be seen in all of the graphs in Fig. 2.11, the pseudo-empirical expression almost coincides with the FEM results, confirming the general applicability of the pseudo-empirical model within the domain of validity determined in Table 2.2, whereas Dowell demonstrates a relatively large difference from FEM. This attribute can be clearly seen in Fig. 2.11(a) and (b) in which Dowell's expression significantly underestimates the actual resistance factor, e.g. with the exception of Fig. 2.11(d), in which Dowell's RF enhanced with a higher rate (because (2.2) is proportional to the square of the  $m$ ), the results obtained by (2.2) are generally inaccurate at  $X_2 \leq 0.6$ .

### 2.3.4 Accuracy Investigation for Round Conductors

Despite the fact that this study was primarily concerned with deriving an analytical tool to accurately evaluate the AC resistance factor in foil conductors, it is possible to extend the applicability of the pseudo-empirical expression into solid round conductors as well by modifying some of the generic parameters used in foil analysis as

$$X_2 = \frac{N \cdot d_r}{h_c} \quad (2.21)$$

$$X_1 = \frac{d_r \sqrt{\pi}}{2\delta} \sqrt{X_2} \quad (2.22)$$

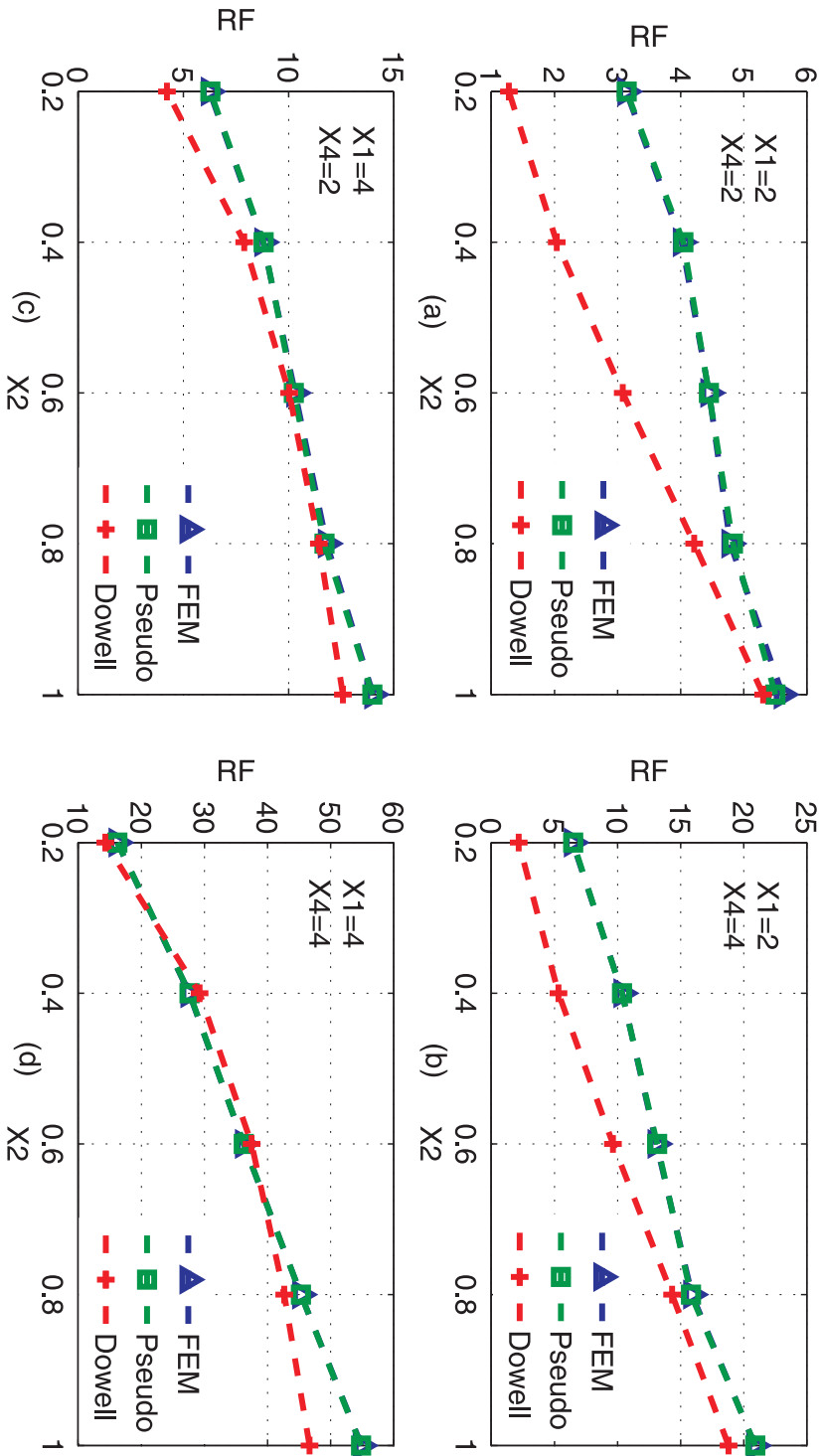


Figure 2.11: Comparison between obtained AC resistance factor,  $RF$ , versus  $X_2$  by FEM simulations, pseudo-empirical formula and Dowell's expression. (a)  $X_1 = 2, X_4 = 2$ . (b)  $X_1 = 2, X_4 = 4$ . (c)  $X_1 = 4, X_4 = 2$ . (d)  $X_1 = 4, X_4 = 4$ .



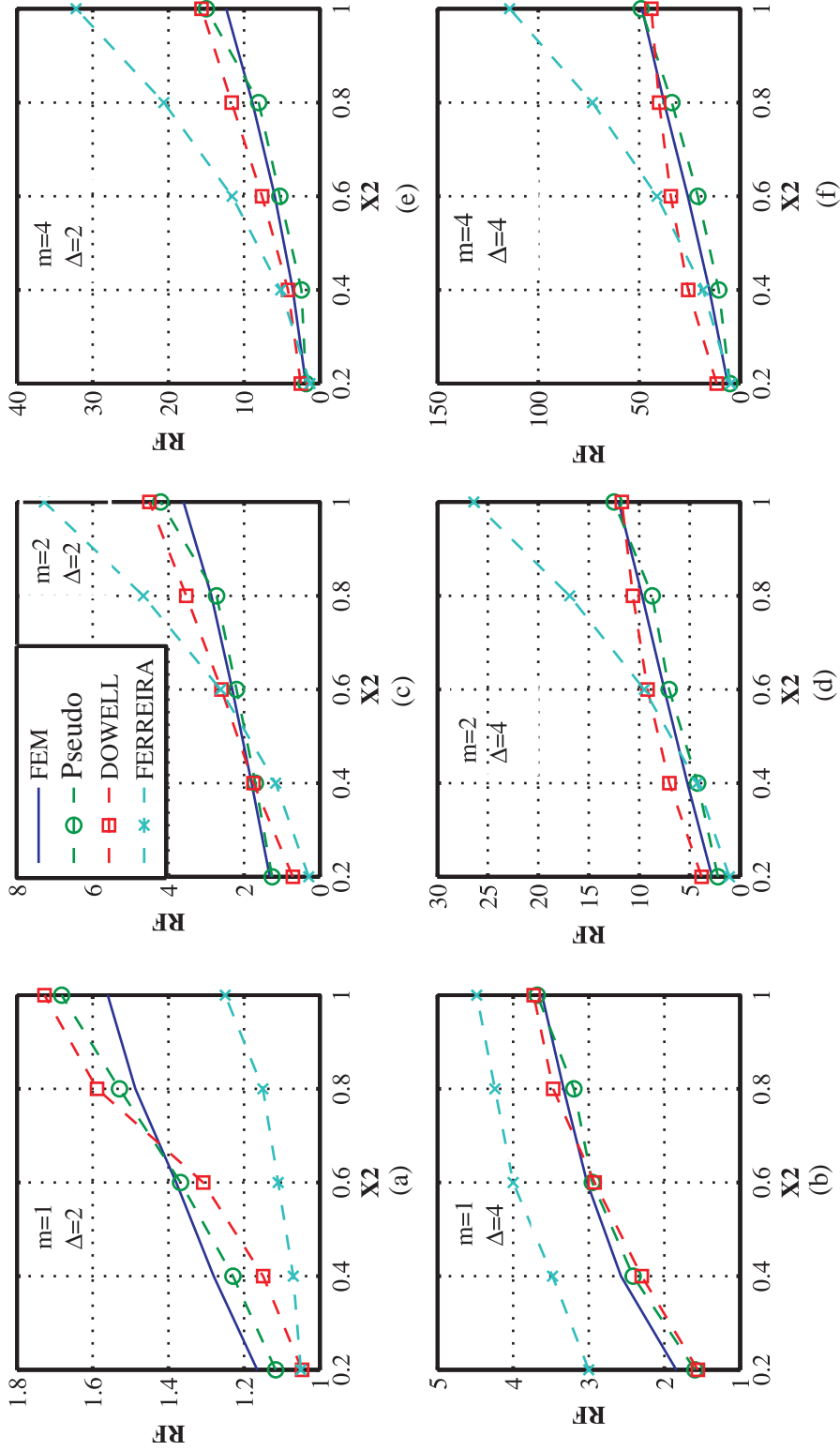


Figure 2.12: Comparison between obtained AC resistance factor, RF, versus  $X_2$  by FEM simulations, pseudo-empirical formula, Dowell and Ferreira's expression. (a)  $m = 1, \Delta = 2$ . (b)  $m = 1, \Delta = 4$ . (c)  $m = 2, \Delta = 2$ . (d)  $m = 2, \Delta = 4$ . (e)  $m = 4, \Delta = 2$ . (f)  $m = 4, \Delta = 4$ .

where  $d_r$  is the diameter of the solid round conductor and  $N$  is the number of turns per layer. The other generic parameters ( $X_3$  to  $X_5$ ), as well as the domain of validity of all the generic parameters is the same as for foil conductors. To investigate the validity of the proposed pseudo-empirical expression for round wires, a comparative analysis between obtained resistance factors from FEM simulations, pseudo-empirical, Dowell and Ferreira's expression have been conducted versus the generic parameter  $X_2$ , varying from 0.2 to 1, at 6 distinct combination of  $m$  and  $\Delta$  indicated in Fig. 2.12.

As can be seen in Fig. 2.12(a) to (f), using the modified pseudo-empirical formula, almost in the whole  $X_2$  range considered, the AC resistance factors were calculated with a negligible difference towards the FEM results indicating the high accuracy of the proposed method even for round conductors. In contrast, Ferreira's formula generally shows a high inaccuracy for almost the whole range of  $X_2$  and all studied combination of  $m$  and  $\Delta$  particularly for  $X_2 > 0.7$  (as in most of the transformers). Furthermore, the results indicate an acceptable accuracy for Dowell's expression in particular for  $\Delta \leq 2$  and  $X_2 > 0.6$  which are the case for most of the practical transformers. According to the graphs illustrated in Fig. 2.12, Dowell's expression leads to deviations of always less than 20% whereas the pseudo-empirical formula exhibit a deviation of always less than 10% within the studied range.

### 2.3.5 Accuracy Investigation for Interleaved Winding

Interleaving is one of the strategies to reduce the magnetic field within the transformer window and accordingly reducing the leakage inductance of the transformer, as well as AC winding loss. Fig. 2.13(a) to (d) demonstrates different interleaving arrangements of a transformer consisting of four layers of primary and four layers of secondary with six turns of round wires in each layer. The current density inside the primary windings as well as the magnetic flux intensity vectors between the windings have been shown in top parts of Fig. 2.13(a) to (d) while the low frequency magnetic field distribution inside the transformer window illustrated right beneath of the corresponding interleaved arrangement. As can be seen in Fig. 2.13(b) by sandwiching the secondary between the primary windings the peak value of the magnetic field has been reduced to half of the one in Fig. 2.13(a). In Fig. 2.13(c) an uniform interleaved arrangement with four winding sections has been shown resulting in similar magnetic field pattern as in Fig. 2.13(b) but with uniform direction while the magnetic field vectors in Fig. 2.13(b) have opposite directions inside the window. The last considered interleaved arrangement is depicted in Fig. 2.13(d) where the windings are divided to five sections while one fourth of the primary windings are located at both sides. This structure results in four times less magnetic field peak value compared to the one in Fig. 2.13(a).

The obtained AC resistance factor of each arrangement by FEM simulations is

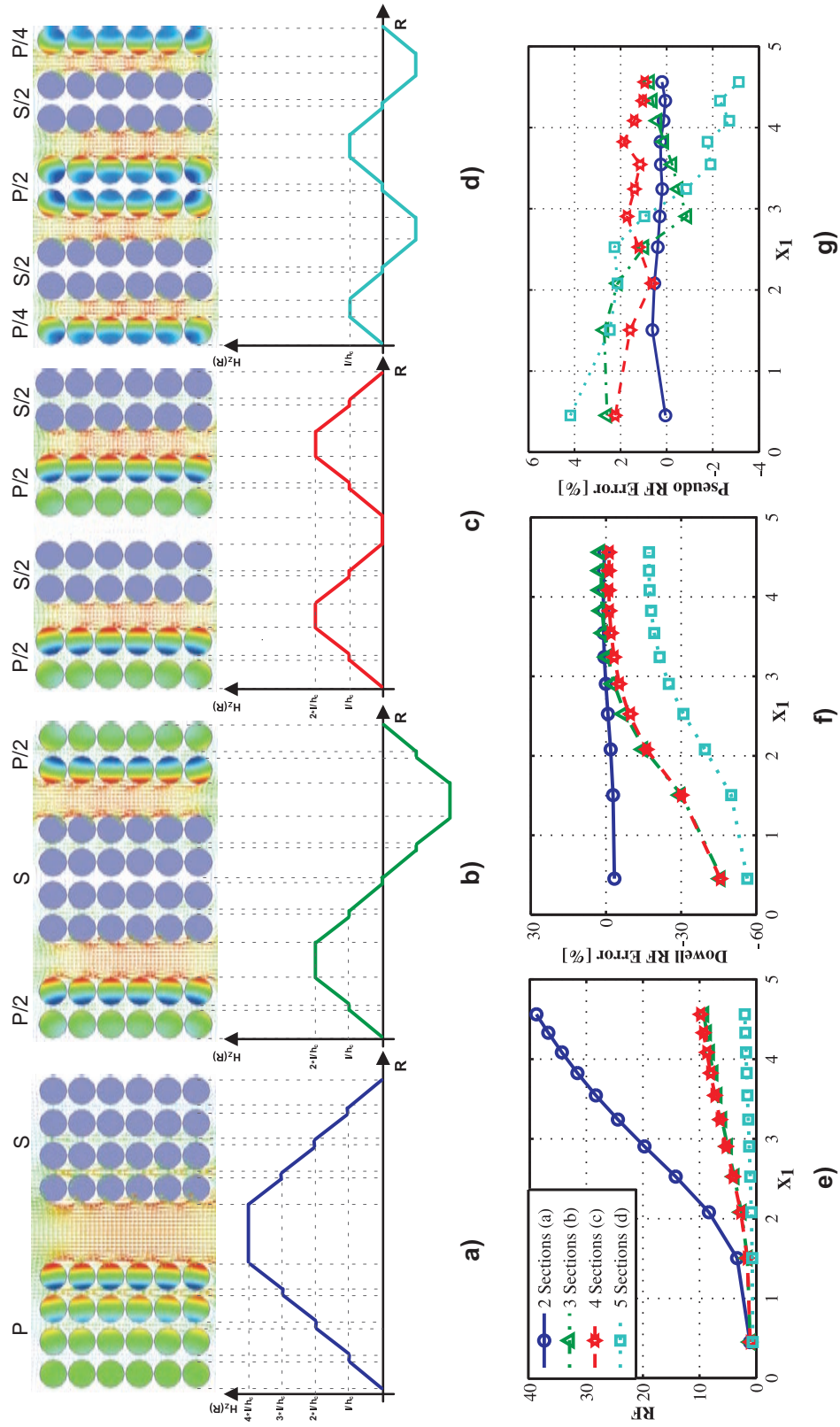


Figure 2.13: Current density and magnetic field intensity of the interleaved winding arrangements with (a) 2 sections, (b) 3 sections, (c) 4 sections, (d) 5 sections. (e) Comparison of the RF between different interleaved structures, (f) Accuracy of the Dowell's expression, (g) Accuracy of the Pseudo-Empirical's expression.

illustrated in Fig. 2.13(e) over a wide range of frequencies ( $X_1$ ), indicating a substantial reduction of the RF value in the interleaved arrangements, Fig. 2.13(b) to (d), compared to the one without interleaving, Fig. 2.13(a). It is interesting to point out that the RF values of the arrangement (b) and (c) are almost the same (about 4 times less than the one without interleaving), although the one in Fig. 2.13(c) consists of more sections which is more complex to be wound. In principle, the arrangement in Fig. 2.13(b) has more advantages over others since the RF value and accordingly its AC winding loss is substantially reduced while the secondary windings are not separated. In particular, this feature is more important when the secondary windings has higher voltages resulting in excess inter-winding capacitances if the high voltage windings is separated.

Fig. 2.13(f) and (g) show the Dowell and Pseudo RF error calculated by (2.6) and (2.23), respectively, over a wide range of frequency ( $X_1$ ).

$$RF_{Error} [\%] = 100 \times \frac{RF_{Pseudo} - RF_{FEM}}{RF_{FEM}} \quad (2.23)$$

As can be seen in Fig. 2.13(f), Dowell expression is only accurate for the non-interleaved case and it shows up to 50% underestimation for the interleaved cases while the deviation of the Pseudo-Empirical's formula is within 4%.

## 2.4 Experimental Validation

In order to verify the accuracy of the proposed pseudo-empirical equation, three transformers, comprising ETD59 ferrite cores, two layers of foil conductors as the primary windings and one layer of solid round wire as the secondary winding, with distinct porosity factors have been manufactured. The thickness of the primary foil conductors is 0.5 mm with different heights for each transformers to achieve the porosity factor or  $X_2$  of 0.92, 0.8 and one extreme case with  $X_2 = 0.4$ , while the secondary windings of all the three transformers consist of 37 turns of magnet wire with 1 mm diameter in 1 layer. Other dimensional parameters which have been kept identical in all the transformers are  $h_c = 45$  mm,  $a = 1.75$  mm,  $b = 1.8$ ,  $d_1 = 1$  mm and  $d_{HV} = 2$  mm while the parameter  $b$  differs at each transformer as follows:  $b = 1.8$ , 4.5 and 13.5 mm corresponding to  $X_2 = 0.92$ , 0.8 and 0.4, respectively.

Using the network analyzer, Bode 100, the impedance of the transformers have been measured from the primary side while the secondary was shorted over a wide range of frequencies from 10 kHz to 300 kHz to ensure that the generic parameter  $X_1$  to be swept from about 0.75 to as high as 4.3 which is sufficiently high to evaluate the accuracy of the proposed expression. The measurement setup and the manufactured transformers are shown in Fig. 2.14.

Fig. 2.15 demonstrates a comparison between the measured resistance and the calculated value by Dowell and pseudo's expression versus frequency at three differ-

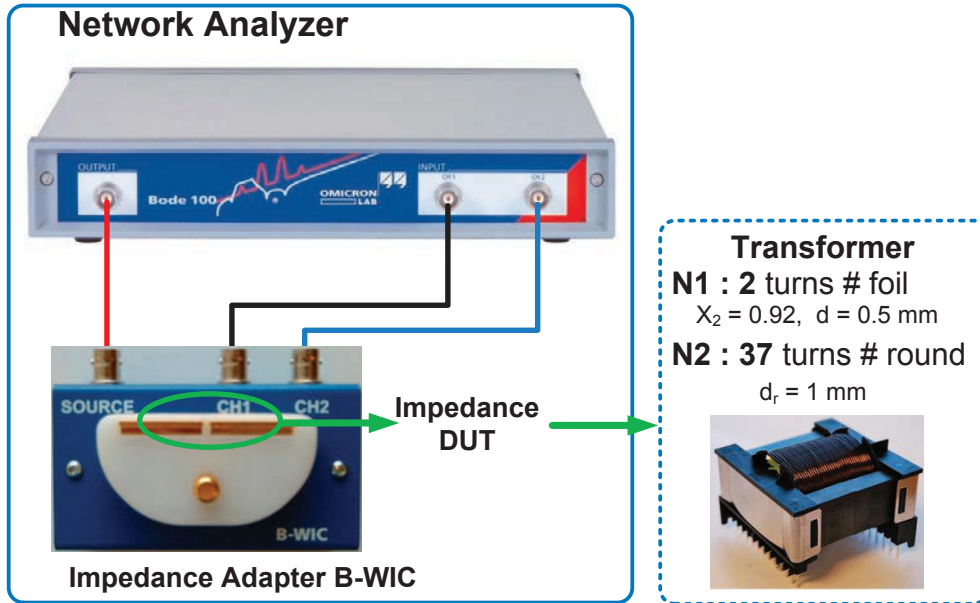


Figure 2.14: Measurement setup and the manufactured transformers.

ent values for  $X_2$ . The noisy measurement data can be attributed to the extremely low resistance of the manufactured transformers which is in the range of some milliohm. The overall results indicate that the pseudo's expression is in good agreement with the experimental results, confirming the accuracy of the proposed method over a wide range where Dowell's expression significantly underestimates the AC resistance value. This attribute is clearly demonstrated in Fig. 2.15 particularly at lower values of  $X_2$  where the second component of the magnetic field within the transformer window is intensified or at higher values of  $X_1$  where the skin depth is substantially low.

## 2.5 Conclusions

The objective of this chapter was primarily to introduce a novel analytical expression to precisely calculate the AC resistance factor of high power-density magnetic components in which precise loss evaluation is the key for designing and implementing a proper thermal management scheme. Hence, a so called pseudo-empirical expression has been derived from a rigorous regression algorithm based on an extensive 2D finite element simulation scenario, resulting in an accurate analytical expression with an average unsigned deviation of 0.51% and the extreme deviations of not higher than 9%. This high accuracy together with its wide range of applicability, taking into account any number of layers, a wide range of penetration ratio, porosity

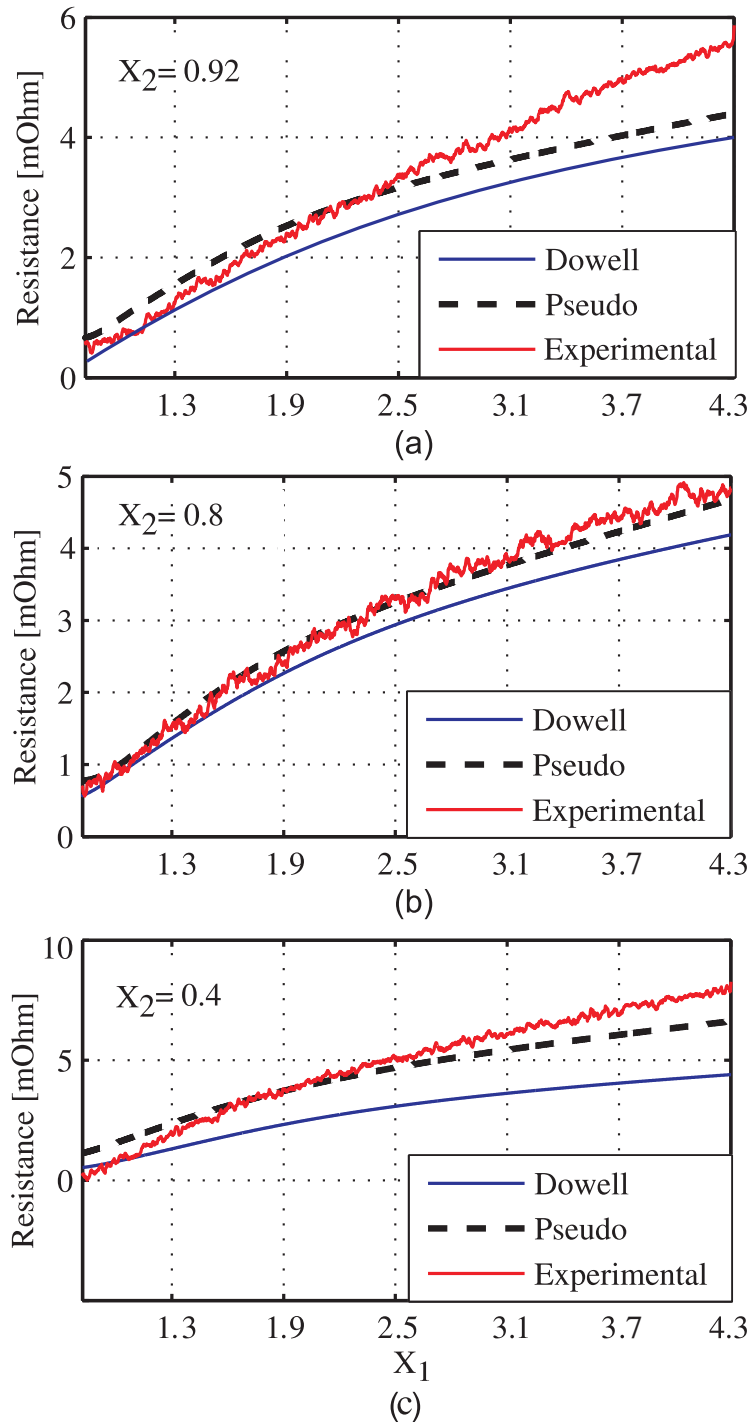


Figure 2.15: Comparison between the measured resistance and the calculated value by Dowell and Pseudo's expression versus frequency.

---

factors, and position of the windings in the transformer window, make the pseudo-empirical expression a useful tool for designers and researchers to easily implement it within any optimization loops with no accuracy compromise.

Moreover, using 2D FEM analysis, a critical review taking the two dimensional edge effect into account has been carried out on the previous well-known models in the AC winding loss calculation in order to determine their corresponding domain of validity in which those models provide an acceptable accuracy, resulting in a set of useful guidelines while using the aforementioned analytical models.





# Chapter 3

## Leakage Inductance

This chapter is based on the following articles:

- [I] Bahmani, M.A.; Thiringer, T., “Accurate Evaluation of Leakage Inductance in High-Frequency Transformers Using an Improved Frequency-Dependent Expression,” *IEEE Transactions on Power Electronics*, vol.30, no.10, pp.5738-5745, Oct. 2015.
- [II] Bahmani, M.A.; Thiringer, T., “An Accurate Frequency-Dependent Analytical Expression for Leakage Inductance Calculation in High Frequency Transformers,” *PCIM South America 2014*, p. 275-282, Oct 2014.

This chapter presents a new analytical expression intended to accurately evaluate the leakage inductance of transformers in the high frequency range in which the behavior of the magnetic field within the windings is altered. Unlike conventional expressions, which usually overestimate the leakage inductance at higher frequencies, this expression accounts for high frequency behavior of the magnetic field and provides high accuracy when operating at high frequencies. These high accuracy and applicability makes the derived expression of interest for designers to avoid time consuming finite element simulations without compromising with accuracy. The expression is validated by 2-D FEM simulation, as well as by measurements.

### 3.1 Introduction

High power densities in power conversion units have become one of the design requirements, particularly in highly restricted applications such as traction and offshore wind farms [3, 4]. To achieve this goal, the bulky 50/60 Hz transformers have been replaced with high power density DC-DC converters consisting of high-frequency transformers with lower weights and volumes. However, being exposed to higher frequencies, one should cope with extra losses coming from eddy current

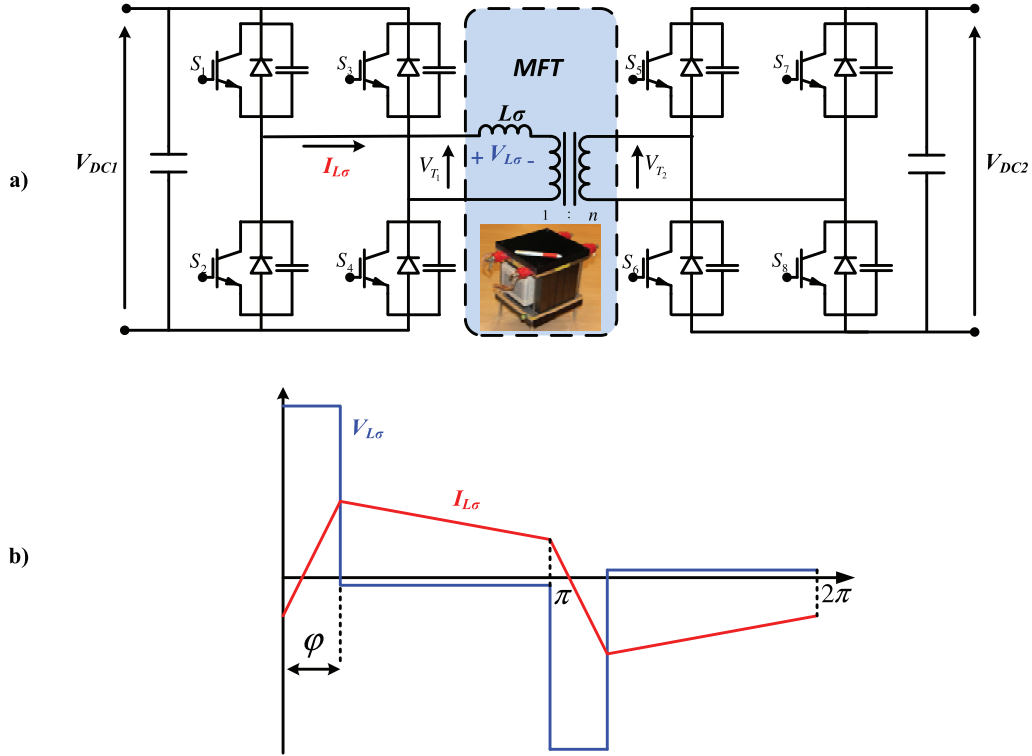


Figure 3.1: (a) Equivalent circuit of a dual active bridge converter along with the leakage inductance integrated in to the medium-frequency transformer. (b) The voltage and current of the leakage inductance.

losses in the magnetic core [65, 66], excess losses in the windings due to enhanced skin and proximity effects [17], as well as parasitic elements, i.e., leakage inductance [67–69] and winding capacitance [70, 71], causing excess switching losses in the power semiconductors which is usually dominant at higher frequencies [18].

Recently, there has been growing interest in utilizing dual active bridge (DAB) converters in high power applications [72]. The equivalent circuit of a DAB converter is shown in Fig. 5.1 in which two square voltage waveforms on two sides of the transformer have been shifted by controlling the input and output bridges. This applies full voltage on the inductance,  $L$ , which is used to shape the current as a power transfer element [2]. In order to achieve zero-voltage switching (ZVS), the phase shift between the bridges,  $\varphi$ , should be higher than a certain value resulting in the minimum series inductance value calculating as

$$L_{min} = \frac{V_{DC1} V_{DC2} \varphi_{min} (\pi - \varphi_{min})}{2P_{out} \pi^2 f_s n} \quad (3.1)$$

where  $V_{DC1}$  and  $V_{DC2}$  are the input and output DC voltages of the DC-DC converter shown in Fig. 3.1, respectively;  $\varphi_{min}$  is the minimum required phase shift between

the primary and secondary voltage of the high frequency transformer highlighted as the key element of the DAB converter in Fig. 3.1,  $P_{out}$  is the desired output power,  $n$  is the turns ratio of the transformer and  $f_s$  is the operating frequency of the high frequency transformer, i.e., switching frequency.

This inductance, as shown in Fig. 3.1, can be seen as an integrated leakage inductance,  $L_\sigma$ , in the high frequency transformer, so that the number and size of components can be reduced, hence achieving higher power densities [73]. It would thus be of great importance to accurately evaluate the leakage inductance of such a transformer in the design stage since an insufficient leakage inductance leads to a shift in soft switching which can adversely affect the converter efficiency. Likewise, higher values of leakage inductance is not desired, because it causes an unnecessary reactive power circulation within the converter which eventually decrease the efficiency and output active power of the converter, nevertheless, this can expand the soft-switching region to some extent.

In addition to high power DAB converters, in some applications, such as resonant converters, the value of  $L_\sigma$  should be tuned in order to incorporate the leakage inductance as one of the resonant elements to retain the resonant conditions [74, 75]. Hence, accurate evaluation of leakage inductance in the design process is of great importance for designers, more specifically in high power density applications where high deviations between the calculated and actual value can not be easily tolerated.

Although considerable research has been devoted to the frequency dependency of winding losses, rather less attention has been paid to this characteristics of leakage inductance. Most of the classical attempts for leakage inductance evaluations focus on the winding build as an indication for high magnetic field region. This approach has been addressed in the Mcllyman [19], Flangan [62] and Mohan [76] handbooks and has later been modified in several publications. Dauharje and Thondapu [77, 78] modified the accuracy of the expression by considering the flux that extends into air in a secondary shorted transformer. Apart from these, more detailed winding dimensions have been taken into account by Naderian [79] while Ouyang [67] proposed a more elaborated modification accounting for different winding arrangements in a planar transformer. Moreover, Krantor [80] proposed a simple expression determining the area of the reduced leakage channel of concentric windings of equal heights with different winding thicknesses, however, all of these expressions might be less effective when high frequency effects are taken into account. The frequency dependency of the leakage inductance in high frequency power electronics with non-sinusoidal waveforms has been extensively studied foremost by Hurley in [81]. The practical validity of the original Hurley's equation has been questioned by Wilson [82] since it was specifically derived for a toroidal core. Utilizing field analysis, Niemla [83] provided an alternative approach accounting for the short-circuit impedance of multi-winding transformers, however, due to several simplifications, an average error of about 10 % was reported as well as the lack of a closed form expression which also

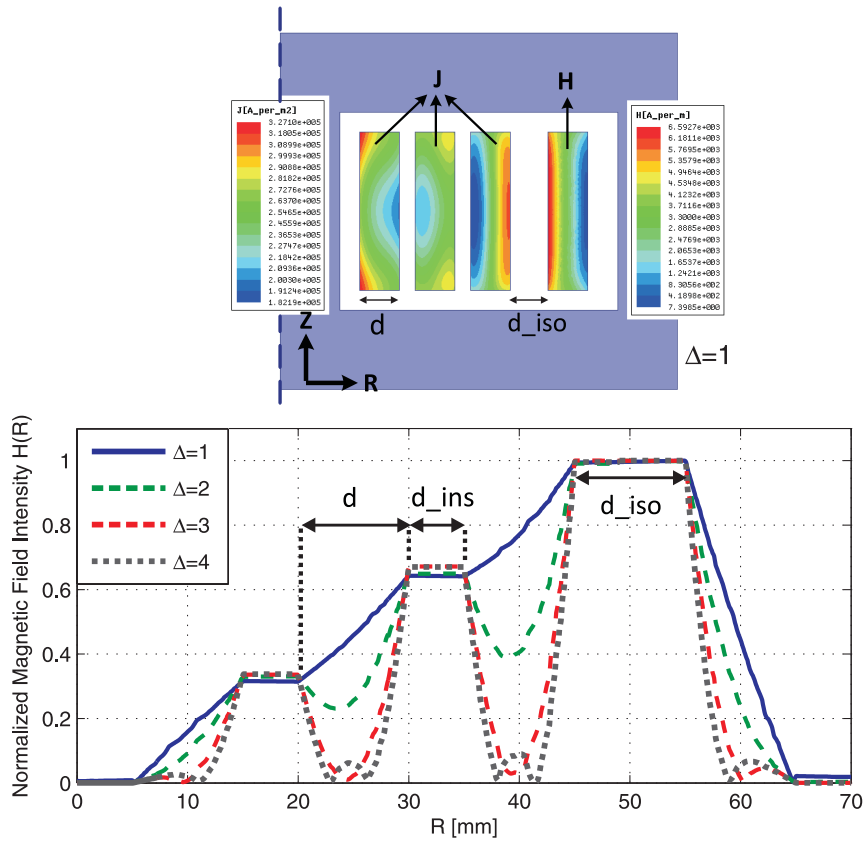


Figure 3.2: The magnetic field distribution profile within the transformer window at different frequencies.

was observed in [82] in which the main focus was to provide a circuit simulation model. Apart from the mentioned studies, only Dowell [39] solved and formulated the multilayer leakage inductance based on simplified 1-D Maxwell equations. This method has been partially adopted in a recent handbook by Hurley [84] indicating higher accuracy in certain ranges of normalized frequency and normalized isolation distance. However, it remains unclear whether the later aforementioned expressions demonstrate enough accuracy, particularly in the special applications mentioned in the beginning of this part. It would seem, therefore, that further investigations are needed in order to specify the accuracy of these expression within a wide range of frequency with special winding arrangements.

The purpose of this chapter is to propose a new analytical expression, to calculate a fairly accurate value of leakage inductance to meet the requirements of the particular applications mentioned earlier. This model takes into account the effects of high frequency fields inside the conductors such as skin and proximity effects, as well as the geometrical parameters of the transformer windings when determining the leakage inductance. Being validated by FEM simulations and measurements on

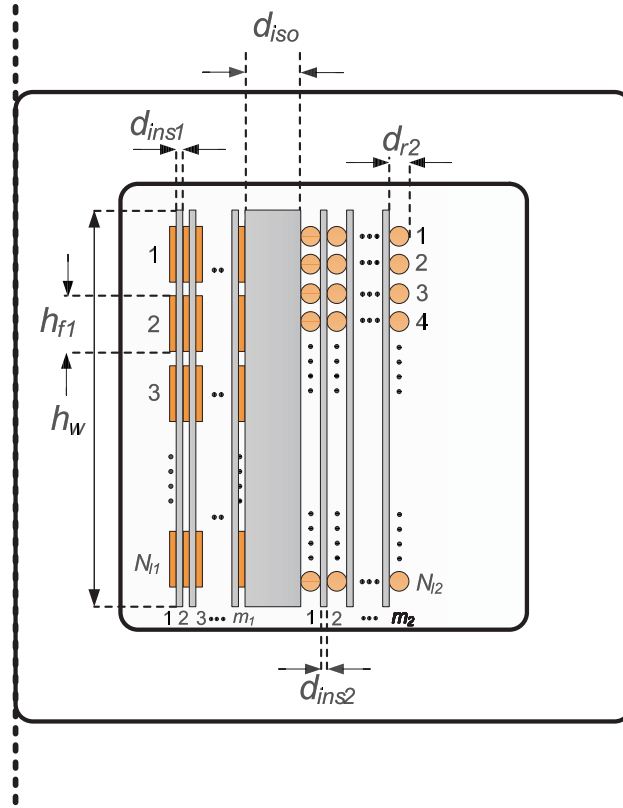


Figure 3.3: Cross-sectional view of the winding configurations according to Dowell's assumptions.

different winding configurations, this model provides a very good accuracy, compared to previously presented analytical expressions, with wide-range applicability which could be of interest for designers to avoid time consuming FEM simulations without compromising with the accuracy.

## 3.2 Expression Derivation

Fig. 3.2 shows a sample 2D axisymmetric FEM simulation of the transformer windings at different values of penetration ratio,  $\Delta$  as defined in (3.2), illustrating the computed current density distribution and magnetic field intensity in the primary and secondary windings respectively. The dimensions of the geometry were kept constant and different values of  $\Delta$  were achieved by applying the frequencies corresponding to those values. In other words, the analysis is based on a dimensionless parameter,  $\Delta$ , taking into account the effects of both frequency and geometrical dimensions. The normalized magnetic field intensity distribution on inter and intra-layer spaces, obtained from the same FEM simulation at four different values of  $\Delta$ ,

are shown in Fig. 3.2 bottom. It should be noted that Fig. 3.2 top illustrates the FEM simulation corresponding to the case in which  $\Delta$  is equal to 1.

$$\Delta = \frac{d}{\delta} \quad (3.2)$$

where  $d$  is the conductor thickness and  $\delta$  is the skin depth at any particular frequency.

As can be seen in Fig. 3.2, the magnetic field intensity inside the copper windings drastically decreases by increasing the frequency or its corresponding  $\Delta$ . Thus results in a reduced stored magnetic energy due to the skin and proximity effects rearranging the magnetic lines. This causes higher ohmic losses on the third layer of the primary windings than the ohmic losses in the first and second layer. This is due to the fact that in contrast to the first layer, which does not suffer from the magnetic field on its left hand side, the second layer and more significantly the third layer suffers from the presence of the magnetic field on their left hand side. This magnetic field drop at higher frequency is often neglected in most of the classical formulas for leakage inductance calculations which might result in inaccuracy in high power density applications.

Fig. 3.3 shows the schematic of a transformer window comprising the magnetic core with a relatively high permeability of 20000 which is a typical permeability of the nanocrystalline soft magnetic material, copper foil primary windings consisting of  $m_1$  layers and  $N_{l1}$  turns per layer, secondary round wires consisting of  $m_2$  layers and  $N_{l2}$  turns per layer and all the corresponding distances, i.e, isolation distance, insulating distance, winding heights and thicknesses and so on.

$$\begin{aligned} W_{leakage} &= \frac{1}{2}\mu_0 \int H^2 dv \\ &= \frac{1}{4}L_{\sigma(pri)}I_1^2 \\ &= W_{pri} + W_{ins(1)} + W_{isolation} + W_{sec} + W_{ins(2)} \end{aligned} \quad (3.3)$$

where  $W_{leakage}$  is the energy stored in the leakage inductance of a transformer,  $H$  is magnetic flux density within the transformer window,  $L_{\sigma(pri)}$  is the leakage inductance referred to the primary of a transformer,  $W_{isolation}$  is the energy stored within the distance between two winding portions,  $W_{ins(1)}$  is the energy stored between inter-layer distances of the primary portion,  $W_{ins(2)}$  is the energy stored between inter-layer distances of the secondary portion,  $W_{pri}$  and  $W_{sec}$  are the energies stored inside the primary and secondary conductor area, respectively.

As shown in (3.3), the energy stored in the magnetic field of a transformer when the secondary windings is shorted is equal to the energy stored in the leakage inductance referred to the primary side of the transformer. Therefore, one can separately derive the stored energy within isolation distance, primary and secondary inter-layer insulations and primary and secondary copper areas, respectively. First,

the energy stored within isolation and insulation distances are calculated since the magnetic field intensity within these regions are constant, hence using (3.3) and considering a one dimensional magnetic field, one can conclude:

$$\begin{aligned} W_{isolation} &= \frac{1}{4}\mu_0 M L T_{isolation} h_w \int_0^{d_{iso}} \left( \frac{N_{l1} m_1 I_1}{h_w} \right)^2 dx \\ &= \frac{1}{4}\mu_0 M L T_{isolation} \frac{N_{l1}^2 m_1^2 I_1^2}{h_w} d_{iso} \end{aligned} \quad (3.4)$$

$$\begin{aligned} W_{ins1} &= \frac{1}{4}\mu_0 M L T_{pri} h_w \left[ \sum_{n=0}^{m_1-1} \frac{N_{l1}^2 n^2 I_1^2}{h_w^2} d_{ins1} \right] \\ &= \frac{1}{4}\mu_0 M L T_{pri} \frac{N_{l1}^2}{h_w} I_1^2 d_{ins1} \frac{m_1(m_1-1)(2m_1-1)}{6} \end{aligned} \quad (3.5)$$

$$\begin{aligned} W_{ins2} &= \frac{1}{4}\mu_0 M L T_{sec} h_w \left[ \sum_{n=0}^{m_2-1} \frac{N_{l2}^2 n^2 I_2^2}{h_w^2} d_{ins2} \right] \\ &= \frac{1}{4}\mu_0 M L T_{sec} \frac{N_{l1}^2}{h_w} I_1^2 d_{ins2} \frac{m_1^2(m_2-1)(2m_2-1)}{6m_2} \end{aligned} \quad (3.6)$$

where  $M L T_{pri}$ ,  $M L T_{sec}$  and  $M L T_{iso}$  are the mean length turns of the primary portion, secondary portion and isolation distance, respectively.  $h_w$  is the winding height,  $n$  is the transformer turn ration,  $I_1$  and  $I_2$  are the peak current values of primary and secondary portions, respectively [73, 85].

However, obtaining a closed formula for the stored energy inside the copper windings is not as straightforward as what were obtained in (3.4) to (3.6) since the magnetic field pattern is not constant or linear at higher frequencies as already shown in Fig. 3.2. In fact, the magnetic field has a hyperbolic pattern according to Dowell's derivation [39]. Substituting this hyperbolic pattern in (3.3), one can derive:

$$\begin{aligned} W_{pri} &= \frac{1}{4}\mu_0 M L T_{pri} h_w \sum_{n=1}^{m_1} \left( \int_0^{d_{pri}} H_x^2 dx \right) \\ &= \frac{1}{4}\mu_0 M L T_{pri} h_w \cdot \\ &\sum_{n=1}^{m_1} \left( \int_0^{d_{pri}} \left[ \frac{H_{ex} \sinh(\alpha x) - H_{in} \sinh(\alpha x - \alpha d_{pri})}{\sinh(\alpha d_{pri})} \right]^2 dx \right) \end{aligned} \quad (3.7)$$

$$\begin{aligned}
W_{sec} &= \frac{1}{4}\mu_0MLT_{sec}h_w \sum_{n=1}^{m_2} \left( \int_0^{d_{sec}} H_x^2 dx \right) \\
&= \frac{1}{4}\mu_0MLT_{sec}h_w \cdot \\
&\sum_{n=1}^{m_2} \left( \int_0^{d_{sec}} \left[ \frac{H_{ex} \sinh(\alpha x) - H_{in} \sinh(\alpha x - \alpha \cdot d_{sec})}{\sinh(\alpha d_{sec})} \right]^2 dx \right) \quad (3.8)
\end{aligned}$$

where  $H_{in}$  and  $H_{ex}$  are the magnetic field intensity at the left and right hand side of each winding layer and can be calculated as (3.9). Also,  $\alpha$  is defined as  $\frac{1+j}{\delta}$  where  $\delta$  is the skin depth at any particular frequency and  $d_{pri}$  and  $d_{sec}$  are the thickness of the primary and secondary conductors, respectively,

$$H_{in} = \frac{(n-1)N_{L1}I_1}{h_w}, \quad H_{ex} = \frac{nN_{L1}I_1}{h_w}. \quad (3.9)$$

Substitution of (3.9) into (3.7) and (3.8) and rearranging for the stored energy gives

$$\begin{aligned}
W_{pri} &= \frac{1}{4}\mu_0MLT_{pri} \frac{N_{L1}^2}{h_w} m_1 I_1^2 \cdot \\
&\left[ \frac{\sin(\frac{2\Delta_1}{\alpha\delta}) 4\alpha\delta^2(m_1^2 - 1) + 4d_{pri}(2m_1^2 + 1)}{24\sin^2(\frac{2\Delta_1}{\alpha\delta})} \right. \\
&\quad \left. - \frac{\alpha\delta^2 \sin(\frac{4\Delta_1}{\alpha\delta})(2m_1^2 + 1) - 8d_{pri}(1 - m_1^2)\cos(\frac{2\Delta_1}{\alpha\delta})}{24\sin^2(\frac{2\Delta_1}{\alpha\delta})} \right] \quad (3.10)
\end{aligned}$$

$$\begin{aligned}
W_{sec} &= \frac{1}{4}\mu_0MLT_{sec} \frac{N_{L1}^2}{h_w} \frac{m_1^2}{m_2} I_1^2 \cdot \\
&\left[ \frac{\sin(\frac{2\Delta_2}{\alpha\delta}) 4\alpha\delta^2(m_2^2 - 1) + 4d_{sec}(2m_2^2 + 1)}{24\sin^2(\frac{2\Delta_2}{\alpha\delta})} \right. \\
&\quad \left. - \frac{\alpha\delta^2 \sin(\frac{4\Delta_2}{\alpha\delta})(2m_2^2 + 1) - 8d_{sec}(1 - m_2^2)\cos(\frac{2\Delta_2}{\alpha\delta})}{24\sin^2(\frac{2\Delta_2}{\alpha\delta})} \right] \quad (3.11)
\end{aligned}$$

where  $\Delta_1$  and  $\Delta_2$  are the penetration ratio of the primary and secondary winding as (3.12)

$$\Delta_1 = \frac{d_{pri}}{\delta}, \quad \Delta_2 = \frac{d_{sec}}{\delta}. \quad (3.12)$$

Finally, substitution of (3.4), (3.5), (3.6), (3.10) and (3.11) into (3.3) and rearranging for  $L_{\sigma(pri)}$  gives the final frequency-dependent expression as



$$\begin{aligned}
L_{\sigma(pri)} = & \mu_0 \frac{N_{L1}^2}{h_w} m_1 \left[ MLL_{iso} m_1 d_{iso} \right. \\
& + MLL_{pri} \frac{(m_1 - 1)(2m_1 - 1)}{6} d_{ins1} \\
& + MLL_{sec} \frac{m_1(m_2 - 1)(2m_2 - 1)}{6m_2} d_{ins2} \\
& + MLL_{pri} \cdot Im \left( \frac{\sin(\frac{2\Delta_1}{\alpha\delta}) 4\alpha\delta^2(m_1^2 - 1) + 4d_{pri}(2m_1^2 + 1)}{24\sin^2(\frac{2\Delta_1}{\alpha\delta})} \right) \\
& - MLL_{pri} \cdot Im \left( \frac{\alpha\delta^2 \sin(\frac{4\Delta_1}{\alpha\delta})(2m_1^2 + 1) - 8d_{pri}(1 - m_1^2)\cos(\frac{2\Delta_1}{\alpha\delta})}{24\sin^2(\frac{2\Delta_1}{\alpha\delta})} \right) \\
& + MLL_{sec} \cdot Im \left( \frac{\frac{m_1}{m_2} \sin(\frac{2\Delta_2}{\alpha\delta}) 4\alpha\delta^2(m_2^2 - 1) + 4d_{sec}(2m_2^2 + 1)}{24\sin^2(\frac{2\Delta_2}{\alpha\delta})} \right) \\
& - MLL_{sec} \cdot Im \left( \frac{\frac{m_1}{m_2} \alpha\delta^2 \sin(\frac{4\Delta_2}{\alpha\delta})(2m_2^2 + 1)}{24\sin^2(\frac{2\Delta_2}{\alpha\delta})} \right) \\
& \left. + MLL_{sec} \cdot Im \left( \frac{\frac{m_1}{m_2} 8d_{sec}(1 - m_2^2)\cos(\frac{2\Delta_2}{\alpha\delta})}{24\sin^2(\frac{2\Delta_2}{\alpha\delta})} \right) \right]. \tag{3.13}
\end{aligned}$$

It should be noted that the final expression has been derived based on foil winding configuration, however, it would be applicable for round conductors by modifying  $\Delta$  of the windings portion with round wire as [17]

$$\Delta = \frac{d_r \sqrt{2}}{2\delta} \sqrt{\frac{N_l d_r \sqrt{\pi}}{2h_w}} \tag{3.14}$$

where  $d_r$  is round wire diameter and  $N_l$  is the number of turns per layer.

### 3.3 Accuracy Investigation

#### 3.3.1 Comparison with Classical Expressions

In order to investigate the accuracy of the aforementioned expression, parametric FEM simulations covering a wide range of frequency, up to 200  $kHz$ , have been performed. The obtained leakage inductances were then compared with the leakage inductances calculated by the classical expressions [19, 62]. The current density distribution at 1  $kHz$  and the investigated winding arrangement, illustrated in Fig. 3.4(a), consists of 20 foil conductors in each winding portion, 5 layers and 4 turns per layer, with the foil thickness of 1.2 mm. All the geometrical dimensions are kept constant while the operating frequency is swept from 50  $Hz$  to 200  $kHz$ .

$$L_{\sigma(classic)} = \mu_0 M L T_{pri} \frac{m_1^2 \cdot N_{l1}^2}{h_w} \left[ d_{iso} + \frac{m_1 d_{pri} + (m_1 - 1) d_{ins1} + m_2 d_{sec} + (m_2 - 1) d_{ins2}}{3} \right]. \quad (3.15)$$

As can be seen in Fig. 3.4(b), the classical expression, (3.15), generally shows a high inaccuracy for almost the whole range of investigation, particularly at higher frequencies. For instance, at 200  $kHz$ , the classical expression estimates the leakage inductance as high as 23  $\mu H$  whereas FEM simulation and the derived frequency-dependent expression shows 18.2  $\mu H$  and 18  $\mu H$  respectively. This significant overestimation can result in an unrealistic and costly magnetic design. This inaccuracy could stem from the rigorous assumption made regarding the linear pattern of the magnetic field within copper conductors which is not a valid assumption when a conductor, conducting high frequency currents, is surrounded by a large number of other conductors with a complex arrangement. In fact, the skin depth decreases and the current density decreases in the middle of the conductors while the proximity effects become more pronounced. Exceeding a certain frequency, depending on geometrical characteristics of the windings, there would be almost no magnetic field within a conductor and thus no further decrease in the obtained leakage inductance. This attribute can be seen in Fig. 3.4(b) when the frequency exceeds 120  $kHz$ .

Fig. 3.4(c) shows the obtained values of leakage inductance at different number of primary and secondary winding layers whereas the frequency is kept constant at 150  $kHz$ . Moreover the deviation of the classical and frequency-dependent expressions from the results obtained by FEM have been calculated by

$$L_{\sigma(deviation)}[\%] = 100 \times \frac{L_{\sigma(calculated)} - L_{\sigma(FEM)}}{L_{\sigma(FEM)}}. \quad (3.16)$$

As can be seen in Fig. 3.4(b) and (c), using the frequency-dependent formula, almost in the whole range of frequency and at different number of winding layers, the leakage inductance were calculated with a negligible difference from the FEM results indicating the high accuracy of the proposed expression. In contrast, the classical formula generally shows a high inaccuracy for almost the whole range of frequency and different number of layers. According to the deviation curves illustrated in Fig. 3.4(c), classical expression leads to deviations of a 30% overestimation (with 10 layers of windings) whereas the frequency-dependent formula exhibit a deviation of always less than 10% underestimation, nevertheless at a lower number of layers it is around 4% ,within the studied range which is substantially more accurate than the classical expression. In addition,  $d_{ins2}$  and  $d_{iso}$  are about 1 and 2 mm, respectively [85].

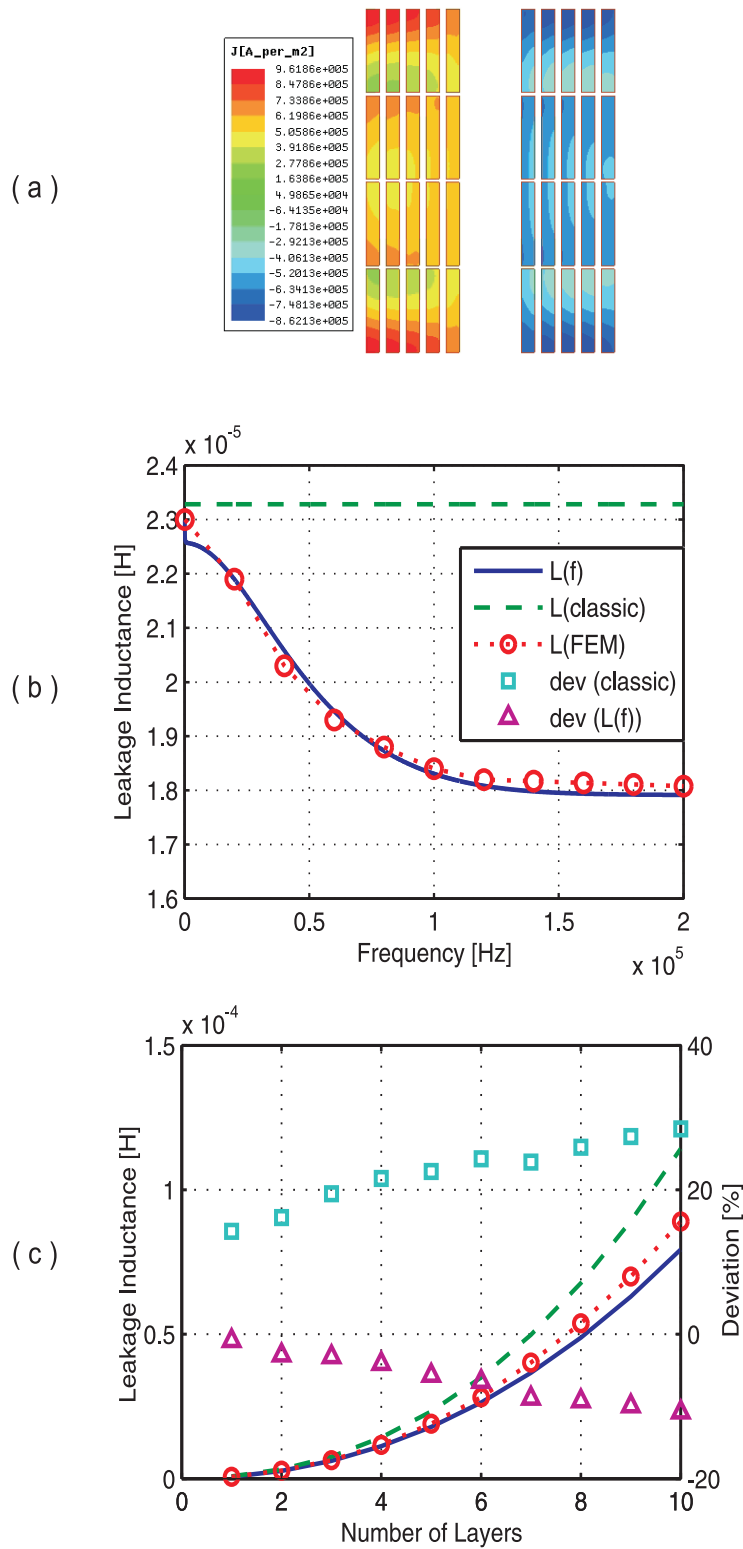


Figure 3.4: (a) A sample FEM simulation result. (b) Calculated Leakage inductance by the studied methods versus frequency. (c) Calculated Leakage inductance by the studied methods versus the number of layers in each windings portion while the frequency is constant.

### 3.3.2 Comparison with Frequency Dependent Expressions

One of the purposes of this chapter is to investigate the validity range of the previous frequency-dependent expressions, particularly the most well-known ones demonstrated by Dowell and Hurley. Dowell's expression was initially derived from solving Maxwell equations under certain circumstances known as Dowell's conditions. Utilizing the imaginary part of the Dowell's ac impedance expression, the ac leakage inductance due to the flux cutting the conductors can be written as

$$L_w = \frac{\mu_0 m^3 N_l^2 d M L T}{3 h_w} \left( \frac{3M'' + (m^2 - 1)D''}{m^2 |\delta^2 d^2|} \right) \quad (3.17)$$

where  $L_w$  is the leakage inductance within one conductor portion,  $M''$  and  $D''$  are the imaginary parts of the functions given in (3.18) [39] as

$$M = \delta d \coth(\delta d) \quad , \quad D = 2\delta d \tanh\left(\frac{\delta d}{2}\right). \quad (3.18)$$

The energy stored within the isolation distance between the windings, as well as the insulation distances between the primary and secondary layers are the same as the ones presented in (3.4), (3.5) and (3.6), respectively. This approach has been partially adopted in [84] with one exception, i.e., the energy stored in the isolation and insulation, which have been calculated with the classical approach,

$$\begin{aligned} L_\sigma = & \frac{\mu_0 m N_l^2 \delta M L T}{2 h_w} \cdot \\ & \left[ \frac{\sinh 2\Delta - \sin 2\Delta}{\cosh 2\Delta - \cos 2\Delta} + \frac{2(m^2 - 1)}{3} \frac{\sinh \Delta + \sin \Delta}{\cosh \Delta + \cos \Delta} \right] \\ & + \mu_0 M L T_{pri} \frac{m_1^2 N_{l1}^2}{h_w} \left[ \frac{d_{iso} + m_1 \cdot d_{pri}}{3} \right. \\ & \left. + \frac{(m_1 - 1)d_{ins1} + m_2 \cdot d_{sec} + (m_2 - 1)d_{ins2}}{3} \right] \end{aligned} \quad (3.19)$$

in which the first component, which is the frequency-dependent component, should be calculated for each winding portion, separately.

In order to determine the limitations and validity range of the aforementioned expressions, the result of a series of numerical simulations, examining the effect of geometrical aspects on ac leakage inductance at different frequencies, are compared with the ac leakage inductances calculated by Dowell, by (3.19) and the here proposed frequency dependent expression. It should be noted that all the geometrical dimensions were kept constant and higher  $\Delta$  achieved by increasing the frequency while the transformer consisted of two windings portions, each comprising of 6 layers of rectangular foil conductor. Each layer consisted of 5 conductors with the total

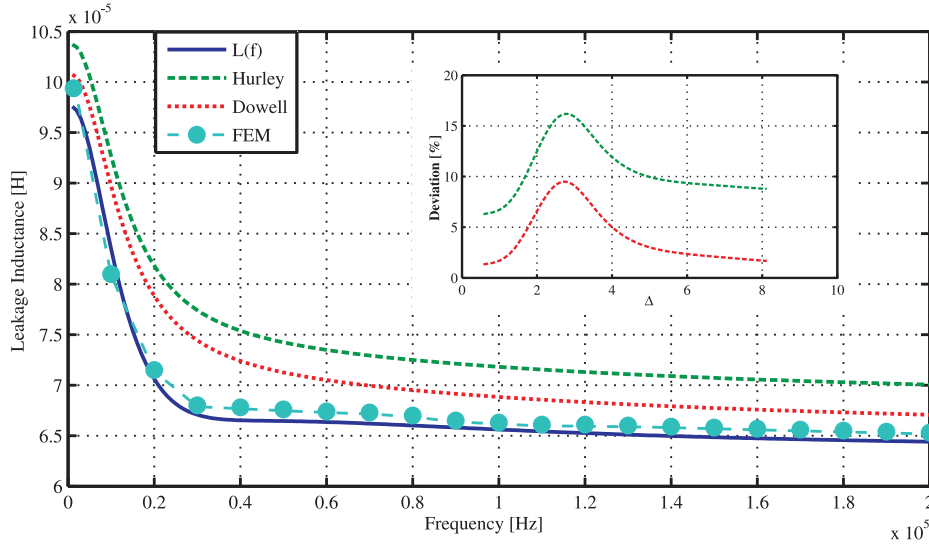


Figure 3.5: Accuracy investigation of the previously presented expressions.

porosity factor of 0.79 which is a typical value in power electronics. Fig. 3.5 shows the leakage inductance of the studied winding configuration calculated by (3.19), Dowell and the here proposed expressions, as well as the values obtained by FEM simulations over a wide range of frequencies.

Some remarks can be highlighted in Fig. 3.5. First, it is worth to point out that all three considered expressions, unlike the classical expressions, clearly demonstrate the influence of higher frequency operation on the leakage inductance value, however the derived frequency dependent expression demonstrates a relatively better accuracy. Moreover, as illustrated in Fig. 3.5, the accuracy of the Dowell's expression, and more significantly the one in (3.19), drops close to the knee point of the leakage inductance curves. This attribute is clearly demonstrated in the sub-figure of Fig. 3.5 in which the deviation of Dowell and the one in (3.19) from the results obtained by FEM simulations has been illustrated based on the corresponding penetration ratio,  $\Delta$ , of each frequency. As can be seen in this sub-figure, the worst deviation from FEM results occurs at  $2 < \Delta < 3$  in which Dowell and (3.19) maximum deviations, respectively, are 9% and 17%. It is worthwhile mentioning that these values are for a specific windings configurations, and in order to obtain a more clear accuracy pictures of studied expressions, one needs to investigate a broader range of winding configurations.

In order to more thoroughly investigate the worst case scenarios highlighted in Fig. 3.5, another set of parametric FEM simulations covering different winding configurations by altering the normalized isolation distance, i.e.,  $2 < \frac{d_{iso}}{b} < 3$  which were performed at a  $\Delta$  corresponding to the knee point of Fig. 3.5 in which the

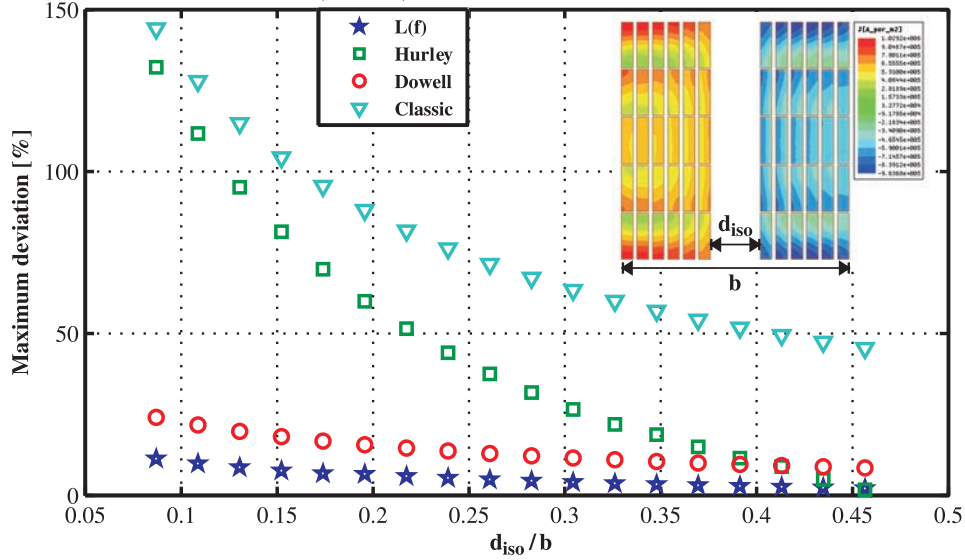


Figure 3.6: Absolute maximum deviations of the studied expressions compared to FEM.

maximum deviations from the FEM simulations are expected to occur. As illustrated in sub-figure of Fig. 3.6,  $d_{iso}$  and  $b$  are the isolation distance and the total winding build, respectively. Fig. 3.6 shows the absolute maximum deviations of the classical and frequency-dependent expressions, calculated by (3.20), versus a practical range of normalized isolation distance.

$$L_{\sigma(max\ dev)}[\%] = \left| 100 \times \frac{L_{\sigma(calculated)} - L_{\sigma(FEM)}}{L_{\sigma(FEM)}} \right|. \quad (3.20)$$

The overall results presented in Fig. 3.6 indicate that the absolute maximum deviations of the classical and frequency-dependent expressions increase by decreasing the normalized isolation distance. This inaccuracy could stem from the rigorous Dowell initial assumption regarding 1-D magnetic field within and between foil layers since, except for the classical expression, other frequency-dependent expression partially adopted the Dowell method. This assumption is usually being violated in many practical designs resulting in the presence of the second component of the magnetic field [17]. Decreasing  $\frac{d_{iso}}{b}$ , the share of conductor area in leakage inductance determination intensifies which is the area that Dowell's initial assumption are applied on; This leads to higher inaccuracy compared to FEM simulations in which a 2-D magnetic field is considered, particularly when  $\frac{d_{iso}}{b}$  is smaller. However, the here derived frequency-dependent expression shows lower maximum deviations from FEM, compared to the ones from Dowell and particularly (3.19). As illustrated in Fig. 3.6, the maximum deviation of the derived expression is within  $\pm 15\%$  which is a relatively acceptable deviation for an analytical tool, while the one of Dowell's is

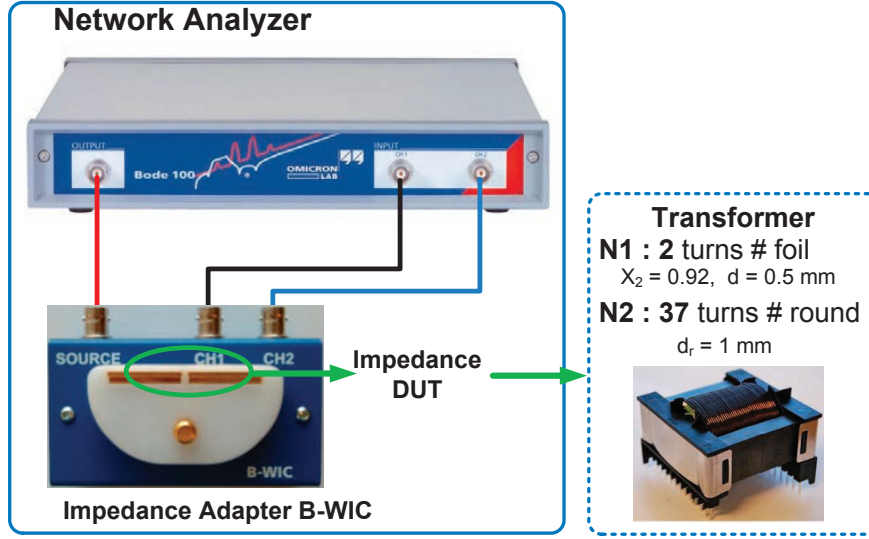


Figure 3.7: Measurement setup and the manufactured transformer.

within  $\pm 24\%$  and the ones in (3.19) and the classical equations can be as high as  $\pm 130\%$  and  $\pm 146\%$ , respectively.

### 3.4 Experimental Validation

In order to verify the accuracy of the proposed frequency dependent expression, a transformer comprising two ETD59 Ferrite cores, two layers of foil conductors as the primary windings and one layer of solid round wire consisting of 37 turns as the secondary windings, has been manufactured. The thickness and diameter of the foil and round conductors are, respectively, 0.5 and 1 mm while the porosity factor, the degree of fulfillment of the core window height, is about 0.92. Using the network analyzer Bode 100, the impedance of the transformer has been measured from the primary side while the secondary is shorted over a wide range of frequency till 300  $kHz$  which is the typical range for most of the power electronic applications. The measurement setup and the manufactured transformer are shown in Fig. 3.7.

It should be noted that shorting the secondary winding and measuring the inductance from the primary side gives the equivalent inductance referred to the primary side. This equivalent inductance comprises of both leakage inductance and magnetizing inductance of the transformer, however, magnetizing inductance is usually much larger than the leakage inductance and therefore it can be neglected in the circuit. The value of magnetizing inductance for the manufactured transformer is about 37  $\mu H$  which is almost thousand time higher than the measured leakage inductance.

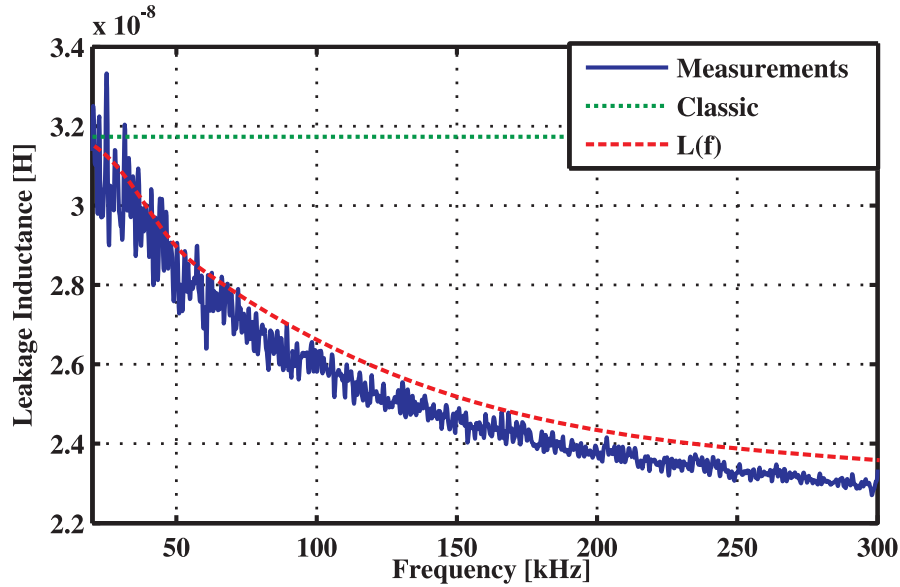


Figure 3.8: Comparison between the measured leakage inductance and the calculated values by the frequency dependent and classical expressions.

Fig. 3.8 demonstrates a comparison between the measured leakage inductance and the values calculated by the frequency dependent and classical expressions. The overall results indicate a good agreement between the frequency dependent expression and the measurements, whereas the classical expression is constant within the whole frequency range, demonstrating about 30% overestimation of the leakage inductance. The noisy measurements data can be attributed to the extremely low impedance of the manufactured transformer.

### 3.5 Conclusions

This chapter introduced an analytical expression to accurately calculate the leakage inductance of high-frequency transformers. Using the energy method, a frequency-dependent expression yielding higher accuracy in comparison with the previous analytical methods has been developed. Moreover, the derived expression has a wide range of applicability taking into account multilayer configuration, a wide range of penetration ratios and frequencies. In addition, it accounts for the position of the windings in the transformer window with its respective dimensions. The high accuracy together with its wide range of applications makes the final expression a useful tool that designers and researchers can easily implement within any optimization loops with almost no accuracy compromise.



# Chapter 4

## Magnetic Core

This chapter is based on the following articles:

- [I] M. A. Bahmani, E. Agheb, T. Thiringer, H. K. Hoildalen and Y. Serdyuk, “Core loss behavior in high frequency high power transformers: Effect of core topology,” *AIP Journal of Renewable and Sustainable Energy*, , vol. 4, no. 3, p. 033112, 2012.
- [II] E. Agheb, M. A. Bahmani, H. K. Hoildalen and T. Thiringer, “Core loss behavior in high frequency high power transformers: Arbitrary excitation,” *AIP Journal of Renewable and Sustainable Energy*, , vol. 4, no. 3, p. 033113, 2012.

### 4.1 Introduction

Estimation of the total loss is difficult in today's converters since the magnetic materials face non-sinusoidal excitations [86,87]. In offshore wind farm, weight and size are critical parameters which have significant effect on the cost and complexity of the installation, foundation and tower. Consequently, higher frequencies are sought to be used in order to decrease the weight and size of the transformer [88]. The voltage and current waveforms in these transformers are non-sinusoidal [89]. Hence, the influence of these non-sinusoidal waveforms on the total loss should be investigated. This non-sinusoidal nature can be handled in winding loss calculations by applying the Fourier transform and superposition [90]. However, core loss evaluation, in contrast, is more difficult because of the nonlinear nature of the magnetic materials. Based on the abovementioned facts, the optimum design of a medium (high) frequency high power transformers requires an accurate investigation of magnetic losses specially for non-sinusoidal waveforms.

The other important issue in medium frequency high power transformers is the magnetic material selection. The favourable magnetic materials for magnetic com-

Table 4.1: Magnetic Material Characteristics

Magnetic Material Type	Material	Manuf.	$B_{sat}$	Specific Losses @ 0.1 T, 100 kHz	Continuous Operating Temperature
Sil.Steel	10JNHF600	JFE [95]	1.87 T	0.24 kW/kg	150°C
Sil.Steel	10NEX900	JFE	1.6 T	0.19 kW/kg	150°C
Amorphous	2605SA1	Metglas [96]	1.56 T	0.2 kW/kg	150°C
Ferrite	3C85 [97]	Ferroxcube	0.45 T	0.009 kW/kg	140°C
Ferrite	3C93	Ferroxcube	0.52 T	0.009 kW/kg	140°C
Powder	Xflux 60	Magnetics [98]	1.6 T	0.26 kW/kg	200°C
Powder	KoolMu 125	Magnetics	1.05 T	0.14 kW/kg	200°C
Nano.Crys	Vitroperm500F	VAC [99]	1.2 T	0.01 kW/kg	120°C
Nano.Crys	Finement	Hitachi [100]	1.23 T	0.011 kW/kg	120°C

ponents in a higher range of frequency and power are the ones with lowest core losses, higher saturation flux densities and higher continuous operating temperature [91]. All these characteristics have to be understood and taken into account in order to have a suitable selection. Among all categories of magnetic materials which are suitable for high frequency applications, ferromagnetic materials are favoured to be used in higher power density applications, due to their higher saturation flux densities than ferrites [92–94]. Particularly, amorphous and nanocrystalline materials are categorized as low loss and high saturation level ferromagnetic material [65, 66].

The aim of this chapter is to investigate the core losses in high power density transformers when subjected to non-sinusoidal waveforms, in order to evaluate the dependency of the magnetic loss on the shape of the waveform. Firstly, general characteristics of different soft magnetic material are investigated. Then, three main methods of core loss evaluations are explained and finally the modified empirical expressions for switch-mode magnetics are derived and investigated over a wide range of duty cycles and rise times.

## 4.2 Magnetic Material Selection

One of the most important steps in designing high power density transformers is most probably selecting the appropriate magnetic material. To have the best selection, the magnetic material characteristics should be studied. In reality, since there is no ideal magnetic material for high frequencies providing low losses, high saturation flux density, high permeability and low magnetostriction, one should make some compromises based on the particular application.

Magnetic materials are classified based on their magnetic properties and also applications. A soft magnetic material is a material which can be easily magnetized and demagnetized. In contrast, hard magnetic materials require essential external magnetic field for their magnetization and demagnetization. Soft magnetic materials are usually used for making transformers cores, which concentrate and shape the magnetic flux. In high frequency high power applications, there are four main parameters that should be taken into consideration

- Specific core loss or core loss density
- Saturation flux density,  $B_{sat}$
- Relative permeability,  $\mu_r$
- Temperature characteristics

Based on these parameters, different kinds of magnetic materials may fulfill high frequency requirements. The performance improvement in these materials has been achieved by changing ingredients, controlling process quality and so on.

A detailed description of the characteristics of magnetic materials which are used in medium to high frequency applications is presented in Table. 5.1. Considering saturation flux density, one can classify these materials starting with the silicon steel family which indicate the highest  $B_{sat}$ , and followed by XFlux, amorphous material, nanocrystalline, KoolMu and ferrite. Powdered iron cores have relatively high specific core losses, as well as low relative permeabilities which make this type of magnetic materials not to be the first choice for the high power high frequency applications.

A transformer core operates at high temperatures and therefore thermal stability of the materials is of great concern. Theoretically, the Curie temperature is the limitation of maximum operating temperature, but practically, it is the thermal capability limits of lamination and coating that determines the maximum temperature. On the other hand, the thermal conductivity of the material determines the cooling of the core. The highest thermal conductivity is typical for powder cores and the lowest value is for ferrite. The thermal conductivity of the laminated cores is anisotropic and it is much higher in rolling direction rather than across the lamination. This should be considered in heat transfer modeling and the design methodology.

Fig. 4.1 shows the specific core losses of different magnetic materials versus magnetic flux density at 5 kHz. As it is seen nanocrystalline materials (Vitroperm500F and Finement) have the lowest specific loss together with relatively high saturation level,  $B_{sat}$ . Among all soft magnetic materials, nanocrystalline and Ferrite have higher priority for high frequency high power applications, however using ferrite material, one should compromise with the larger core cross sections, due to lower

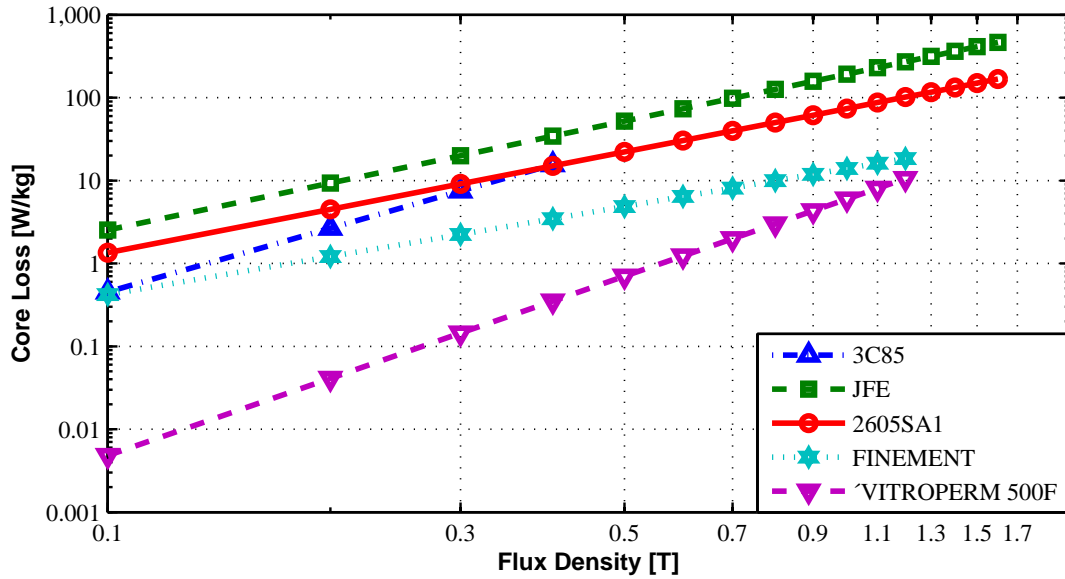


Figure 4.1: Specific core loss comparison of different soft magnetic material versus magnetic flux density at 5 kHz.

saturation level, resulting in larger and heavier components which is not desirable in high power density applications.

Fig. 4.2 shows the P-B characteristics of Vitroperm500F at different frequencies from datasheet provided by VAC.

### 4.3 Core Loss Calculation Methods

Each magnetic material has a special working temperature limit which should not be exceeded. Hence, the permitted loss for a particular design will be limited. Consequently, modeling and understanding of losses inside the winding and the core is of great importance and are the basic knowledge to have an optimal design of the transformers specially in high frequency applications [86]. In principle, there are three methods to calculate the core losses of magnetic materials, i.e, loss separation methods, empirical methods and time domain approach which are discussed in this chapter.

#### 4.3.1 Loss Separation Methods

Within this approach, the total losses are divided into three categories: static hysteresis loss,  $P_h$ , dynamic eddy current loss,  $P_e$ , and excess loss or anomalous loss,  $P_{ex}$ .

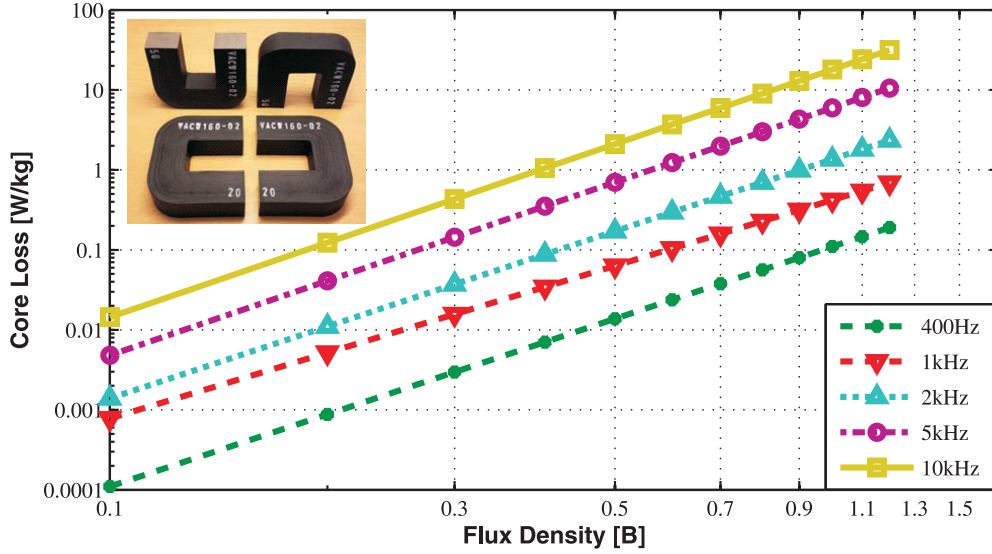


Figure 4.2: Specific core loss of Vitroperm500F at different frequencies.

#### 4.3.1.1 Eddy Current Losses

When a conductive material is exposed to a time-varying magnetic field, some current loops (eddy currents) are induced. To formulate these currents, a thin lamination is considered while exposed to a one directional magnetic field [101]. The time averaged value of the eddy current losses can be calculated by

$$P_e = \frac{\sigma \cdot d^2}{12T} \int_0^T \left( \frac{\partial B(t)}{\partial t} \right) dt \quad (4.1)$$

where  $\sigma$  is the conductivity of the core material,  $d$  is the thickness of each lamination and  $T$  is the excitation voltage period. In case of sinusoidal excitation, (4.1) gives

$$P_e = \frac{\sigma d^2}{12T} \int_0^T \omega^2 B_m^2 \sin^2(\omega t) dt = \frac{\sigma d^2}{24} \omega^2 B_m^2 \quad (4.2)$$

#### 4.3.1.2 Hysteresis Losses

Dependence of magnetic induction on the field is usually non-linear for magnetic materials (ferromagnetics) and it takes a form of so-called hysteresis loop. The hysteresis loss occurs due to movement and rotation of microscopic magnetic domains and it also depends on grain size and material composition. At very low frequencies, eddy current loss is negligible and hence, the total measured loss is equal to hysteresis loss or so called static hysteresis loss [101]. There are several theoretical

methods to calculate this type of loss in magnetic materials, among those the Jiles Atherton and Preisach [102, 103] are the most common ones, however these methods are not within the scope of this thesis since they require extensive experiments and parameter fitting procedures in order to have an acceptable parameter identification.

#### 4.3.1.3 Excess Losses or Anomalous

In practice, there is a difference between the measured total magnetic loss and sum of static hysteresis and classical eddy current losses, specially for higher frequencies. This difference is considered as excess or anomalous losses. This loss is a result of domain wall movement during the magnetization which induces microscopic eddy current loss [101]. In 1983 and 1984, Bertotti [104, 105] proposed a statistical loss theory based on the description of the magnetization. In this theory, a number of active correlation regions are considered which are distributed randomly in the material. These active regions are specified by the microstructure of the material such as grain size reflected in the time averaged expression of the excess loss as

$$P_{ex} = \sqrt{\sigma G_0} \frac{1}{T} \int_0^T \left| \frac{dB(t)}{dt} \right|^{1.5} dt \quad (4.3)$$

where  $G$  is the magnetic object friction coefficient,  $V_0$  is the parameter describing the microstructure of the material and  $A$  is the core cross section. Obtaining these coefficients can be difficult due to the lack of enough information from the manufacturer.

#### 4.3.1.4 Total Core Losses

The total magnetic field intensity inside a material can be defined as

$$H_{total} = H_{st-hyst} + H_{eddy} + H_{excess} \quad (4.4)$$

which means that the total field is the combination of three components: static hysteresis, eddy current and the field due to excess losses. The first component is static and it is independent of frequency, but the other two components are frequency dependant and broaden the B-H curve when measuring the total core losses. The total power loss density per loop of the magnetic material is

$$P_{total} = \frac{1}{T} \int_0^T \left( H_{st-hyst} \frac{dB(t)}{dt} + \frac{\sigma d^2}{12} \left( \frac{dB(t)}{dt} \right)^2 + \sqrt{\sigma G_0} \left| \frac{dB(t)}{dt} \right|^{1.5} \right) dt \quad (4.5)$$

It should be mentioned that the static hysteresis loss is dominant at low frequencies, while the excess loss is the highest in the mid-range of frequencies. For higher frequencies, the classical eddy current loss is dominant [106].

### 4.3.2 Time Domain Model

The core loss density is obtained by using the loss separation method in the frequency domain according to

$$\begin{aligned} P_v &= P_e + P_h + P_{ex} \\ &= k_e f^2 B_m^2 + k_h f B_m^\beta + k_{ex} f^{1.5} B_m^{1.5} \end{aligned} \quad (4.6)$$

Here,  $P_v$  is the core loss per unit volume,  $P_e$  is eddy current loss,  $P_h$  is hysteresis loss,  $P_{ex}$  is excess loss,  $\beta$  is the power factor (usually equal to 2),  $f$  is the operating frequency,  $B_m$  is the maximum value of the magnetic flux density,  $k_e$ ,  $k_h$  and  $k_{ex}$  are the loss coefficients which are to be extracted from the provided P-B curves, as seen in Fig. 4.1 and Fig. 4.2, of the studied magnetic material and other characteristics of the core material [107].

As mentioned before, the time averaged value of the eddy current loss can be calculated using the expression

$$P_e = \frac{\sigma \cdot d^2}{12T} \int_0^T \left( \frac{\partial B(t)}{\partial t} \right)^2 dt \quad (4.7)$$

The coefficient  $k_e$  is determined by equating  $P_e$  in (4.6) and (4.7) under sinusoidal excitation since (4.6) is only valid for sinusoidal waveforms. Therefore the instantaneous value for the eddy current loss can be evaluated through

$$P_e(t) = \frac{1}{2\pi^2} k_e \left( \frac{dB(t)}{dt} \right)^2, \quad k_e = \frac{\sigma \pi^2 d^2}{6} \quad (4.8)$$

As mentioned before, The time averaged value of the excess loss is obtained as

$$P_{ex} = \sqrt{\sigma \cdot G \cdot A \cdot V_0} \frac{1}{T} \int_0^T \left| \frac{dB(t)}{dt} \right|^{1.5} dt \quad (4.9)$$

Since a complete material characterization is not usually available from manufacturers,  $k_{ex}$  in (4.6) cannot be directly extracted. One can notice, by comparing (4.9) with the corresponding term in (4.6), that the magnitude of the coefficient,  $k_{ex}$ , is dependent on  $G$  and  $V_0$ . Therefore, a curve fitting is necessary to determine the value of  $k_{ex}$  [88]. Assuming pure sinusoidal excitation and equating one can write

$$k_{ex} = \sqrt{2\pi\sigma G_0} \frac{2\pi}{T} \int_0^T |\sin(2\pi ft)|^{1.5} dt \quad (4.10)$$

hence, the instantaneous value of excess loss can be calculated by

$$P_{ex}(t) = \frac{1}{8.76} k_{ex} \left| \frac{dB(t)}{dt} \right|^{1.5} \quad (4.11)$$

The time averaged hysteresis loss density can be calculated as

$$P_h = \frac{1}{T} \int_0^T H(t) \frac{dB(t)}{dt} dt \quad (4.12)$$

In order to calculate hysteresis losses in the time domain, the equivalent elliptical loop (EEL), which was originally introduced in [107] and implemented in the finite element software Maxwell, method is used. The magnetic hysteresis loss is described as a function of the irreversible component of the magnetic field  $H_{irr}$  and the ellipse parameters are represented as

$$B = B_m \sin(\theta) \quad , \quad H_{irr} = H_m \cos(\theta) \quad (4.13)$$

where  $\theta = 2\pi ft$  and  $H_m$  is the peak value of the magnetic field intensity. The area of the resulted ellipse is equal to the hysteresis loss. substituting (4.13) into (4.12), the time averaged value of  $P_h$  can be written as

$$P_h = \frac{1}{T} \int_0^T H_m B_m 2\pi f \cos^2(\theta) dt = \pi f H_m B_m \quad (4.14)$$

equating (4.14) and  $P_h$  in (4.6) and rearranging for  $k_h$  gives

$$k_h = \frac{\pi H_m}{B_m^{\beta-1}} \quad (4.15)$$

substituting  $H_m$  from (4.15) into (4.13), one can derive

$$H_{irr} = \frac{k_h}{\pi} B_m^{\beta-1} \cos(\theta) \quad (4.16)$$

hence

$$P_h = \frac{k_h}{C_\beta} \frac{1}{T} \int_0^T |B_m \cos(2\pi ft)|^{\beta-1} \frac{dB(t)}{dt} dt \quad (4.17)$$

where

$$C_\beta = 4 \int_0^{\frac{\pi}{2}} \cos^\beta(\theta) d\theta \quad (4.18)$$

The time averaged loss  $P_h$  is derived using the irreversible component of magnetic field intensity. Therefore, the instantaneous hysteresis loss can be written as

$$P_h(t) = \frac{k_h}{C_\beta} |B_m \cos(2\pi ft)|^{\beta-1} \frac{dB(t)}{dt} \quad (4.19)$$



Thus, the three components of the instantaneous magnetic loss in 3D cases for soft magnetic materials are as follows

$$\begin{aligned}
P_v(t) &= P_e(t) + P_h(t) + P_{ex}(t) \\
&= \frac{k_e}{2\pi^2} \left( \left( \frac{dB_x(t)}{dt} \right)^2 + \left( \frac{dB_y(t)}{dt} \right)^2 + \left( \frac{dB_z(t)}{dt} \right)^2 \right) \\
&\quad + \frac{k_h}{C_\beta} \cdot |B_m \cdot \cos(2\pi ft)|^{\beta-1} \left( \left| \frac{dB_x(t)}{dt} \right| + \left| \frac{dB_y(t)}{dt} \right| + \left| \frac{dB_z(t)}{dt} \right| \right) \\
&\quad + \frac{k_{ex}}{8.76} \left( \left( \frac{dB_x(t)}{dt} \right)^{1.5} + \left( \frac{dB_y(t)}{dt} \right)^{1.5} + \left( \frac{dB_z(t)}{dt} \right)^{1.5} \right)
\end{aligned} \tag{4.20}$$

Here,  $P_h(t)$ ,  $P_e(t)$  and  $P_{ex}(t)$  are the instantaneous values for the hysteresis, eddy current and excess loss, respectively [108].

It should be noted that the time dependent method are used for all of the FEM derived core loss calculations in this thesis. The loss coefficients,  $k_h$  and  $k_{ex}$ , are identified applying the least square method on the difference between the loss density obtained from measurements provided by the manufacturer, (Fig. 4.2), and the loss density calculated by (4.6) as

$$Error(k_h, k_{ex}) = \sum_{i=1}^n \left( P_{vi} - \left( k_e f^2 B_m^2 + k_h f B_{mi}^\beta + k_{ex} f^{1.5} B_{mi}^{1.5} \right) \right)^2 \tag{4.21}$$

where  $B_{mi}$  and  $P_{vi}$  are the values corresponding to  $i^{th}$  point on the P-B curve at any given frequency.

### 4.3.3 Empirical Methods

Loss separation methods give the capability of estimating the core loss for arbitrary waveforms. Nevertheless, only eddy current loss can be calculated and the factors and coefficients in the other two components should be obtained through extensive experiments and parameter fitting procedures. Due to this drawback, this model seems to be insufficient and impractical for the designers who prefer to use easy methods and lower amount of data resources of materials. In 1892, Steinmetz presented an equation to estimate the magnetic loss inside the materials which was only dependent on the peak value of the magnetic induction [109].

#### 4.3.3.1 OSE

Currently, a more general and verified version of the Steinmetz equation is used by the designers of magnetic devices known as the original Steinmetz equation (OSE)

which basically resulted from the curve fitting of several experiments under sinusoidal excitations at different frequencies and peak magnetic inductions as follows

$$P_c = k f^\alpha B_m^\beta \quad (4.22)$$

where  $f$  is the fundamental frequency of the excitation and  $B_m$  is the peak magnetic induction. Furthermore,  $k$ ,  $\alpha$  and  $\beta$  are determined by material characteristics and can be easily obtained using manufacturer datasheets without requiring any detailed knowledge of the materials. This expression has a very good accuracy for sinusoidal excitations. However, due to the increasing use of power electronic conversion systems, there is an urgent need to find a method with acceptable accuracy for non-sinusoidal flux waveforms. To overcome this problem, the Fourier transform was applied in [110], which could be used for any arbitrary waveform to decompose it into a series of sinusoidal waves. Then, (4.22) was applied on each sinusoidal component and using the superimposed effect of harmonics, the total loss could be obtained. However, this summation has a considerable difference with the measured values, since there is no orthogonality between different harmonics due to the nonlinear nature of magnetic materials.

#### 4.3.3.2 MSE

The empirical Steinmetz equations have been the most practical and useful tool for the evaluation of magnetization losses in recent years. Therefore, several modifications have been implemented to extend them for non-sinusoidal waveforms. The first improvement was done based on the physical understanding of hysteresis dynamics and correlating the magnetic loss with the rate of the change of magnetic flux density. Based on this idea, an equivalent frequency,  $f_{eq}$ , was introduced [111] which is depending on  $\frac{dB}{dt}$ .

$$f_{eq} = \frac{2}{\Delta B^2 \pi^2} \int_0^T \left( \frac{dB(t)}{dt} \right)^2 dt \quad (4.23)$$

where  $T$  is the period of the flux waveform and  $\Delta B$  is the peak to peak flux amplitude. Considering this equivalent frequency, the magnetic loss density is determined by the modified Steinmetz equation (MSE) as

$$P_c = (k f_{eq}^{\alpha-1} B_m^\beta) f \quad (4.24)$$

where  $f$  is the excitation fundamental frequency.

#### 4.3.3.3 GSE

To correct the mismatch between the MSE and OSE for sinusoidal waveforms, another modification was proposed [112]. This idea is based on the physical assump-

tion that the loss inside the material is not only depending on the rate of changes in magnetic induction, but also related to the instantaneous value of flux density. Taking this assumption into account, the generalized Steinmetz equation (GSE) was presented as

$$P_c = \frac{1}{T} \int_0^T k k_i \left| \frac{dB(t)}{dt} \right|^\alpha |B(t)|^{\beta-\alpha} dt \quad (4.25)$$

where

$$k_i = \frac{1}{(2\pi)^{\alpha-1} \int_0^{2\pi} |\cos(\theta)|^\alpha |\sin(\theta)|^{\beta-\alpha} d\theta} \quad (4.26)$$

#### 4.3.3.4 IGSE

The other commonly used expression for core loss calculations is known as the improved generalized Steinmetz equation (IGSE) [113] .

$$P_c = \frac{1}{T} \int_0^T k k_i \left| \frac{dB(t)}{dt} \right|^\alpha \Delta B^{\beta-\alpha} dt \quad (4.27)$$

where

$$k_i = \frac{1}{(2\pi)^{\alpha-1} \int_0^{2\pi} |\cos(\theta)|^\alpha 2^{\beta-\alpha} d\theta} \quad (4.28)$$

In this method, the instantaneous value of  $B$  is replaced by the peak to peak value  $\Delta B$  and the waveform could be split into one major and several minor loops and the derived expression would be applied to each loop separately. In [114], a similar approach was introduced and named as the natural Steinmetz equation resulting in the same expression as IGSE.

#### 4.3.3.5 WCSE

The latest modification on Steinmetz equation was done by Shen which is known as Waveform-coefficient Steinmetz equation (WCSE) [115]. He presented a coefficient for (4.22), to establish a relationship between any arbitrary waveform with the sinusoidal one with the same peak flux density. This flux waveform coefficient (FWC) can be obtained by calculating the area of the flux waveform and divide it by the corresponding value of the sinusoidal flux.

$$FWC = \frac{\int_0^{\frac{T}{4}} \phi_{arb}(t)}{\int_0^{\frac{T}{4}} \phi_{sin}(t)} \quad (4.29)$$

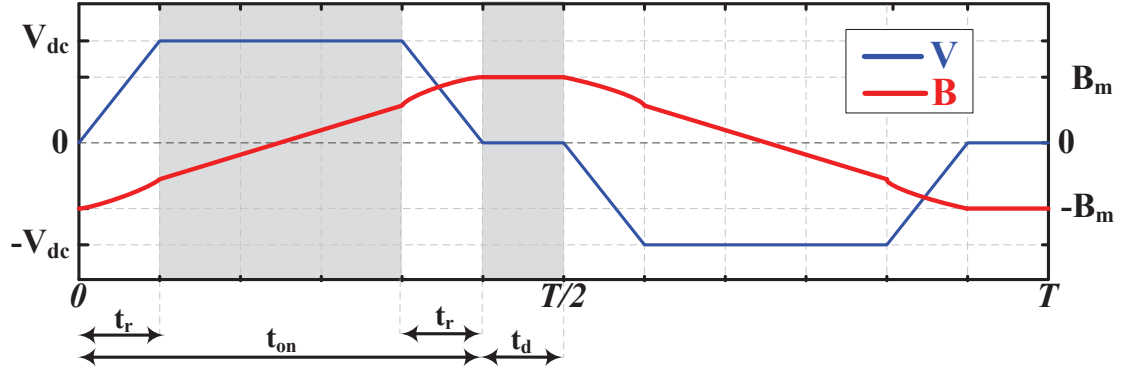


Figure 4.3: Example of the excitation voltage and the corresponding instantaneous value of magnetic flux density.

where  $\phi_{arb}(t)$  and  $\phi_{sin}(t)$  are the instantaneous value of magnetic flux inside the core associated with arbitrary and sinusoidal excitations, respectively. This correction factor is directly multiplied by the core loss expression of OSE, (4.22) as follows

$$P_c = FWC.k.f^\alpha B_m^\beta \quad (4.30)$$

## 4.4 Modified Empirical Expressions for Non-Sinusoidal Waveforms

In this part, the aforementioned empirical loss calculation methods are modified to be applicable for rectangular waveforms considering the respective duty cycles and rise times which is the typical waveforms in switch-mode magnetics. In order to have an appropriate comparison of core losses by varying the waveform characteristics, the maximum value of the applied voltage is considered as a constant value. However, the peak induction will be fixed. Consequently, by changing the shape of the voltage waveform, for instance the rise time or duty cycle, the effective cross section of the core is varied to have a constant value of  $B_m$ . The required core cross section for the mentioned waveforms can be obtained as

$$A_c = \frac{V_{rms}}{k_f k_c N B_m f} \quad (4.31)$$

where  $V_{rms}$  is the rms value of the voltage depicted in Fig. 4.3,  $k_c$  is the filling factor of the core,  $N$  is the number of primary or secondary turns depending on the corresponding voltage and  $f$  is the fundamental frequency. The coefficient  $k_f$  is defined as

$$k_f = \frac{2\sqrt{2D - \frac{8}{3}R}}{D - R} \quad (4.32)$$

where  $D$  is the duty cycle and  $R$  is the relative rise time in the rectangular waveform with respective rise and fall time defined as

$$D = \frac{t_{on}}{T} \leq \frac{1}{2} \quad , \quad R = \frac{t_r}{T} \leq \frac{1}{4}. \quad (4.33)$$

The waveforms of the instantaneous voltage and the corresponding flux density for one period are depicted in Fig. 4.3 where the time periods  $t_{on}$  and  $t_r$  are illustrated. The flux density waveform can be easily obtained by integration of the voltage and dividing it by the number of respective winding turns and cross section of the core. As can be seen, whenever the voltage is constant, the induction has a linear behavior, but in rise and fall times when voltage is changing, the induction has a second order pattern.

#### 4.4.0.6 Modified MSE

Using the previously presented empirical equation of loss method for the MSE and also using (6.50) and (4.32) for the cross sections, an easy to use expression for magnetic core loss is derived as

$$P_{c-MSE} = \left[ \frac{2(2D - \frac{8}{3}R)}{\pi^2(D - R)^2} \right]^{\alpha-1} k f^\alpha B_m^\beta \quad (4.34)$$

#### 4.4.0.7 Modified IGSE

Similarly, the calculated expression for the IGSE method, suitable for loss evaluation of the waveform presented in Fig. 4.3, is derived as

$$P_{c-IGSE} = \left( 2D - \frac{4\alpha}{\alpha+1}R \right) \frac{2^\beta}{(D - R)^\alpha} k k_i f^\alpha B_m^\beta \quad (4.35)$$

#### 4.4.0.8 Modified WCSE

The modified WCSE expression is derived as

$$P_{c-WCSE} = \frac{4\pi}{D - R} \left[ \frac{(D - 2R)^2}{8} + \frac{R^2}{3} + \frac{(1 - 2D)(D - R)}{8} \right] k f^\alpha B_m^\beta \quad (4.36)$$

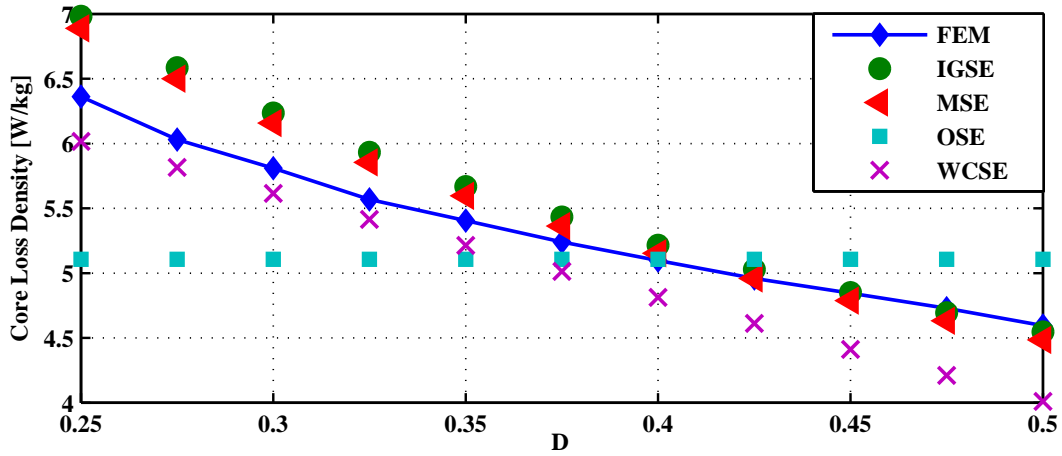


Figure 4.4: Accuracy investigation of the modified Steinmetz equations with different values of  $D$  and  $R = 0$ .

Based on the assumptions and procedure of the methods, correction coefficients were added to the main OSE equation, to extend and adapt it to the studied non-sinusoidal waveform. These coefficients are only dependent on two main factors,  $R$  and  $D$  which were previously defined in (5.7). The important issue to mention from the equations presented above are that the magnetic loss density depends not only on the frequency and peak magnetic induction, but also on  $D$  and  $R$  of the waveform depicted in Fig. 4.3.

It should be noted that, due to the presence of a second order term with a non-integer exponent ( $\beta - \alpha$ ) within integration process, it is not possible to achieve any closed form expression for GSE accounting for core losses in non-sinusoidal waveform shown in Fig. 4.3.

#### 4.4.1 Validity Investigation for Different Duty Cycles, $D$

In this part, different waveforms with various values of  $D$ , with  $R = 0$ , have been applied on a case study transformer which is a 1 MVA, 1/10 kV transformer operating at 5 kHz with 6 turns of the primary windings and the peak value of the magnetic flux density is set to 0.9 T. The core material used for all simulations in this comparison is Vitroperm500F as its core loss characteristics presented in Fig. 4.2.

To study the effect of the duty cycle,  $D$  has been changed from 0.25 to its maximum, 0.5. The obtained results are depicted in Fig. 4.4. In order to have a fixed maximum flux density in all simulations, the dimension of the transformer at each simulation should be changed according to (6.50) which simply means that by increasing the duty cycle, the cross section of the core will increase.

The results presented in Fig. 4.4 can be interpreted from two points of view.

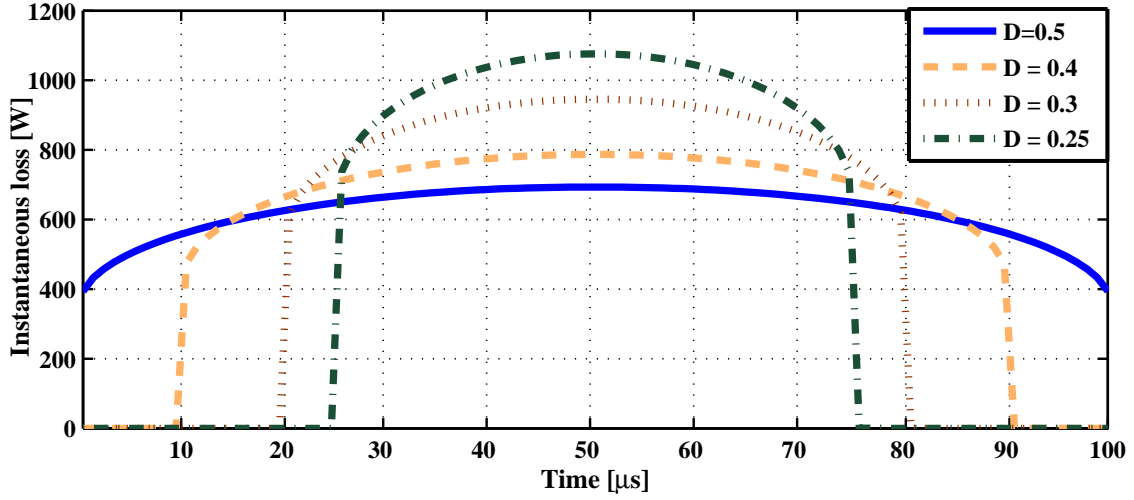


Figure 4.5: Instantaneous core loss waveform in a half period with different values of  $D$  and  $R = 0$ .

Firstly, reducing the duty cycle leads to higher magnitude of losses inside the core. Secondly, for high duty cycles, the OSE which only considers the sinusoidal waveforms has a good accuracy and its deviation from the result obtained by FEM is less than 10 percent. However, there are considerable deviations at lower values of  $D$  between the core loss densities obtained by the OSE and FEM simulations. The most acceptable accuracy is around  $D = 0.4$  where almost all the methods provide similar results. In general the modified IGSE and MSE methods has a higher accuracy compared to OSE and WCSE. Therefore they will be later utilized in the high power density transform design.

Fig. 4.5 shows the computed instantaneous core loss of four different duty cycles for half a period using a FEM software at 5 kHz. By decreasing the duty cycle, the maximum value of the instantaneous loss will increase since the rate of change of  $B$ ,  $\frac{dB(t)}{dt}$ , increases. This is the most important term in the transient loss calculation methods. The other interesting point regarding Fig. 4.5 is that the peak value of instantaneous core loss occurs at  $t = \frac{T}{4}$  which is due to the term  $|B_m \cdot \cos(2\pi ft)|$  in (4.20). Moreover, for lower duty cycles, the peak value of the core loss is higher.

#### 4.4.2 Validity Investigation for Different Rise Times, $R$

In addition to the duty cycle, the rise and fall time,  $R$ , of the excitation voltage has a significant effect on the magnetic core loss. The comparison between the calculated average core loss density obtained by different modified Steinmetz equations, as well as FEM simulations has been shown in Fig. 4.6. It should be mentioned that, as

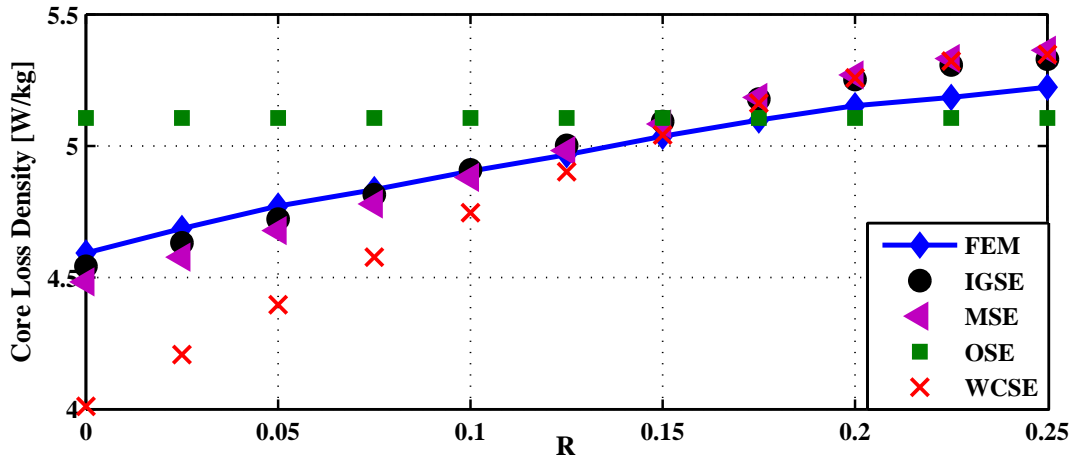


Figure 4.6: Accuracy investigation of the modified Steinmetz equations with different  $R$  values and  $D = 0.5$ .

in the previous section, all the calculations and simulations for different values of  $R$  were performed in the condition of similar  $V_{dc}$  and  $B_m$ .

As can be seen in Fig. 4.6 the magnetic loss increases at higher  $R$  values except for the OSE. The longer the rise time, the higher the loss inside the core will be. Changing  $R$  from zero to 0.25 which means from rectangular to triangular, results in almost a 35 percent increase in the core loss. For values of  $R$  close to 0.25, i.e.  $t_r$  close to  $\frac{T}{4}$ , the voltage waveform approaches the triangular shape. In this case, the voltage increases linearly which generates a parabolic flux density waveform. In order to compare the resulting loss densities properly,  $B_m$  should be kept constant. The quadratic polynomial flux density results in a higher magnitude of the magnetic loss.

Moreover, as can be seen in Fig. 4.6, the modified IGSE and MSE have an acceptable accuracy at almost all values of  $R$  particularly when  $R$  is very small which is the case of most power electronic waveforms. By decreasing the rise time, the OSE and its modification, WCSE, deviates more from the results obtained by FEM simulations whereas the other group including IGSE and MSE has negligible deviations from FEM.

The instantaneous core loss at four different values of  $R$  in one period are illustrated Fig. 4.7. As can be seen, during the transition time, the core loss has a polynomial behavior. Besides, the highest loss occurs at  $R$  equal to 0.25.



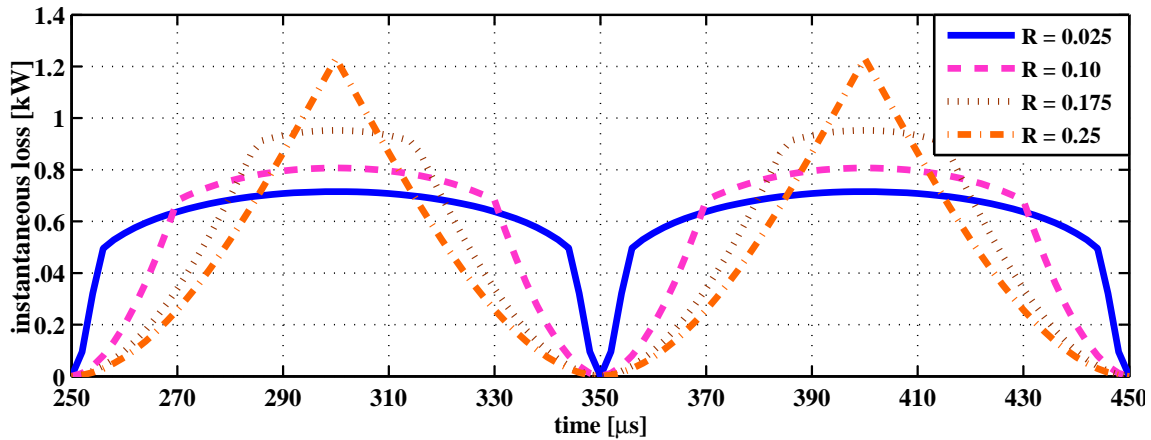


Figure 4.7: Instantaneous core loss waveform with different values of  $R$  and  $D = 0.5$ .

## 4.5 Conclusions

The transformers used in power electronic converters are frequently subjected to non-sinusoidal voltages. As a consequence of the increasing use of these waveforms, the effects of arbitrary wave-shapes on the efficiency of the transformers should be investigated. The magnetic losses due to sinusoidal excitation can be easily calculated using datasheets provided by manufacturers. In non-sinusoidal and harmonic cases, due to the nonlinear behavior of magnetic materials, more complex methods are necessary. The main aim of this chapter was to study the effect of the commonly used power electronic waveforms on the core losses. Accordingly, using the proposed modification of the Steinmetz equation in literature, such as MSE, IGSE and WcSE, some general expressions were derived and presented for the rectangular waveforms with their associated duty cycle and rise time. In each of these expressions, a correction factor is introduced to relate the Steinmetz expression to these waveforms.



# Chapter 5

## Design Methodology with Prototypes

This chapter is based on the following articles:

- [I] Bahmani, M.A.; Thiringer, T.; Kharezy, M., “Design, Optimization and Experimental Verification of Medium-Frequency High-Power Density Transformer Using Rectangular Litz Conductors,” Submitted to *IEEE Transactions on Power Electronics*.
- [II] 1. Bahmani, M.A.; Thiringer, T.; Kharezy, M., “Optimization and Experimental Validation of a Medium-Frequency High Power Transformer in Solid-State Transformer Applications,” Accepted in *Applied Power Electronics Conference and Exposition (APEC), 2016 IEEE 10th International Conference on*, March 2016.

### 5.1 Introduction

High power isolated DC-DC converters are likely to provide solutions for many technical challenges associated with power density, efficiency and reliability in potential applications such as offshore wind farms, inter-connection of DC grids, MVDC in data centers and in future solid state transformer applications. The Medium-Frequency Power Transformer (MFPT) is one of the key elements of such a converter to realize the voltage adaption, isolation requirements, as well as high power density. This chapter describes a design and optimization methodology taking into account the loss calculation, isolation requirements and thermal management. Incorporating this design methodology, an optimization process with a wide range of parameter variations is applied on a 50 kW, 1 / 3 kV, 5 kHz transformer to find the highest power density while the efficiency, isolation, thermal and leakage inductance

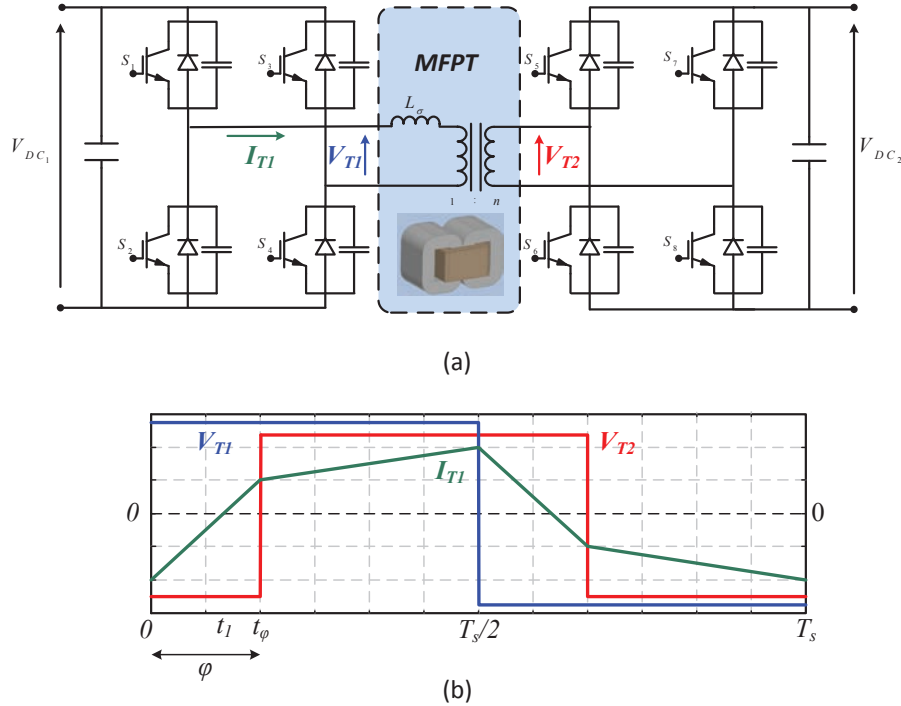


Figure 5.1: (a) Dual active bridge circuit. (b) Steady state medium-frequency power transformer voltage and current waveforms for single-phase shift modulation.

requirements are all met. The optimized transformers are then manufactured and measured. The result is presented in this chapter.

## 5.2 DC-DC Converter Topology

Recently, there has been growing interest in utilizing dual active bridge (DAB) converters in high power applications. The equivalent circuit of a DAB converter is shown in Fig. 5.1(a) in which two square wave voltage waveforms on the two sides of the transformer has been shifted by controlling the input and output bridges, applying full voltage over the inductance,  $L_\sigma$ , which is used to shape the current for the power transfer [2]. The steady state transformer voltage and current waveforms of a DAB converter with simple phase shift modulation are shown in Fig. 5.1(b). It is worth to point out that in order to have soft switching at turn on, the anti-parallel diode of each switch should start conducting prior to the turn on moment. In order to achieve zero-voltage switching (ZVS) at turn on, the phase shift between the bridges,  $\varphi$ , should be higher than a certain value resulting in a minimum value of the series inductance as presented in (5.1). This inductance is preferably integrated as the leakage inductance of the medium-frequency transformer, Fig. 5.1(a), in order

to reduce the number of components, hence achieving higher power densities.

$$L_{\sigma(min)} = \frac{V_{DC1} V_{DC2} \varphi_{min} (\pi - \varphi_{min})}{2P_{out} \pi^2 f_s n} \quad (5.1)$$

where  $\varphi_{min}$  which is associated with the worst case condition, in which the maximum output voltage deviation occurs, can be calculated as

$$\begin{aligned} \varphi_{min} &= \frac{\pi(d-1)}{2d} \quad \text{for } d > 1 \\ \varphi_{min} &= \frac{\pi(1-d)}{2} \quad \text{for } d < 1 \end{aligned} \quad (5.2)$$

and  $d$ , the DC conversion ratio for the worst case condition, is defined as

$$d = \frac{V_{DC2}(worst\ condition)}{nV_{DC1}}. \quad (5.3)$$

It should be noted that in normal conditions,  $d$  equals 1. The waveforms illustrated in Fig. 5.1(b) will later, in this chapter, be used as the transformer excitations and consequently they will affect the transformer losses, i.e, copper and core losses. Using (5.3), the apparent power of the transformer can be calculated from

$$\begin{aligned} S_T &= \frac{1}{2} (V_{T1(rms)} I_{T1(rms)} + V_{T2(rms)} I_{T2(rms)}) \\ &= \frac{1}{2} V_{DC1} I_{T1(rms)} (1 + d) \end{aligned} \quad (5.4)$$

## 5.3 Optimization Procedure

In contrast to most of the proposed design methodologies for high-frequency transformers, focusing on core selection based on a parameter called area product,  $A_p$ , [19,20] the design methodology proposed in this chapter utilizes the integrated leakage inductance of the transformer and its corresponding phase shift within the DAB topology. In addition, the isolation requirements introduced by the medium voltage DC link is considered as one of the design inputs making this design suitable for high-power medium frequency offshore dc-dc converters [73]. Moreover, unlike the conventional design of magnetic components where the core will be initially selected from a manufacturer look-up table, the core dimensions are not a limiting factor in this optimization [21,76]. It is assumed that specific core dimensions for specific high power density applications can be tailored by core manufacturers. Fig. 5.2 shows the proposed optimization flowchart used for designing a medium-frequency

high power transformer which is supposed to meet the mentioned requirements. Different parts of this design and optimization process are explained in details further in this chapter.

### 5.3.1 System Requirements and Considerations

The first step is to introduce the converter level requirements, i.e, output power,  $P_{out}$ , DC voltage levels,  $V_{DC1}$  and  $V_{DC2}$ , operating frequency,  $f$ , transformer turn ratio,  $n$ , required leakage inductance,  $L_\sigma$ , and isolation requirements,  $V_{iso}$ , as well as the maximum operating temperature,  $T_{max}$ . The transformer is exposed to the voltage and current waveforms shown in Fig. 5.1(b) which are typical waveforms of a DAB converter. However, the proposed design methodology can easily be applied on other types of modulations with duty cycles,  $D_1$  and  $D_2$ , being below 0.5. It is worth to point out that because of the power rating limitations of modern semiconductor devices, a modular concept comprising of building blocks enabling parallel connection on the low voltage side and series connection on the high voltage side, will most likely be considered [31], particularly in high power and high voltage applications. Fig. 5.3 illustrates an example of this kind of modularity with paralleled input and series output connection (PISO). It is worth to point out that the medium-frequency transformer of each single module must withstand the total voltage over the output series connected modules, the HVDC voltage.

### 5.3.2 Fixed Parameters

Prior to the iterative optimization part, the magnetic core material, insulation material, the windings type and inter-layer distances need to be set.

#### 5.3.2.1 Magnetic Core Material

The favorable magnetic materials for magnetic components in a higher range of frequency and power are the ones with lowest core losses, higher saturation flux densities and higher continuous operating temperature [91]. All these characteristics have to be understood and taken into account in order to make a suitable selection. Among all categories of magnetic materials which are suitable for high frequency applications, ferromagnetic materials are favored to be used in higher power density applications, due to their higher saturation flux densities compared to ferrites [92–94] since the required magnetic core cross section is inversely proportional to the induction level as defined by the relation

$$A_c = \frac{V_{rms1}}{k_f k_c N_1 B_m f} \quad (5.5)$$

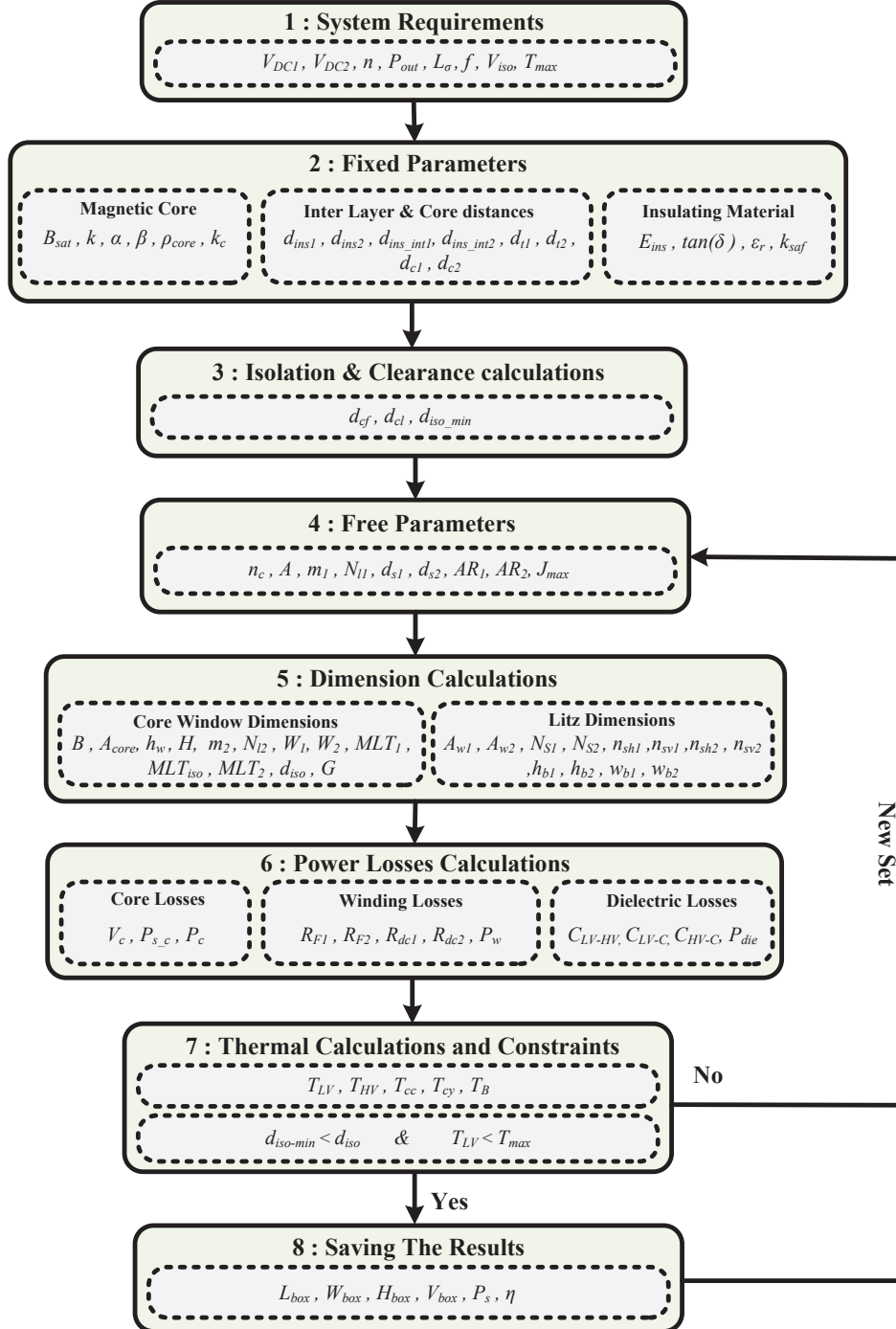


Figure 5.2: Design Algorithm.

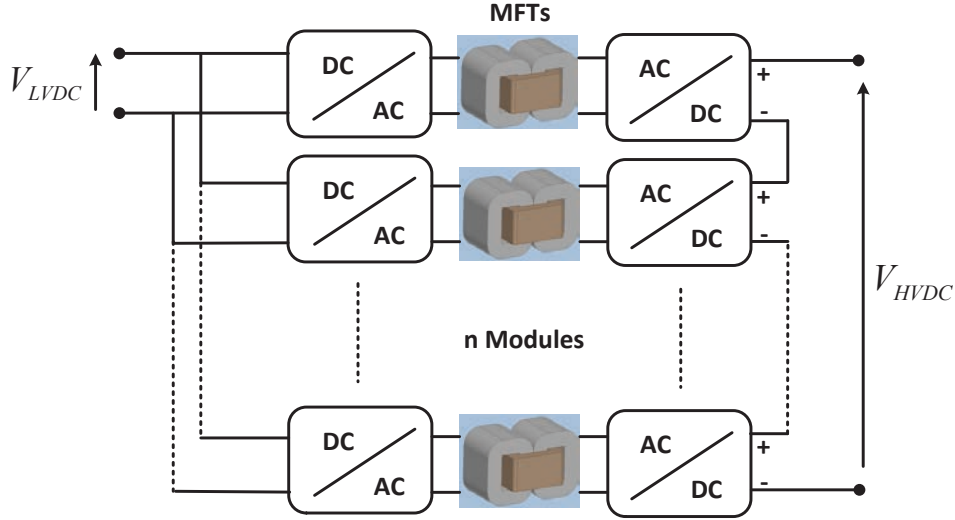


Figure 5.3: Parallel input series output connection of building blocks of an isolated DC-DC converter for HVDC offshore applications.

where  $V_{rms}$  is the RMS value of the primary voltage,  $k_c$  is the filling factor of the core,  $N_1$  is the number of primary turns, and  $f$  is the fundamental frequency. The coefficient  $k_f$  is defined as

$$k_f = \frac{2\sqrt{2D - \frac{8}{3}R}}{D - R} \quad (5.6)$$

where  $D$  is the duty cycle and  $R$  is the relative rise time in the rectangular waveform with respective rise and fall time defined as

$$D = \frac{t_{on}}{T} \leq \frac{1}{2} \quad , \quad R = \frac{t_r}{T} \leq \frac{1}{4}. \quad (5.7)$$

It should be noted that for the phase shift modulation in the DAB converter which is shown in Fig. 5.1(b), the value of  $D$  is 0.5 and  $R$  is equal to zero. Moreover, in order to avoid core saturation due to an unwanted magnetic flux density fluctuation, the maximum induction level,  $B_m$ , is considered as 80% of the saturation level of the selected magnetic core.

A detailed characteristics of magnetic materials which are used in medium to high frequency applications are presented in Table. 5.1. Considering saturation flux density, one can classify these materials starting with the silicon steel family having the highest  $B_{sat}$ , and followed by XFlux, amorphous material, nanocrystalline, KoolMu and ferrite. Powdered iron cores have relatively high specific core losses, as well as low relative permeability making this type of magnetic materials not to be the first choice for the high power high frequency applications. Accordingly, considering



Table 5.1: Magnetic Material Characteristics

Magnetic Material Type	Material	$B_{sat}$	Specific Losses @ 0.1 T, 100 $kHz$
Sil.Steel	10JNHF600 [95]	1.87 T	0.24 $kW/kg$
Sil.Steel	10NEX900	1.6 T	0.19 $kW/kg$
Amorphous	2605SA1 [96]	1.56 T	0.2 $kW/kg$
Ferrite	N87 [116]	0.39 T	0.009 $kW/kg$
Ferrite	3C85 [97]	0.45 T	0.009 $kW/kg$
Ferrite	3C93	0.52 T	0.009 $kW/kg$
Powder	Xflux 60 [98]	1.6 T	0.26 $kW/kg$
Powder	KoolMu 125	1.05 T	0.14 $kW/kg$
Nano.Crys	Vitroperm500F [99]	1.2 T	0.01 $kW/kg$
Nano.Crys	Finement [100]	1.23 T	0.011 $kW/kg$

both magnetic flux density and specific losses together, one can conclude that the amorphous and noncrystalline materials seem to be the favorable candidates [65,66]. Therefore, Vitroperm500F is chosen as the primary magnetic material used in this study.

### 5.3.2.2 Windings

As in magnetic material, windings need to exhibit certain characteristics in order to be used in high power density applications. Among those is high current carrying capabilities, high filling factor, good heat dissipation capability and more importantly less power losses. Considering the filling factor, rectangular foil conductors seem to be the most effective one, however, it suffers from a relatively high interwinding capacitance as well as the practical difficulty to wind it. The second type of conductors are round solid conductors, magnet wires, which are widely used in transformers, motors and other magnetic components since they are commercially available in a wide range of diameters with a relatively low price [51,61]. Moreover, round wires require less practical efforts to be tightly wound around a core [19,62], nevertheless, it suffers from enhanced high frequency losses because of excess skin and proximity effects. The other type of windings which has caught much attentions are litz wires. The litz wire shows a substantial reduction of skin and proximity effects since it consists of multiple individually insulated conductor strands which have been twisted along the wire length. In order to improve the filling factor, rectangular litz wires are more favorable than the round ones when the reduction of size is a design goal. A further reason for choosing a rectangular litz wire is that its AC

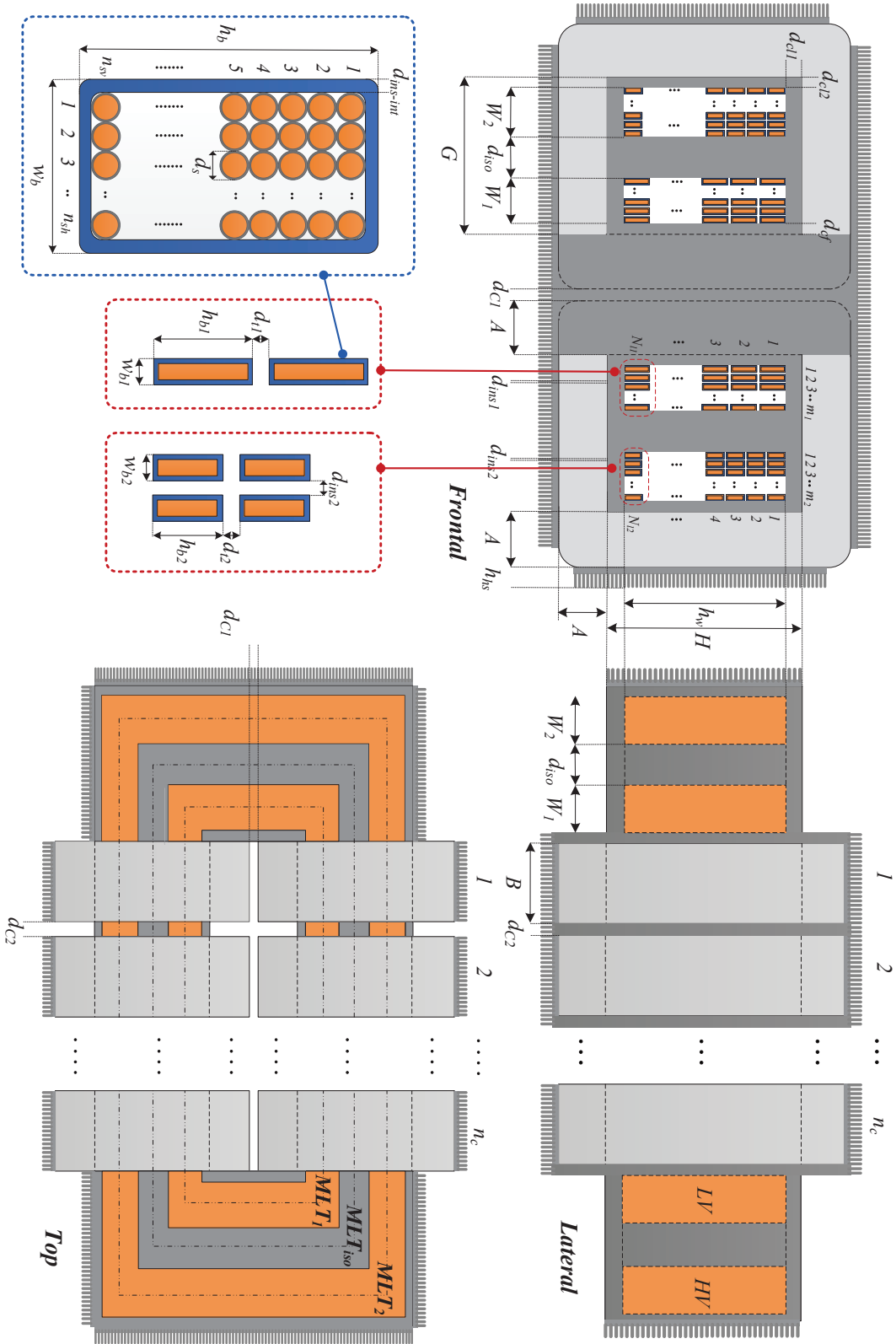


Figure 5.4: Design sketch.

resistance factor and winding losses can be calculated by the existing winding loss calculation expression with a good approximation [117]. A schematic of this kind of conductors is depicted in Fig. 5.4 together with all the geometrical dimensions already presented in Fig. 5.2.

### 5.3.2.3 Insulation Material and Distances

The insulation material determines the other set of fixed parameters used in the proposed design methodology. As can be seen in Fig. 5.4, a dry type insulating material, which provides high dielectric strength, is used within the isolation and clearance distances,  $d_{iso}$  and  $d_{cl}$ . In addition, as shown in Fig. 5.4, the coil former which provides a distance between the inner layer of the primary windings and the core,  $d_{cf}$ , is composed of a thermally conductive polymeric material, CoolPoly-D5108, enabling a proper heat conduction to the heat sinks implemented on the core surfaces as well as providing enough isolation between the primary windings and the core [118]. The dielectric and thermal characteristics of some insulating materials are tabulated in Table 5.2. As can be seen there, the selected material, D5108, has superior thermal and dielectric characteristics compared to other commonly used insulating material, particularly its thermal conductivity which is nearly two orders of magnitude higher than the ones of the other presented materials. With the insulating material selected, the required clearances can be calculated by

$$d_{cf} = \lceil \frac{V_{LVDC}}{k_{saf} E_{ins}} \rceil \quad , \quad d_{cl1,2} = \lceil \frac{V_{MVDC}}{k_{saf} E_{ins}} \rceil \quad (5.8)$$

where, a safety factor of 30%, for  $k_{saf}$ , is considered for the dielectric strength of the isolating medium and  $E_{ins}$  is the dielectric strength of the selected insulating medium presented in Table 5.2. The minimum value of the isolation distance,  $d_{iso-min}$ , can accordingly be calculated as

$$d_{iso-min} = \lceil \frac{V_{iso}}{k_{saf} E_{ins}} \rceil. \quad (5.9)$$

However, this is only a criterion and the actual value will later be calculated with respect to the desired leakage inductance.

The other group of fixed parameters are the horizontal and vertical distances between the litz conductors,  $d_{ins1}$ ,  $d_{ins2}$ ,  $d_{t1}$  and  $d_{t2}$ , respectively, as shown in Fig. 5.4. These distances are in addition to the outer insulation thicknesses of the litz bundles.

### 5.3.3 Free Parameters

After selecting the magnetic core material, dielectric material and the required fixed distances, several free parameters composed from geometrical and electrical parameters are chosen and swept within a wide range, in order to find the minimum

Table 5.2: Electrical and thermal characteristics of some insulating materials [56,118–120]

Dielectric Material	Thermal Conductivity $[\frac{W}{m.K}]$	Dielectric Strength $[\frac{kV}{mm}]$	$\tan\delta$
Air (@70°C)	0.03	3	0
CoolPoly-D5108	10	29	0.022 (@100Hz)
Mica	0.71	11-43	-
Transformer oil	0.12	10-15	2e-6 (@50MHz)
Paper	0.05	22-49	6e-5 (@1kHz)
NOMEX	-	27	5e-3(@ 60Hz)

transformer volume meeting the efficiency, isolation, leakage inductance and heat dissipation requirements. Once a set of free parameters are established, one can determine all the geometrical dimensions of the transformer addressing the required distances to achieve the desired leakage inductance, winding and core dimensions and the other geometrical parameters shown in Fig. 5.2 and Fig. 5.4 which illustrates all the frontal, lateral and top dimensions of the desired transformer design.

For the purpose of this study, nine free parameters which are swept over a wide range are designated as the number of the magnetic core stacks,  $n_c$ , the frontal side of the core cross section,  $A$ , the number of layers and the number of litz bundle turns per layer in the primary windings portion,  $m_1$  and  $N_{l1}$ , the diameter of the strands in the primary and secondary litz wires,  $d_{s1}$  and  $d_{s2}$ , the aspect ratios of the primary and secondary litz bundles which is the ratio between the respective total height and width,  $AR_1$  and  $AR_2$ , and finally the maximum allowed RMS value of the current density through a conductor,  $J_{max}$ . The selection of free parameters highly depends on the optimization targets and restrictions, as well as the considered core and winding topologies. For instance, in case of foil conductors, one can consider the thickness of the foil conductors as the complementary free parameter.

All possible combinations of these free parameters will be applied to the optimization flowchart shown in Fig. 5.2, resulting in distinct transformer geometries corresponding to its set of free variables. Utilizing the modified and developed expressions, the core, windings and dielectric losses are then being evaluated for each set of free parameters [121,122]. The efficiency, power density and temperature rise of each transformer are then extracted and compared in order to obtain the optimum combination that meets the requirements.

### 5.3.4 Geometry Determination with Rectangular Litz Conductors

Having the fixed and free parameters, the transformer geometry can be defined as follows. First, the required magnetic core cross section is defined as

$$A_c = \frac{V_{DC1}}{\frac{2\sqrt{2D-\frac{8}{3}R}}{D-R} k_c m_1 N_{l1} B_m f}. \quad (5.10)$$

Considering the geometry structure shown in Fig. 5.4 and considering the number of core stacks,  $n_c$ , the lateral side length of the magnetic core can be calculated as

$$B = \frac{A_c}{2n_c A} \quad (5.11)$$

where  $A$  is the frontal side length of each core stack. With a specific set of strand diameters and the allowed current density given by the free parameters, the number of strands at the primary and secondary litz bundles can be respectively calculated as

$$N_{s1} = \left\lceil \frac{4I_{T1}}{\pi d_{s1}^2 J_{max}} \right\rceil, \quad N_{s2} = \left\lceil \frac{4I_{T1}}{n\pi d_{s2}^2 J_{max}} \right\rceil \quad (5.12)$$

where  $I_{T1}$ , the transformer primary RMS current, is the function of the applied phase shift,  $\varphi$ , which is in this case the minimum allowed value ensuring the soft switching and yet having a reasonable amount of reactive power circulation. On the basis of the waveforms presented in Fig. 5.1(b),  $I_{T1}$  can be calculated from

$$I_{T1} (rms) = Z \sqrt{\frac{4t_1^2 t_\varphi + T_s t_1^2 - 4t_\varphi^2 t_1 - T_s t_1 t_\varphi + T_s t_\varphi^2}{3T_s}} \quad (5.13)$$

where  $Z$ ,  $t_1$  and  $t_\varphi$  are respectively calculated by

$$Z = \frac{nV_{DC1} + V_{DC2}}{nL_\sigma} \quad (5.14)$$

$$t_1 = \frac{\pi + 2\varphi d - \pi d}{4\pi f (1 + d)}, \quad t_\varphi = \frac{\varphi}{2\pi f}. \quad (5.15)$$

After determining the number of strands in each litz bundle, the number of strands in each internal row of the litz bundle,  $n_{sh}$  as shown in Fig. 5.4, can be calculated as

$$n_{sh} = \left\lceil \frac{k + \sqrt{k^2 + N_s d_s^2 \cdot AR}}{d_s \cdot AR} \right\rceil \quad (5.16)$$

where  $k$  is

$$k = d_{ins-int}(1 - AR). \quad (5.17)$$

It should be pointed out that (5.16) and (5.17) are used for both the primary and secondary windings,  $n_{sh1}$  and  $n_{sh2}$ , with their corresponding free parameters. This internal arrangement of the litz bundle will be used later to calculate the winding losses. Accordingly, the number of strands in each internal column within a litz bundle of primary and secondary windings, with corresponding free parameters, can be defined by

$$n_{sv1} = \left\lceil \frac{N_{s1}}{n_{sh1}} \right\rceil, \quad n_{sv2} = \left\lceil \frac{N_{s2}}{n_{sh2}} \right\rceil. \quad (5.18)$$

As a result, the winding height,  $h_w$ , the core window height,  $H$ , and the primary windings build are respectively calculated as

$$h_w = (N_{l1} + 1)(n_{sv1}d_{s1} + 2d_{ins-int1}) + N_{l1}d_{t1} \quad (5.19)$$

$$H = h_w + 2d_{cl} \quad (5.20)$$

$$W_1 = m_1(n_{sh1}d_{s1} + 2d_{ins-int1}) + (m_1 - 1)d_{ins1} \quad (5.21)$$

where  $d_{t1}$ ,  $d_{ins1}$ ,  $d_{ins-int1}$  and other parameters were already illustrated in Fig. 5.4. Hence, the mean length turn of the primary windings,  $MLT_1$ , which will be later used for the windings loss calculation is obtained from

$$MLT_1 = 2(2A + d_{c1} + 4d_{cf} + n_c B + (n_c - 1)d_{c2} + 2W_1). \quad (5.22)$$

Likewise, the number of turns per layer and the number of layers at the secondary litz winding are respectively calculated by

$$N_{l2} = \left\lceil \frac{h_w - (n_{sv2}d_s + 2d_{ins-int2})}{(n_{sv2}d_s + 2d_{ins-int2}) + d_{t2}} \right\rceil \quad (5.23)$$

$$m_2 = \left\lceil \frac{nm_1 N_{l1}}{N_{l2}} \right\rceil. \quad (5.24)$$

Accordingly, the secondary winding build is calculated from

$$W_2 = m_2(n_{sh2}d_{s2} + 2d_{ins-int2}) + (m_2 - 1)d_{ins2}. \quad (5.25)$$

### 5.3.4.1 Isolation Distance, $d_{iso}$

In order to be able to calculate the rest of the geometrical dimensions, i.e, the core window width, the total length and width of the transformer box and consequently the total volume of the box, the first parameter to be determined is the required isolation distance,  $d_{iso}$ , fulfilling the minimum isolation requirements,  $V_{iso}$ , as well as providing the desired leakage inductance,  $L_\sigma$ , ensuring ZVS operation of the DC-DC converter.

For this purpose, the analytical expression presented in [122], accounting for the high frequency effect on the leakage inductance value, is rearranged as

$$d_{iso} = \frac{-8k_1 - k_2m_1 + \sqrt{(k_2m_1 + 8k_1)^2 - 16k_3m_1}}{8m_1} \quad (5.26)$$

where  $k_1$  to  $k_3$  can be calculated according to the expressions presented in [73] for the foil and round conductors. However, in case of the rectangular litz wire used in this chapter, those coefficients should be adapted as follows

$$\begin{aligned} k_1 &= \frac{m_1(m_2 - 1)(2m_2 - 1)}{6m_2} d_{ins2} \\ &+ Im\left(\frac{m'_1}{m'_2} \frac{\sin(\frac{2\Delta_2}{\alpha\delta})4\alpha\delta^2(m'_2{}^2 - 1) + 4d'_{s2}(2m'_2{}^2 + 1)}{24\sin^2(\frac{2\Delta_2}{\alpha\delta})}\right) \\ &+ Im\left(\frac{m'_1}{m'_2} \frac{-\alpha\delta^2\sin(\frac{4\Delta_2}{\alpha\delta})(2m'_2{}^2 + 1) + 8d'_{s2}(1 - m'_2{}^2)\cos(\frac{2\Delta_2}{\alpha\delta})}{24\sin^2(\frac{2\Delta_2}{\alpha\delta})}\right) \end{aligned} \quad (5.27)$$

where the number of layers, strand diameters and the penetration ratios are adapted for the rectangular litz conductor as

$$m'_1 = n_{sh1}m_1 \quad , \quad m'_2 = n_{sh2}m_2 \quad (5.28)$$

$$d'_{s1} = d_{s1} \frac{\sqrt{\pi}}{2} \quad , \quad d'_{s2} = d_{s2} \frac{\sqrt{\pi}}{2} \quad (5.29)$$

$$\Delta_1 = \frac{d_{s1}}{2\delta} \sqrt{\frac{\pi N_{l1} n_{sv1} d_{s1} \sqrt{\pi}}{2H}} \quad , \quad \Delta_2 = \frac{d_{s2}}{2\delta} \sqrt{\frac{\pi N_{l2} n_{sv2} d_{s2} \sqrt{\pi}}{2H}} \quad (5.30)$$

where  $\delta$  is the skin depth at any particular frequency and  $\alpha$  is defined as  $\frac{1+j}{\delta}$ . Furthermore,  $k_2$  can be calculated as

$$k_2 = MLT_1 + 4W_1 \quad (5.31)$$

and  $k_3$  are calculated as

$$k_3 = (MLT_1 + 4(W_1 + W_2))k_1 - k_4 \quad (5.32)$$

where  $k_4$  with the rectangular litz conductor's parameters can be calculated as

$$\begin{aligned} k_4 = & \frac{h_w}{\mu m_1 N_{l1}^2} L_{\sigma 1} \\ & - MLT_1 \frac{(m_1 - 1)(2m_1 - 1)}{6} d_{ins1} \\ & - MLT_1 \cdot \text{Im} \left( \frac{\sin(\frac{2\Delta_1}{\alpha\delta}) 4\alpha\delta^2 (m_1'^2 - 1) + 4d'_{s1} (2m_1'^2 + 1)}{24\sin^2(\frac{2\Delta_1}{\alpha\delta})} \right) \\ & + MLT_1 \cdot \text{Im} \left( \frac{\alpha\delta^2 \sin(\frac{4\Delta_1}{\alpha\delta}) (2m_1'^2 + 1) - 8d'_{s1} (1 - m_1'^2) \cos(\frac{2\Delta_1}{\alpha\delta})}{24\sin^2(\frac{2\Delta_1}{\alpha\delta})} \right). \end{aligned} \quad (5.33)$$

Thus, the expression in (5.26) gives the required isolation distance providing the desired leakage inductance as one of the design specifications. It should be noted that the obtained value of  $d_{iso}$  must be sufficient enough to withstand the isolation voltage level,  $V_{iso}$ . Otherwise, the design is not acceptable and the next transformer geometry construction with a new set of the free parameters will be initiated.

Having  $V_{iso}$  determined, one can uniquely draw the transformer sketch, shown in Fig. 5.4, with all the geometrical details. Therefore, it is possible to utilize the loss evaluation methods, in order to calculate the power losses of each transformer corresponding to each set of free parameters.

### 5.3.5 Losses Calculations

The magnetic components volume reduction at higher frequencies is at the expense of enhanced core losses as well as increased winding losses due to intensified skin and proximity effects. Although the main focus is to mitigate this loss enhancement by utilizing the proper magnetic material, winding type as well as the right thermal management strategy, it is also important to more accurately evaluate the aforementioned power losses in order to properly implement a thermal management scheme. For this purpose, various analytical and empirical loss evaluation methods have been studied and modified in some cases. Finally the most suitable ones have been selected to be used in this work.

#### 5.3.5.1 Core Losses

In order to evaluate the core losses, the modified expression of the improved generalized Steinmetz equation (IGSE) adapted for the square-wave excitation with arbitrary duty cycles and rise times presented in [73, 123] has been used as



$$P_{core} = \left(2D - \frac{4\alpha}{\alpha + 1}R\right) \frac{2^\beta}{(D - R)^\alpha} k_i k_f^\alpha B_m^\beta V_c \rho \quad (5.34)$$

where  $D$  and  $R$  are equal to 0.5 and 0 respectively for the standard phase shift DAB converter,  $\rho$  is the magnetic core density,  $\alpha$  and  $\beta$  are the Steinmetz core loss coefficients. Moreover, the coefficient,  $k_i$ , which is a function of  $\alpha$  and  $\beta$  can be calculated as

$$k_i = \frac{1}{(2\pi)^{\alpha-1} \int_0^{2\pi} |\cos(\theta)|^\alpha 2^{\beta-\alpha} d\theta}. \quad (5.35)$$

Accordingly, the magnetic core volume,  $V_c$ , can be determined as follows

$$V_c = 4n_c AB (H + 2A) + 4n_c ABG \quad (5.36)$$

in which  $H$  is the window height previously calculated in (6.33) and  $G$  is the core window width calculated from

$$G = d_{cf} + W_1 + d_{iso} + W_2 + d_{cl}. \quad (5.37)$$

### 5.3.5.2 Windings Losses

The winding losses can be calculated using the harmonic contents of the excitation current, thus

$$P_{w1} = \sum_{h=1}^n R_{DC1} \cdot RF_{1h} \cdot I_{1h}^2, \quad P_{w2} = \sum_{h=1}^n R_{DC2} \cdot RF_{2h} \cdot I_{2h}^2 \quad (5.38)$$

where  $R_{DC1}$  and  $R_{DC2}$  are the DC resistance of the primary and secondary windings portion,  $RF_{1h}$  and  $RF_{2h}$  are respectively the AC resistance factor of the primary and secondary windings portion at the  $h^{th}$  harmonic. In addition,  $I_{1h}$  and  $I_{2h}$ , are respectively the rms values of the primary and secondary currents through the transformer windings for the  $h^{th}$  harmonic. The DC resistance of the primary and secondary windings portion associated with rectangular litz winding arrangement shown in Fig. 5.4 are calculated from

$$R_{DC1} = \frac{4m_1 N_{l1} MLL_1}{\sigma \pi d_{s1}^2 N_{s1}}, \quad R_{DC2} = \frac{4m_2 N_{l2} MLL_2}{\sigma \pi d_{s2}^2 N_{s2}} \quad (5.39)$$

where  $\sigma$  is the conductivity of the conductors, here copper,  $MLL_1$  is previously defined in (6.37) and  $MLL_2$  is the mean length turn of the secondary winding which is calculated, as can be seen in top view of Fig. 5.4, as

$$MLL_2 = MLL_1 + 4W_1 + 4W_2 + 8d_{iso}. \quad (5.40)$$

As shown in Fig. 5.1(b), the transformer voltages and currents are not sinusoidal. Therefore, AC resistance factors,  $RF_{1_h}$  and  $RF_{2_h}$ , should be, separately for each harmonic content, calculated from the expression in [124] which, in this chapter, is adapted to account for the rectangular litz configuration shown in Fig. 5.4.

$$RF(\Delta_h) = \Delta_h \left( \frac{\sinh(2\Delta_h) + \sin(2\Delta_h)}{\cosh(2\Delta_h) - \cos(2\Delta_h)} \right) + \frac{2\Delta_h(m^2 n_{sh}^2 - 1)}{3} \left( \frac{\sinh(\Delta_h) - \sin(\Delta_h)}{\cosh(\Delta_h) + \cos(\Delta_h)} \right) \quad (5.41)$$

where  $\Delta_h$  is the penetration ratio of the  $h^{th}$  harmonic defined in (5.30) in which, it is clear that  $\Delta_h$  increases at higher harmonic numbers, because it is inversely proportional to the skin depth.

Finally, the RMS value of the  $h^{th}$  harmonic of the transformer currents, to be used in (5.38), is derived as

$$I_{1_h} = \frac{4V_{DC1}\sqrt{1+d^2-2d\cos(h\varphi)}}{2\sqrt{2}\pi^2fh^2L_\sigma} \quad , \quad I_{2_h} = \frac{I_{1_h}}{n} \quad (5.42)$$

### 5.3.5.3 Dielectric Losses

In low frequency applications, dielectric losses are often negligible, however when operating at higher frequencies, this type of losses are also important to be considered particularly in high power density applications where the design already is pushed to its limits. The dielectric losses are calculated from

$$P_{ins} = \Delta V_{ins}^2 2\pi f C_{ins} \tan(\delta) \quad (5.43)$$

in which  $\tan(\delta)$  is the dissipation factor of the dielectric material, already presented in Table. 5.2,  $C_{ins}$  and  $\Delta V_{ins}$  are respectively the capacitance of the dielectric medium and the voltage over it. It should be pointed out that for simplicity, the magnetic field within the isolation distance,  $d_{iso}$ , coil former distance,  $d_{cf}$ , as well as the clearing distances,  $d_{cl}$ , is considered to be uniform.

### 5.3.6 Thermal Analysis

The thermal aspects of a magnetic design is one of the most crucial issues since, in principle, it is the main design limitation, specifying the geometrical boundaries in which the magnetic component can continuously operates without exceeding the critical temperature, as one of the design criteria. Accordingly, a proper thermal management scheme is a key to dissipate the power losses and consequently to achieve higher power densities.

The combination of two thermal management methods, shown in Fig. 5.5(right), are implemented in the current design approach. First of all, as in planar transformers, heat sinks are considered to be placed on the core surfaces in order to increase the effective surface area resulting in thermal resistance reduction and consequently higher power dissipation capability of the design. The main drawback of this method, besides increasing the total volume of the transformer box, is that due to the poor thermal contact of the core and the primary windings, the heat around the middle limbs, usually the hottest spot of the transformer, can not easily be conducted to the heat sink. For this reason, a complementary thermal management method has been incorporated placing a thermally conductive material between the primary windings and the core in order to directly conduct the heat to the top and bottom part of the transformer where heat sinks are assembled. As a result, with a negligible increase in the transformer total volume, heat can be extracted from the hot spots deep inside the transformer. Copper or aluminum straps are suitable candidates for this purpose due to their relatively high thermal conductivity. However, in the current design methodology, a thermally conductive, electrically dielectric, polymeric material, which simultaneously can be considered both as the heat removal medium and a dielectric bobbin or coil-former for the transformer, is used, as can be seen in Fig. 5.5(right). In addition, using the polymeric material, the possibility of eddy current losses in the copper or aluminum due to an unwanted air gap in the core, is considerably reduced.

In principle, defining the convection coefficients is one of the biggest uncertain parts of any magnetic design, due to many practical factors affecting the heat transfer process. Therefore, it may be hard to justify the use of very elaborated methods for specifying these coefficients [56]. Therefore, two different approaches with different level of detail have been considered in this chapter for the thermal design.

### 5.3.6.1 Isotherm Surface Model

Having the outer surface of the magnetic component determined and assuming that all the open surfaces of the magnetic component have the same temperature, the maximum power dissipation capability of each transformer corresponding to each set of free parameters can be evaluated from

$$\begin{aligned} P_{core} + P_{windings} + P_{ins} &= P_{conv} + P_{rad} \\ &= h_{conv}A_{conv}(T_s - T_a) + h_{rad}A_{rad}(T_s - T_a) \end{aligned} \quad (5.44)$$

where  $P_{conv}$  and  $P_{rad}$  are the heat transfer rates by convection and radiation heat transfer mechanisms, respectively.  $A_{conv}$  and  $A_{rad}$  are the convective and radiating area, respectively, and  $T_s$  and  $T_a$  are the temperature of the surface and ambient temperature, in the same order [56].  $h_{rad}$  is the radiation heat transfer coefficient calculated by

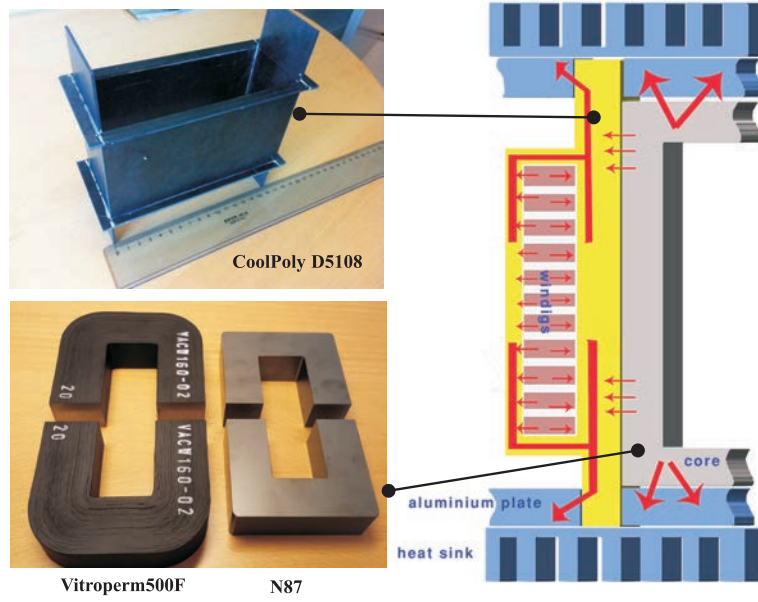


Figure 5.5: Thermally conductive, electrically dielectric polymeric coil-former which extracts the heat from hot spots to the heat sinks.

$$h_{rad} = \frac{\varepsilon\sigma(T_s^4 - T_a^4)}{T_s - T_a} \quad (5.45)$$

where  $\varepsilon$  is the emissivity of the radiating surface and  $\sigma$  is the Stefan-Boltzmann constant,  $\sigma = 5.67 \times 10^{-8} \frac{W}{m^2 \cdot K^4}$ .

The convection heat transfer coefficient,  $h_{conv}$ , is probably the most uncertain coefficient in any magnetic design requiring a reliable thermal evaluation since it depends on physical dimensions and orientation of the object, type of the fluid, density, velocity and several other parameters which are not often possible to be reliably determined. One of the accurate presentations of the convection coefficient is reported in [56] in which the convection heat transfer coefficient is proportional to the Nusselt number,  $Nu$ , as follows

$$h_{conv} = Nu \frac{k}{L} \quad (5.46)$$

where  $k$  is the thermal conductivity and  $L$  is the characteristic length of the object defined as the total distance passed by the fluid cooling the magnetic component as follows

$$L = n_c B + (n_c - 1)d_{c2} + H + 2\sqrt{A^2 + G^2} \quad (5.47)$$

There are several presentations of Nusselt number, however the one reported in [56], in addition to its high accuracy, is valid for a wide range of Rayleigh number as follows

$$Nu = 0.68 + \frac{0.67Ra^{1/4}}{\left(1 + (0.492/Pr)^{9/16}\right)^{4/9}} \quad \text{for } Ra < 10^9 \quad (5.48)$$

where  $Ra$ ,  $Gr$  and  $Pr$  are Rayleigh number, Grashof number and Prandtl number, respectively calculated from

$$Gr = \frac{g \left(\frac{2}{T_s + T_a}\right) (T_s - T_a) L^3}{\nu^2} \quad (5.49)$$

$$Ra = Gr.Pr \quad , \quad Pr = c_p \frac{\mu}{k} \quad (5.50)$$

where  $g$  is the gravity,  $c_p$  is the specific heat capacity,  $\nu$  and  $\mu$  are the kinematic and dynamic viscosities, respectively. The values of these parameters can be found in heat transfer textbooks and handbooks for different materials at different temperatures [56,125]. As a result, the convection heat transfer coefficient can be calculated from

$$h_{conv} = \left( 0.68 + \frac{0.67 \left( g \left( \frac{2}{T_s + T_a} \right) (T_s - T_a) L^3 . Pr / \nu^2 \right)^{1/4}}{\left( 1 + (0.492/Pr)^{9/16} \right)^{4/9}} \right) \frac{k}{L} \quad (5.51)$$

### 5.3.6.2 Thermal Network Model

The isotherm surface method does not provide any information about the real heat distribution inside the components and merely indicates the maximum heat dissipation capability of the component with respect to its assumed surface temperature and its respective dimensions and orientation. Hence, it remains unclear whether there are hot spots which passed the critical temperature inside the components or not. It would thus be of interest to implement a more detailed presentation of the heat distribution inside the transformer. This can be achieved by considering the thermal network composed of several thermal resistances which govern the heat transfer between different internal parts as well as the surface area of the transformer.

The equivalent thermal network of the proposed transformer is depicted in Fig. 5.6 in which six different temperature nodes connected by the thermal resistances have been considered. These temperature nodes are the HV winding temperature,  $T_{HV}$ , LV winding temperature,  $T_{LV}$ , center limb core temperature,  $T_{cc}$ , yokes and side

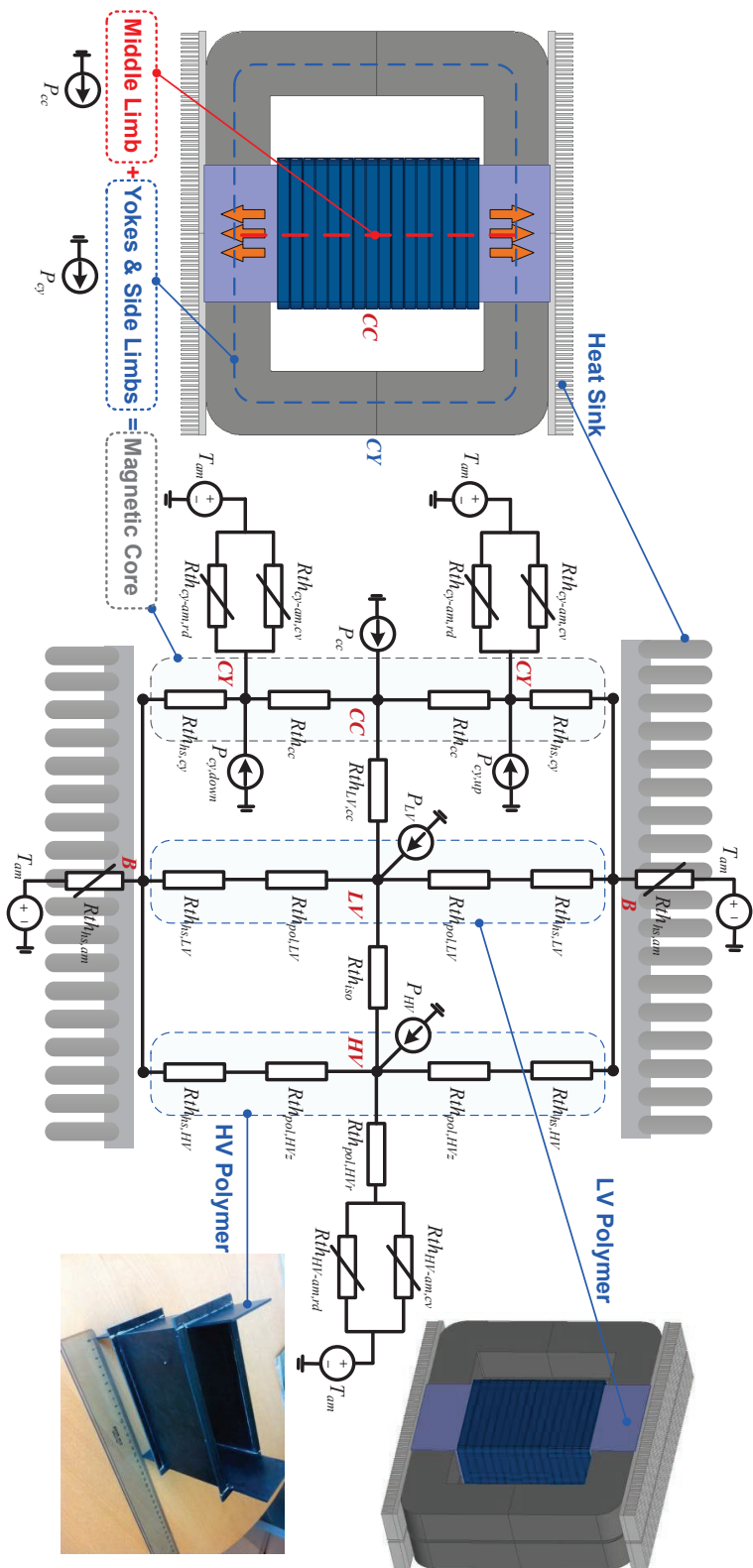


Figure 5.6: Equivalent thermal network of the proposed transformer topology with six temperature nodes, i.e, (a) HV winding temperature,  $T_{HV}$  (b) LV winding temperature,  $T_{LV}$  (c) Center limb core temperature,  $T_{cc}$  (d) Yokes and side limbs temperature,  $T_{cy}$  (e) heat sink base temperature,  $T_b$  and (f) Ambient temperature,  $T_{am}$  .

limbs temperature,  $T_{cy}$ , heat sink base temperature,  $T_b$  and finally the ambient temperature,  $T_{am}$ . In shell type transformers the middle limb is surrounded by the windings. Hence its surfaces are not exposed to the air and its corresponding heat should be first conducted to the surface areas which are exposed to the open air and then be dissipated by means of convection and radiation. Therefore, the magnetic core is divided into two areas, the middle limb with the temperature,  $T_{cc}$ , and the rest of the core consisting of side limbs and the yokes with the temperature,  $T_{cy}$ . The main assumption here is that each of the aforementioned sections are assumed to have a uniform temperature distribution, e.g., all copper areas inside the LV winding portion is assumed to have one temperature,  $T_{LV}$ .

It should be mentioned that the heat exchange inside the transformer is mainly taking place due to the heat conduction mechanism, whereas the outer parts, the heat sinks and the open surfaces, transfer heat to the surrounding fluid, air, by means of convection and radiation mechanisms. Therefore, the thermal resistances illustrated in Fig. 5.6 are composed of conduction thermal resistances, as well as the convection and radiation ones. These thermal resistances are here calculated with respect to the transformer design sketch shown in Fig. 5.4.

The equivalent thermal resistance created by conduction through a solid material can be calculated from

$$R_{th} = \frac{1}{h_{cond} \cdot A_{cond}} = \frac{l_{cond}}{k_{cond} A_{cond}} \quad (5.52)$$

where  $h_{cond}$  is the conduction heat transfer coefficient,  $k_{cond}$  is the thermal conductivity of the material,  $l_{cond}$  and  $A_{cond}$  are, respectively, the length and cross section of the material. Using (5.52), the thermal resistance of the middle core limb in the considered transformer geometry can be calculated as

$$R_{th_{cc}} = \frac{H}{4n_c k_c k_{cc} AB} \quad (5.53)$$

where  $k_{cc}$  is the thermal conductivity of the core material. Similarly, the thermal resistances of the isolation distance, LV and HV polymeric heat conducting material are calculated, respectively, as

$$R_{th_{iso}} = \frac{d_{iso}}{k_{iso} h_w M L T_{iso}} \quad (5.54)$$

$$R_{th_{pol,LV}} = \frac{H}{4k_{pol} d_{cf} (2d_{cf} + 2A + d_{c1})} \quad (5.55)$$

$$R_{th_{pol,HVz}} = \frac{H}{4k_{pol} d_{cf} (2d_{iso} + 2W_1 + 2d_{cf} + 2A + d_{c1})} \quad (5.56)$$

where  $k_{pol}$  is the thermal conductivity of the thermally-conductive polymeric material, one of the heat management strategies for this design. The main functionality of the polymeric plates is to conduct the heat along the z axis towards the heat-sinks; however, they also contribute in radial heat conduction between the LV windings and the magnetic core middle limb as well as the heat conduction between the HV windings and the external surfaces of the HV windings as

$$R_{th_{LV,cc}} = \frac{d_{cf}}{2k_{pol}h_w(2A + n_cB)} \quad (5.57)$$

$$R_{th_{pol,HVr}} = \frac{d_{cl}}{2k_{pol}h_w(4G + 2A + d_{c1})}. \quad (5.58)$$

The interfaces between polymeric plates and the heat-sinks are filled by the high thermal conductivity paste. The corresponding thermal resistances,  $R_{th_{hs,LV}}$  and  $R_{th_{hs,HV}}$ , can be analytically calculated, similar to other thermal resistances. Nevertheless, due to the very thin layers of thermal interface, those thermal resistances become relatively small. Therefore, in this chapter, the conservative fixed values in the order of  $0.01 \frac{K}{W}$  will be considered instead of the analytical expressions. This also applies on the interface between the core yokes and heat-sink corresponding to the thermal resistance,  $R_{th_{hs,cy}}$ .

Apart from the conduction heat transfer which was the governing mechanism inside the transformer, the transferred heat is dissipated from the open surfaces of the component by means of convection and radiation heat transfer mechanisms. There are three different open surfaces in the current design, heat-sinks, open surfaces of the HV windings and the open surfaces of the core side limbs. The equivalent thermal resistance of the heat-sink,  $R_{th_{hs,am}}$ , can be extracted from the data-sheet with respect to its geometrical characteristics. This thermal resistance can be significantly reduced in the case of force cooling.

The equivalent thermal resistance between the HV winding open surfaces and the air,  $R_{th_{HV,am}}$ , as well as the thermal resistance between the core limbs and the air,  $R_{th_{cy,am}}$ , can be considered as the parallel connection of convection and radiation thermal resistances as

$$\frac{1}{R_{th_{eq}}} = \frac{1}{R_{th_{conv}}} + \frac{1}{R_{th_{rad}}}. \quad (5.59)$$

where  $R_{th_{conv}}$  and  $R_{th_{HV,am}}$  can be calculated, respectively, as

$$R_{th_{conv}} = \frac{1}{h_{conv}A_{conv}} \quad , \quad R_{th_{rad}} = \frac{1}{h_{rad}A_{rad}} \quad (5.60)$$



where  $A_{conv}$  and  $A_{rad}$  are, respectively, the convective and radiating area of the heat dissipating surfaces. Substitution of (5.60) into (5.59) gives the equivalent thermal resistances of the considered object as

$$R_{theq,am} = \frac{1}{h_{conv}A_{conv} + h_{rad}A_{rad}} \quad (5.61)$$

which should be independently calculated for the HV winding and core open surfaces. Accordingly, the total HV surface areas contributing in convection and radiation heat transfer are calculated, separately, with the assumption that the top and bottom part of the HV windings do not contribute in the convection mechanism. Similarly, the surfaces between the corners of the HV windings which radiate to each other are not considered as the radiation surfaces [56]. Under these assumptions, the convection and radiation total area for convection and radiation, respectively, in the HV external surfaces are

$$A_{conv_{HV}} = H(8G + 4A + 2dc_1) \quad (5.62)$$

$$A_{rad_{HV}} = 2H(2G + 2A + dc_1) \quad (5.63)$$

Likewise, the convection and radiation total area for convection and radiation, respectively, for the core side limbs can be calculated as

$$A_{conv_{cy}} = 2n_c H(2A + B) \quad (5.64)$$

$$A_{rad_{cy}} = 2H(2A + n_c B). \quad (5.65)$$

Apart from the convection and radiation surface areas, the convection and radiation heat transfer coefficients also need to be determined in order to calculate the equivalent thermal resistances in (5.60). The radiation heat transfer coefficient,  $h_{rad}$ , can be calculated by

$$h_{rad} = \frac{\varepsilon\sigma(T_s^4 - T_a^4)}{T_s - T_a} \quad (5.66)$$

where  $\varepsilon$  is the emissivity of the radiating surface,  $\sigma$  is the Stefan-Boltzmann constant,  $\sigma = 5.67 \times 10^{-8} \frac{W}{m^2.K^4}$ ,  $T_s$  and  $T_a$  are the temperature of the surface and ambient temperature, in the same order [56].

The convection heat transfer coefficient,  $h_{conv}$ , is probably the most uncertain coefficient in any magnetic design requiring a reliable thermal evaluation since it

depends on physical dimensions and orientation of the object, type of the fluid, density, velocity and several other parameters which are not often possible to be reliably determined. One of the accurate presentations of the convection coefficient is reported in [56] in which the convection heat transfer coefficient is proportional to the Nusselt number,  $Nu$ , as follows

$$h_{conv} = Nu \frac{k}{L} \quad (5.67)$$

where  $k$  is the thermal conductivity of the fluid, i.e., air.  $L$  is the characteristic length of the object defined as the total distance passed by the coolant fluid as follows

$$L_{conv_{HV}} = H + 2G \quad , \quad L_{conv_{cy}} = H \quad (5.68)$$

There are several presentations of Nusselt number, however the one reported in [56], in addition to its high accuracy, is valid for a wide range of Rayleigh number as follows

$$Nu = 0.68 + \frac{0.67Ra^{1/4}}{\left(1 + (0.492/Pr)^{9/16}\right)^{4/9}} \quad \text{for} \quad Ra < 10^9 \quad (5.69)$$

where  $Ra$ ,  $Gr$  and  $Pr$  are Rayleigh number, Grashof number and Prandtl number, respectively calculated from

$$Gr = \frac{g \left(\frac{2}{T_s + T_a}\right) (T_s - T_a) L^3}{\nu^2} \quad (5.70)$$

$$Ra = Gr.Pr \quad , \quad Pr = c_p \frac{\mu}{k} \quad (5.71)$$

where  $g$  is the gravity,  $c_p$  is the specific heat capacity,  $\nu$  and  $\mu$  are the kinematic and dynamic viscosities, respectively. The values of these parameters can be found in heat transfer textbooks and handbooks for different materials at different temperatures [56,125]. As a result, the convection heat transfer coefficient can be calculated from

$$h_{conv} = \left( 0.68 + \frac{0.67 \left( g \left( \frac{2}{T_s + T_a} \right) (T_s - T_a) L^3 . Pr / \nu^2 \right)^{1/4}}{\left( 1 + (0.492/Pr)^{9/16} \right)^{4/9}} \right) \frac{k}{L} \quad (5.72)$$

The presented expressions of  $h_{conv}$  and  $h_{rad}$  in (5.72) and (5.66), together with their corresponding surface areas and characteristic lengths presented, respectively,

in (5.62) to (5.65) and (5.68), should be separately applied on (5.60) and (5.61) in order to find the equivalent surface thermal resistances.

Identifying the thermal network of the proposed design and calculating its corresponding thermal resistances, one can generally define the first-order differential equations as follows

$$\begin{aligned}
c_{HV} \frac{dT_{HV}}{dt} &= \frac{2}{R_{th_{pol,HVz}} + R_{th_{hs,HV}}} (T_B - T_{HV}) + \frac{1}{R_{th_{iso}}} (T_{LV} - T_{HV}) + \frac{1}{R_{th_{pol,HVr}} + R_{th_{HV,am}}} (T_{am} - T_{HV}) + P_{HV} \\
c_{LV} \frac{dT_{LV}}{dt} &= \frac{2}{R_{th_{pol,LV}} + R_{th_{hs,LV}}} (T_B - T_{LV}) + \frac{1}{R_{th_{iso}}} (T_{HV} - T_{LV}) + \frac{1}{R_{th_{LV,cc}}} (T_{cc} - T_{LV}) + P_{LV} \\
c_{cc} \frac{dT_{cc}}{dt} &= \frac{1}{R_{th_{LV,cc}}} (T_{LV} - T_{cc}) + \frac{2}{R_{th_{cc}}} (T_{cy} - T_{cc}) + P_{cc} \\
c_{cy} \frac{dT_{cy}}{dt} &= \frac{2}{R_{th_{cc}}} (T_{cc} - T_{cy}) + \frac{2}{R_{th_{hs,cy}}} (T_b - T_{cy}) + \frac{2}{R_{th_{cy,am}}} (T_{am} - T_{cy}) + P_{cy} \\
c_B \frac{dT_B}{dt} &= \frac{2}{R_{th_{pol,HVz}} + R_{th_{hs,HV}}} (T_{HV} - T_B) + \frac{2}{R_{th_{pol,LV}} + R_{th_{hs,LV}}} (T_{LV} - T_B) + \frac{2}{R_{th_{hs,cy}}} (T_{cy} - T_b) + \frac{2}{R_{th_{hs,am}}} (T_{am} - T_B)
\end{aligned}
\tag{5.73}$$

where  $c_n$  is the heat capacity of the node with the temperature,  $T_n$ . It can be used for the transient thermal analysis, however, for the purpose of this study, the steady-state analysis to find the final temperature of each node is sufficient. Hence, the left-hand sides of all the differential equations will be considered as zero. Therefore, the matrix representation of the differential equations in (5.73) is

$$AT + BU = 0 \Rightarrow T = -A^{-1}BU \tag{5.74}$$

where the matrices ,  $T$ ,  $U$  and  $B$  can be respectively represented as

$$T = \begin{bmatrix} T_{HV} \\ T_{LV} \\ T_{cc} \\ T_{cy} \\ T_B \end{bmatrix}_{5 \times 1}, \quad U = \begin{bmatrix} P_{HV} \\ P_{LV} \\ P_{cc} \\ P_{cy} \\ P_B \\ T_{am} \end{bmatrix}_{6 \times 1} \tag{5.75}$$

$$B = \begin{bmatrix} 1 & 0 & 0 & 0 & 0 & \frac{1}{R_{th_{pol,HV_r}} + R_{th_{HV,am}}} \\ 0 & 1 & 0 & 0 & 0 & 0 \\ 0 & 0 & 1 & 0 & 0 & 0 \\ 0 & 0 & 0 & 1 & 0 & \frac{2}{R_{th_{cy,am}}} \\ 0 & 0 & 0 & 0 & 0 & \frac{2}{R_{th_{hs,am}}} \end{bmatrix}_{5 \times 6} \quad (5.76)$$

and  $A$  can be presented by

$$A = \begin{bmatrix} R_1 & \frac{1}{R_{th_{iso}}} & 0 & 0 & \frac{2}{R_{th_{HV_z}}} \\ \frac{1}{R_{th_{iso}}} & R_2 & \frac{1}{R_{th_{LV,cc}}} & 0 & \frac{2}{R_{th_{LV_z}}} \\ 0 & \frac{1}{R_{th_{LV,cc}}} & R_3 & \frac{2}{R_{th_{cc}}} & 0 \\ 0 & 0 & \frac{2}{R_{th_{cc}}} & R_4 & \frac{2}{R_{th_{hs,cy}}} \\ \frac{2}{R_{th_{HV_z}}} & \frac{2}{R_{th_{LV_z}}} & 0 & \frac{2}{R_{th_{hs,cy}}} & R_5 \end{bmatrix} \quad (5.77)$$

where  $R_1$  to  $R_5$  are defined as

$$R_1 = \frac{-2}{R_{th_{HV_z}}} + \frac{-1}{R_{th_{iso}}} + \frac{-1}{R_{th_{HV_r}}} \quad (5.78)$$

$$R_2 = \frac{-2}{R_{th_{LV_z}}} + \frac{-1}{R_{th_{iso}}} + \frac{-1}{R_{th_{LV,cc}}} \quad (5.79)$$

$$R_3 = \frac{-1}{R_{th_{LV,cc}}} + \frac{-2}{R_{th_{cc}}} \quad (5.80)$$

$$R_4 = \frac{-2}{R_{th_{cc}}} + \frac{-2}{R_{th_{hs,cy}}} + \frac{-2}{R_{th_{cy,am}}} \quad (5.81)$$

$$R_5 = \frac{-2}{R_{th_{HV_z}}} + \frac{-2}{R_{th_{LV_z}}} + \frac{-2}{R_{th_{hs,cy}}} + \frac{-2}{R_{th_{hs,am}}} \quad (5.82)$$

and the axial and radial equivalent thermal resistance of the polymeric plates are calculated as

Table 5.3: Design specification of the prototypes.

Output Power, $P_{out}$	50 kW
Low voltage side, $V_{LV}$	1 kV
High voltage side, $V_{HV}$	3 kV
Leakage inductance, $L_{\sigma}$	38 and 29 $\mu H$
Transformer turn ratio, $n$	3
Isolation level, $V_{iso}$	6 kV
Switching frequency, $f$	5 kHz

$$R_{th_{HVz}} = R_{th_{pol,HVz}} + R_{th_{hs,HV}} \quad (5.83)$$

$$R_{th_{HVr}} = R_{th_{pol,HVr}} + R_{th_{HV,am}} \quad (5.84)$$

$$R_{th_{LVz}} = R_{th_{pol,LV}} + R_{th_{hs,LV}}. \quad (5.85)$$

Unlike the conduction heat transfer coefficient, the convection and radiation heat transfer coefficients are strongly temperature dependent as can be seen in (5.66) and (5.72). Therefore, the matrix equation in (5.74) should be solved iteratively to achieve the steady state temperature of each node. The iterations start with the initial temperature as the ambient temperature for all the nodes and continue with the updated thermal resistances in each iteration until it yields the steady state value.

## 5.4 Down-Scaled Prototype Design and Optimization

To validate the proposed design approach, two down-scaled 50 kW, 1 / 3 kV, 5 kHz medium-frequency transformer prototypes with two different core materials, i.e., Vitroperm500F and N87, were designed and manufactured. The specification of the prototypes are tabulated in Table. 5.3. The transformer prototypes are designed to operate with the voltage and current waveforms shown in Fig. 5.1(b) which are the typical waveforms of a DAB converter, although, the proposed design methodology can easily be applied on the other type of modulations with duty cycles,  $D_1$  and  $D_2$ ,

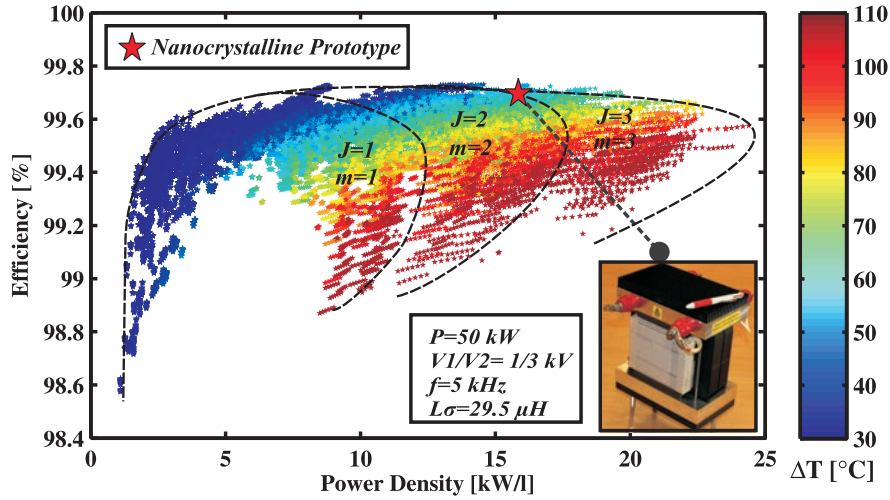


Figure 5.7: Efficiency versus power density of feasible nanocrystalline-based transformers according to the proposed design methodology.

being below 0.5. The isolation level, 6 kV, is considered to account for two times the voltage of the high voltage side. The desired values of the leakage inductances are on the basis of maximum 4% and 3% output voltage deviation for the prototypes with N87 and Vitroperm500F, respectively.

#### 5.4.1 Design and Optimization Results

The proposed design methodology explained in this chapter has been applied on the prototype specification shown in Table. 5.3. For this purpose, each free parameter, shown in the fourth step in Fig. 5.2, is swept over a wide range resulting in more than 400000 different combination of free parameters. Each unique combination of free parameters corresponds to a unique transformer geometry based on the design approach explained in this chapter. The great majority of the considered cases are discarded since they do not fulfill either the thermal requirements or the isolation distances required to obtain the desired leakage inductance. All the dimensional and electrical data of the remaining passed transformers are then saved, step 8 in Fig. 5.2, and will be used to form the Pareto-front optimization curve and consequently to choose the optimum point.

The optimization outcome showing the efficiencies and power densities of the nanocrystalline-based transformers corresponding to the accepted sets of free parameters illustrated in Fig. 5.7 in which each colored star represents a distinct transformer which meets all the design requirements and its color indicates the corresponding temperature rise of that particular transformer. The effect of the maximum allowed current density,  $J_{max}$ , and the number of primary layers,  $m_1$ , as

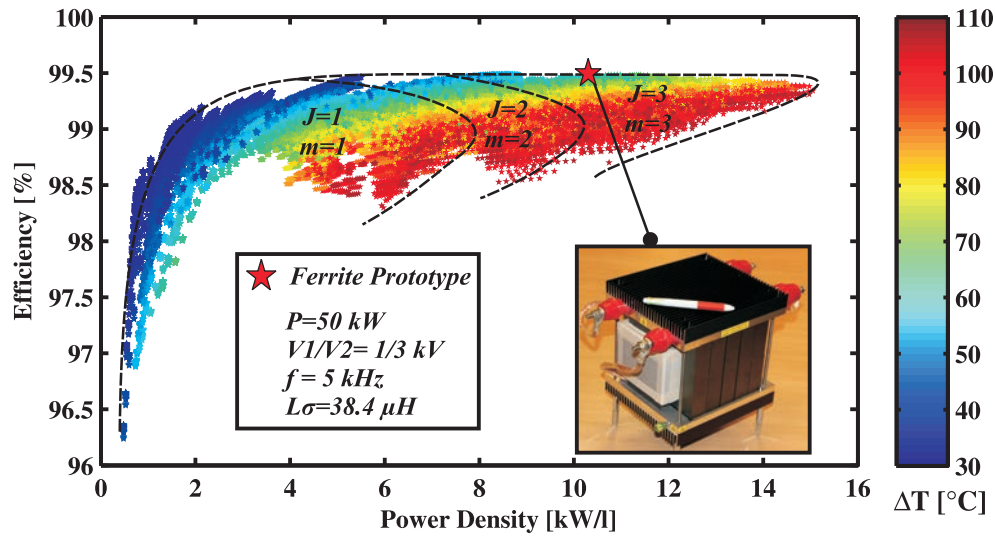


Figure 5.8: Efficiency versus power density of feasible ferrite-based transformers according to the proposed design methodology.

two of the optimization free parameters are illustrated in Fig. 5.7. It can be seen that the achieved power densities increases by allowing higher current densities and number of winding layers; however, this is on the expense of higher loss densities and consequently higher temperature increase as one of the design constraints. The approximate borders between different  $J_{max}$  and  $m_1$  are drawn in Fig. 5.7.

The nanocrystalline-based transformer design is highlighted in Fig. 5.7 with the large red star. According to the design approach, it is expected to reach a power density of  $15.1 \text{ kW/l}$  and the efficiency of  $99.67\%$ . These quantities will be evaluated on the manufactured prototype in the next parts of this chapter. The reason that the highest achievable power density is not selected for manufacturing the prototype, is that the author had limited selection of magnetic core dimensions, particularly for the nanocrystalline prototype, as well as the limited dimensions of rectangular litz conductors which are available on the market. Similarly, the optimization outcome and the selected prototype design of the ferrite-based transformers are shown in Fig. 5.8 in which the selected design, highlighted with a large red star, is expected to exhibit  $99.54\%$  efficiency while the power density is about  $11.5 \text{ kW/l}$ . These quantities, together with the measured loss breakdown and the leakage inductance will be experimentally evaluated on the manufactured prototypes in the next parts of this chapter.

As stated before, two different types of magnetic material, i.e., Vitroperm500F and N87, are used to design and manufacture the prototype transformers. Both noncrystalline and Ferrite material are suitable for high frequency applications and it can be of interest to investigate their performance on two transformer prototypes



Figure 5.9: Built prototypes.

with the same specifications. As can be seen in Fig. 5.7 and Fig. 5.8, Vitroperm500F demonstrates higher efficiencies for the same power density which can be explained by the lower specific losses of Vitroperm500F compared to N87. Furthermore, Fig. 5.7 and Fig. 5.8 show that Vitroperm500F based designs at 5 kHz can achieve substantially higher power densities of up to about  $23 \text{ kW/l}$  with maximum  $70^\circ\text{C}$  temperature increase compared to the one of about  $13 \text{ kW/l}$  for N87. This also can be explained by the relatively higher saturation level of Vitroperm500F compared to the one with N87 ferrite core. It is worth to mention that the high isolation requirements of the case study transformer, 6 kV isolation for a 3/6 kV transformer, together with the desired leakage inductance as two of the design inputs, play an important role in determining the power density of the final optimum design.

#### 5.4.2 Built Prototypes

The finally built nanocrystalline and ferrite-based transformer prototypes are presented in Fig. 5.9 in which the relatively smaller volume of the nanocrystalline-based prototype, the left one, is clear. The geometrical and electrical parameters of the built prototypes are shown in Table. 5.4. The ferrite transformer design consists of 5 core stacks, i.e., ten pairs of U-core, of U 93/76/30 N87 material. Whereas, 4 pairs of W160 U-core, i.e., two core stacks, of Vitroperm500F are used to manufacture the nanocrystalline-transformer prototype. The HV rectangular litz wire comprises of 180 strands with a thickness of 0.2 mm for both prototype designs. The LV side litz wire comprises of 540 strands of the same diameter, however, due to lack of availability, the author utilized three parallel litz wires of the same type



as in the HV side to make the required copper cross-section of the LV side. The winding strategy is wave-type and both the LV and HV litz conductors are tightly placed into the polymeric compartments, CoolPoly D5108 [118], with the dielectric strength of  $29 \text{ kV/mm}$  that provide enough clearance distances from the core surfaces. The thickness of these compartments are 2 mm and 4 mm for the ferrite-based and nanocrystalline-based transformers, respectively. In addition to the dielectric performances of CoolPoly D5108, due to its relatively high thermal conductivity,  $10 \text{ W/mK}$ , it can contribute in the heat conduction towards the heat sinks as explained in the thermal management part. The inter-layer distances,  $d_{ins}$ , between two consecutive layers of the LV and HV windings are, respectively, isolated with one and two layers of a 0.19 mm thermally conductive adhesive tape, 3M 8940 [126], with the typical dielectric strength of  $55 \text{ kV/mm}$  and thermal conductivity of  $0.9 \text{ W/mK}$ .

The isolation distance between the LV and HV windings,  $d_{iso}$ , comprises of 4 mm of molded CoolPoly and 5.6 mm of air distance for the ferrite-based prototype which is tuned to obtain the required leakage inductance which is one of the design specifications. This distance is 21.5 mm, i.e., 8 mm of CoolPoly and 13.5 mm of air distance, for the nanocrystalline-based prototype. The isolation distance,  $d_{iso}$ , was initially considered to be entirely filled with the thermally conductive polymer, CoolPoly, however, because of the practical difficulty of molding thick plates of CoolPoly, it was inevitable to consider the air distance between the windings in these transformer prototypes. It should be noted that the aforementioned thicknesses of the CoolPoly plates are the dedicated thermally conductive plates which are connected to the heat sinks on the top and bottom of the prototypes. Fig. 5.6 bottom-right, shows the manufactured coil former with the projected polymeric plates, built for the nanocrystalline-based prototype.

The prototypes dimensional and electrical characteristics of the nanocrystalline and ferrite-based designs are tabulated in Table. 5.4 for the selected design points highlighted in Fig. 5.7 and Fig. 5.8, respectively. Whereas, the second and forth columns of Table. 5.4 shows the actual dimensions of the built prototypes, as well as the calculated electrical performances based on the actual dimensions which are not far from the selected design. The reason for these slight discrepancy is that, as mentioned before, the author had a limited selection of magnetic cores and rectangular litz conductor dimensions. As an example, the lateral sides of the Vitroperm500F cores,  $B$ , is 28.6 mm for the selected optimized design, red star in Fig. 5.7, whereas the actual value of  $B$  in Vitroperm500F cut-core used in the prototype is 30 mm which fortunately is in an acceptable range. Nevertheless, these discrepancies are expected to slightly alter the power losses and electrical characteristics of the prototypes. For this reason, these characteristics are analytically re-evaluated for the actual dimensions of the built prototypes, as tabulated in the second and forth columns of Table. 5.4 for the nano and ferrite-based transformers, respectively.

Table 5.4: Transformer characteristics of the optimal design transformer versus the final assembled prototypes.

Parameter	Nanocrystalline Design		Ferrite Design		
	Optimum point	Prototype	Optimum point	Prototype	
Magnetic Core	Number of core stacks, $n_c$	2	2	5	5
	$A$ [mm]	36	36	28	28
	$B$ [mm]	28.6	30	29.5	30
	$G$ [mm]	35.1	39	29.5	34
	$H$ [mm]	104.6	120	83.8	92
Windings	$N_1/N_2$	16/48	16/48	18/54	18/54
	$m_1 \times N_{l1}/m_2 \times N_{l2}$	$2 \times 8 / 2 \times 24$	$2 \times 8 / 2 \times 24$	$3 \times 6 / 3 \times 18$	$3 \times 6 / 3 \times 18$
	$N_{s1} \times d_{s1}$ [mm]	$536 \times 0.2$	$540 \times 0.2$	$540 \times 0.2$	$540 \times 0.2$
	$N_{s2} \times d_{s2}$ [mm]	$179 \times 0.2$	$180 \times 0.2$	$180 \times 0.2$	$180 \times 0.2$
	$h_w$ [mm]	102.6	112	79.8	88
Isolation	$d_{iso}$ [mm]	19	21.5	8.5	9.6
	$d_{cf}$ [mm]	4	4	2	2
	$d_{ins}$ [mm]	0.2	0.2	0.2	0.2
Losses	Core Losses [W]	112.9	119.7	109.5	116
	Winding Losses [W]	48	46.4	85.1	80.1
	Total Power Losses [W]	160.9	166.1	194.6	196.1
	Efficiency [%]	99.68	99.67	99.61	99.61
	Power Density [kW/l]	15.1	12.2	11.5	9.7
Design Constraints	Leakage Inductance, $L_\sigma$ [ $\mu H$ ]	29.5	29.1	38.4	37.6
	$B_{max}$ [T]	0.96	0.92	0.33	0.32
	$J_{max}$ [A/mm <sup>2</sup> ]	3	3	3	3

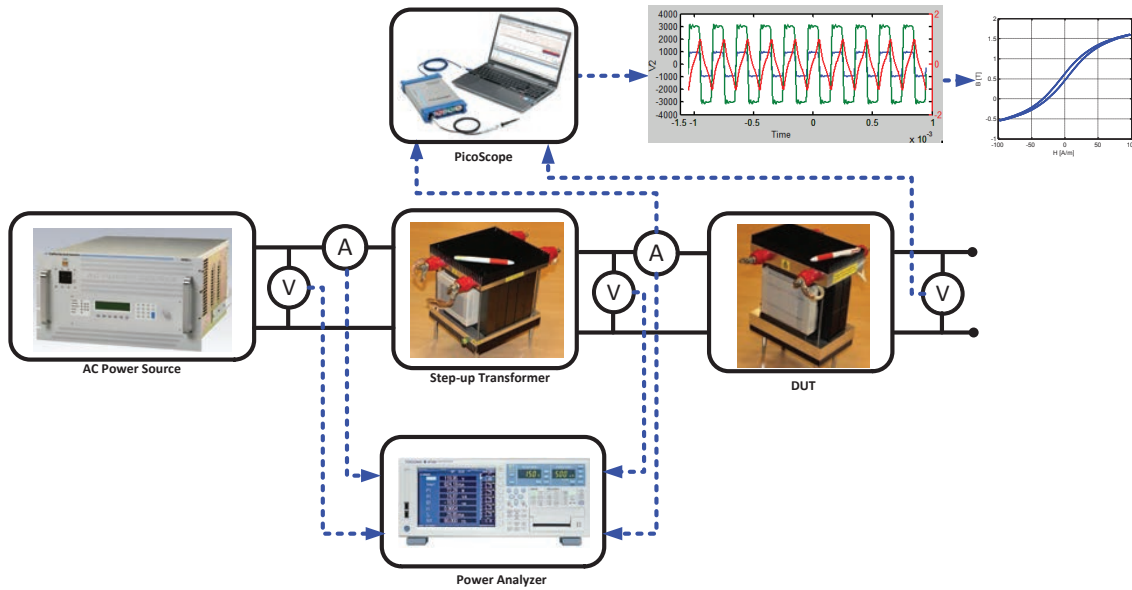


Figure 5.10: Core loss measurement setup.

After design and assembly of the prototypes, it is important to verify the design parameters and losses, e.g., efficiency, core losses, winding losses, leakage inductance and power density. Therefore, extensive experimental verifications have been carried out to measure the mentioned losses.

## 5.5 Experimental Verification

The prototypes were exposed to extensive open and short circuit measurements for core and winding loss evaluations, respectively. The total expected losses of the nanocrystalline-based transformer was 166.1 W with the expected efficiency of 99.67%. The measurement results indicated a power loss of 176.1 W with the corresponding efficiency of 99.66%. The ferrite-based transformer was expected to have the efficiency of 99.52% with 241.5 W power losses. The experimental results showed 99.48% efficiency with the total power losses of 259.8 W. In order to measure the core losses, the actual waveform of the transformer has been applied on the LV side of the prototype under the test while the HV side was open. The measured leakage inductance of the nanocrystalline-based transformer is  $29.9 \mu H$  which is only 3% higher than the intended design value, i.e,  $29 \mu H$ . In the case of ferrite-based transformer, the design target of the leakage inductance was  $38 \mu H$  while the measurement showed  $40 \mu H$  which is a 5% deviation from the initial target. The measurement results are further explained in the following sections.

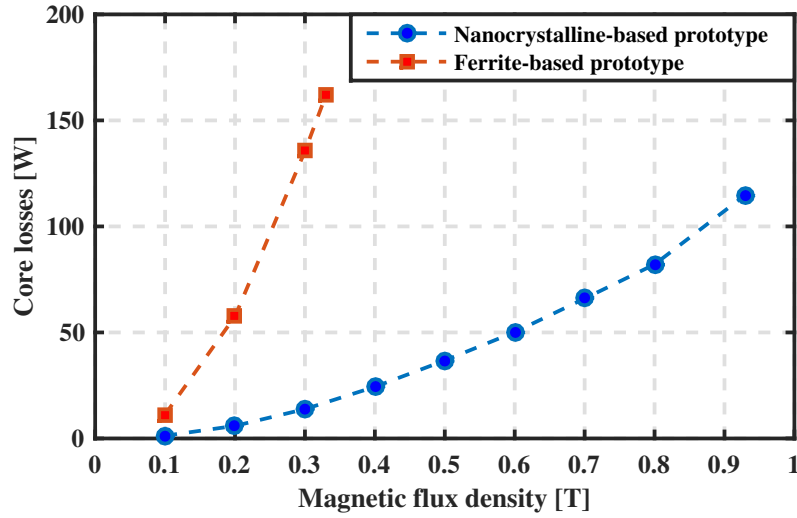


Figure 5.11: Measured core losses of the transformer prototypes at 5 kHz and 25°C.

### 5.5.1 Core Losses Verification

The two wire method is selected to measure the B-H loop and consequently the core losses of the transformer prototypes. The schematic of the measurement setup is illustrated in Fig. 5.10 in which one of the transformer prototypes is used as the step-up transformer for the transformer under the test, DUT, since the nominal excitation voltage of the designed prototypes, i.e., 1000 V, is higher than the maximum voltage of the utilized power supply. This method is known for its accuracy since the winding losses are excluded. Moreover, the method is known for its quickness compared to colorimetric measurement method [91, 113]. However, at very high frequencies, the phase discrepancy can potentially affect the measurement accuracy [127].

In this method, the LV side of the transformer under the test is excited with a square waveform at the nominal LV voltage while the HV side of the transformer is left with an open circuit. The current in the LV side represents the magnetic field intensity

$$H(t) = \frac{N_1 i_1(t)}{l_e} \quad (5.86)$$

where  $i_1(t)$  is the LV side instantaneous current measured with an Aim I-prober 520 and  $l_e$  is the mean magnetic path length of the core. The magnetic induction of the core,  $B(t)$ , is measured by integrating the HV side induced voltage,  $v_2(t)$ , as in

$$B(t) = \frac{1}{N_2 A_c k_c} \int_0^T v_2(t) dt \quad (5.87)$$

where  $A_c$  is the core cross-section and  $k_c$  is the magnetic core stacking factor. The

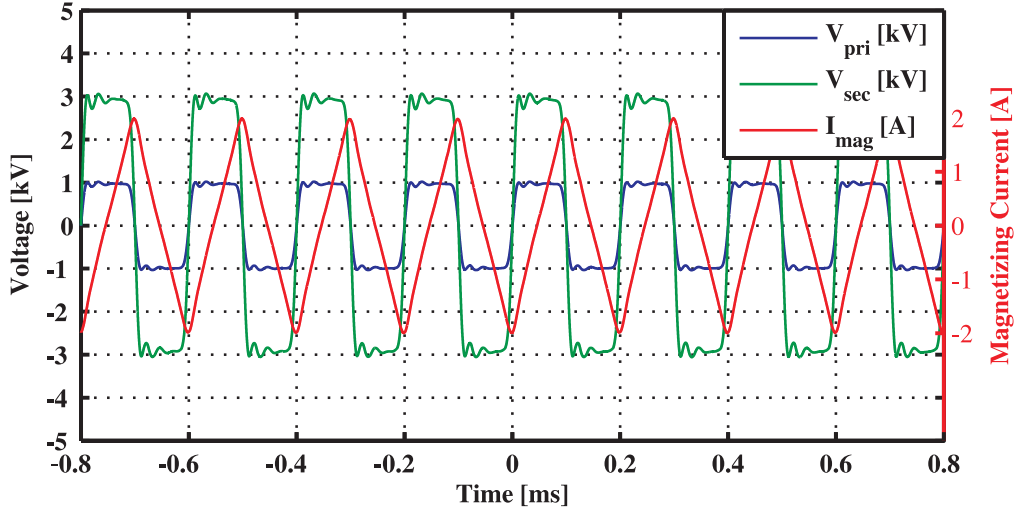


Figure 5.12: Open circuit voltages and current waveforms used for the core loss measurements at 5 kHz.

induced voltage,  $v_2(t)$ , is measured with a TESTEC high voltage differential probe. The square-waveform excitation voltage is applied on the LV side of the transformer by a California Instrument 4500LX AC power supply. This voltage is magnified by one of the prototype transformers to achieve 1 kV square-waveform at 5 kHz for the prototype under the test. The measured current and voltage are then saved with a PicoScope 6000 series and finally, the data are post-processed by MATLAB program to calculate the corresponding core losses.

Utilizing the above measurement setup, the core losses of the nanocrystalline-based transformer were measured as 114.9 W at 5 kHz and at 1 kV excitation level. This value reached to 171.4 W for the ferrite-based transformer at the same excitation level. These values can be seen in Fig. 5.11 in which the measured core losses of both transformer prototypes at different induction levels are illustrated. The measurements were performed at 5 kHz, room temperature of about  $25^\circ\text{C}$  and with different excitation voltages corresponding to different induction levels. As an example, the excitation voltage, the induced secondary voltage and the magnetizing current of the nanocrystalline-based transformer at 5 kHz, 0.93 T in open-circuit measurement are illustrated in Fig. 5.12.

Using the modified IGSE expression, introduced in Chapter 4, the expected core losses of the nanocrystalline-based and ferrite-based transformers at operating point are calculated as 119.7 W and 165.8 W, respectively.

It should be noted that all measurements were performed at  $25^\circ\text{C}$ , while the core temperature of the prototypes at steady-state are expected to be about  $85^\circ\text{C}$  at center-limbs and about  $70^\circ\text{C}$  on the side-limbs. According to the datasheet, the specific core losses of Vitroperm500 is almost temperature-independent and its

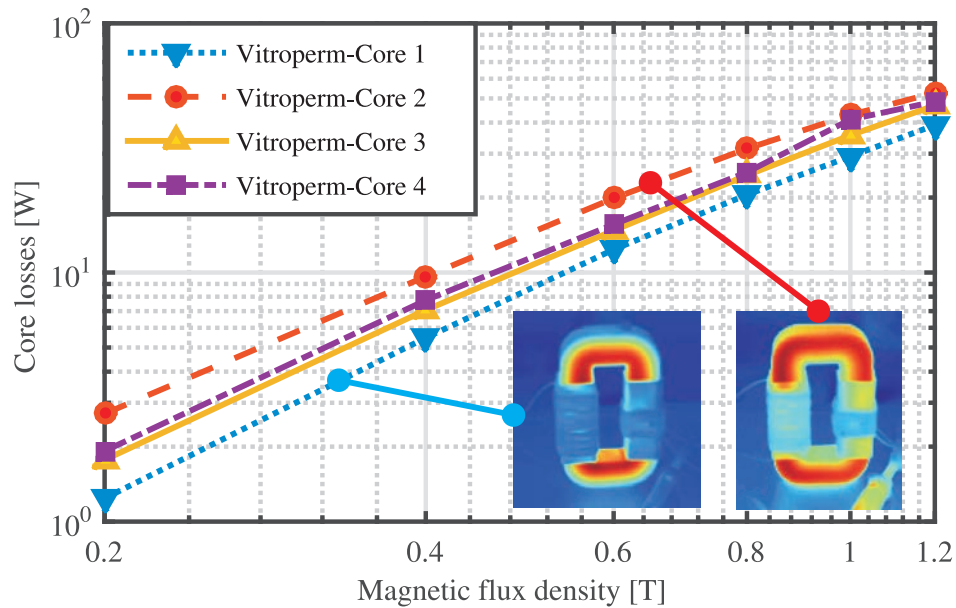


Figure 5.13: Measured P-B curves of Vitroperm500F cores, used to build the prototype, at 5 kHz and 25°C.

saturation flux density decreases by only few percent in the temperature range from  $-40^{\circ}\text{C}$  to  $150^{\circ}\text{C}$ . Whereas in ferrite cores, the saturation flux density and specific core losses can decline up to 40%, depending on the material type [99]. Therefore, the measured and calculated core losses of the ferrite-based transformer can be scaled down to, respectively, 119.9 W and 116 W based on the temperature profile in N87 ferrite datasheet [116].

#### 5.5.1.1 Cut-Core Effects

It should be noted that the calculated core losses, mentioned in the previous section, are based on the measured Steinmetz coefficients extracted from the P-B curves shown in Fig. 5.13. To measure the P-B curves of the Vitroperm500F cut-cores, each of the four core pairs were exposed to sinusoidal waveform at different frequencies and magnitudes. Fig. 5.13 illustrates the P-B curves of four cut-cores at 5 kHz. It is found that different nanocrystalline cut-cores demonstrate different magnetic characteristics, in particular there is about 40% difference in core losses between the best and the worst set of cut-cores used to build the transformer prototype. This discrepancy can be attributed to different surface qualities of the cut-cores, which probably caused by different machining during cutting and impregnation of the cores. This difference in surface quality can be clearly seen in thermal photos of two of the cut-cores shown in Fig. 5.13.

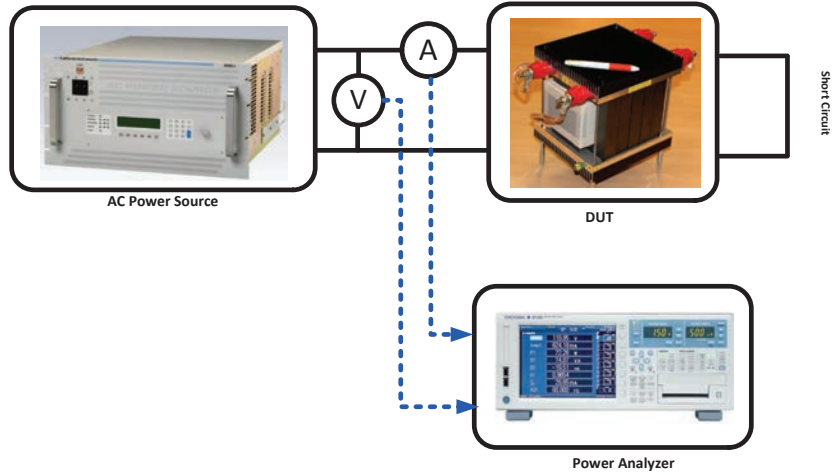


Figure 5.14: Windings loss measurement setup.

Although it seems almost impossible to model all the cut-core effects, it is important to consider the extra losses due to the cut-cores in practical design. Therefore, it was important to characterize the cut-cores separately.

## 5.5.2 Winding Losses Verification

In order to measure the copper losses, the LV-side of the prototypes are short-circuited while the HV-side is excited with the nominal current. In this way, the effect of the core is excluded, to a great extent, since the induction level is low. The measurement setup can be seen in Fig. 5.14 in which the transformer is excited by the California Instrument 4500LX AC power supply and the power losses is measured by a high-precision power analyzer, Yokogawa WT1800.

A RMS current of 15 A at 5 kHz applied on the HV-side of the prototype transformers and the power losses were measured by the power analyzer. Although the actual current comprises of different harmonics, the total windings losses can be evaluated by using the linearity of the system. Fig. 5.15 shows the HV-side current harmonics content of the nanocrystalline-based transformer which is calculated by the expression presented in (5.42). Using this approach, the total measured copper losses of the nanocrystalline-based transformer is evaluated as 54.4 W and 88.4 W for the nanocrystalline and ferrite-based transformers, respectively. The expected copper losses of the prototypes, presented in Table. 5.4, were calculated as 46.4 W and 80.1 W in the same order which are, respectively, 17% and 10% lower than the measured values. The difference between expected and measured results may be due to the un-transposed litz conductors on the LV-sides of the prototypes. This was because of the limited available rectangular litz conductors which made the author

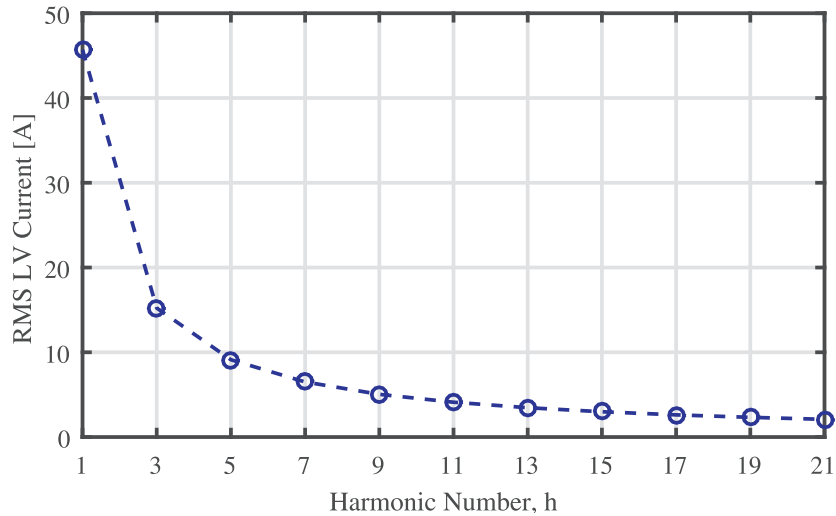


Figure 5.15: Current harmonics content at 5 kHz,  $L_{\sigma}=29.5 \mu H$  and  $\varphi=0.047$  rad.

to use three narrower litz conductor in parallel. This is obviously different from a standard litz conductor in which all the strands are transposed uniformly.

### 5.5.3 Leakage Inductance Verification

Using the network analyzer Bode 100, the impedance of the prototype transformers have been measured from the primary side while the secondary is shorted. The measurement setup is the same as the one shown in Fig. 3.7 in Chapter 3.

Fig. 5.16 demonstrates the measured leakage inductance of the prototype transformers up to 20 kHz. The measured leakage inductance of the nanocrystalline-based transformer at 5 kHz is  $29.9 \mu H$  which is only 3% higher than the intended design value, i.e,  $29 \mu H$ . In case of the ferrite-based transformer, the design target of the leakage inductance at 5 kHz was  $38 \mu H$  while the measurement shows  $40 \mu H$  which is a 5% deviation from the initial target.

It should be noted that shorting the secondary winding and measuring the inductance from the primary side gives the equivalent inductance referred to the primary side. This equivalent inductance comprises of both leakage inductance and magnetizing inductance of the transformer, however, magnetizing inductance is usually much larger than the leakage inductance and therefore it can be neglected in the circuit. However, measuring at frequencies below 10 Hz, this assumption is not valid, resulting in higher inductance as can be seen in Fig. 5.16.



Table 5.5: Measured characteristics of the prototypes versus the design targets.

Parameter	Nanocrystalline Design		Ferrite Design	
	Calculated	Measured	Calculated	Measured
Core Losses [W]	119.7	114.9	116	119.9
Winding Losses [W]	46.4	54.4	80.1	88.4
Leakage Inductance, $L_\sigma$ [ $\mu H$ ]	29.1	29.9	37.6	40
Total Power Losses [W]	166.1	169.3	196.1	208.3
Efficiency [%]	99.67	99.66	99.61	99.58

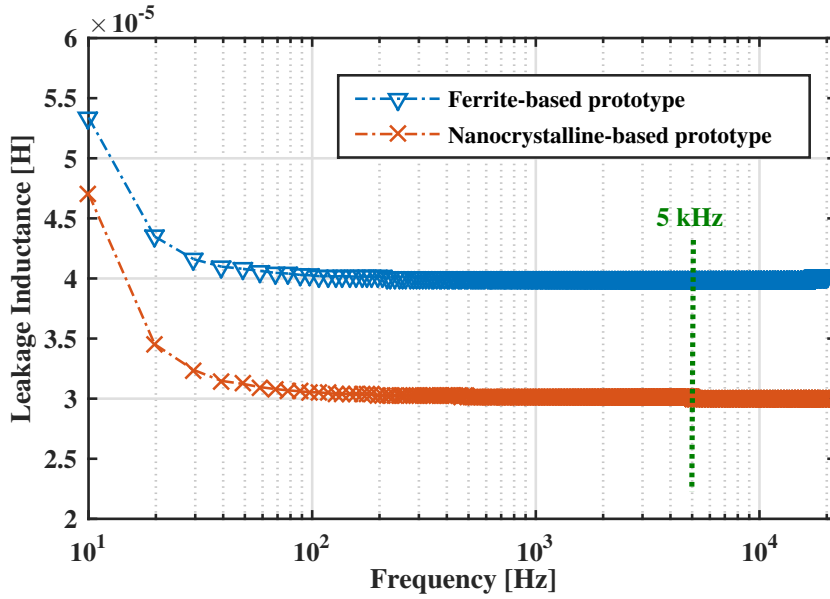


Figure 5.16: Measured leakage inductances of the prototypes.

## 5.6 Conclusions

This chapter presented a design and optimization method for medium-frequency transformers in SST applications. Tuned value of the leakage inductance, high isolation requirements, applicability of the square-type litz conductors and nanocrystalline magnetic material are different design aspects addressed in the proposed approach. Utilizing the proposed design method, two down-scaled prototype transformers have been design and manufactured. The nanocrystalline-based prototype reached an efficiency of 99.66%, whereas the ferrite-based transformer showed a measured efficiency of 99.58%, which are almost the same as the theoretically predicted one. Moreover, the targeted leakage inductance were proved to be carefully implemented in the transformer prototypes. The summary of the measured characteristics of the prototype transformers are tabulated in Table. 5.5.



## Chapter 6

# High-Power Isolated DC-DC Converter in All-DC Offshore Wind Farms

This chapter is based on the following articles:

- [I] Bahmani, M.A.; Thiringer, T.; Rabiei, A.; Abdulahovic, T., “Comparative Study of a Multi-MW High Power Density DC Transformer with an Optimized High Frequency Magnetics in All-DC Offshore Wind Farm” *To be Appeared in IEEE Transactions on Power Delivery*, 2016.
- [II] Bahmani, M.A.; Thiringer, T.; Kharezy, M., “Design methodology and optimization of a medium-frequency transformer for high power DC-DC applications,” *in Applied Power Electronics Conference and Exposition (APEC), 2015 IEEE*, pp.2532-2539, March 2015.

In this chapter, the design of a 1/30 kV, 10 MW modular isolated DC-DC converter is presented. The design and optimization of a medium-frequency transformer as the key part of such a converter is addressed. Efficiency curves for different semiconductor choices and frequencies are presented in order to find an optimum frequency enabling an adequate transformer volume reduction with a suitable compromise with the converter efficiency. It was found that for this voltage level and size, it is no point to go above 6 kHz from the transformer perspective since the isolation requirement leads to that the size is not reduced much more for even higher frequencies. At 5 kHz, the efficiency of the transformer having a nanocrystalline core reached 99.7% while the power density was about 22 kW/l. For the whole DC-DC converter, an efficiency of 98.5% was reached at 5 kHz switching frequency using SiC MOSFETs as switching elements while the efficiency when using IGBTs reached 97.2% at the same frequency.

## 6.1 Introduction

The power rating of future offshore wind parks is expected to reach a multi GW range which might require new installation of offshore wind parks far from the coast. These distances are today reaching such lengths that high voltage DC transmissions (HVDC) are starting to be used due to the AC cable transmission length limitations [27]. However, for these first cases with HVDC transmissions, the collection radials are still in AC causing higher power losses, particularly where the distance between the HVDC platform and turbines are likely to be increased. Accordingly, a qualified guess is that in the future, DC could be used here as well [29, 30].

This, among other factors, leads to an increasing attention towards all-DC offshore wind parks in which both the collection grid and transmission stage are DC based. Such a wind park topology, as shown in Fig. 6.1 (a), is based on high power isolated DC-DC converters, often referred to as the solid state transformer [12] or even the DC transformer [6]. Utilizing high frequency, Fig. 6.1 (c), the weight and volume of the medium-frequency transformer within such a converter becomes substantially smaller, which is a key advantage in any weight and volume restricted application, and definitely in an offshore application in which the wind turbine construction and installation cost will be reduced by utilizing the lower weight and volume of a medium-frequency transformer. Apart from the voltage adaptation, this transformer should account for the relatively high isolation level dictated by the wind-park voltage levels.

In order to obtain another voltage scalability factor for the high voltage DC voltage and more importantly, because of the power rating limitations of modern semiconductor devices, a modular concept enabling parallel connection on the input low voltage side and series connection on the high voltage side (PISO) as shown in Fig. 6.1 (b), will most likely be considered [31]. The benefit of using this concept is investigated in a recent contribution by Engel [32] in which the modular multilevel dc converter (M2DC) is compared with the modular concepts based on dual active bridge converters as the building blocks. There, it was shown that the M2DC is not suitable for high voltage ratios in HVDC and MVDC grids, mainly because of the circulating current and consequently lower efficiency compared to the modular DAB based converter. Moreover, M2DC converter requires a substantially higher number of semiconductors which are highly cost contributive elements in the total cost of the converter. It is worth to point out that the high/medium-frequency transformer of each single module must withstand the total voltage over the output series connected modules, MVDC voltage.

Lee in [128] provided a systematic comparison of high power semiconductor devices in a 5 MW PMSG wind turbine while Barrera-Cardenas in [129] and [130] presented, respectively, the efficiency comparison of two converter topologies based on the single phase transformer and a comparison of a single phase vs a three-phase high

Table 6.1: Design Specification of the Converter

Converter Power, $P_{tur}$	10 MW
Voltage level, $V_{LVDC}/V_{MVDC}$	1 kV / 30 kV
Number of modules,	15
Module output Power, $P_{out}$	666 kW
Module LV side voltage, $V_{LV}$	1 kV
Module HV side voltage, $V_{HV}$	2 kV
Module leakage inductance, $L_{\sigma}$	3.49 $\mu$ H
Transformer turn ratio, $n$	2
Isolation level, $V_{iso}$	60 kV
Switching frequency, $f$	5 kHz

frequency AC link. Moreover, Qin in [131] investigated the efficiency evaluation of four candidate solid-state transformer topologies addressing the medium-frequency transformer performance. Similar approaches have been reported in [132, 133] with more emphasis on all-DC offshore wind park concept. However, although considerable research has been devoted to the efficiency evaluation of different converter topologies with various semiconductor types and arrangements, rather less attention has been paid to the design and characterization of the medium-frequency transformer.

In the light of this scenario, it is necessary to incorporate the medium-frequency high power design and optimized methodology while investigating the energy efficiency of such a converter with different switching frequencies and semiconductor devices. Accordingly, the purpose of this chapter is to investigate the effect of higher switching frequencies for a 1/2 kV, 666 kW module of a 1/30 kV, 10 MW turbine-mounted converter with an appropriate medium-frequency transformer design and optimization methodology in which the high isolation requirements, desired leakage inductance, skin and proximity effect and extra magnetic core losses has been taken into consideration. Moreover an objective is to investigate the consequence of using SiC MOSFETs instead of ordinary IGBTs by using analytical expressions for switches and diode currents and voltages based on the ideal operating waveforms. In addition, a target is to find an optimum operating frequency in which the volume of the transformer is considerably reduced while the efficiency requirements are not violated.

## 6.2 Design and Optimization Approach

In order to perform a comparative study based on the optimized medium-frequency transformer design, three different types of losses should be evaluated: semiconductor conduction and switching losses as well as medium-frequency transformer losses comprising magnetic core losses, windings and dielectric losses. In contrast to most of the proposed design methodologies for medium-frequency transformers [19], the design and optimization methodology utilized in this chapter [73] stands for the incorporated leakage inductance of the transformer and its corresponding phase shift within the dual active bridge topology (DAB). Moreover, the isolation requirements introduced by the medium voltage DC link is considered as one of the design inputs in order to make this design suitable for high-power medium frequency off-shore dc-dc converters.

### 6.2.1 System Specifications

A 10 MW, 1/30 kV turbine based isolated DC-DC converter has been considered as a case study in this chapter. Similar to the configuration presented in Fig. 6.1 (b), this converter can be considered as 15 modules connected in parallel at the low voltage side (generator side) and in series at the high voltage side (MVDC link). The specification of each module are tabulated in Table. 6.1. For safety reasons, it is assumed that each module should withstand twice the total MVDC voltage of 30 kV. Accordingly, the isolation level of each module is considered to be 60 kV. The designated value of the leakage inductance ensures soft switching of the converter with a maximum 5% output voltage deviation.

### 6.2.2 Converter Topology

In contrast to medium power DC-DC converters (5 to 100 kW) which have been essentially investigated for automotive and traction applications, the megawatt and medium voltage range isolated converters with several kilohertz isolation stage are still in an expansive research phase, resulting in both resonant and non-resonant topologies being of interest.

In principle, there are mainly three types of converters which are suitable for high power applications. These converters are the series-resonant converter (SRC), dual-active bridge (DAB) and dual-half bridge (DHB) [134]. The limitations of the conventional full-bridge converters (FBC) at higher frequency and power levels resulted in the appearance of resonant type converters [135, 136]. One of the resonant converters which is most cited in literature for high power applications is the SRC converter which provides a comprehensive soft switching in the primary and secondary sides of the converter by utilizing a series resonant tank comprising of a capacitor in series with an inductor. However, the main drawback of this topology

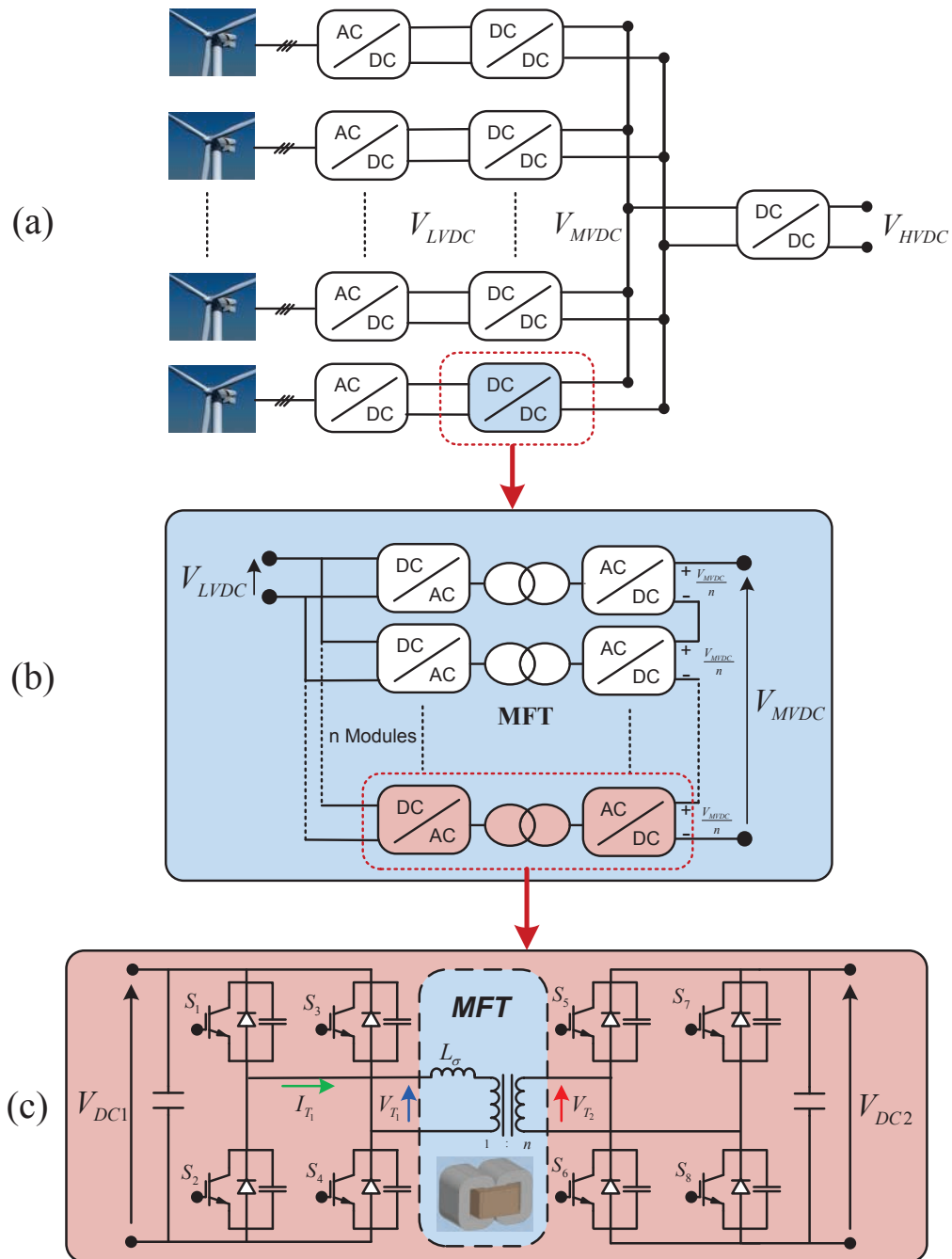


Figure 6.1: (a) Sample configuration of an all-DC offshore wind park with high power isolated DC-DC converter. (b) Parallel input, series output modular configuration of the isolated DAB DC-DC converter. (c) Schematic of a DAB converter.

is the need for a high voltage and high current resonant capacitor as well as a large resonant inductor [134].

Among non-resonant converters, the single active bridge (SAB) with phase-shift modulation can be one of the alternative topologies. The SAB is in fact the soft-switching enabled version of the classic non-resonant FBC converters in which ZVS can be achieved by means of a proper phase-shift modulation under certain conditions. Apart from the SAB, there has been a growing interest in utilizing DAB converters in high power applications, mainly because of the easy control capability and the relatively extended region of soft switching, zero-voltage switching (ZVS) at turn-on, without snubber circuits [2] compared with the single active bridge counterpart which has a smaller ZVS region as well as the disadvantage of hard switching in output diodes [137]. Both topologies can benefit from the integration of a resonant inductor into the medium-frequency transformer as leakage inductance. Accordingly, the desired value of the leakage inductance, which performs as the resonant inductor, can be considered as one of the design requirements of the medium-frequency transformer [122]. Therefore, the energy stored in the leakage inductance is interchanged with the snubber capacitors, resulting in soft-switching at turn-off and consequently achieving higher efficiencies. It should be noted that this chapter has been primarily concerned with the design and implementation of the medium-frequency transformer in high power applications. Therefore, the effects of snubber capacitors in switching loss reduction are neglected, thus, the total efficiencies calculated in this chapter can be further improved by implementing the proper snubber capacitors resonating with the leakage inductance of the medium-frequency transformer.

The simpler version of a DAB converter is the DHB converter which benefits from a lower number of devices, however it results in higher circulating reactive power and consequently higher current through the transformer compared to the one with the DAB topology. As a result, for the purpose of this chapter, the DAB converter with the standard phase shift modulation has been chosen as the main topology of the converter's building blocks.

### 6.2.2.1 DAB Operation

The equivalent circuit of a DAB converter is shown in Fig. 6.1 (c), in which two square voltage waveforms on the two sides of the medium-frequency transformer have been shifted by controlling the input and output bridges. This applies full voltage on the inductance,  $L$ , which is used to shape the current as a power transfer element. In order to achieve ZVS at turn on, the phase shift between the bridges,  $\phi$ , should be higher than a certain value resulting in the series inductance minimum value calculating as

$$L_{min} = \frac{V_{DC1}V_{DC2}\phi_{min}(\pi - \phi_{min})}{2P_{out}\pi^2 f_s n} \quad (6.1)$$



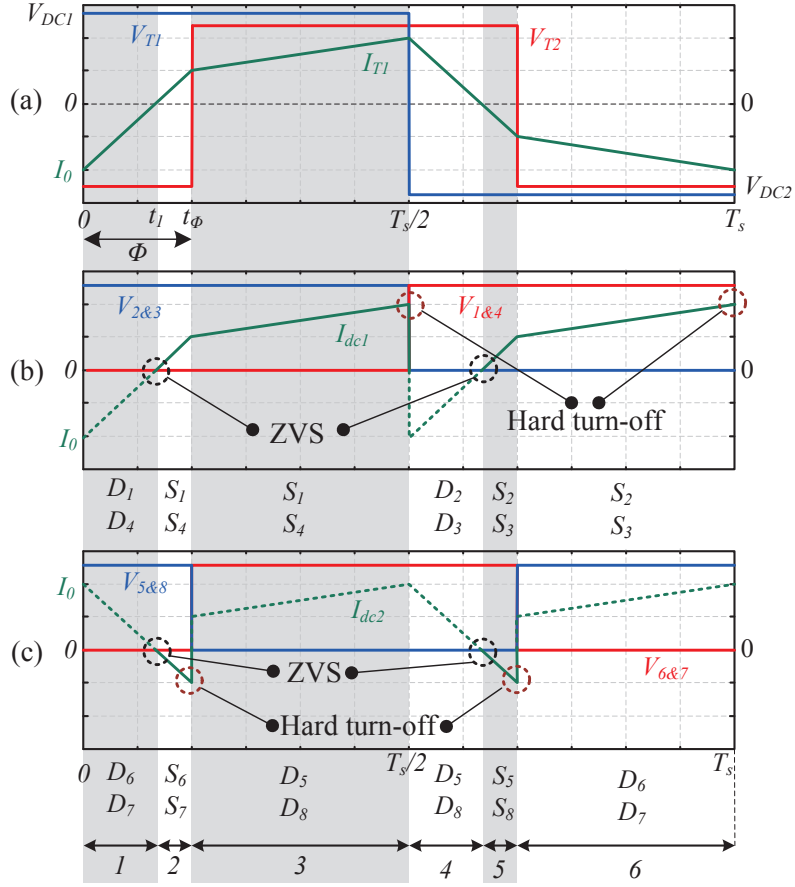


Figure 6.2: Steady state voltage and current waveforms of a DAB converter with simple phase shift modulation, (a) high/medium-frequency transformer. (b) Inverting side. (c) Rectifying side.

where  $V_{DC1}$  and  $V_{DC2}$  are the input and output DC voltages of each module shown in Fig. 6.1 (c), respectively;  $\phi_{min}$  is the minimum required phase shift between the primary and secondary voltage of the medium-frequency transformer highlighted as the key element of the DAB converter in Fig. 6.1 (c). The value of  $\phi_{min}$  can be calculated by

$$\begin{aligned} \phi &> \frac{\pi(d-1)}{2d} \quad \text{for } d > 1 \\ \phi &> \frac{\pi(1-d)}{2} \quad \text{for } d < 1 \end{aligned} \quad (6.2)$$

where  $d$  is the DC transformation ratio which can be considered for the worst case output voltage deviation, i.e, 5% for the purpose of this study.

This inductance, as shown in Fig. 6.1 (c), can be seen as an integrated leakage inductance,  $L_\sigma$ , in the medium-frequency transformer, so that the number and size of components can be reduced, hence achieving higher power densities [73]. It would thus be of great importance to accurately evaluate and implement the leakage inductance of such a transformer in the design stage since an insufficient leakage inductance leads to a shift in soft switching which can adversely affect the converter efficiency. Likewise, higher values of leakage inductance is not desired, because it causes an unnecessary reactive power circulation within the converter which eventually decreases the efficiency and output active power of the converter. Nevertheless, this can expand the soft-switching region to some extent.

The steady state transformer voltage and current waveforms of a DAB converter with simple phase shift modulation are shown in Fig. 6.2 (a). There are six distinct states of switches and diodes conduction as shown in Fig. 6.2 (b) and (c). It is worth to point out that in order to have soft switching at turn on, the anti-parallel diode of each switch should start conducting prior to the turn on moment of a transistor. This attribute is clearly demonstrated in Fig. 6.2 (b) and (c) when the voltage over each switch is zero prior to turn on, whereas the turn off process is not necessarily soft.

On the basis of constant input and output DC voltages, one can derive the analytical expression of the transformer current which linearly changes through the leakage inductance of the medium-frequency transformer. Between the time instance of zero and  $t_1$ , current zero crossing instance, the transformer current flowing through the diodes  $D_1$  and  $D_4$  can be written as

$$i(\theta) = i(0) + Z_1 \frac{\theta}{w} \quad (6.3)$$

where  $w$  is the angular frequency and  $Z_1$  is defined as

$$Z_1 = \frac{nV_{DC1} + V_{DC2}}{nL_\sigma} \quad (6.4)$$

At the time instance  $t_1$ , corresponding to the phase angle  $\phi_1$ , switches  $T_1$  and  $T_4$  turn on in ZVS since their anti-parallel diodes were conducting prior to the turn on instance. Until the time instant  $t_\phi$ , corresponding to the applied phase shift  $\phi$  between the bridges, the transformer current conducting through  $T_1$  and  $T_4$  is calculated as

$$i(\theta) = \frac{Z_1}{w} (\theta - \phi_1) \quad (6.5)$$

while from the time instance  $t_\phi$  until  $\frac{T_s}{2}$ , it can be calculated as

$$i(\theta) = i(\phi) + \frac{Z_2}{w} (\theta - \phi) \quad (6.6)$$

where

$$Z_2 = \frac{nV_{DC1} - V_{DC2}}{nL_\sigma} \quad (6.7)$$

These waveforms will later in this chapter be used as the excitation currents within the transformer design and optimization process as well as to identify the instantaneous current at turn-off in order to accurately calculate the switching losses. The average and RMS value of the currents through all switches, diodes and the medium-frequency transformer are the analytically calculated and used for power losses calculations in the design stage. The RMS value of the transformer current, transferred to the primary side, can be calculated by

$$I_{T1(rms)} = \frac{Z_1}{\omega} \sqrt{\frac{4\phi_1^2\phi + 2\pi\phi_1^2 - 4\phi^2\phi_1 - 2\pi\phi_1\phi + 2\pi\phi^2}{6\pi}} \quad (6.8)$$

where  $\phi_1$  can be calculated by

$$\phi_1 = \frac{\pi + 2\phi d - \pi d}{2(1 + d)}. \quad (6.9)$$

In order to analytically evaluate the conduction and switching losses of the converter module, the average and RMS current value flowing through each switch and diode needs to be defined. As a result, the average current values conducting through LV sides diodes and switches can be obtained, respectively, from

$$I_{D1,2,3,4(avg)} = \frac{-Z_1}{4\pi\omega} \phi^2 \quad (6.10)$$

$$I_{S1,2,3,4(avg)} = \frac{Z_1}{4\pi\omega} (\phi_1^2 - 2\phi_1\phi + \pi\phi_1). \quad (6.11)$$

Moreover, the RMS values of currents conducting through the LV diodes and switches can be respectively evaluated from

$$I_{D1,2,3,4(rms)} = \frac{Z_1\phi_1}{\omega} \sqrt{\frac{\phi_1}{6\pi}} \quad (6.12)$$

$$I_{S1,2,3,4(rms)} = \frac{Z_1}{\omega} \sqrt{\frac{\phi(\pi - 2\phi_1)(\phi - \phi_1) + \phi_1^2(\pi - \phi_1)}{6\pi}}. \quad (6.13)$$

Similarly, the HV side diodes and switches average current equations are derived as

$$I_{D5,6,7,8(avg)} = \frac{Z_1}{4\pi n\omega} (\phi_1^2 + \pi\phi - \phi^2) \quad (6.14)$$

$$I_{S5,6,7,8(avg)} = \frac{-Z_1}{4\pi n\omega} (\phi - \phi_1)^2. \quad (6.15)$$

Finally, the RMS current values of HV side diodes and switches are respectively obtained from

$$I_{D5,6,7,8(rms)} = \frac{Z_1}{n\omega} \sqrt{\frac{(\phi^2 + \phi_1^2)(\pi + \phi_1 - \phi) - \pi\phi\phi_1}{6\pi}} \quad (6.16)$$

$$I_{S5,6,7,8(rms)} = \frac{Z_1}{4n\pi\omega} (\phi - \phi_1) \sqrt{\frac{\phi - \phi_1}{6\pi}}. \quad (6.17)$$

### 6.2.3 Semiconductor losses

The semiconductor conduction losses is due to the forward voltage drop,  $V_F(t)$ , during the conducting period and can approximately be estimated by a constant voltage drop,  $V_{F0}$ , and a resistance,  $R_S$ , as

$$V_F(t) = V_{F0} + R_S I_S(t) \quad (6.18)$$

where  $V_{F0}$  and  $R_S$  depend on the forward characteristics of the switching semiconductor which can be found from the datasheets. Conduction power loss can therefore be calculated by integration of the voltage drop and the current over a period of current repetition as

$$P_{cond} = \int_{t_{on}} (V_F(t) I_S(t)) dt = V_{F0} I_{S(avg)} + R_S I_{S(rms)}^2. \quad (6.19)$$



When semiconductors turn on or off, there is a very short amount of time that both current and voltage are present over the semiconductor. It generates an energy loss every time the semiconductor turns on ( $E_{on}^*$ ) or turns off ( $E_{off}^*$ ). This energy depends on physical characteristics of the semiconductor and the surrounding circuit properties. It can be either obtained from the manufacture through datasheets (in case of IGBTs and some MOSFETs) or estimated using the dynamic physical characteristics of the semiconductor (certain MOSFETs). In either case, the switching energy is only valid under the condition the calculation or measurement is performed, i.e, the voltage across the switch,  $V_S^*$ , and current through the switch,  $I_S^*$ . However, the switching losses ( $E_{on}$  and  $E_{off}$ ) can be scaled for other voltages ( $V_S$ ) and currents ( $I_S$ ) as [138–140]

$$E_{on} = E_{on}^* \left(\frac{I_S}{I_S^*}\right)^{k_{I,on}} \left(\frac{V_S}{V_S^*}\right)^{k_{V,on}} \quad (6.20)$$

$$E_{off} = E_{off}^* \left(\frac{I_S}{I_S^*}\right)^{k_{I,off}} \left(\frac{V_S}{V_S^*}\right)^{k_{V,off}} \quad (6.21)$$

$$P_{switching} = f(E_{on} + E_{off}) \quad (6.22)$$

Table 6.2: Power Semiconductor Parameters.

Device	SiC MOSFET	IGBT
		
Manufacturer	CREE	Infineon
Code	CAS300M17BM2	FF225R17ME4
Blocking Voltage	1700V	1700V
$I_{C,nom}$	225A	225A
$V_{F0}[V]$	0	0.8
$R_S [m\Omega]$	16	7.7
$E_{on}^* [mJ]$	13	105
$E_{off}^* [mJ]$	10	103
$k_{I,on}$	0.63	0.9
$k_{I,off}$	1.46	0.81
$k_{V,on}$	1.83	N/A
$k_{V,off}$	1.17	N/A
Meas. cond( $T_j^*$ )	150°C	150°C
Meas. cond( $V_S^*, I_S^*$ )	900V, 300A	900V, 300A
Freewheeling diode	Built-in SiC	Built-in pn diode
$V_{F0}[V]$	0.7	0.8
$R_S [m\Omega]$	5.3	5.8
$E_{rec} [mJ]$	0	53

where the current and voltage coefficients ( $k_{I,on}$ ,  $k_{I,off}$ ,  $k_{V,on}$  and  $k_{V,off}$ ) can be obtained from the manufactures datasheets. These semiconductor and diodes parameters are tabulated in Table 6.2 for the semiconductors and diodes considered in this chapter. It should be noted that in case of using SiC MOSFET,  $I_{T1}$  has a slightly different path than the one shown in Fig. 6.2 (b) and (c) during the reverse current time period resulting in slightly lower conduction losses on the HV side.

### 6.3 Optimized Medium-Frequency Power Transformer

Taking the high power, high voltage and high-frequency effects into account, there are several challenges to be addressed since the design technology in this field is not mature enough yet. These challenges are basically related to the extra losses as a result of eddy current in the magnetic core, excess losses in the windings due to enhanced skin and proximity effects [17] and evaluation of parasitic elements. These extra losses together with the reduced size of the transformer lead to higher loss densities requiring a proper optimized design with a suitable thermal management scheme in order to dissipate the higher power losses from a smaller component.

### 6.3.1 Transformer Topology

Generally, there are four different single phase transformer construction concepts in high frequency applications, i.e., coaxial winding transformer (CWT) [141], core type, shell type, and matrix transformer [121]. The application of CWT concept is limited to high frequencies and low power ratings, due to their restriction in current carrying capabilities in the tubular structure [65]. The core type transformer consists of one magnetic core with two winding portions wound around the core limbs while the shell type consists of two magnetic cores connected in a way to make a three-limb transformer and the middle limb is wound by both the primary and secondary windings as depicted in Fig. 6.3. The last feasible topology is the Matrix transformer which in fact is the combination of shell and core type transformers and is based on several parallel magnetic cores with LV windings on the outer legs of the cores and one central HV winding around the middle legs [121].

The main advantage of the core type is the possibility of reducing the height of the transformer by making two parallel low voltage windings on each core limb [142]. However, due to the fact that the magnetic core in this topology is surrounded by the windings and due to the poor thermal conductivity of the insulation material within the windings, the magnetic core can suffer from the temperature increase, particularly at high voltage and low current applications. Therefore, the shell type transformer, in which the windings are surrounded by the magnetic core, seems to be a better option in high voltage low current applications since it has more core surfaces [121, 143]. The matrix type transformer presents both the advantages of the core and shell type transformers, because it is in fact a combined solution. However, it results in higher weight and volume since it consists of separated core units. Moreover, because of the separated primary and secondary windings, it is more difficult to tune the leakage inductance compared to the one in the other two topologies. For these reasons, the shell type topology has been selected to be used in this design and optimization process explained in this chapter. The author would like to point out that the proposed design and optimization approach is applicable on the other two topologies by defining new variables accounting for all the transformer dimensions. Unfortunately, this would probably results in bulkier transformer design compared to the shell type transformer used in this chapter.

### 6.3.2 Transformer Design

Fig. 6.3 shows the front view of the transformer geometry defining all the geometrical aspects which are used in the optimization process.

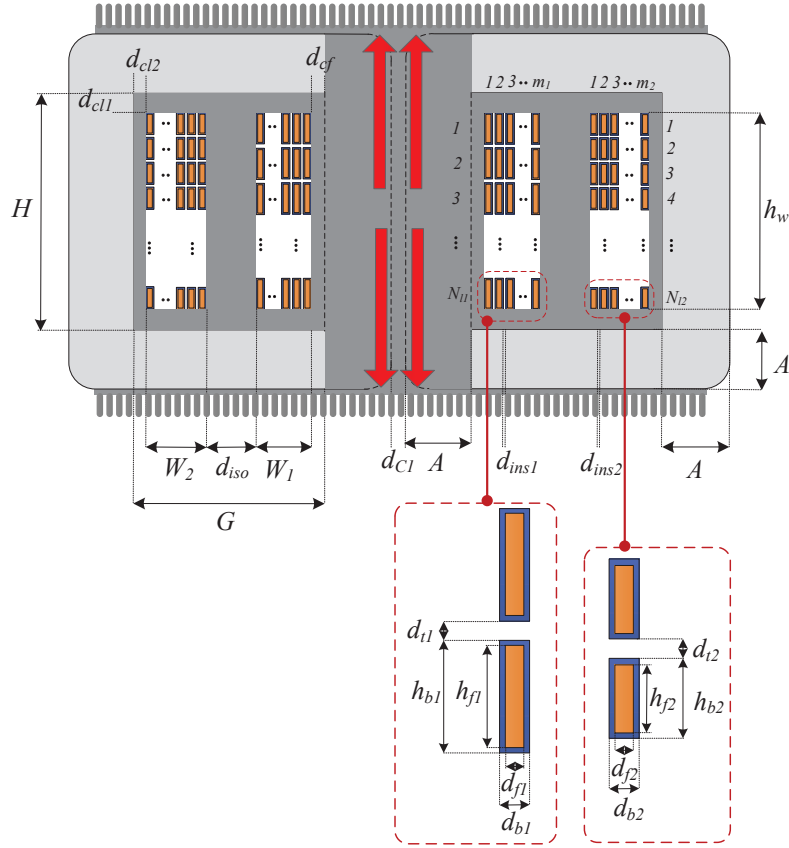


Figure 6.3: Frontal view of the proposed transformer geometry illustrating the thermally conductive polymer and heat sinks.

### 6.3.3 Geometry Construction with Foil Conductors

Having the fixed and free parameters, the transformer geometry can be defined as follows. First, the required magnetic core cross section is defined, as explained in Chapter 4, as

$$A_c = \frac{V_{rms1}}{k_f k_c N_1 B_m f} \quad (6.23)$$

where  $V_{rms}$  is the rms value of the primary voltage,  $k_c$  is the filling factor of the core,  $N_1$  is the number of primary turns,  $N_1 = m_1 N_{11}$ , and  $f$  is the fundamental frequency. The coefficient  $k_f$  is defined as

$$k_f = \frac{2\sqrt{2D - \frac{8}{3}R}}{D - R} \quad (6.24)$$

It should be noted that for the phase shift modulation in the DAB converter,

the value of  $D$  is considered as 0.5 and  $R$  equals to zero. Moreover, in order to avoid the core saturation due to unwanted magnetic flux density fluctuation, the maximum induction level,  $B_m$ , is considered as 80% of the saturation level of the selected magnetic core. Hence, considering the geometry structure shown in Fig. 6.3 and considering the number of core stacks,  $n_c$ , the lateral side of the magnetic core can be calculated as

$$B = \frac{A_c}{2n_c A} \quad (6.25)$$

where  $A$  is the frontal side length of each core stack. The required clearances can be calculated by

$$d_{cf} = \lceil \frac{V_{LVDC}}{k_{saf} E_{ins}} \rceil, \quad d_{cl1,2} = \lceil \frac{V_{MVDC}}{k_{saf} E_{ins}} \rceil, \quad d_{iso-min} = \lceil \frac{V_{iso}}{k_{saf} E_{ins}} \rceil \quad (6.26)$$

where, a safety factor of 30 %,  $k_{saf}$ , is considered for the dielectric strength of the isolating medium, resulting in  $d_{cf} = 1$  mm,  $d_{cl1,2} = 4$  mm and  $d_{iso-min} = 7$  mm which is the minimum allowed isolation distance between the primary and secondary windings in order to meet the isolation requirements of 60 kV. However, the actual value of  $d_{iso}$  will later be calculated with respect to the desired leakage inductance.

The copper foil heights of the primary and secondary windings are then calculated as

$$h_{b1} = 2d_{ins-int1} + \frac{I_{T1}}{d_{f1} J_{max}}, \quad h_{b2} = 2d_{ins-int2} + \frac{I_{T1}}{nd_{f2} J_{max}} \quad (6.27)$$

where  $I_{T1}$  is the function of the applied phase shift,  $\varphi$ , which is the minimum allowed value ensuring the soft switching and yet having a reasonable amount of reactive power circulation. Assuming a maximum voltage deviation of 5 % and using (6.2), the minimum value of  $\varphi$ , ensuring ZVS turn on, is 0.075 rad or 4.3 degree.

$$I_{T1} (rms) = \frac{nV_{DC1} + V_{DC2}}{nL_\sigma} \sqrt{\frac{4t_1^2 t_\varphi + T_s t_1^2 - 4t_\varphi^2 t_1 - T_s t_1 t_\varphi + T_s t_\varphi^2}{3T_s}} \quad (6.28)$$

where  $t_1$  and  $t_\varphi$  can be respectively calculated by

$$t_1 = \frac{\pi + 2\varphi d - \pi d}{4\pi f (1 + d)} \quad (6.29)$$

$$t_\varphi = \frac{\varphi}{2\pi f} \quad (6.30)$$

As a result, the winding height,  $h_w$ , the core window height,  $H$ , and the primary windings build are respectively calculated as



$$h_w = (N_{l1} + 1) h_{b1} + N_{l1} d_{t1} \quad (6.31)$$

$$W_1 = m_1 (d_{f1} + 2d_{ins-int1}) + (m_1 - 1) d_{ins1} \quad (6.32)$$

$$H = h_w + 2d_{cl} \quad (6.33)$$

Likewise, the number of turns and layers at the secondary windings are calculated by

$$N_{l2} = \left\lfloor \frac{h_w - h_{b2}}{h_{b2} + d_{t2}} \right\rfloor \quad (6.34)$$

$$m_2 = \left\lceil \frac{nm_1 N_{l1}}{N_{l2}} \right\rceil \quad (6.35)$$

Accordingly, the secondary winding build is calculated from

$$W_2 = m_2 (d_{f2} + 2d_{ins-int2}) + (m_2 - 1) d_{ins2} \quad (6.36)$$

Hence, the mean length turn of the primary windings,  $MLT_1$ , which will be later used for the windings loss calculation is calculated from

$$MLT_1 = 2(2A + d_{c1} + 4d_{cf} + n_c B + (n_c - 1) d_{c2} + 2W_1) \quad (6.37)$$

### 6.3.3.1 Isolation Distance

In order to be able to calculate the rest of the geometrical dimensions, i.e, the core window width, the total length and width of the transformer box and consequently the total volume of the box, the first parameter to be determined is the required isolation distance,  $d_{iso}$ , fulfilling the minimum isolation requirements as well as providing the desired leakage inductance ensuring the ZVS operation of the DC-DC converter.

For this purpose, the analytical expression in (3.16) derived in Chapter 3, accounting for the high-frequency effect on the leakage inductance value, is rearranged as

$$MLT_{iso} \cdot m_1 d_{iso} = \frac{h_w}{\mu m_1 N_{l1}^2} L_{\sigma 1} - k_1 - k_2 MLT_2 - k_3 - k_4 MLT_2 \quad (6.38)$$

where  $k_1$  to  $k_4$  are defined as

$$k_1 = MLT_1 \frac{(m_1 - 1)(2m_1 - 1)}{6} d_{ins1} \quad (6.39)$$

$$k_2 = \frac{m_1(m_2 - 1)(2m_2 - 1)}{6m_2} d_{ins2} \quad (6.40)$$

$$k_3 = MLL_1 \cdot \text{Im} \left( \frac{\sin(\frac{2\Delta_1}{\alpha\delta}) 4\alpha\delta^2(m_1^2 - 1) + 4d_{f1}(2m_1^2 + 1)}{24\sin^2(\frac{2\Delta_1}{\alpha\delta})} \right) \\ + MLL_1 \cdot \text{Im} \left( \frac{-\alpha\delta^2 \sin(\frac{4\Delta_1}{\alpha\delta})(2m_1^2 + 1) + 8d_{f1}(1 - m_1^2)\cos(\frac{2\Delta_1}{\alpha\delta})}{24\sin^2(\frac{2\Delta_1}{\alpha\delta})} \right) \quad (6.41)$$

$$k_4 = \text{Im} \left( \frac{m_1}{m_2} \frac{\sin(\frac{2\Delta_2}{\alpha\delta}) 4\alpha\delta^2(m_2^2 - 1) + 4d_{f2}(2m_2^2 + 1)}{24\sin^2(\frac{2\Delta_2}{\alpha\delta})} \right) \\ + \text{Im} \left( \frac{m_1}{m_2} \frac{-\alpha\delta^2 \sin(\frac{4\Delta_2}{\alpha\delta})(2m_2^2 + 1) + 8d_{f2}(1 - m_2^2)\cos(\frac{2\Delta_2}{\alpha\delta})}{24\sin^2(\frac{2\Delta_2}{\alpha\delta})} \right) \quad (6.42)$$

On the other hand,  $MLL_2$  and  $MLL_{iso}$  in (6.38) are functions of  $d_{iso}$ . Therefore, solving (6.38) for  $d_{iso}$  gives

$$d_{iso} = \frac{-8k_8 - k_5m_1 + \sqrt{(k_5m_1 + 8k_8)^2 - 16m_1(k_7k_8 - k_6)}}{8m_1} \quad (6.43)$$

where  $k_5$  to  $k_8$  are defined as

$$MLL_{iso} = 2(2A + d_{c1} + 4d_{cf} + 4W_1 + n_c B + (n_c - 1)d_{c2} + 2d_{iso}) \\ = k_5 + 4d_{iso} \quad (6.44)$$

$$k_6 = \frac{h_w}{\mu m_1 N_{l1}^2} L_{\sigma 1} - k_1 - k_3 \quad (6.45)$$

$$MLL_2 = 2(2A + d_{c1} + 4d_{cf} + 4W_1 + n_c B + (n_c - 1)d_{c2} + 2W_2 + 4d_{iso}) \\ = k_7 + 8d_{iso} \quad (6.46)$$

and

$$k_8 = k_2 + k_4 \quad (6.47)$$

Thus, the expression in (6.43) gives the required isolation distance providing the desired leakage inductance as one of the design specification. The obtained value of

$d_{iso}$  must withstand the isolation voltage level,  $V_{iso}$  as well. Otherwise the design is not acceptable and the next calculation with a new set of the free parameters is initiated.

Having  $V_{iso}$  determined, one can uniquely draw the transformer sketch, shown in Fig. 6.3, with all the geometrical details. Therefore, it is possible to utilize the loss evaluation methods, in order to calculate the power losses of each transformer corresponding to each set of free parameters.

### 6.3.3.2 Core Losses

In order to evaluate the core losses, the modified expression of the improved generalized Steinmetz equation (IGSE) adopted for non-sinusoidal waveforms has been used as

$$P_{core} = \left(2D - \frac{4\alpha}{\alpha + 1}R\right) \frac{2^\beta}{(D - R)^\alpha} k \cdot k_i f^\alpha B_m^\beta V_c \rho \quad (6.48)$$

where  $D$  and  $R$  are equal to 0.5 and 0 respectively for the standard phase shift DAB converter,  $k$ ,  $\alpha$  and  $\beta$  are the Steinmetz coefficients of the magnetic material which can be extracted from the manufacturer's datasheet,  $\rho$  is the core density and  $V_c$ , is the core volume corresponding to the dimensions illustrated in Fig. 6.3. Moreover, the coefficient,  $k_i$ , which is a function of  $\alpha$  and  $\beta$  can be calculated as [73]

$$k_i = \frac{1}{(2\pi)^{\alpha-1} \int_0^{2\pi} |\cos(\theta)|^\alpha 2^{\beta-\alpha} d\theta}. \quad (6.49)$$

In addition, the relation between the required core cross-section,  $A_c$ , and the maximum induction level,  $B_m$  is obtained from

$$B_m = \frac{V_{DC1}}{\frac{2\sqrt{2D - \frac{8}{3}R}}{D-R} k_c N_1 A_c f} \quad (6.50)$$

where  $k_c$  is the filling factor of the core,  $N_1$  is the number of transformer primary turns and  $f$  is the fundamental frequency [123].

### 6.3.3.3 Conductor Losses

To accurately evaluate the winding losses as an essential step in a high power density magnetic design, the pseudo-empirical method developed in [17] has been utilized. On the basis of the fact that copper has linear characteristics, the winding losses can be calculated using the harmonic contents of the applied current, thus

$$P_{w1} = \sum_{h=1}^n R_{DC1} R F_{1h} I_{1h}^2, \quad P_{w2} = \sum_{h=1}^n R_{DC2} R F_{2h} I_{2h}^2 \quad (6.51)$$

where  $R_{DC1}$  and  $R_{DC2}$  are the DC resistance of the primary and secondary windings portion,  $RF_{1h}$  and  $RF_{2h}$  are respectively the AC resistance factor of the primary and secondary windings portion at the  $h^{th}$  harmonic, as well as  $I_{1h}$  and  $I_{2h}$ , which are respectively the RMS value of the primary and secondary currents through the transformer windings for the  $h^{th}$  harmonic. It should be noted that the first 21 harmonics, above which the harmonic content is insignificant, have been considered in this chapter. Moreover, the transformer current contains only odd harmonics and all even harmonics are zero. The DC resistance of the primary and secondary windings portion are calculated from

$$R_{DC1} = \frac{m_1 N_{l1} MLL_1}{\sigma d_{f1} h_{f1}} \quad , \quad R_{DC2} = \frac{m_2 N_{l2} MLL_2}{\sigma d_{f2} h_{f2}} \quad (6.52)$$

where  $m_1$  and  $m_2$  are the number of primary and secondary turns, respectively.  $N_{l1}$  and  $N_{l2}$ , as shown in Fig. 6.3, are the number of turns per layer in the primary and secondary windings, respectively. In addition,  $\sigma$  is the conductivity of the conductors, here copper,  $MLL_1$  and  $MLL_2$  are mean length turn of the primary and secondary windings, respectively. Moreover,  $d_{f1,2}$  and  $h_{f1,2}$  are the width and height of the primary and secondary foil conductors used in this design and optimization process.

As shown in Fig. 6.2 (a), the transformer voltages and currents are not sinusoidal. Therefore, AC resistance factors,  $RF_{1h}$  and  $RF_{2h}$ , should be, separately for each harmonic content, calculated from the expression derived in [17] as

$$\begin{aligned} RF_h &= f(X_1, X_2, X_3, X_4, X_5) \\ &= \sum_{i=0}^5 \sum_{j \geq i}^5 \sum_{m \geq j}^5 \sum_{n \geq m}^5 \sum_{s \geq n}^5 \sum_{t \geq s}^5 P_{ijmnst} X_i X_j X_m X_n X_s X_t \\ &+ \sum_{m=1}^3 \sum_{i=0}^5 \sum_{j \geq i}^5 P_{ijm} X_i X_j e^{-(X_1 X_2)^m} + \sum_{i=1}^5 P_i \frac{X_4^2}{(X_1 X_2)^i} \end{aligned} \quad (6.53)$$

where  $X_1$  to  $X_5$  are five generic dimensionless parameters which can be used for a wide range of winding dimensions.

#### 6.3.3.4 Dielectric Losses

In low frequency applications, dielectric losses are often negligible, however when operating in higher frequencies, this type of loss are also important to be considered particularly in high power density applications where the design already is pushed to its limits. The dielectric losses are calculated from

$$P_{ins} = \Delta V_{ins}^2 2\pi f C_{ins} \tan(\delta) \quad (6.54)$$

in which  $\tan(\delta)$  is the dissipation factor of the dielectric material,  $C_{ins}$  and  $\Delta V_{ins}$  are respectively the capacitance of the dielectric medium and the voltage over it. It should be pointed out that for simplicity, the magnetic field within the isolation distance,  $d_{iso}$ , coil former distance,  $d_{cf}$ , as well as the clearing distances,  $d_{cl}$ , is considered to be uniform.

### 6.3.3.5 Thermal Management

The combination of two thermal management methods, shown in Fig. 6.3, are implemented in the current design approach. First of all, as in planar transformers, heat sinks are considered to be placed on the core surfaces in order to increase the effective surface area resulting in thermal resistance reduction and consequently higher power dissipation capability of the design. In addition, a complementary thermal management method has been incorporated placing a thermally conductive material between the primary windings and the core in order to directly conduct the heat to the top and bottom part of the transformer where heat sinks are assembled. As a result, with a negligible increase in transformer total volume, heat can be extracted from the hot spots deep inside the transformer. As shown in Fig. 6.3, in the current design methodology, a thermally conductive, electrically dielectric, polymeric material, which simultaneously can be considered both as the heat removal medium and an electrically isolating bobbin, coil former, is used.

In order to set one of the design boundaries, an estimation of the transformer temperature is needed to be implemented in the optimization process. Having the outer surface of the magnetic component determined, the maximum power dissipation capability of each transformer corresponding to each set of free parameters can be calculated from

$$\begin{aligned} P_{core} + P_{windings} + P_{ins} &= P_{conv} + P_{rad} \\ &= h_{conv}A_{conv}(T_s - T_a) + h_{rad}A_{rad}(T_s - T_a) \end{aligned} \quad (6.55)$$

where  $P_{conv}$  and  $P_{rad}$  are the heat transfer rates by convection and radiation heat transfer mechanisms, respectively.  $A_{conv}$  and  $A_{rad}$  are the convective and radiating area, respectively, and  $T_s$  and  $T_a$  are the temperature of the surface and ambient temperature, in the same order. Moreover,  $h_{rad}$  and  $h_{conv}$  are, respectively, the radiation and convection heat transfer coefficients [56].

### 6.3.4 Transformer Optimization Approach

Fig. 6.4 shows the design flowchart of a MFTPT based on foil conductor. Similar to Chapter 5, in order to obtain the optimum trade-off between the transformer efficiency and the power density, 7 different parameters, called free parameters, have

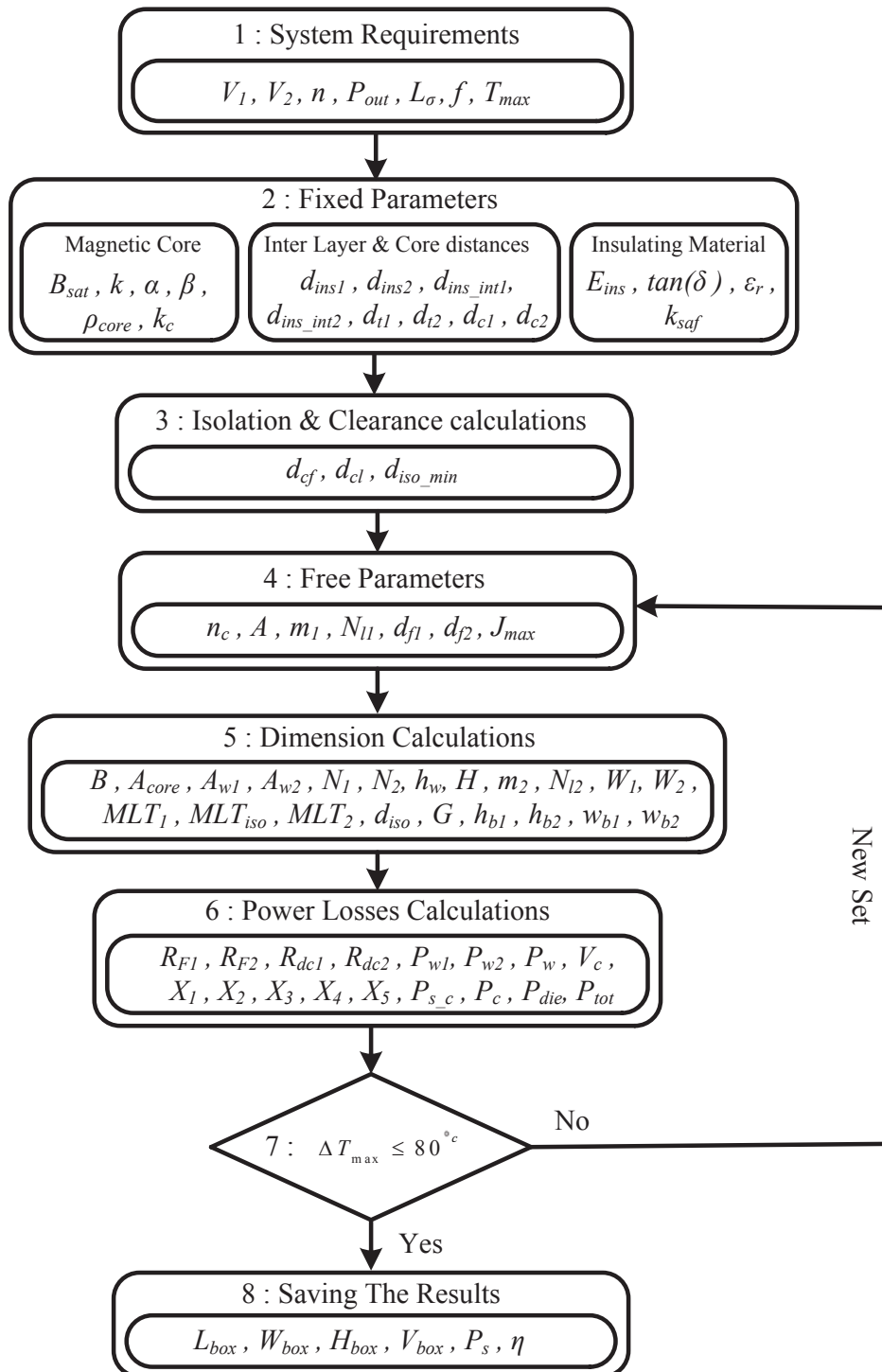


Figure 6.4: Design flowchart.

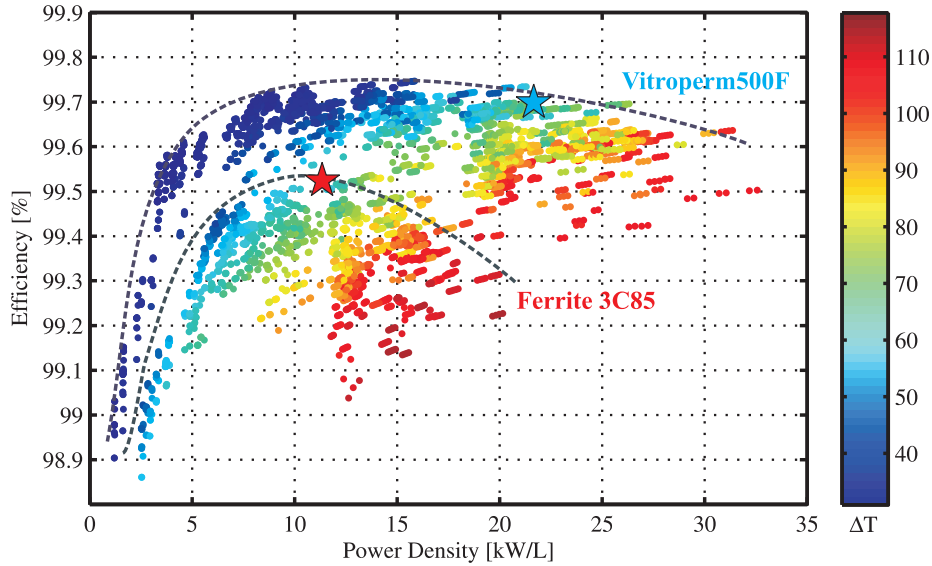


Figure 6.5: Efficiency versus Power density of feasible cases study transformers according to the proposed design methodology with two different core materials.

been designated to be swept over a wide range which can be conceivable for a power transformer. These free parameters are the number of the magnetic core stacks,  $n_c$ , the frontal side of the core cross section,  $A$ , the number of layers and the number of turns per layer in the primary windings portion,  $m_1$  and  $N_{l1}$ , the effective thickness of the primary and secondary copper foils,  $d_{f1}$  and  $d_{f2}$  and finally the maximum allowed RMS value of the current density through a conductor,  $J_{max}$ .

Once a set of the free parameters are established, one can determine all the geometrical dimensions of the transformer addressing the required distances to achieve the desirable leakage inductance, winding and core dimensions and other geometrical parameters shown in Fig. 6.3.

The next stage is the losses evaluation performed by utilizing the modified empirical methods and FEM derived analytical methods explained in this chapter. On the other hand the maximum heat dissipation capability of the transformer corresponding to each combination of free parameters are calculated in order to discard those combinations of free parameters which resulted in unacceptable power losses. Finally, the optimal set of free parameters resulting in the highest efficiency while meeting the loss dissipation, isolation and leakage inductance requirements are presented. These steps are described in details in [73].

Table 6.3: Optimal transformer characteristics for Vitroperm500F.

Volume	30.11 liter
Isolation distance, $d_{iso}$	38 mm
Winding losses	1427 W
Core losses	681 W
Dielectric losses	2.1 W
Total losses	2111.1 W
Efficiency	99.68%
Power density	22.11 kW/l

### 6.3.5 Optimization Results

The proposed design methodology explained in this chapter has been applied on the transformer specification shown in Table. 6.1. For this purpose, each free parameter is swept over a wide range of inputs resulting in more than 600000 combinations of the free parameters corresponding to 600000 unique transformers to be analyzed. The optimization outcome showing the efficiencies and power densities of the transformer designs corresponding to the accepted sets of free parameters illustrated in Fig. 6.5. Therefore, each colored dot represents a distinct transformer which met all the design requirements and its color indicates the corresponding temperature rise of that particular transformer.

The design procedure is performed using two different core materials, Vitroperm500F and 3C85, both suitable for high-frequency applications. As can be seen in Fig. 6.5, Vitroperm500F demonstrates higher efficiencies for the same power density which can be explained by the lower specific losses of Vitroperm500F compared to 3C85. Furthermore, Fig. 6.5 shows that Vitroperm500F can achieve substantially higher power densities of about 22  $kW/l$  with maximum 60°C temperature increase compared to the one of about 12  $kW/l$  for 3C85. This also can be explained by the relatively higher saturation level of Vitroperm500F compared to the one of 3C85.

It is worth to mention that the high isolation requirements of the transformer, 60 kV isolation for a 1/2 kV transformer, together with the desired leakage inductance as the design inputs, play an important role in determining the power density of the final optimum design. The geometrical and electrical characteristics of one of the optimized 666 kW transformer on the pareto-front of the Vitroperm500F in Fig. 6.5, highlighted by the blue star, are summarized in Table. 6.3.

As can be seen in Table. 6.3, using the design methodology proposed in this chapter, a 666 kW, 1/2 kV transformer operating at 5 kHz can be as compact as 30.11 liters while the efficiency is about 99.7% and the maximum temperature rise considering natural cooling is 60°C.



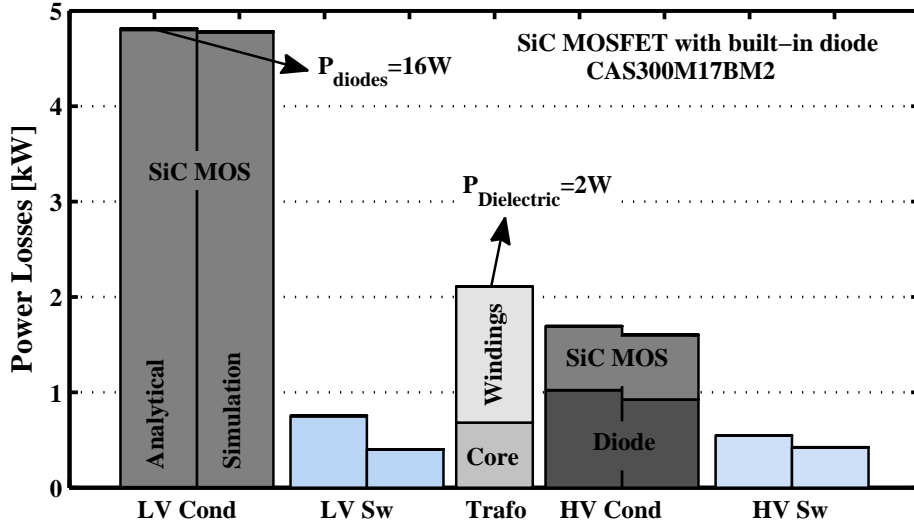


Figure 6.6: Converter power losses breakdown based on SiC MOSFET CAS300M17BM2 at 5 kHz according to the proposed transformer design methodology with  $\Delta T = 60^\circ\text{C}$ .

## 6.4 Losses Breakdown

Considering the introduced converter topology, the DC voltages of each module and the current rating, the 1700 V SiC MOSFET is considered to be used on the LV side in which three of those need to be placed in parallel in order to meet the current requirement of the LV side, whereas on the HV side of the converter, each switching device consists of 4 such MOSFETs, 2 in parallel and 2 in series in order to fulfill both current and voltage requirements. For the IGBTs case, the number of semiconductors on the LV and HV side is exactly the same as the case with SiC MOSFETs since both have the same voltage and current ratings. It should be noted that the HV side current is mainly conducted by the anti-parallel diodes, not the switches. This has already been illustrated in Fig. 6.2 in which the conduction period of each diode and switch is illustrated for IGBTs. Considering the medium-frequency transformer, the Vitroperm500F noncrystalline magnetic material is chosen because of higher power densities and lower losses resulting in a more compact design which is the main reason of increasing the frequency.

Based on the design methodology explained and performed in the previous sections, the theoretical loss breakdown of the converter, the diodes conduction losses, MOSFETs conduction losses, MOSFETs turn-off losses at the LV and HV sides as well as the optimized transformers windings, core and dielectric losses, are shown in Fig. 6.6. A total efficiency of about 98.56% at 5 kHz is achieved for a 666 kW DAB converter module at the specified voltage levels accounting for the optimized medium-frequency transformer as highlighted with a blue star in Fig. 6.5. As can be

seen in Fig. 6.6, the total switching losses on both LV and HV sides are about 12% of the total losses which can be justified considering the facts that the DAB converter enables ZVS at turn on as already shown in Fig. 6.2 (b) and (c), alongside with the relatively low turn off losses of the SiC MOSFETs used on the LV side. Despite ZVS at turn on, resulting in theoretically zero turn-on losses, turn-off of the DAB converter with standard phase shift modulation is mainly hard switched as already highlighted in Fig. 6.2 (b) and (c). Therefore, there is one hard turn-off per switch in each period that makes it inefficient to utilize the power IGBTs at this frequency, 5 kHz, and this power level. Compared to the theoretical calculations, the simulations yielded lower switching losses due to an ideal interpretation of switching events by PLECS, where the exponents, i.e.,  $k_{I,off}$  and  $k_{V,off}$ , are not used. In contrast to the switching losses, the conduction losses of the switches on the LV side and the diodes on the HV side contributes to the largest portion of the power losses, about 67%, of the converter. Moreover the optimized medium-frequency transformer stands for about 21% of the converter losses. These losses are essentially associated with the copper and core losses as well as an insignificant portion of the dielectric losses that can hardly be differentiated at the top of the transformer losses in Fig. 6.6. It should also be noted that the diodes reverse recovery losses are zero since, as already shown in Fig. 6.2 (b) and (c), the diodes turn off at ZVS condition.

## 6.5 Optimum Frequency

In order to investigate the effect of frequency on the possibility of transformer volume reduction while maintaining an acceptable total converter efficiency, the total power losses of the converter have been calculated at 20 different frequencies from 500 Hz until 10 kHz. To do that, all the steps explained in the previous sections were repeated for each frequency and the power losses and the optimized transformer volume, had to be recalculated. All the design requirements comprising the output power, voltage levels, isolation requirements, 60 kV, and the maximum temperature increase,  $70^{\circ}C$ , are kept constant whereas the frequency and consequently the required leakage inductance of the transformer reduces inversely by increasing the frequency as presented in (6.1). Each operating frequency requires a complete optimization process, investigating hundred of thousands of different transformer geometries. The optimum design at each frequency is then extracted and presented in Fig. 6.7, Fig. 6.8 and Fig. 6.9 together with the total efficiency of the converter.

Fig. 6.7 shows the total power losses of the converter at different frequencies, comprising of the conduction, switching and optimized medium-frequency transformer total power losses corresponding to the particular frequency. As can be seen in Fig. 6.7, the switching losses of the LV and HV sides increases at higher frequencies, whereas the conduction losses does not changes significantly. It should be noted that the lower switching losses are at the expense of substantially higher conduction

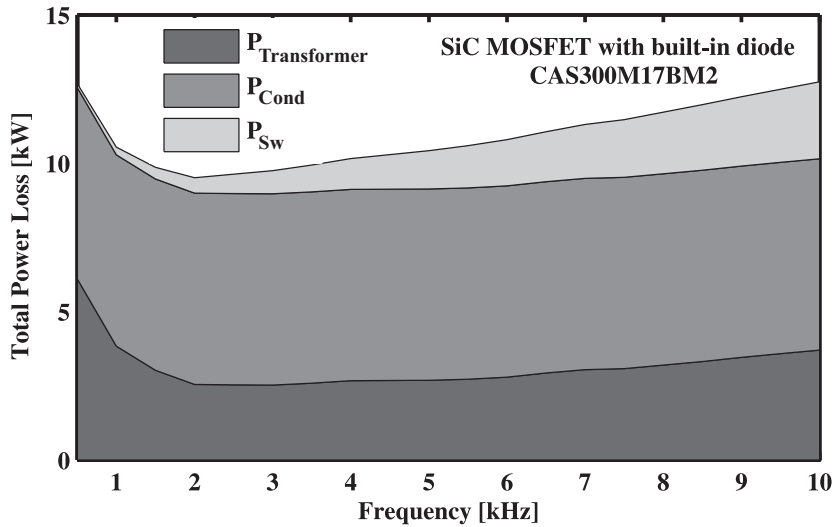


Figure 6.7: Converter power losses breakdown at different frequencies using SiC MOSFET CAS300M17BM2.

losses which are the dominant power losses using SiC MOSFETs.

On the basis of the power losses presented above, the efficiency of the SiC based converter module compared with the one using the IGBT FF225R17ME4 are shown in Fig. 6.8 in which the power density of the optimized medium-frequency transformer, as the heaviest and bulkiest part of the converter is also presented. As can be seen in Fig. 6.8, replacing the SiC MOSFETs with IGBTs, the converter efficiency substantially decreases by increasing the frequencies. This low efficiency, up to 95.7% at around 10 kHz, can be attributed to the relatively high turn-off losses of IGBTs. Moreover, the results indicate that there is an optimum frequency at which the transformer can nearly obtain its minimum dimensions and any further increase in frequency does not have a considerable effect on the transformer volume reduction, whereas the DAB converter suffers from the enhanced switching losses at those unnecessary high frequencies. This attribute is clearly demonstrated in Fig. 6.8 where the power density of the optimum design does not significantly increase after 6 kHz. In fact, increasing the frequency from 1 to 6 kHz results in a 50% reduction in transformer volume, while the efficiency only slightly decreases by about 0.04% in the SiC MOSFET based converter.

As shown in Fig. 6.9, up to 6 kHz, the portion of the optimum transformers made of magnetic core, windings and insulation distances continuously decrease, while the share of insulation material increases until it reaches to about 32% of the total volume of the optimum design at frequencies above 6 kHz, indicating the fact that there is a critical frequency above which the transformer does not benefit

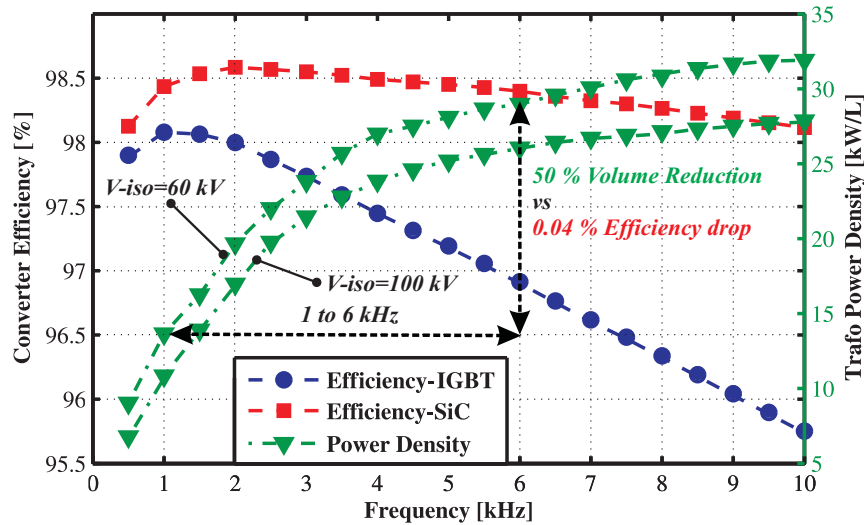


Figure 6.8: Efficiency comparison between the MOSFET and IGBT based converters versus power density of the optimized transformer, with  $70^{\circ}\text{C}$  temperature increase and two different isolation levels, within the investigated frequency range.

from volume reduction any further. This critical frequency is lower at high voltage applications where relatively high isolation requirement is needed. This can be seen in Fig. 6.8 in which the transformer with 100 kV isolation requirement does not benefit from the frequency increase beyond 4 kHz, whereas this frequency is about 6 kHz for the transformer with an isolation requirement of 60 kV. This can be explained by the fact that the transformer with higher isolation requirement requires more isolation distances. The total insulation volume, together with the whole transformer volume, decreases by increasing the frequency until it reaches to the minimum amount of insulation volume required to meet the isolation requirements.

## 6.6 Conclusion

A 666 kW module of a 10 MW, 1/30 kV DC-DC converter with an optimized medium-frequency transformer was investigated in this chapter. It was found that the efficiency of the transformer can reach 99.7 % using the noncrystalline core while the power densities can reach up to 22 kW/l. The power semiconductors used were both 1700 V Si IGBTs as well as 1700 V SiC MOSFETs. The total efficiency for the whole converter reached up to 98.6 and 98 % respectively for a 2 kHz switching frequency. When using very high switching frequencies, the size goes down as expected. An important finding was, however, that above a certain frequency, in this case 6 kHz, there is hardly any size reduction when increasing the frequency further, which is due to the isolation requirement. Moreover, at 5

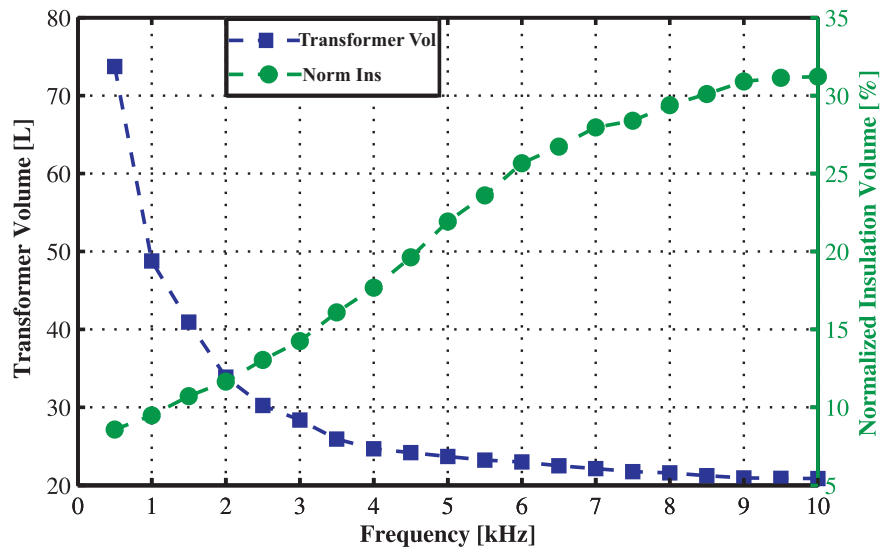


Figure 6.9: Transformer volume and normalized insulation volume.

kHz, where the transformer reached almost to its minimum volume, the efficiency when using SiC MOSFETs is still high, 98.5 %, while the IGBT solution lead to an efficiency of 97.2 %.



# Chapter 7

## Conclusions and Future Work

### 7.1 Conclusions

This work proposed a design and optimization methodology of a medium-frequency power transformer accounting for a tuned leakage inductance of the transformer, core and windings losses mitigation, thermal management by means of a thermally conductive polymeric material as well as high isolation requirements. An analytical expression to accurately calculate leakage inductance, particularly at higher frequencies was derived. The expression takes into account the effects of high frequency fields inside the conductors as well as the geometrical parameters of the transformer windings. This expression is validated using FEM simulations as well as measurements. In addition, a regressive-derived expression has been proposed to more accurately calculate the AC resistance factor of foil and round type conductors in switch-mode magnetics. The validity and usage of the expression is experimentally validated. Moreover, extensive validity investigations were performed on the conventional models comprising of theoretical investigations, simulations and measurements.

Utilizing the proposed design method, two down-scaled prototype transformers, 50 kW / 5 kHz, have been designed and manufactured. The prototypes are exposed to extensive measurements for core and winding loss evaluations. The nanocrystalline-based prototype reached an efficiency of 99.66%, whereas the ferrite-based transformer showed a measured efficiency of 99.58%, which are almost the same values as the theoretically predicted ones. The prototypes reached a power density of 12.2 and 9.7 kW/liter, respectively. Moreover, the targeted value of prototype's leakage inductances were achieved through the proposed design method and were validated by measurements.

Finally, using SiC MOSFETs and based on the contribution above, the efficiency and power density of a 1 / 30 kV, 10 MW turbine-mounted DC-DC converter with medium-frequency transformer are quantified. It was found that, with respect to

the isolation requirements, there is a critical operating frequency above which the transformer does not benefit from further volume reduction, due to an increased frequency.

## 7.2 Future Work

In principle, a comprehensive evaluation of a high-power isolated DC-DC converter design is a complex task in which both the power electronic topology and the magnetic stage should be optimized simultaneously. In this work, the system requirements such as the converter topology, modulation and the number of modules in a PISO configuration were considered as pre-determined. However, considering the proposed method as a basis, optimization from a higher level can be an interesting future study.

During the core-loss measurements, it was found that different nanocrystalline cut-cores demonstrate different magnetic characteristics. This discrepancy can be attributed to different surface qualities of the cut-cores, which probably caused by different machining during cutting and impregnation of the cores. Therefore, further investigation is required to quantify the effects of this phenomenon on the overall design of the transformers, as well as to identify the origin of this phenomenon.

Parasitic capacitances, i.e. between winding turns, winding layers, winding sections as well as the stray capacitances, are important design aspects in an MFT. These parasitic capacitances can become large, so that resonances, with leakage and magnetizing inductances, occur that could lead to excessive voltage spikes which eventually stress the insulation systems. Therefore, further investigations accounting for more accurate evaluation of parasitic capacitances are required.

One important future work is to identify a proper insulation system which can handle the medium-frequency high voltage high-rise time waveforms during the full life length of the unit. This requires an extensive research on different insulation materials at different operating conditions.

Further developments can be done by implementing a more detailed thermal analysis accounting for different thermal managements such as forced cooling, oil-immersed transformer and other heat-dissipation solutions.

When measuring the losses in the transformer prototypes and specifically when characterizing the core-materials at 1 to 5 kHz, it was observed that the noise level of the MFT at this range of frequency can be problematic, specially for SSTs in future smart grids. This, together with the reliability-related issues of SSTs, in particular MFT, are among the main challenges to be faced in order to further promote the SST technology as an enabling technology for the future.



# Bibliography

- [1] G. Ortiz, J. Biela, D. Bortis, and J. Kolar, "1 megawatt, 20 khz, isolated, bidirectional 12kv to 1.2kv dc-dc converter for renewable energy applications," in *Power Electronics Conference (IPEC), 2010 International*, june 2010, pp. 3212 –3219.
- [2] R. De Doncker, D. Divan, and M. Kheraluwala, "A three-phase soft-switched high-power-density dc/dc converter for high-power applications," *IEEE Trans. Ind. Appl.*, vol. 27, no. 1, pp. 63–73, 1991.
- [3] D. Dujic, F. Kieferndorf, F. Canales, and U. Drofenik, "Power electronic traction transformer technology," in *Power Electronics and Motion Control Conference (IPEMC), 2012 7th International*, vol. 1, june 2012, pp. 636 –642.
- [4] T. Kjellqvist, S. Norrga, and S. Ostlund, "Design considerations for a medium frequency transformer in a line side power conversion system," in *Power Electronics Specialists Conference, 2004. PESC 04. 2004 IEEE 35th Annual*, vol. 1, june 2004, pp. 704 – 710 Vol.1.
- [5] S. Inoue and H. Akagi, "A bidirectional isolated dc ndash;dc converter as a core circuit of the next-generation medium-voltage power conversion system," *IEEE Trans. Power Electron.*, vol. 22, no. 2, pp. 535–542, March 2007.
- [6] D. Jovcic, "Bidirectional, high-power dc transformer," *IEEE Trans. Power Del.*, vol. 24, no. 4, pp. 2276–2283, Oct 2009.
- [7] L. Heinemann, "An actively cooled high power, high frequency transformer with high insulation capability," in *Applied Power Electronics Conference and Exposition, 2002. APEC 2002. Seventeenth Annual IEEE*, vol. 1, 2002, pp. 352–357 vol.1.
- [8] D. Aggeler, J. Biela, S. Inoue, H. Akagi, and J. Kolar, "Bi-directional isolated dc-dc converter for next-generation power distribution - comparison of converters using si and sic devices," in *Power Conversion Conference - Nagoya, 2007. PCC '07*, April 2007, pp. 510–517.

- [9] K. Mainali, S. Madhusoodhanan, A. Tripathi, D. Patel, and S. Bhattacharya, "Start-up scheme for solid state transformers connected to medium voltage grids," in *Applied Power Electronics Conference and Exposition (APEC), 2015 IEEE*, March 2015, pp. 1014–1021.
- [10] X. She and A. Huang, "Solid state transformer in the future smart electrical system," in *Power and Energy Society General Meeting (PES), 2013 IEEE*, July 2013, pp. 1–5.
- [11] M. Bahmani, T. Thiringer, A. Rabiei, and T. Abdulahovic, "Comparative study of a multi-mw high power density dc transformer with an optimized high frequency magnetics in all-dc offshore wind farm," *IEEE Trans. Power Del.*, vol. PP, no. 99, pp. 1–1, 2015.
- [12] X. She, A. Huang, and R. Burgos, "Review of solid-state transformer technologies and their application in power distribution systems," *Emerging and Selected Topics in Power Electronics, IEEE Journal of*, vol. 1, no. 3, pp. 186–198, Sept 2013.
- [13] J. Wang, T. Zhao, J. Li, A. Huang, R. Callanan, F. Husna, and A. Agarwal, "Characterization, modeling, and application of 10-kv sic mosfet," *IEEE Trans. Electron Devices*, vol. 55, no. 8, pp. 1798–1806, Aug 2008.
- [14] Z. Chen, D. Boroyevich, R. Burgos, and F. Wang, "Characterization and modeling of 1.2 kv, 20 a sic mosfets," in *Energy Conversion Congress and Exposition, 2009. ECCE 2009. IEEE*, Sept 2009, pp. 1480–1487.
- [15] K. Vechalapu, A. Kadavelugu, and S. Bhattacharya, "High voltage dual active bridge with series connected high voltage silicon carbide (sic) devices," in *Energy Conversion Congress and Exposition (ECCE), 2014 IEEE*, Sept 2014, pp. 2057–2064.
- [16] [Online]. Available: <http://www.cree.com/>
- [17] A. Bahmani, T. Thiringer, and H. Jimenez, "An accurate pseudo-empirical model of winding loss calculation for hf foil and round conductors in switch-mode magnetics," *IEEE Trans. Power Electron.*, vol. PP, no. 99, pp. 1–1, 2013.
- [18] R. T. Naayagi, A. Forsyth, and R. Shuttleworth, "High-power bidirectional dc-dc converter for aerospace applications," *IEEE Trans. Power Electron.*, vol. 27, no. 11, pp. 4366–4379, 2012.
- [19] W. Colonel and K. T. McLyman, *Transformer and Inductor Design Handbook, Fourth Edition*. CRC Press, 2011.

- [20] S. Farhangi and A. Akmal, "A simple and efficient optimization routine for design of high frequency power transformers," in *Proceeding of 9th EPE Conference*, Sep 1999.
- [21] R. Petkov, "Optimum design of a high-power, high-frequency transformer," *IEEE Trans. Power Electron.*, vol. 11, no. 1, pp. 33–42, Jan 1996.
- [22] W. Hurley, W. Wolfle, and J. Breslin, "Optimized transformer design: inclusive of high-frequency effects," *IEEE Trans. Power Electron.*, vol. 13, no. 4, pp. 651–659, Jul 1998.
- [23] S. Meier, T. Kjellqvist, S. Norrga, and H.-P. Nee, "Design considerations for medium-frequency power transformers in offshore wind farms," in *Power Electronics and Applications, 2009. EPE '09. 13th European Conference on*, Sept 2009, pp. 1–12.
- [24] I. Villar, L. Mir, I. Etxeberria-Otadui, J. Colmenero, X. Agirre, and T. Nieva, "Optimal design and experimental validation of a medium-frequency 400kva power transformer for railway traction applications," in *Energy Conversion Congress and Exposition (ECCE), 2012 IEEE*, Sept 2012, pp. 684–690.
- [25] G. Ortiz, M. Leibl, J. Kolar, and O. Apeldoorn, "Medium frequency transformers for solid-state-transformer applications ; design and experimental verification," in *Power Electronics and Drive Systems (PEDS), 2013 IEEE 10th International Conference on*, April 2013, pp. 1285–1290.
- [26] G. Ortiz, "High-power dc-dc converter technologies for smart grid and traction applications," Ph.D. dissertation, ETH ZURICH, 2014.
- [27] A. Nami, J. Liang, F. Dijkhuizen, and G. Demetriades, "Modular multilevel converters for hvdc applications: Review on converter cells and functionalities," *IEEE Trans. Power Electron.*, vol. 30, no. 1, pp. 18–36, Jan 2015.
- [28] R. U. Lenke, "A Contribution to the Design of Isolated DC-DC Converters for Utility Applications," Ph.D. dissertation, RWTH Aachen University.
- [29] N. Holtsmark, H. Bahirat, M. Molinas, B. Mork, and H. Hoidalén, "An all-dc offshore wind farm with series-connected turbines: An alternative to the classical parallel ac model?" *IEEE Trans. Ind. Electron.*, vol. 60, no. 6, pp. 2420–2428, June 2013.
- [30] N. Flourentzou, V. Agelidis, and G. Demetriades, "Vsc-based hvdc power transmission systems: An overview," *IEEE Trans. Power Electron.*, vol. 24, no. 3, pp. 592–602, March 2009.

- [31] C. Meyer, “Key components for future offshore dc grids,” Ph.D. dissertation, RWTH Aachen University, Germany, 2007.
- [32] S. Engel, M. Stieneker, N. Soltau, S. Rabiee, H. Stagge, and R. De Doncker, “Comparison of the modular multilevel dc converter and the dual-active bridge converter for power conversion in hvdc and mvdc grids,” *IEEE Trans. Power Electron.*, vol. 30, no. 1, pp. 124–137, Jan 2015.
- [33] M. Steiner and H. Reinold, “Medium frequency topology in railway applications,” in *Power Electronics and Applications, 2007 European Conference on*, Sept 2007, pp. 1–10.
- [34] C. Zhao, D. Dujic, A. Mester, J. Steinke, M. Weiss, S. Lewdeni-Schmid, T. Chaudhuri, and P. Stefanutti, “Power electronic traction transformer x2014;medium voltage prototype,” *IEEE Trans. Ind. Electron.*, vol. 61, no. 7, pp. 3257–3268, July 2014.
- [35] [Online]. Available: <http://www.abb.com/>
- [36] H. De Keulenaer, D. Chapman, and S. Fassbinder, “The scope for energy saving in the eu through the use of energy-efficient electricity distribution transformers,” in *16th International Conference and Exhibition on Electricity Distribution*, 2001, p. 5.
- [37] J. Pedro, B. A., and S. N., *Electromagnetic modeling by finite element methods*. Markel Dekker, 2003.
- [38] E. Bennett and S. C. Larson, “Effective resistance to alternating currents of multilayer windings,” *Transactions of the American Institute of Electrical Engineers*, vol. 59, no. 12, pp. 1010–1017, dec. 1940.
- [39] P. Dowell, “Effects of eddy currents in transformer windings,” *Electrical Engineers, Proceedings of the Institution of*, vol. 113, no. 8, pp. 1387–1394, august 1966.
- [40] A. Reatti and M. Kazimierczuk, “Comparison of various methods for calculating the ac resistance of inductors,” *IEEE Trans. Magnet.*, vol. 38, no. 3, pp. 1512–1518, may 2002.
- [41] F. Robert, P. Mathys, and J.-P. Schauwers, “Ohmic losses calculation in smps transformers: numerical study of dowell’s approach accuracy,” *IEEE Trans. Magnet.*, vol. 34, no. 4, pp. 1255–1257, jul 1998.
- [42] F. Robert, P. Mathys, B. Velaerts, and J.-P. Schauwers, “Two-dimensional analysis of the edge effect field and losses in high-frequency transformer foils,” *IEEE Trans. Magnet.*, vol. 41, no. 8, pp. 2377–2383, aug. 2005.

- [43] A. Lotfi and F. Lee, "Two dimensional field solutions for high frequency transformer windings," in *Power Electronics Specialists Conference, 1993. PESC '93 Record., 24th Annual IEEE*, jun 1993, pp. 1098 –1104.
- [44] —, "Two-dimensional skin effect in power foils for high-frequency applications," *IEEE Trans. Magnet.*, vol. 31, no. 2, pp. 1003 –1006, march 1995.
- [45] G. Dimitrakakis and E. Tatakis, "High-frequency copper losses in magnetic components with layered windings," *IEEE Trans. Magnet.*, vol. 45, no. 8, pp. 3187 –3199, aug. 2009.
- [46] U. Kirchenberger, M. Marx, and D. Schroder, "A contribution to the design optimization of resonant inductors for high power resonant dc-dc converters," in *Industry Applications Society Annual Meeting, 1992., Conference Record of the 1992 IEEE*, oct 1992, pp. 994 –1001 vol.1.
- [47] J. Ferreira, "Appropriate modelling of conductive losses in the design of magnetic components," in *Power Electronics Specialists Conference, 1990. PESC '90 Record., 21st Annual IEEE*, 0-0 1990, pp. 780 –785.
- [48] —, "Analytical computation of ac resistance of round and rectangular litz wire windings," *Electric Power Applications, IEE Proceedings B*, vol. 139, no. 1, pp. 21 –25, jan 1992.
- [49] C. Sullivan, "Computationally efficient winding loss calculation with multiple windings, arbitrary waveforms, and two-dimensional or three-dimensional field geometry," *IEEE Trans. Power Electron.*, vol. 16, no. 1, pp. 142 –150, jan 2001.
- [50] W. Hurley, E. Gath, and J. Breslin, "Optimizing the ac resistance of multilayer transformer windings with arbitrary current waveforms," *IEEE Trans. Power Electron.*, vol. 15, no. 2, pp. 369 –376, mar 2000.
- [51] R. Wojda and M. Kazimierczuk, "Analytical optimization of solid-round-wire windings," *IEEE Trans. Ind. Electron.*, vol. 60, no. 3, pp. 1033 –1041, march 2013.
- [52] F. Robert, P. Mathys, and J.-P. Schauwers, "A closed-form formula for 2d ohmic losses calculation in smps transformer foils," in *Applied Power Electronics Conference and Exposition, 1999. APEC '99. Fourteenth Annual*, vol. 1, mar 1999, pp. 199 –205 vol.1.
- [53] *Maxwell 3D user's manual*, Ansoft Corporation, February 2009, REV4.0, Pittsburgh, USA, 2009.

- [54] R. Prieto, J. Oliver, and J. Cobos, "Study of non-axisymmetric magnetic components by means of 2d fea solvers," in *Power Electronics Specialists Conference, 2005. PESC '05. IEEE 36th*, june 2005, pp. 1074 –1079.
- [55] A. Hoke and C. Sullivan, "An improved two-dimensional numerical modeling method for e-core transformers," in *Applied Power Electronics Conference and Exposition, 2002. APEC 2002. Seventeenth Annual IEEE*, vol. 1, 2002, pp. 151 –157 vol.1.
- [56] A. Bossche and V. Valchev, *Inductors and Transformers for Power Electronics*, Taylor and Francis Group. CRC Press, 2005.
- [57] J.-P. Vandelac and P. Ziogas, "A novel approach for minimizing high-frequency transformer copper losses," *IEEE Trans. Power Electron.*, vol. 3, no. 3, pp. 266 –277, july 1988.
- [58] C. Hawkes, T. Wilson, and R. Wong, "Magnetic-field-intensity and current-density distributions in transformer windings," in *Power Electronics Specialists Conference, 1989. PESC '89 Record., 20th Annual IEEE*, jun 1989, pp. 1021 –1030 vol.2.
- [59] M. Bahmani and T. Thiringer, "A high accuracy regressive-derived winding loss calculation model for high frequency applications," in *Power Electronics and Drive Systems (PEDS), 2013 IEEE 10th International Conference on*, April 2013, pp. 358–363.
- [60] P. Evans and K. Al-Shara, "Losses in foil-wound secondaries in high-frequency transformers," *IEEE Trans. Magnet.*, vol. 25, no. 4, pp. 3125 –3132, jul 1989.
- [61] M. Heldwein, H. Ertl, J. Biela, and J. Kolar, "Implementation of a transformer-less common mode active filter for off-line converter systems," in *Applied Power Electronics Conference and Exposition, 2006. APEC '06. Twenty-First Annual IEEE*, march 2006, p. 7 pp.
- [62] W. F. Flanagan, *Handbook of Transformer Design and Applications, Second Edition*. McGraw-Hill, 1992.
- [63] M. Bartoli, N. Noferi, A. Reatti, and M. K. Kazimerczuk, "Modelling winding losses in high-frequency power inductors," *Journal of Circuits, Systems and Computers*, vol. 05, no. 04, pp. 607–626, 1995.
- [64] M. Albach, "Two-dimensional calculation of winding losses in transformers," in *Power Electronics Specialists Conference, 2000. PESC 00. 2000 IEEE 31st Annual*, vol. 3, 2000, pp. 1639 –1644 vol.3.

- [65] M. A. Bahmani, E. Agheb, T. Thiringer, H. K. Hidalen, and Y. Serdyuk, “Core loss behavior in high frequency high power transformers—i: Effect of core topology,” *Journal of Renewable and Sustainable Energy*, vol. 4, no. 3, p. 033112, 2012.
- [66] M. Wasekura, C.-M. Wang, Y. Maeda, and R. Lorenz, “A transient core loss calculation algorithm for soft magnetic composite material,” in *Energy Conversion Congress and Exposition (ECCE), 2013 IEEE*, 2013, pp. 3719–3725.
- [67] Z. Ouyang, O. Thomsen, and M. A. E. Andersen, “The analysis and comparison of leakage inductance in different winding arrangements for planar transformer,” in *Power Electronics and Drive Systems, 2009. PEDS 2009. International Conference on*, Nov 2009, pp. 1143–1148.
- [68] F. de Leon, S. Purushothaman, and L. Qaseer, “Leakage inductance design of toroidal transformers by sector winding,” *IEEE Trans. Power Electron.*, vol. 29, no. 1, pp. 473–480, Jan 2014.
- [69] J. Li, C. Hu, and X. Pang, “Analysis of the leakage inductance of planar transformer,” in *Electronic Measurement Instruments, 2009. ICEMI '09. 9th International Conference on*, Aug 2009, pp. 1–273–1–276.
- [70] J. Collins, “An accurate method for modeling transformer winding capacitances,” in *Industrial Electronics Society, 1990. IECON '90., 16th Annual Conference of IEEE*, Nov 1990, pp. 1094–1099 vol.2.
- [71] F. Blache, J.-P. Keradec, and B. Cogitore, “Stray capacitances of two winding transformers: equivalent circuit, measurements, calculation and lowering,” in *Industry Applications Society Annual Meeting, 1994., Conference Record of the 1994 IEEE*, Oct 1994, pp. 1211–1217 vol.2.
- [72] A. Alonso, J. Sebastian, D. Lamar, M. Hernando, and A. Vazquez, “An overall study of a dual active bridge for bidirectional dc/dc conversion,” in *Energy Conversion Congress and Exposition (ECCE), 2010 IEEE*, Sept 2010, pp. 1129–1135.
- [73] M. A. Bahmani, “Design and optimization of hf transformers for high power dc-dc applications,” Licentiate Thesis, Chalmers University of Technology, Gothenburg, Sweden, April 2014.
- [74] A. Pernia, F. Nuno, E. Corominas, and J. Lopera, “Resonant converter controlled by variable leakage inductance in the transformer (lic),” in *Power Electronics and Applications, 1993., Fifth European Conference on*, Sep 1993, pp. 124–129 vol.3.

- [75] B. Nathan and V. Ramanarayanan, "Analysis, simulation and design of series resonant converter for high voltage applications," in *Industrial Technology 2000. Proceedings of IEEE International Conference on*, vol. 1, Jan 2000, pp. 688–693 vol.2.
- [76] N. Mohan, T. Undeland, and W. Robbins, *Power electronics Converter, Applications and Design, Second Edition*. John Wiley and Sons Inc, 1995.
- [77] A. Dauhajre and R. Middlebrook, "modeling and estimation of leakage phenomenon in magnetic circuits," in *Power Electronics Specialists Conference, 1986. PESC, 1986*, pp. 213–226.
- [78] S. R. Thondapu, M. B. Borage, Y. D. Wanmode, and P. Shrivastava, "Improved expression for estimation of leakage inductance in e core transformer using energy method," *Advances in Power Electronics*, vol. 2012, no. 635715, pp. 1–6, 2012.
- [79] A. Jahromi, J. Faiz, and H. Mohseni, "Calculation of distribution transformer leakage reactance using energy technique," 1986.
- [80] V. Krantor, "methods of calculating leakage inductance of transformer windings," vol. 80, 2009, pp. 214–218.
- [81] W. Hurley and D. Wilcox, "Calculation of leakage inductance in transformer windings," *IEEE Trans. Power Electron.*, vol. 9, no. 1, pp. 121–126, Jan 1994.
- [82] P. Wilson and R. Wilcock, "Advanced electromagnetics," vol. 1, no. 3, 2012.
- [83] V. Niemela, G. Skutt, A. Urling, Y.-N. Chang, T. Wilson, J. Owen, H.A, and R. Wong, "Calculating the short-circuit impedances of a multiwinding transformer from its geometry," in *Power Electronics Specialists Conference, 1989. PESC '89 Record., 20th Annual IEEE*, Jun 1989, pp. 607–617 vol.2.
- [84] W. Hurley and W. Wolfe, *Transformers and Inductors For Power Electronics, Theory, Design and Applications, First Edition*. John Wiley Sons Ltd, 2013.
- [85] M. A. Bahmani and T. Thiringer, "An accurate frequency-dependent analytical expression for leakage inductance calculation in high frequency transformers," in *PCIM South America 2014. The International Conference*, Oct 2014, pp. 275–282.
- [86] W. Roshen, "A practical, accurate and very general core loss model for non-sinusoidal waveforms," *IEEE Trans. Power Electron.*, vol. 22, no. 1, pp. 30–40, Jan 2007.



- [87] R. Liu, C. Mi, and D. Gao, "Modeling of eddy-current loss of electrical machines and transformers operated by pulsewidth-modulated inverters," *IEEE Trans. Magnet.*, vol. 44, no. 8, pp. 2021–2028, Aug 2008.
- [88] I. Villar, U. Viscarret, I. Etxeberria-Otadui, and A. Rufer, "Global loss evaluation methods for nonsinusoidally fed medium-frequency power transformers," *IEEE Trans. Ind. Electron.*, vol. 56, no. 10, pp. 4132–4140, Oct 2009.
- [89] Y. Nie, Q. Hu, and Y. Huang, "The measurement and prediction of iron loss under nonsinusoidal voltage waveform with arbitrary frequency," in *Electrical Machines and Systems, 2008. ICEMS 2008. International Conference on*, Oct 2008, pp. 232–236.
- [90] G. Dimitrakakis and E. Tatakis, "High-frequency copper losses in magnetic components with layered windings," *IEEE Trans. Magnet.*, vol. 45, no. 8, pp. 3187–3199, Aug 2009.
- [91] W. Shen, F. Wang, D. Boroyevich, and C. Tipton, "Loss characterization and calculation of nanocrystalline cores for high-frequency magnetics applications," *IEEE Trans. Power Electron.*, vol. 23, no. 1, pp. 475–484, Jan 2008.
- [92] M. Rylko, K. Hartnett, J. Hayes, and M. Egan, "Magnetic material selection for high power high frequency inductors in dc-dc converters," in *Applied Power Electronics Conference and Exposition, 2009. APEC 2009. Twenty-Fourth Annual IEEE*, Feb 2009, pp. 2043–2049.
- [93] B. Lyons, J. Hayes, and M. Egan, "Magnetic material comparisons for high-current inductors in low-medium frequency dc-dc converters," in *Applied Power Electronics Conference, APEC 2007 - Twenty Second Annual IEEE*, Feb 2007, pp. 71–77.
- [94] Y. Han, G. Cheung, A. Li, C. Sullivan, and D. Perreault, "Evaluation of magnetic materials for very high frequency power applications," in *Power Electronics Specialists Conference, 2008. PESC 2008. IEEE*, June 2008, pp. 4270–4276.
- [95] [Online]. Available: <http://www.jfe-steel.co.jp/>
- [96] [Online]. Available: <http://www.metglas.com/>
- [97] [Online]. Available: <http://www.ferroxcube.com/>
- [98] [Online]. Available: <http://www.mag-inc.com/>
- [99] [Online]. Available: <http://www.vacuumschmelze.com/>

- [100] [Online]. Available: <http://www.hitachimetals.com/>
- [101] J. Pedro, B. A., and S. N., *Electromagnetic modeling by finite element methods*. Markel Dekker, 2003.
- [102] D. Jiles and D. Atherton, "Theory of ferromagnetic hysteresis," *Journal of Magnetism and Magnetic Materials*, vol. 61, no. 12, pp. 48 – 60, 1986.
- [103] B. Lederer, H. Igarashi, A. Kost, and T. Honma, "On the parameter identification and application of the jiles-atherton hysteresis model for numerical modelling of measured characteristics," *IEEE Trans. Magnet.*, vol. 35, no. 3, pp. 1211–1214, May 1999.
- [104] G. Bertotti, *Hysteresis in magnetism*. Academic press, San diego, 1998.
- [105] —, "General properties of power losses in soft ferromagnetic materials," *IEEE Trans. Magnet.*, vol. 24, no. 1, pp. 621–630, Jan 1988.
- [106] D. Ribbenfjard, *Electromagnetic transformer modelling including the ferromagnetic core*, 2010, Stockholm.
- [107] D. Lin, P. Zhou, W. N. Fu, Z. Badics, and Z. Cendes, "A dynamic core loss model for soft ferromagnetic and power ferrite materials in transient finite element analysis," *IEEE Trans. Magnet.*, vol. 40, no. 2, pp. 1318–1321, March 2004.
- [108] M. Mobarrez, M. Fazlali, M. A. Bahmani, and T. Thiringer, "Performance and loss evaluation of a hard and soft switched 2.4 mw, 4 kv to 6 kv isolated dc-dc converter for a wind energy application," in *IECON 2012 - 38th Annual Conference on IEEE Industrial Electronics Society*, Oct 2012, pp. 5086–5091.
- [109] C. Steinmetz, "On the law of hysteresis," *American Institue of Electrical Engineers Transactions*, vol. 9, pp. 3–64, 1982.
- [110] R. Severns, "Hf-core lossesfor non-sinusoidal waveforms," in *Proceedings of HFPC*, 1991, pp. 140–148.
- [111] J. Reinert, A. Brockmeyer, and R. W. De Doncker, "Calculation of losses in ferro- and ferrimagnetic materials based on the modified steinmetz equation," in *Industry Applications Conference, 1999. Thirty-Fourth IAS Annual Meeting. Conference Record of the 1999 IEEE*, vol. 3, 1999, pp. 2087–2092 vol.3.
- [112] J. Li, T. Abdallah, and C. Sullivan, "Improved calculation of core loss with nonsinusoidal waveforms," in *Industry Applications Conference, 2001. Thirty-Sixth IAS Annual Meeting. Conference Record of the 2001 IEEE*, vol. 4, Sept 2001, pp. 2203–2210 vol.4.

- [113] K. Venkatachalam, C. Sullivan, T. Abdallah, and H. Tacca, "Accurate prediction of ferrite core loss with nonsinusoidal waveforms using only steinmetz parameters," in *Computers in Power Electronics, 2002. Proceedings. 2002 IEEE Workshop on*, June 2002, pp. 36–41.
- [114] A. Van den Bossche, V. Valchev, and G. Georgiev, "Measurement and loss model of ferrites with non-sinusoidal waveforms," in *Power Electronics Specialists Conference, 2004. PESC 04. 2004 IEEE 35th Annual*, vol. 6, June 2004, pp. 4814–4818 Vol.6.
- [115] W. Shen, "Design of high-density transformer for high frequency high power converters," Ph.D. dissertation, Virginia Polytechnic Institute.
- [116] [Online]. Available: <http://en.tdk.eu/>
- [117] I. Villar, "Multiphysics characterization of medium-frequency power electronic transformer," Ph.D. dissertation, EPFL, Lausanne, Switzerland, 2010.
- [118] [Online]. Available: <http://www.coolpolymers.com/>
- [119] [Online]. Available: [http://www.kayelaby.npl.co.uk/general\\_physics/2.6/2.6\\_5.html](http://www.kayelaby.npl.co.uk/general_physics/2.6/2.6_5.html)
- [120] [Online]. Available: <http://www.rfcafe.com/references/electrical/dielectric-constants-strengths.htm>
- [121] E. Agheb, M. A. Bahmani, H. K. Hoidalén, and T. Thiringer, "Core loss behavior in high frequency high power transformers—ii: Arbitrary excitation," *Journal of Renewable and Sustainable Energy*, vol. 4, no. 3, p. 033113, 2012.
- [122] M. A. Bahmani and T. Thiringer, "Accurate evaluation of leakage inductance in high frequency transformers using an improved frequency-dependent expression," *IEEE Trans. Power Electron.*, vol. PP, no. 99, pp. 1–1, 2014.
- [123] M. Bahmani, T. Thiringer, and M. Kharezy, "Design methodology and optimization of a medium frequency transformer for high power dc-dc applications," in *Applied Power Electronics Conference and Exposition (APEC), 2015 IEEE*, March 2015, pp. 2532–2539.
- [124] W.-J. Gu and R. Liu, "A study of volume and weight vs. frequency for high-frequency transformers," in *Power Electronics Specialists Conference, 1993. PESC '93 Record., 24th Annual IEEE*, Jun 1993, pp. 1123–1129.
- [125] J. Holman, *Heat Transfer, 8th Edition*. McGraw-Hill, New York, 1997.

- [126] [Online]. Available: <http://multimedia.3m.com/mws/media/920152O/3mtm-thermally-conductive-adhesive-tape-8940-tds.pdf>
- [127] J. Muhlethaler, J. Biela, J. Kolar, and A. Ecklebe, "Core losses under the dc bias condition based on steinmetz parameters," *IEEE Trans. Power Electron.*, vol. 27, no. 2, pp. 953–963, Feb 2012.
- [128] K. Lee, K. Jung, Y. Suh, C. Kim, H. Yoo, and S. Park, "Comparison of high power semiconductor devices losses in 5mw pmsg mv wind turbines," in *Applied Power Electronics Conference and Exposition (APEC), 2014 Twenty-Ninth Annual IEEE*, March 2014, pp. 2511–2518.
- [129] R. Barrera-Cardenas and M. Molinas, "Comparative study of the converter efficiency and power density in offshore wind energy conversion system with single-phase transformer," in *Power Electronics, Electrical Drives, Automation and Motion (SPEEDAM), 2012 International Symposium on*, June 2012, pp. 1085–1090.
- [130] —, "Comparison of wind energy conversion systems based on high frequency ac-link: Three-phase vs. single-phase," in *Power Electronics and Motion Control Conference (EPE/PEMC), 2012 15th International*, Sept 2012, pp. LS2c.4-1–LS2c.4-8.
- [131] H. Qin and J. Kimball, "A comparative efficiency study of silicon-based solid state transformers," in *Energy Conversion Congress and Exposition (ECCE), 2010 IEEE*, Sept 2010, pp. 1458–1463.
- [132] W. Chen, A. Q. Huang, C. Li, G. Wang, and W. Gu, "Analysis and comparison of medium voltage high power dc/dc converters for offshore wind energy systems," *IEEE Trans. Power Electron.*, vol. 28, no. 4, pp. 2014–2023, April 2013.
- [133] C. Zhan, C. Smith, A. Crane, A. Bullock, and D. Grieve, "Dc transmission and distribution system for a large offshore wind farm," in *AC and DC Power Transmission, 2010. ACDC. 9th IET International Conference on*, Oct 2010, pp. 1–5.
- [134] M. Jimenez Carrizosa, A. Benchaib, P. Alou, and G. Damm, "Dc transformer for dc/dc connection in hvdc network," in *Power Electronics and Applications (EPE), 2013 15th European Conference on*, Sept 2013, pp. 1–10.
- [135] F. C. Schwarz, "A method of resonant current pulse modulation for power converters," *IEEE Trans. Indust. Electron. Contr. Instrum.*, vol. IECI-17, no. 3, pp. 209–221, May 1970.

- 
- [136] —, “An improved method of resonant current pulse modulation for power converters,” *IEEE Trans. Indust. Electron. Contr. Instrum.*, vol. IECI-23, no. 2, pp. 133–141, May 1976.
- [137] R. Steigerwald, R. De Doncker, and M. Kheraluwala, “A comparison of high-power dc-dc soft-switched converter topologies,” *IEEE Trans. Ind. Appl.*, vol. 32, no. 5, pp. 1139–1145, Sep 1996.
- [138] P. M. Dushan, G., “Igbt power losses calculation using the data-sheet paramters,” Infineon, , Application Note, V1.1 , January 2009, .
- [139] —, “Mosfet power losses calculation using the data-sheet paramters,” Infineon, , Application Note, V1.1 , July 2006, .
- [140] A. Rabiei, “Energy efficiency of an electrical vehicle propulsion inverter using various semiconductor technologies,” Licentiate Thesis, Chalmers Univeristy of Technology, 2013.
- [141] M. Rauls, D. Novotny, and D. Divan, “Design considerations for high-frequency coaxial winding power transformers,” *IEEE Trans. Ind. Appl.*, vol. 29, no. 2, pp. 375–381, Mar 1993.
- [142] G. Ortiz, J. Biela, D. Bortis, and J. Kolar, “1 megawatt, 20 khz, isolated, bidirectional 12kv to 1.2kv dc-dc converter for renewable energy applications,” in *Power Electronics Conference (IPEC), 2010 International*, june 2010, pp. 3212 –3219.
- [143] I. Villar, A. Garcia-Bediaga, U. Viscarret, I. Etxeberria-Otadui, and A. Rufer, “Proposal and validation of medium-frequency power transformer design methodology,” in *Energy Conversion Congress and Exposition (ECCE), 2011 IEEE*, Sept 2011, pp. 3792–3799.